UNIVERSITY OF SOUTHAMPTON
FACULTY OF ENGINEERING, SCIENCE AND MATHEMATICS
School of Ocean and Earth Sciences

Antarctic Climate: Ocean fluxes and variability

Thesis for the degree of Doctor of Philosophy

by

Adam Peter Williams

September 2007

Graduate School of the

National Oceanography Centre, Southampton

This PhD dissertation by

Adam Williams

has been produced under the supervision of the following persons

Supervisor/s

Sheldon Bacon
Eelco Rohling

Chair of Advisory Panel

Peter Killworth

Member/s of Advisory Panel

George Nurser

UNIVERSITY OF SOUTHAMPTON

Abstract

FACULTY OF ENGINEERING, SCIENCE AND MATHEMATICS
School of Ocean and Earth Sciences
Doctor of Philosophy

Antarctic Climate: Ocean fluxes and variability

by Adam Peter Williams

The Southern Ocean plays a major role in the global overturning circulation, providing an important route for the return flow of deep water subducted in the North Atlantic. The World Ocean Circulation Experiment (WOCE) provided an unprecedented picture of the state of the world's oceans and set new standards for high quality in-situ hydrographic data. This study combines the existing WOCE data set with new hydrographic sections, and output from global and regional ocean models to examine the mean state of the Southern Ocean circulation and the balance of fluxes around the Antarctic Circumpolar current.

A historical data set in the region of Drake Passage is examined to study the large-scale water mass variability between 1926-2005. The water mass properties of the Lower Circumpolar Deep Water is constant within error bounds throughout the data set. A warming and freshening signal in the surface waters from 1997-2005 to the north of the Sub-Antarctic Front along SR01b is also presented.

The major part of this work is based around an inverse study of the Southern Ocean that combines the WOCE data-set with contemporary sections, and other forcing fields to examine the balance of fluxes throughout the Southern Ocean. The study examines the effect of different parameterisations of the dianeutral mixing in the Southern Ocean, in light of the differing views of localised deep turbulent mixing from observations, and an adiabatic ocean interior from residual mean studies, The freshwater balance in the model is presented and its implications on the water mass formation and transformation of the upper and lower cells of the overturning circulation is discussed in detail.

Contents

List of Tables

Table 4.1: Meridional property transports from Inverse studies across WOCE lines A10 and A11, adapted from McDonagh and King (2005). A northward net flux is positive.

Table 4.2: Details of additional constraints applied to the model in the Atlantic sector, and the model solution. The errors stated are from the residual noise terms from each conservation equation related to the individual constraints. Specific details of constraint boundaries are given in Appendix AD.

Table 4.3: A table of flux estimates from a range of studies in the Indian Ocean. A positive flux is northward.

Table 4.4: A table showing a compilation of fluxes from selected studies across P6/32 S in the Pacific Ocean.

Table 6.1. A summary of the fluxes across major sections around the Southern Ocean from the main model runs. The errors are not shown, but due to the method of error definition, the a-posteriori error ranges are all similar to the errors from the standard solution.

List of Figures

Figure 1.1: Taken from Olbers and Visbeck (2005). A schematic representation of the Southern Ocean meridional overturning circulation adapted from Speer et al. (2000). Definitions of water masses (AABW, NADW, UCDW, AAIW) are given in chapter 2.

Figure 1.2: Adapted from Marshall and Radko (2003). Schematic representation of the Eulerian mean and eddy streamfunctions ($\overline{\psi},\psi^*$) in the region of the ACC.

Figure 1.3: Taken from Gille (2002). Annual gridded temperature trends (° C/year), between 700-1100m between historical hydrographic record and ALACE floats (1990's).

Figure 2.1: Mean frontal locations from observational data, taken from Southern Ocean Database (Orsi and Whitworth 2005), STF=Sub-Tropical Front, SAF=Sub-Antarctic Front, PF=Polar Front, SACCF=Southern ACC Front, SB=Southern Boundary.

Figure 2.2: Salinity distribution at SR1b line across Drake Passage, taken from a mean of 11 NOC/BAS sections (1993-2005), averaged onto a uniform grid with latitude as the horizontal co-ordinate. (Dark=fresh, light =saline). A schematic of the main water mass locations is included. SASW=Sub-Antarctic surface water. AASW=Antarctic Surface Water, SAMW=Sub-Antarctic Mode Water, AAIW=Antarctic Intermediate Water, U/LCDW= Upper/Lower Circumpolar Deep Water, SEPDW=Southeast Pacific Deep Water (a regional variety of LCDW), WSDW=Weddell Sea Deep Water.

Figure 2.3: Map of the Drake Passage sector of the Southern Ocean. The three main section locations, SR01, SR01b and SR01W are marked by red dots. The mean positions of the three main fronts at Drake Passage (SAF,PF,SACCF) (Orsi et al. 1995) are marked by yellow lines. FI=Falkland Islands, TF= Tierra del Fuego, SFZ=Shackleton Fracture Zone, EI=Elephant Island.

Figure 2.4: Upper Segment: Geostrophic Velocity profile referenced to the deepest common level from the 1996 NOC/BAS section along SR01b. The main frontal positions are marked. The black dots mark the location of the LCDW salinity maximum (see figure 2.2 for the mean salinity structure at Drake Passage). Lower segment: Salinity of LCDW salinity maximum surface (red) and mean salinity on 250m thick layer centred on the salinity maximum surface (blue).

Figure 2.5: Mean salinity (top/blue) and potential temperature (bottom/red) values of the LCDW salinity maximum at Drake Passage vs. time (1926-2005). The black dashed lines represent the mean from 1970-2005. Error bars include a combination of the systematic and standard errors and an additional bias due to bottle sampling where appropriate.

Figure 2.6: Mean Salinity (S)(top) and Potential Temperature (θ)(bottom) from CTD sections (1990-2005)- showing mean S/θ values at the salinity maximum (thick blue lines), and on three iso-neutral surfaces (γ^n=28.07-28.08 kg/m^3 (red), γ^n=28.08-28.09 kg/m^3 (black) and γ^n=28.09-28.10 kg/m^3 (green)). Error bars are ±1 standard error.

Figure 2.7: Top: Mean baroclinic transport in neutral density layers, with a thickness of 0.02kg/m^3 for the NOC/BAS SR01b sections (1993-2005). The yellow envelope is ±1 standard deviation. Bottom: Baroclinic transports from the NOC/BAS sections (black line), with mean (thick dashed red line), and ±1 standard deviation (dash-dot lines).

Figure 2.8: Mean properties on neutral density surfaces in the NOC/BAS SR1b sections focussing on the upper intermediate waters/ SAMW (γ^n=27.10-27.35 kgm^{-3}). Top: Potential Temperature (° C) with contour spacing of 0.2 °C. Bottom: Salinity (psu) with contour spacing 0.02 psu.

Figure 2.9: Top panel: Geostrophic transport across Drake Passage in the density layers > 28.26 kgm^{-3} associated with WSDW, and (bottom panel): Polar Front location from the NOCS/BAS SR01b hydrographic sections.

Figure 2.10: A time-series of transport per unit density on neutral density surfaces from the SR01b NOC/BAS repeat hydrographic data-set. The transport is calculated in bins of 0.04 kgm^{-3}.

Figure 3.1 Mean fields of Windstress (top), Net Heat flux (middle), and Freshwater flux (bottom) from NOC Climatology (Grist and Josey, 2003). AUS=Australia, AF=Africa, SA=South America. A positive/negative flux is out of/into the ocean.

Figure 3.2: The locations of the hydrographic stations forming the boxes of the standard configuration of the Southern Ocean Inverse Model.

Figure 3.3: Transport variability on neutral density surfaces across SR1 from a.) SR01b sections (1993-2005) (red), b.) OCCAM 1/4° Model run 202, 1992-1997, five-day means (blue-thick), c.) same as b,), but divided by 2 for comparison with a.) (blue-dashed).

Figure 3.4: An Example of correction velocities (top) and posteriori errors (bottom) along I05 (see Appendix $$) from an Indian Ocean Sector Box model, comparing different correlation schemes in the a-priori error covariance matrix: no station correlation (black), small cross-correlation (blue), large cross-correlation (green).

Figure 3.5: Top: Cumulative zonal transport (moving northwards) taken from the BRIOS mean fields. Bottom: Cumulative meridional transport on latitude circles, starting from zero at 180 °E.

Figure 3.6: Vertically integrated transport vectors from the BRIOS mean field focusing on the flow field in the region of Prydz Bay and the Kerguelen Plateau.

Figure 3.7. a.) The distribution function of turbulent eddy diffusivities (k) calculated from stations located in the Indian Ocean box 3 (see figure 3.2) from the WOCE data-set. The thick blue line shows the location of the mean value of k (0.0024 m^{2}s^{-1}). The thick red line shows the location of the statistic obtained from the mean of log(k). b.) Probability distribution function of log(k), showing a Gaussian-like structure (Red line: mean log(k)=-9.21, equivalent to k=0.00010 m^{2}s^{-1}).

Figure 3.8: Turbulent eddy diffusivity coefficients (m^2s^{-1}) calculated from stations within each model box. The blue line represents the modified mean values on neutral density surfaces, the dashed red line represents the standard mean that is biased by large values.

Figure 4.1: Schematic diagram of the Southern Ocean Inverse model showing the division of the model domain into three sectors (Atlantic, Indian and Pacific Oceans). The red arrow represents the ACC, which forms the dominant flow structure in the Southern Ocean. The purple arrows do not represent water mass fluxes.

Figure 4.2: A topographic map of the Atlantic Sector of the Southern Ocean detailing the important features. MAR=Mid-Atlantic Ridge. Red lines show locations of hydrographic sections forming the boundaries of boxes 1 and 2.

Figure 4.3: Schematic representation of the standard Inverse model for the Atlantic sector of the Southern Ocean. The Box is divided into five core neutral density layers: Surface waters (γ^n=25.00-27.10 kgm^{-3}); Intermediate/Mode waters (γ^n=27.10-27.65 kgm^{-3}); Upper Circumpolar Water (γ^n=27.65-27.95 kgm^{-3}); Lower Circumpolar Water (γ^n=27.95-28.18 kgm^{-3}); and Antarctic Deep/Bottom Water and ACCbw (γ^n=28.18-28.50 kgm^{-3}). The directions of advective dianeutral fluxes are depicted by the cylinders, with flow into or out of each respective layer. Fluxes are shown in Sv ($1x10^6$ m^3s^{-1}).

Figure 4.4: A topographic map of the Indian Ocean sector of the Southern Ocean. Hydrographic stations are shown by red dots. NV= Natal valley; MOB=Mozambique Basin; MAB= Madagascar Basin; CIB= Central Indian Basin; NER= Ninety-East Ridge; WAB= West Australian Basin; BP= Broken Plateau; SAB= South Australian Basin; PET= Princess Elizabeth Trough; PB= Prydz Bay; CS= Cosmonaut Sea.

Figure 4.5: Schematic representation of the standard Inverse model for the Indian sector of the Southern Ocean. The Box is divided into five core neutral density layers: Surface waters (γ^n=25.00-27.10 kgm^{-3}); Intermediate/Mode waters (γ^n=27.10-27.65 kgm^{-3}); Upper Circumpolar Water (γ^n=27.65-27.95 kgm^{-3}); Lower Circumpolar Water (γ^n=27.95-28.18 kgm^{-3}); and Antarctic Deep/Bottom Water and ACCbw (γ^n=28.18-28.50 kgm^{-3}). The direction of advective dianeutral fluxes are depicted by the cylinders, with flow into or out of each respective layer. Fluxes are shown in Sv ($1x10^6$ m^3s^{-1}).

Figure 4.6: Meridional Overturning Circulation (Cumulative transport from sea floor) in depth and neutral density co-ordinates. Black line: overturning streamfunction calculated on density surfaces, blue line: overturning streamfunction calculated on depth surfaces.

Figure 4.7: A topographic map of the Pacific Ocean sector of the Southern Ocean. Hydrographic stations are shown by red dots. SFB= South Fiji Basin; KT= Kermadec Trench; CP= Campbell Plateau; AS= Amundsen Sea; BHS= Bellingshausen Sea; DP= Drake Passage.

Figure 4.8: Schematic representation of the standard Inverse model for the Pacific sector of the Southern Ocean. The Box is divided into five core neutral density layers: Surface waters (γ^n=25.00-27.10 kgm^{-3}); Intermediate/Mode waters (γ^n=27.10-27.65

kgm^{-3}); Upper Circumpolar Water (γ^n=27.65-27.95 kgm^{-3}); Lower Circumpolar Water (γ^n=27.95-28.18 kgm^{-3}); and Antarctic Deep/Bottom Water and ACCbw (γ^n=28.18-28.50 kgm^{-3}). The direction of advective dianeutral fluxes are depicted by the cylinders, with flow into or out of each respective layer. Fluxes are shown in Sv (1x10^6 m^{3}s^{-1}).

Figure 4.9: a.) Total Mass fluxes (and errors) from the Standard Inverse Model (Sv). b.) Total heat/Potential Temperature fluxes across the box boundaries from the Standard Inverse Model (1x10^{13}W).

Figure 4.10: Mass Imbalance component of solution error from the mass conservation layer equations for each box 1-9 (black line). The a-priori error determined from the OCCAM model is shown by the red region. The yellow region shows the posteriori model error for each box. Each box contains 20 layers, but for clarity, the errors are plotted vs. neutral density rather than layer number. Boxes 9-11 are not shown as some equations were removed from the solution because these boxes only contain denser water masses.

Figure 4.11: Dianeutral velocities (w*, ms^{-1}) for boxes 1-9 from the standard solution (black lines). The a-priori error boundaries are in blue, and the a-posteriori error bounds are shown by the yellow region.

Figure 4.12: Dianeutral advective transports (in Sv) for boxes 1-9 from the standard solution (black lines). The a-priori error boundaries are in blue, and the a-posteriori error bounds are shown by the yellow region.

Figure 4.13: Dianeutral effective diffusivities (k*, m^{2}s^{-1}) for boxes 1-9 from the standard solution (black lines). The a-priori error boundaries are in blue, and the a-posteriori error bounds are shown by the yellow region.

Figure 4.14: Conversion chart between neutral density surfaces and mean depths obtained from the WOCE Climatology of the Southern Ocean (Gouretski 2004).

Figure 4.15: Air-Sea freshwater fluxes from the model solution. Black line=flux from NOC climatology. Dashed blue line = corrections to flux from model solution (indistinguishable from initial flux). Yellow region = A-posteriori error boundaries.

Figure 4.16: Air-sea heat fluxes due to exchanges with the atmosphere (positive flux=out of the ocean). Black line=flux from NOC climatology. Dashed blue line=corrected flux, Yellow region=a-priori error boundary. Red regions=a-priori error boundaries (in most cases indistinguishable from the a-posteriori errors).

Figure 4.17: Dianeutral air-sea flux induced mass flux (kg/s). Black line= Initial fluxes derived from NOC Climatology. Dashed blue line= correction to flux from model solution, red region= a-priori error boundary, yellow region= a-posteriori error boundary. A positive flux is into a denser layer.

Figure 5.1: Transport on 0.01 kgm^{-3} neutral density surfaces from the model solution at the three major ACC choke points, SR01-Drake Passage (black), I06-Africa (blue) and SR03-Australia (red).

Figure 5.2: Fluxes and circulation on the three model layers representing the Intermediate waters: γ^n=26.90-27.20 kgm^{-3} (Top of the SAMW); γ^n=27.20-27.40 kgm^{-3} (SAMW/AAIW); and γ^n=27.40-27.60 kgm^{-3} (AAIW). The direction of diapycnal fluxes is show for each box, with the magnitude of significant fluxes shown (small lettering). The fluxes are in Sv and represent the total flux across the section, with significant re-circulations shown by the curved arrows.

Figure 5.3: Fluxes and circulation on the three model layers representing the Upper Circumpolar Deep Water (UCDW): γ^n=27.60-27.70 kgm^{-3} (Top of the UCDW); γ^n=27.70-27.90 kgm^{-3} (core of UCDW); and γ^n=27.90-27.98 kgm^{-3} (bottom of UCDW/top of LCDW). The direction of diapycnal fluxes are show for each box, with the magnitude of significant fluxes greater than errors shown (small lettering). The fluxes are in Sv and represent the total flux across the section, with significant re-circulations shown by the curved arrows.

Figure 5.4: Salinity (blue) and Potential Temperature (red) difference between the mean property values on the zonal faces of box 3 (I06 value minus I08 value).

Figure 5.5: Mean Salinity/Potential temperature relationships on model density layers around the Southern Ocean, centred on the LCDW, from selected sections, I06/30 E (blue), I08/85 E (red), SR03/140 E (green), 170 W/P15 (yellow), and SR01b (black). Top: Salinity (psu) vs. neutral density (kgm^{-3}); Middle: Potential temperature (°C) vs. neutral density (kgm^{-3}); Bottom: Salinity vs. Potential Temperature plot.

Figure 5.6: A schematic representation of the model solution on three neutral density layers associated with the LCDW (γ^n=27.94-28.02 kgm^{-3} (top), γ^n=28.02-28.10 kgm^{-3} (middle), γ^n=28.10-28.18 kgm^{-3} (bottom)). The direction of dianeutral fluxes at the upper and lower interfaces of each layer for each box are shown by the vertical arrows. Significant meridional transports are shown (Sv).

Figure 5.7: Cumulative total transport around the southern boundary of the box (Sv), integrated eastward from the Weddell Sea (50° W). Positive/upward transports are northward. There is a net imbalance of 0.5 Sv across the southern boundary.

Figure 5.8: Cumulative transport on the deepest model layer (γ^n=28.27-28.45 kgm^{-3}), associated with AABW. The main regions of net northward transport and AABW export are located on the figure. The total northward transport is 14.6 Sv.

Figure 5.9: Cumulative transport on two density layers integrated eastward around the southern boundary of the box model from the Weddell Sea (50 °W). The blue line represents the density layer γ^n=28.18-28.27 kgm^{-3}, associated with ACCbw. the green line (γ^n=28.02-28.18 kgm^{-3}) covers the LCDW.

Figure 5.10: Left: Cumulative East-to-West (right-to-left) transport on neutral density surfaces across the Weddell Sea. Right: Total transport on neutral density surfaces in the ACCbw (γ^n=28.18-28.27 kgm^{-3}) and AABW (γ^n=28.27-28.45 kgm^{-3}) in layers of thickness 0.02 kgm^{-3}. In both figures, a positive transport is northward.

Figure 5.11.a: Cumulative West-East (right to left) transport on density layers of thickness 0.02kgm^{-3}. The dashed line shows the boundary between the AACbw and AABW.

Figure 5.11.b: Oxygen concentrations (μmols/kg) averaged on density surfaces (of thickness 0.02 kgm^{-3}) in the bottom two density layers in the box model around the Southern boundary between 100°E and 80 °W.

Figure 5.12: a.) Meridional overturning streamfunction at 30° S in Atlantic Ocean (black), Indian Ocean (red) and Pacific Ocean (blue), summed on density layers and integrated from the surface. The dashed lines represent ± correlated layer flux uncertainties from the posterior error matrix. b.) Total Meridional overturning circulation on depth layers (blue), and net meridional transport on neutral density layers (black-dashed) plotted with a representative depth scale.

Figure 5.13: Model transports on density layers associated with the upper (top panel) and lower (bottom panel) across the 30 °S boundary. Yellow=total transport, blue= transport across A10 (Atlantic), red=transport across I05 (Indian), and black= transport across P6 (Pacific). Positive transports are northwards.

Figure 6.1: Effective diffusivities from the standard model run (blue), and from the model run with property-specific diffusivity coefficients, salt (black) and heat (red). It is plotted on a representative depth co-ordinate, but the flux is across constant neutral density surfaces. The yellow region shows the a-posteriori errors from the standard model solution.

Figure 6.2: Dianeutral velocities from model run with property-specific advective velocities. Mass (blue), salt (black), and heat (red). The a-posteriori errors are shown by the yellow region.

Figure 6.3: Dianeutral tracer-specific velocities, mass (blue), salt anomaly (black) and heat (red) (all ms^{-1}). Velocities are plotted on a representative depth scale, and are velocities on neutral density surfaces.

Figure 6.4: Representative Effective diffusivity coefficients calculated from the model run with property-specific dianeutral velocities from the salt velocity (blue), the heat velocity (red). The mean strain-derived eddy diffusivities from the WOCE data set (see chapter 3.5.1) are shown (black line).

Figure 6.5: (Left) Dianeutral velocities from the standard model (blue), tracer-specific diffusivity coefficients (black) and tracer-specific advective velocities (red). (Right) total volume transports from the same model runs.

Figure 6.6: Top: Meridional overturning integrated from depth across the I05 Indian Ocean section (WOCE (red), 2002 (blue)). The magnitude and location of the deep overturning maximum is noted. Bottom: Cumulative transport along the P6 Pacific section (WOCE (red), 2003 (blue)), from west to east.

Figure 6.7: A comparison of the overturning streamfunctions across the Atlantic (left) and Pacific Oceans (right panel) at 30 °S using the WOCE data (black line) and the

2002/2003 sections (red line). The dashed lines represent error limits calculated from the a-posteriori error matrix.

Figure 6.8: Mean volume/heat transport across Drake Passage: Mean ± 1 standard deviation from SR1b hydrographic data (red region); Model solutions using SR1b data (1993-2006) (blue region). The model mean transport is shown by the black line and the mean of the data is shown by the dashed yellow line.

Figure 7.1: Mean salinity (top) and temperature (bottom) of the surface layer (top 75m) in the locations of the Polar Front (blue) and Southern boundary (black) from monthly fields from the WOA2005 Climatology (Locarnini et al. 2005). The annual mean values are shown for each front.

Figure 7.2: Schematic diagram of the freshwater forcing on the upper and lower overturning cells of the Southern Ocean. P-E= Precipitation - Evaporation, A= Ablation, PF= Polar Front, SB= Southern Boundary.

Figure 7.3: Mean tracer properties averaged over the top 200m from the WOCE Climatology (Gouretski and Koltermann, 2004). Top: Mean PF(blue) and SB(red) locations. Middle: Mean salinity (psu) of the top 200m around Antarctica in the PF(blue) and SB (red) latitude locations. Bottom: Mean temperature of the top 200m around Antarctica.

Figure 7.4: Total dianeutral fluxes from the model solution, interior dianeutral transports (blue), air-sea buoyancy flux induced transports (red), and total dianeutral transports (dashed black line). A positive transport is into a lighter density layer.

Figure 7.5a : A slide adapted from the WOCE Southern Ocean Atlas (Orsi and Whitworth, 2005), showing the salinity on the γ^n=28.05 kgm^{-3} neutral density surface, associated with the LCDW salinity maximum layer. The box boundaries are shown by dashed black lines. An approximate Polar Frontal position is shown (red line) from Orsi et al. 1995.

Figure 7.5b : A slide adapted from the WOCE Southern Ocean Atlas (Orsi and Whitworth, 2005), showing the depth of the γ^n=28.05 kgm^{-3} neutral density surface, associated with the LCDW salinity maximum layer. The box boundaries are shown by dashed black lines. An approximate Polar Frontal position is shown (red line) from Orsi et al. 1995.

Figure 7.6: Salt anomaly transports (Ggs^{-1}) on a.) UCDW density layers (γ^n=27.70-27.98 kgm^{-3}) and b.) LCDW density layers (γ^n=27.98-28.18 kgm^{-3}). The values in brackets are the net salt anomaly flux into the layer (i.e. positive value = flux into the layer).

Figure 7.7: A schematic representation of the major salt anomaly fluxes around the ACC in the LCDW layer (γ^n=27.98-28.18 kgm^{-3}).

DECLARATION OF AUTHORSHIP

I, Adam Williams declare that the thesis entitled *Antarctic Climate: Ocean fluxes and variability*, and the work presented in the thesis are both my own, and have been generated by me as the result of my own original research. I confirm that: this work was done wholly or mainly while in candidature for a research degree at this University; where any part of this thesis has previously been submitted for a degree or any other qualification at this University or any other institution, this has been clearly stated; where I have consulted the published work of others, this is always clearly attributed; where I have quoted from the work of others, the source is always given. With the exception of such quotations, this thesis is entirely my own work; I have acknowledged all main sources of help; where the thesis is based on work done by myself jointly with others, I have made clear exactly what was done by others and what I have contributed myself; parts of this work have been published as:

Williams, A.P., S. Bacon, and S.A. Cunningham, 2006: Variability of the Lower Circumpolar deep water in Drake Passage 1926-2004., *Geophys. Res. Lett.* **33**, L03603.

ACKNOWLEDGEMENTS

Firstly, I would like to thank Sheldon for all of his help and support over the last four years, and for making sure that this thesis finally came to fruition. I am also grateful for his efforts in enlisting the support of Alberto in the latter stages of my research, whom deserves special thanks for providing input and support during the vital stages of the development and analysis of my model.

I would like to thank Teri Chereskin for agreeing to host my as an exchange student at Scripps Institution of Oceanography for three months, Brian King for allowing me the opportunity to lead last year's Drake Passage repeat hydrographic section and the experiences that provided, and Hartmut Hellmer for providing output from the BRIOS model which was an invaluable resource that added a great deal to my study.

I would also like to thank the many members of the OOC and OMF groups who have helped to answer my questions, especially Joel Hirschi, who's Tuesday meetings were of great support during the first half of my PhD.

Finally I would like to thank Rebecca for putting up with me for the last four years and supporting me throughout my PhD and tolerating my long absences away from home. I would have not been able to do it without your encouragement and support,

Acronyms and Abbreviations

AABW=Antarctic Bottom Water
AAIW= Antarctic Intermediate Water
AASW= Antarctic Surface Water
AAZ=Antarctic Zone
ACC= Antarctic Circumpolar Current
CDW= Circumpolar Deep Water
CTD= Conductivity-Temperature-Depth, (in-situ measurements)
EAC= East Australia Current
ISOS= International Southern Ocean Study (1975-1979)
ITF= Indonesian Throughflow
IW=Intermediate Waters (SAMW+AAIW)
LCDW= Lower Circumpolar Deep Water
NADW= North Atlantic Deep Water
PF= Polar Front
PFZ= Polar Frontal Zone
RSBW= Ross Sea Bottom Water
SACCF= Southern ACC Front
SAMW= Sub-Antarctic Mode Water
SASW= Sub-Antarctic Surface Water
SAZ= Sub-Antarctic Zone
SB= Southern Boundary
SEPDW= Southeast Pacific Deep Water
UCDW= Upper Circumpolar Deep Water
WOCE= World Ocean Circulation Experiment
WSBW= Weddell Sea Bottom Water
WSDW= Weddell Sea Deep Water

Chapter 1: Introduction

1.1 Background

Issues associated with the changing global climate have been declared by some as the greatest challenge facing the global community for the next century. Improving our understanding of the climate system and how it behaves has taken on an increased importance as scientists strive to determine what the consequences of a warming world will be. The oceans form an important component of the climate system, acting as a large reservoir of heat and greenhouse gases, transporting properties around the globe and regulating the climate on a timescale of years to centuries. Direct observations of the ocean are essential in improving our understanding of the state of the ocean and the scales of variability within it. The last twenty years have seen a rapid increase in the quality, coverage and scope of observations, providing greater insights into the structure, processes and interactions of this vital component of the climate system. This presents new challenges in combining large data sets from a diverse group of measurements to develop an improved view of the ocean.

Within the ocean system, the Southern Ocean plays an important role, linking all of the world's major ocean basins and forming a connection between the Atlantic, Indian and Pacific Oceans. The Antarctic Circumpolar Current (ACC) dominates the mean flow structure, transporting properties eastward around Southern Ocean and separating the warmer sub-tropical waters to the north from the colder waters to the south, isolating the Antarctic continent (a more detailed description of the region is given in chapter 2). The region forms an important part of the global overturning circulation (e.g. Schmitz, 1996), a schematic representation of mean global ocean transport that describes the transport and renewal of water masses around the world's oceans. An understanding of the fluxes around the Southern Ocean is vital in understanding this circulation as a whole and any large-scale changes that may happen in this changing environment.

1.2 The dynamical balance of the Southern Ocean

1.2.1 Wind and buoyancy driven flow regimes

Understanding and modelling the complicated interaction of physical processes that determine the main state of the Southern Ocean presents an enormous challenge. The dominant westerly winds in the latitudes associated with the ACC act to drive a northward Ekman flux. This is compensated for by a southward geostrophic transport below the depths unblocked by topography. The sill of the Drake Passage is approx. 2000m, causing a cut-off of eastward water transport with a neutral density (γ^n, Jackett and McDougall (1997)) greater than 28.26 kgm^{-3}. There can be no net transport at water depths shallower than this as there can be no net zonal pressure gradient to drive a geostrophic flow for a circumpolar ocean (e.g. Johnson and Bryden, 1989). The zonal wind stress is then balanced by a bottom form stress caused by pressure differences across major topographic features. This mechanism was first proposed by Munk and Palmen (1951) and is now a widely held view of the dominant balance of the zonal wind-stress.

There have been attempts to apply the theory of Sverdrup balance that describes the circulation in the interior of the sub-tropical gyres by assuming that topographic features act as ‘effective continents’ forming a series of gyre circulations around the Southern Ocean (e.g. Stommel (1957, Baker (1992), Webb (1993), Hughes (2002)). This has caused some controversy (e.g. Warren et al. 1996, Hughes 1997, Olbers (1998)), Arguments against the application of Sverdrup balance in the Southern Ocean cite the importance of the interaction with topography on the flow of the ACC, where the southward flow driven by the wind-stress flow is balanced by bottom pressure torques, and not by viscous terms (e.g. in a northward boundary current) (Rintoul et al. 2000, Olbers et al. 2004).

The circulation of the Southern Ocean cannot be described by the wind-driven component alone, as there is a significant component due to buoyancy forcing. A full description of the circulation must combine the wind and buoyancy components with the complicated effects of topography and stationary and transient eddies. There are various models describing the meridional overturning circulation (MOC) of the Southern Ocean, forming the connection between the northward flowing wind-driven surface waters and the southward flux of deeper waters. Figure 1.1 (adapted from Olbers and Visbeck, 2005) shows a widely accepted view of the mean two-dimensional structure of the MOC. There are two main circulation cells in this representation. The northward Ekman flux is balanced by an ageostrophic eddy-driven transport at depths shallower than the topography. Eddy mass transports are required to explain a net southward mass flux in the presence of no net zonal pressure gradient (Speer et al. 2000). Net meridional transports can be created by correlations in eddy velocities and density layer thicknesses, resulting in a net southward transport. There is also a lower cell, with the southward flow of deeper waters below the level of intervening topography balanced by a northward transport of bottom waters created by the transformation of Antarctic surface waters and the downwelling of Circumpolar Deep Water (CDW). In this case, eddies refer only to time dependent eddies, as longitudinal meanders (i.e. stationary eddies) do not contribute to the eddy-driven fired when examining the circulation on iso-neutral surfaces (e.g. Karsten and Marshall 2002).

As the large momentum flux due to the zonal winds in the Southern Ocean can not be balanced by the large-scale zonal pressure gradients, the momentum must be transferred vertically down through the water column. The mechanism for this vertical momentum transfer is eddy interfacial form stress (e.g. Olbers et al. 2004) that transfers horizontal momentum across sloped isopycnals through eddy fluctuations in the zonal pressure gradient. This transports down through the water column to the ocean floor where the momentum is transferred into the earth through bottom form stress. Integrating vertically through the water column resulting in an overall balance in the Southern Ocena between the wind-stress at the ocean surface and the bottom form stress and frictional stress at the ocean floor.

Data-based representations of the overturning appear to fall within the two limits of wind-driven and buoyancy driven flow regimes. In the wind-driven regime, eddies transport the wind-stress down through layers in the ocean (Inter-facial form stress), until the bottom is reached and the stress is taken up by bottom form drag (Johnson and Bryden 1989). This model requires no deep upwelling and therefore no diapycnal fluxes between density layers. At the other extreme, the southward flowing deep water upwells and is converted to Antarctic Surface water that is then advected northward in the Ekman flow. This limit requires no process to flux momentum down through the water column and requires large amounts of water mass transformation (e.g. Gnanadesikian and Hallberg, 2000).

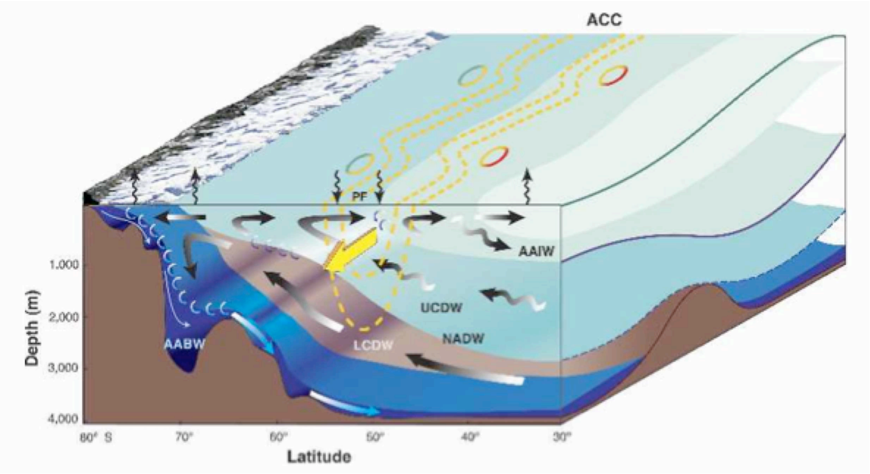

Figure 1.1: Taken from Olbers and Visbeck (2005). A schematic representation of the Southern Ocean meridional overturning circulation adapted from Speer et al. (2000). Definitions of water masses (AABW, NADW, UCDW, AAIW) are given in chapter 2.

1.2.2 The residual mean picture

The traditional picture of the Deacon cell is an overturning cell in the Southern Ocean, with southward transport of deep water closed by a northward return flow at the surface, with upwelling to the south and downwelling further north. This picture implies large diapycnal velocities (of order 10^{-6} ms^{-1}, McIntosh and McDougall, 1996) within the Southern Ocean to close the cell. Döös and Webb (1994) examined output from the FRAM model and found that this was an artefact of zonal averaging on depth surfaces. When a streamfunction was calculated on constant density surfaces the cell disappears because north and southward moving water on the same density surface, but at different depths can create the appearance of an overturning cell when viewed in depth co-ordinates. The Deacon cell is analogous to the Ferrell Cells in the atmosphere that disappear when they are averaged over density surfaces (e.g. Andrews et al. 1987, Townsend and Johnson,1985).

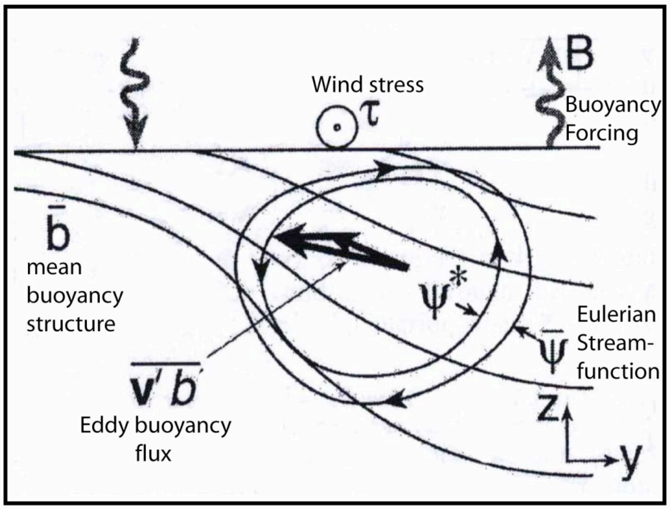

Figure 1.2: Adapted from Marshall and Radko (2003). Schematic representation of the Eulerian mean and eddy streamfunctions ($\overline{\psi},\psi^*$) in the region of the ACC.

Residual mean theory was originally developed to describe the circulation in the stratosphere (e.g. Andrews and MacIntrye, 1978) and has been recently applied to explain the circumpolar circulation of the Southern Ocean (e.g McIntosh and McDougall (1996), Karsten and Marshall (2002), Marshall and Radko (2003)). Residual Mean theory incorporates the eddy flux terms in the standard Eulerian mean equations, resulting in a residual velocity (v_{res}) that is the sum of the Eulerian mean velocity (v) and a non-divergent eddy-induced velocity (v^*) ($v_{res} = v + v^*$) . Figure 1.2 shows a schematic diagram adapted from Marshall and Radko (2003) depicting the competing effects of the mean and eddy circulations that add together to form the residual circulation. In the case of adiabatic eddies, and in the deep ocean where horizontal scales are much greater than the vertical scale (e.g. $\partial/\partial z >> \partial/\partial x, \partial/\partial y$), the horizontal eddy velocities can be expressed in terms of the buoyancy gradients by examining the time-mean buoyancy budget (e.g. Radko and Marshall, 2006):

$$u^* = \frac{\partial}{\partial z}\left(\frac{\overline{u'b'}}{b_z}\right) \tag{1.1.a}$$

$$v^* = \frac{\partial}{\partial z}\left(\frac{\overline{v'b'}}{b_z}\right) \tag{1.1.b}$$

These velocity equations can be integrated over the ocean interior to produce a streamfunction due to transient eddies. The buoyancy equation can be written in terms of the residual velocities, the background buoyancy structure and the buoyancy forcing

(B), which is dominated by the explicit air-sea forcing, and is used to set the internal flow structure.

$$v_{res} \cdot \nabla b = \frac{\partial B}{\partial z} \tag{1.2}$$

The zonal-mean picture of buoyancy gain into the ocean south of the ACC and buoyancy loss to the north leads to an additional cell structure in the thermocline (Karsten and Marshall 2002). This cell is superimposed on the northward circulation of surface waters in the Ekman layer and intermediate water, and the southward flux and upward shoaling of denser waters in the ACC. The residual circulation includes a subduction of mode waters to the north of the ACC, forming a circulation of mode waters, with northward export on the deeper intermediate water layers. The zonal picture has been expanded by Marshall and Radko (2006) to try and incorporate the zonal variations in buoyancy forcing with a positive buoyancy flux around the Atlantic and Indian sectors of the ACC, that becomes negative as the ACC moves further south in the Pacific sector. They found that the overturning in the thermocline was predominantly in the Atlantic and Indian sectors, north of the ACC. The applications of Residual mean theory assume that the interior flow is adiabatic, so it does not take into account the effect of diabatic effects, including diapycnal mixing, that may also play an important role in the Southern Ocean meridional overturning and stratification.

1.2.3 Deep interior mixing

Deep mixing is essential in maintaining the abyssal stratification of the global oceans against the formation of deep and bottom water. Munk (1966) and Munk and Wunsch (1998) examine the mean diffusivity required to maintain the abyssal stratification, leading to a value of the order of 1×10^{-4} m^{2}s^{-1} for the diapycnal diffusivity, assuming 25/30 Sv of global upwelling of deep water respectively. The mechanical energy required to maintain this mixing must come predominantly from the winds and tides (Munk and Wunsch, 1998). The latter study also found considerable vertical variations in the magnitude of the diapycnal diffusivities. Wunsch and Ferrari (2004) provides an overview of the issues surrounding vertical mixing and the effects on the general ocean circulation, examining the different sources of energy required to drive the ocean circulation.

Direct measurements of turbulence (Gregg, 1987) and dye diffusion (Ledwell et al. 1998) in the pycnocline have found background levels that are an order of magnitude less that the mean values predicted by Munk and Wunsch (1998), presenting the question of where the mixing is coming from? Mauritzen et al (2002) and Naveira Garabato et al (2004) found regions of intense turbulent mixing around regions of complex topography in the Brazil Basin and Scotia Sea respectively, suggesting that topographically enhanced mixing can account for the differences in the open ocean and global mean diffusivities. Sloyan (2005) examined a large number of measurements around the Southern Ocean, finding that elevated diffusivity profiles were due to the interaction of the mean geostrophic current and the bottom topography. Wunsch and Ferrari (2004) conclude that over most of the open ocean, significant deep mixing is confined to these topographically complex boundary regions, and that it has a major effect on the ocean interior circulations, compared to the mean mixing case. This is also important as models generally use fixed diffusivities and do not take into account this localised intense mixing.

Recently, Naveira Garabato et al (2007) found intense mixing across density surfaces and upwelling along isopycnals in a region around Drake Passage, using helium injected into the ocean from hydrothermal vents as a tracer for this mixing. They suggest that this mixing acts to create a short circuit of the overturning circulation of the ACC. There are a number of regions across the path of the ACC where the complex topography could cause intense mixing and therefore form an important component of the overturning circulation of the Southern Ocean.

1.2.4 Linking observations with theory

Theoretical predictions and model studies can only be verified from observations, to determine the real balance of processes within the Southern Ocean. Inverse Models provide a useful technique to combine individual hydrographic sections to obtain a balanced picture of the mean circulation around the Southern Ocean, and to provide insight into the physical processes that dominate this balance. Numerous studies have been conducted in the Southern Ocean (e.g. Sloyan and Rintoul (2000), Ganachaud (2003), Lumpkin and Speer (2007)) as the quality and distribution of hydrographic data increased due to the World Ocean Circulation Experiment (WOCE) (e.g. Siedler et al 2000). These studies have been useful in producing representations of the fluxes around the Southern Ocean and to examine various physical schemes for diapycnal mixing and air-sea fluxes.

1.3 Variability within the Southern Ocean

The observational data record of the Southern Ocean is very sparse due to its remote location and the notoriously difficult weather conditions. A consequence of this is that until recently, there have been very few observations, so it has been difficult to obtain an idea of the long-term scales of variability within the region. Gille (2002) combined hydrographic and float data from 1950-2000 to analyse property changes in the mid-ocean layer between 700-1100m in the Southern Ocean. Figure 1.2 (figure 3, Gille (2002)), shows trends in temperature changes over this period. The main features are a significant warming centred on the ACC of 0.17° C between the 1950's and the 1980's. This can be (at least partially) explained by a southward movement of the ACC caused by a shift in the westerly wind patterns, resulting in a reduction in the volume of cold, polar waters around Antarctica. This trend in the winds appears to be related to the decline in stratospheric ozone over the last 30 years.

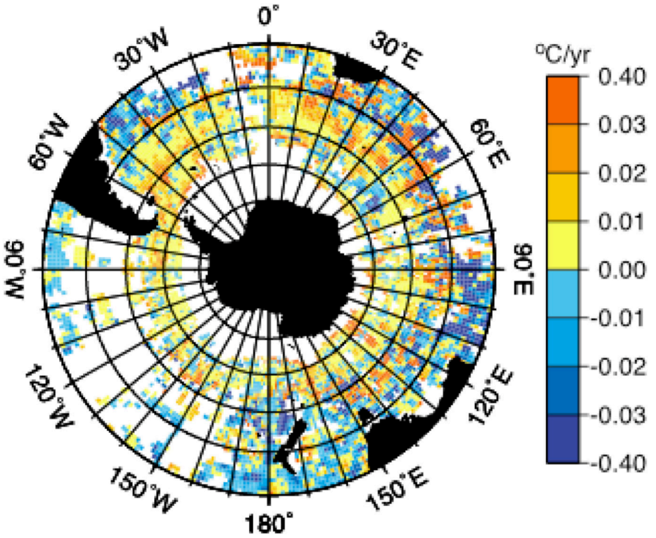

Figure 1.3: Taken from Gille (2002). Annual gridded temperature trends (° C/year), between 700-1100m between historical hydrographic record and ALACE floats (1990's).

Various studies have examined historical hydrographic sections with modern stations to comment on regional long-term trends within the Southern Ocean. Aoki et al. (2005) found warm, saline, low oxygen anomalies and a deepening of density surfaces south of the Polar front in the Upper Circumpolar Deep water (γ^n=27.7-28.0 kgm^{-3}), and cool, fresh anomalies to the north of the Sub-Antarctic front centred in the Antarctic Intermediate water (γ^n=27.0 kgm^{-3}) from hydrographic stations between 1950's and 1990's in the Indian/West Pacific region (30°E-160°E). They also found an increase in geopotential anomaly, consistent with a strengthening of the ACC and with observations of a strengthening of the zonal winds in the Southern Ocean over the last 50 years (Thompson and Solomon, 2002).

Wong et al. (1999) found large-scale freshening in the intermediate waters of the Pacific and Indian Oceans in data between 1930 and 1994. This is consistent with a freshening in the surface waters of the Southern Ocean and is caused by an increase in precipitation over the polar gyres. They predict an increase of 33mmyr^{-1} between the historical data (1930-1990) and a series of modern sections over the latitude range 55°-65° S around the Southern Ocean, which is ~8.5 % of the mean annual rainfall around the Southern Ocean south of 55° S. Bindoff and McDougall (2002) compared sections across the Indian Ocean at 32° S from 1962 and 1987 and found that Antarctic Intermediate Water and Sub-Antarctic Mode Water had cooled and freshened, caused by a surface warming in the Mode Water formation region and increased precipitation in the Intermediate water source region. These observations are in agreement with climate model studies (Banks et al. 2000, Banks and Bindoff, 2003) that attribute the changes to surface warming and localised increased precipitation. Bryden et al. (2003) analysed five sections across the Indian Ocean between 1936 and 2002, but found a reversal of the observed Intermediate Water trend in the 2002 section. This study highlighted the large-scale property variability in the mode waters in the Indian Ocean, and the difficulty in separating out trends from long-term oscillations, especially when comparing a limited number of sections.

Observations of a freshening signal in the deep water formed in the North Atlantic between 1960-2000 (Dickson et al. 2002), could have consequences in the Southern Ocean, with a decrease in the salinity of the North Atlantic Deep water entering the Southern Ocean in the South Atlantic. This is also linked to observations of changes in the meridional overturning circulation in the North Atlantic (e.g. Bryden et al (2005)) that will have an effect on the meridional flux balance between the Atlantic Ocean and the Southern Ocean.

Cunningham et al. (2003) and Rintoul and Sokolov (2001) present studies based on a series of repeat hydrographic sections undertaken as part of WOCE across the major choke points of the Southern Ocean, Drake Passage and south of Tasmania, respectively. This has improved our picture of the variability of the geostrophic baroclinic transport round the Southern Ocean. This built on the work of Whitworth (1983) and Whitworth and Peterson (1985), which was based on a mooring array across Drake Passage between January 1979 and February 1980, providing observations of the barotropic transport variability. Cunningham et al.(2003) also calculated baroclinic transports from sections between 1975-2000 and found no significant trend, with a transport relative to and above 3000m of 107.3±10.4 Sv.

1.4 A study of the Southern Ocean

This study is divided into two main parts examining two key themes that have been introduced above: the long-term variability/stability of the ACC and water masses, focussing on Drake Passage; and the three-dimensional mean circulation of the Southern Ocean over the WOCE period.

Chapter 2 details the main Southern Ocean water masses and circulation features. The results of an investigation into the long-term variability at Drake Passage are outlined, based around the SR1b repeat hydrography carried out by the National Oceanography Centre, Southampton (NOC) and its predecessor organisations, in conjunction with the British Antarctic Survey (BAS). These transects are combined into a data set of over 50 sections across Drake Passage between 1926-2006. An analysis of variability detected in the main water masses is presented.

The main part of the study is introduced in chapter 3; an Inverse Model of the Southern Ocean. To understand the structure of the water masses found at Drake Passage, it is important to understand the constituent parts and the details of their journey in the Southern Ocean before they reach Drake Passage. Chapter 3 outlines the details of the Inverse Model, and the methodologies used in the model set-up. This includes a description of the physical parameters explored in the model and the methods used to create an initial ocean state for the model.

Chapter 4 describes the results of the standard model solution and compares the large-scale fluxes to other large-scale and regional inverse studies in the Southern Ocean. The circulation and changes of the major Southern Ocean water masses are explored in the model solution in Chapter 5. The three-dimensional variability of the circulation and the balance of fluxes across the meridional boundaries of the model domain are discussed.

Chapter 6 describes a series of other model runs examining the stability of the model solution and the effect of different mixing schemes. A contemporary (2002/2003) northern boundary is examined in the model to examine the stability and variability of the overturning circulation within the Southern Ocean, and the fluxes across 30° S. The repeat sections at Drake Passage are used to examine the stability of the solutions to changing the transport and fluxes of the ACC. Chapter 7 examines the balance of the dianeutral fluxes that are found in the model and their implications for the overturning circulation in the Southern Ocean. Chapter 8 summaries the observations from the inverse study and discusses the implications of the model results on the current understanding of the Southern Ocean, and the future applications and areas of research that the model could be useful tool to explore.

Chapter 2: Drake Passage, the Southern Ocean Choke Point

2.1 Background and definitions

The Drake Passage is a choke point in the Southern Ocean between South America and the Western Antarctic Peninsula. It forms the smallest gap around the Southern Ocean, forcing the Antarctic Circumpolar Current through a 1000km channel, with a sill depth in the region of 2000m. In the following section, the basic flow structure and water masses found at Drake Passage will be defined, with generalisations around the whole of the Southern Ocean outlined. Details of the historical data set and methods used to examine the long-term property variability at Drake Passage are presented in section 2.2. The remaining sections discuss the variability observed in the data set in the major water masses at Drake Passage and the large-scale geostrophic transports.

2.1.1 Flow structure

The main feature of the Southern Ocean is the Antarctic Circumpolar Current (ACC) that flows eastward around Antarctica. It links the Pacific, Atlantic and Indian Oceans, transporting in the region of 125-150 Sv ($Sv=1\times10^{6}kg/m^{3}$) on its 20,000km path around Antarctica. The flow is concentrated in a series of fronts that separate the cold, polar waters to the south from the warmer sub-tropical waters to the north. Some commonly used frontal definitions are presented in Orsi et al.(1995) and are outlined below, starting at the northern edge of the ACC and moving southward to Antarctica. Figure 2.1 shows the mean frontal positions from this paper (Southern Ocean Database, Orsi and Whitworth 2005). The review of historical definitions of the major fronts by Belkin and Gordon (1995) is also used in the following discussion.

Sub-Tropical Front (STF):

This front forms the Northern boundary of the ACC, where there is an increased surface meridional temperature gradient between the sub-tropical and sub-Antarctic surface waters (e.g. Belkin and Gordon 1996). This front is not found at Drake Passage, due to the southward extent of South America, disappearing in the Chile Basin, and reappearing again in the Argentine Basin to the east of the continent. The STF has been found to split into a number of sub-fronts in the South Pacific and Atlantic Ocean basins, making it difficult to define the exact properties of this front throughout the Southern Ocean.

Sub-Antarctic Front (SAF):
Sievers and Emery (1978) define the SAF as the maximum sub-surface temperature gradient between 3°C- 5°C at a depth of 300m. It also marks the southern extent of Sub-Antarctic Mode Water (defined in section 2.1.2). The majority of the transport of the ACC is found in the SAF and Polar Front, the balance in transport strengths varying in time and with zonal location around the Southern Ocean.

Polar Front (PF):
The traditional definition of the PF is the northern-most extent of the 2°C isotherm at 200m depth (Botnikov 1963). Physically, it marks the region where the cold, denser Antarctic waters subduct beneath the warmer, lighter Sub-Antarctic water, and used to be known as the Antarctic Convergence (e.g. Deacon 1937). Another definition was proposed by Moore et al.(1997) based on the maximum in surface temperature gradient. This enables the use of satellite sea surface temperature data to monitor the PF around the whole of the Southern Ocean. At Drake Passage, Sprintall (2003) found a wide disparity between the PF from the two methods, stating that the in-situ method was the more physically justifiable method. Cunningham et al. (2003) noted that when examining the Potential Temperature (θ) vs. Salinity (S) relationship from hydrographic data, there is a jump in the θ/S curve in the region of the point (θ=1°C, S=34.20psu), between stations across the southern boundary of the PF. This change in water properties is useful for determining the southern extent of the PF from in-situ measurements and is used in this study to determine the frontal positions from hydrographic data.

Southern ACC Front (SACCF):
The SACCF marks the most southern core of the ACC. It is defined by the southern-most extent of the 1.8°C isotherm along the maximum between 200-500m depth.

Southern Boundary (SB):

The SB (or Continental Water Boundary) marks the boundary between the Antarctic and Continental Zones, as defined by a difference in the core water properties. It is defined as the northern extent of temperatures below 0°C, along the maximum temperature gradient between depths of 150-500m.

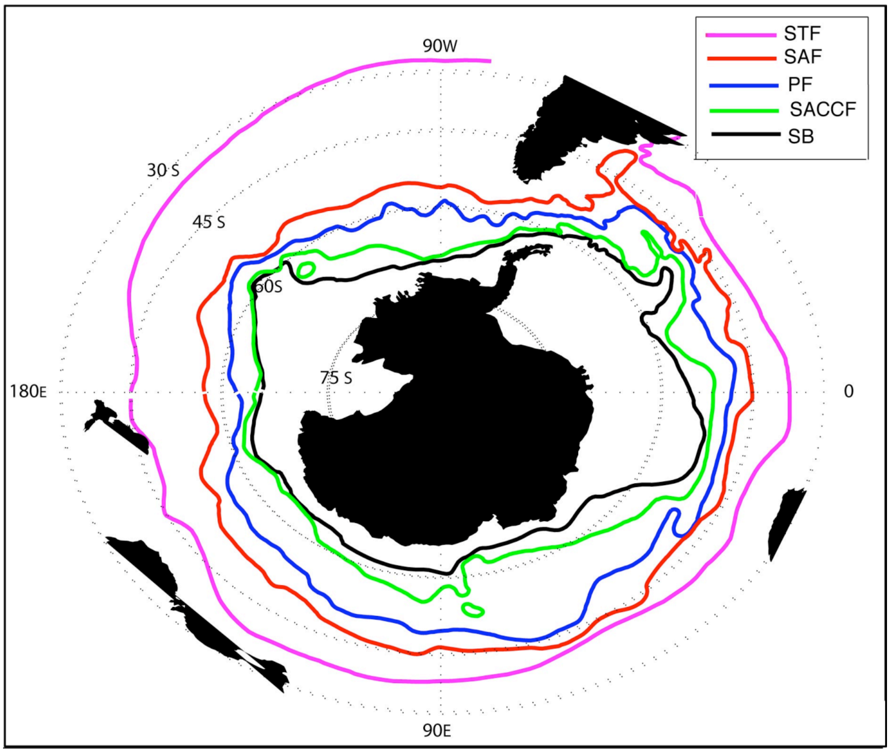

Figure 2.1: Mean frontal locations from observational data, taken from Southern Ocean Database (Orsi and Whitworth 2004), STF=Sub-Tropical Front, SAF=Sub-Antarctic Front, PF=Polar Front, SACCF=Southern ACC Front, SB=Southern Boundary.

The regions in-between the fronts are divided up into zones. The STF and SAF form the boundaries of the Sub-Tropical Zone (STZ). The Polar Frontal Zone (PFZ) is between the SAF and PF. South of the PF, is the Antarctic Zone (AAZ), and south of the Southern Boundary is the Continental Zone (CZ). In reality, the frontal structure of the ACC is more complicated than the five basic fronts described above. The fronts can split and merge, varying in space and time, so these definitions and the frontal locations should be taken as a mean picture that is also biased by the fact that most in-situ measurements used in these studies are from the summer months (November-April).

2.1.2 Water Masses

The International Southern Ocean Study 1975-1980 (ISOS) attempted to examine the variability and structure of the ACC on a then unprecedented scale. It resulted in higher resolution data sets enabling the detailed analysis of water mass properties and the structure of the ACC fronts. It also provided the first picture of the time variability of the ACC transport by using a mooring array (Whitworth et al. 1980). Sievers and Nowlin (1984) used the hydrographic data collected during the study to define the properties of the major water masses found at Drake Passage. Some of the property definitions are specific to Drake Passage and these will be expanded upon to highlight the variations throughout the Southern Ocean to make them more general. This will be important for the discussion of the water masses in the following chapters. There are four main categories of water mass in the Southern Ocean: Surface; Intermediate; Deep; and Bottom water.

i.) Surface Waters

The PF divides the cooler surface waters to the South from the warmer sub-tropical surface waters to the north. The main features of Antarctic Surface Water (AASW) are that it is cold and fresh. In the summer months there is sub-surface temperature minimum layer due to the sea-ice melt (the Winter Water) with a warmer layer above it due to air-sea interactions. Figure 2.2 shows the tongue of fresh water associated with AASW and the injection of sea-ice melt at Drake Passage, south of the PF. The Sub-Antarctic Surface Water (SASW) to the north is warmer and saltier. The ranges of property variability at Drake Passage are quite small (~8 °C, 0.3 psu) due to its southerly location but in the region of the other ACC choke points south of Australia and Africa, the SASW can contain the most saline (and warmest) water found in the Southern Ocean.

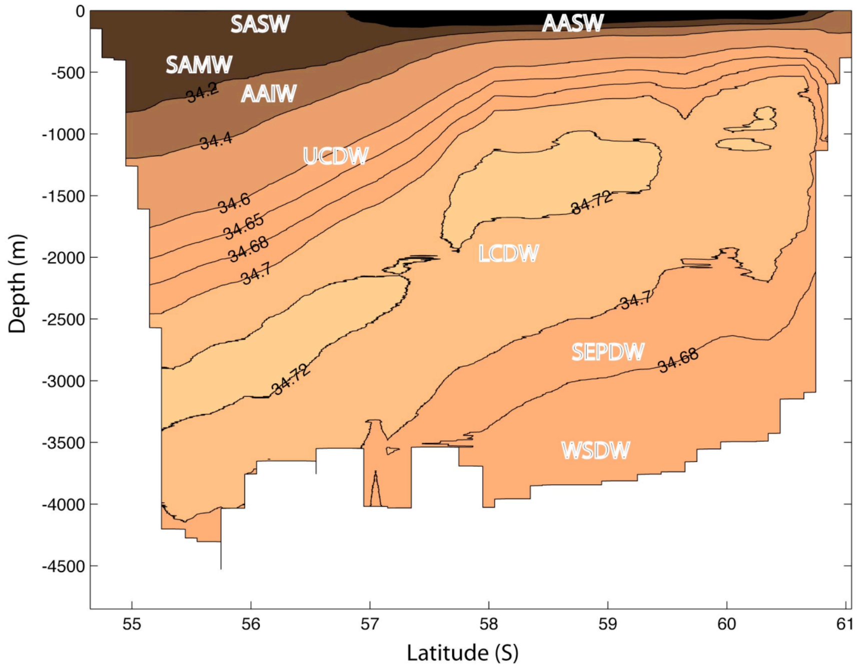

Figure 2.2: Salinity distribution at SR1b line across Drake Passage, taken from a mean of 11 NOC/BAS sections (1993-2005), averaged onto a uniform grid with latitude as the horizontal co-ordinate. (Dark=fresh, light =saline). A schematic of the main water mass locations is included. SASW=Sub-Antarctic surface water. AASW=Antarctic Surface Water, SAMW=Sub-Antarctic Mode Water, AAIW=Antarctic Intermediate Water, U/LCDW= Upper/Lower Circumpolar Deep Water, SEPDW=Southeast Pacific Deep Water (a regional variety of LCDW), WSDW=Weddell Sea Deep Water.

ii.) Intermediate Waters

There are two main classes of intermediate waters in the Southern Ocean, Sub-Antarctic Mode Water (SAMW) and Antarctic Intermediate Water (AAIW). Mode waters are layers of nearly homogeneous water found over relatively large geographical areas, occurring near the top of the permanent pynocline (Hanawa and Talley, 2001). SAMW is formed by convection in winter that allows water to flow through the mixed layer to ventilate the ocean interior. Mode Waters are generally characterised by a minimum in potential vorticity. SAMW formation occurs most strongly in the Southeast Indian Ocean (Ribbe and Tomczak, 1997) and in the Southeast Pacific Ocean

(McCartney,1982). At Drake Passage, SAMW is also characterised by a sub-surface local salinity maximum (S>34.2psu).

A salinity minimum layer that descends near the SAF, below the SAMW, defines AAIW at Drake Passage. There are different viewpoints on the formation of AAIW. The old theory (e.g. Deacon 1937) believed that it was created due to the sinking of AASW below the SAF, meaning that AAIW is renewed all around the ACC. The accepted viewpoint now is that AAIW is renewed in specific regions around the Southern Ocean, mainly in the Southeast Pacific and also in the Southwest Atlantic. There is still some debate over the mixing mechanisms involved in the production and there is an area of active research trying to observe the formation of AAIW. McCartney (1977) and Talley (1996) believe that AAIW is made from SAMW as it is continually cooled and freshened by deep winter mixing events, mainly in the Southeast Pacific. Molinelli (1981) suggests that AAIW is formed by isopyncal exchange across the PF, and Piola and Gordon (1989) demonstrate the need for mixing with Antarctic waters to explain the water mass property changes of the AAIW. Observational evidence seems to find two distinct pools of AAIW in the Southern Ocean that support a combination of both recent theories (Sloyan and Rintoul 2001a).

iii.) Deep Waters

Circumpolar Deep Water forms the most voluminous of the water mass of the Southern Ocean. It is broadly divided into two groups: Upper and Lower Circumpolar Deep Water (U/LCDW). UCDW is found below AAIW, and is characterised by an oxygen minimum. This oxygen minimum is due to biological depletion of the oxygen rich North Atlantic Deep Water (Gordon, 1967), and low-oxygen water entering the Southern Ocean from the Indian and Pacific Oceans (Callahan, 1972). UCDW has a neutral density between γ^n=27.65 and γ^n=28.0 kg/m^3.

A sub-surface salinity maximum defines the centre of the Lower Circumpolar Deep Water at Drake Passage. This signal originates from the warm and saline North Atlantic Deep Water (NADW) that enters the Southern Ocean in the South Atlantic at a neutral density in the region of 28.0 kg/m^3. This warm, saline signal is transported eastward around the Southern Ocean, mixing with the surrounding waters, as far Drake Passage, where the salinity maximum is found between γ^n=28.08-28.12 kg/m^3. The temporal and spatial variability of this water mass will be examined in more detail in the following chapters.

The waters below the LCDW salinity maximum are sometimes defined as South east Pacific Deep Water (SEPDW) (Sievers and Nowlin, 1984), as are similar regional variations in CDW properties e.g. Indian Deep Water, Pacific Deep Water, denoting the origin of the water before it is transported by the ACC. In the western side of Drake Passage, a final water mass, Weddell Sea Deep Water is also found (γ^n>28.26 kg/m^3), but its westward passage is blocked by the Shackleton Fracture Zone (see figure 2.3) to the west of the SR1b line (see section 2.2) (Naveira Garabato et al. 2002).

iv.) Bottom Waters

The sill of Drake Passage only allows water lighter than γ^n=28.27 kgm^{-3}, so no bottom water is found in this area. The main sources of Antarctic bottom water (AABW) come from the Weddell (WSBW) and Ross (RSBW) Seas, with additional formation along the Adelie Coast. Orsi et al. (1999) provides a comprehensive assessment of bottom water varieties in the Southern Ocean. They define an additional water mass, ACC Bottom Water (ACCbw) between the density range γ^n = 28.18-28.27kg/m^3, that is comprised of old LCDW that has made many circuits of the ACC so is not directly advected in from the north, but forms a major part of the Antarctic Bottom Water that is exported northward into the major ocean basins. This definition will be useful later when analysing the Inverse Box Model solutions (see chapter 4). The term AABW is therefore used to describe two different water masses depending on the context: around Antarctica, AABW is coldest and densest water, formed due to deep mixing processes; further north and into the Atlantic, Indian and Pacific oceans, AABW refers to a modified form of AABW that is a mixture of LCDW and the denser bottom waters formed around Antarctica.

2.2 A historical Drake Passage data set

To examine the long-term variability of the water masses of the Southern Ocean at Drake Passage, a data set of historical hydrographic sections across Drake Passage was compiled to add to the high-quality annual repeat hydrographic section occupied by the National Oceanography Centre, Southampton (NOCS) and its predecessor organisations in collaboration with the British Antarctic Survey (BAS) (1993-ongoing). This section will describe the details of the data set and the associated errors relating to the data from different time periods. The data set only includes sections across Drake Passage, rather than all the available stations so that a synoptic snapshot of a vertical slice across the whole passage could be examined. This also removes biases due to the number of stations occupied in a given section and allows the decomposition of the property variability in the different zones across Drake Passage (full section details can be found in Appendix AC).

2.2.1 Details of the data set

a.) The Inter War Period (1926-1934)

The first hydrographic measurements in the Southern Ocean began in the 1920's and were carried out by German researchers as part of the Meteor Expeditions (Wust 1935). This was quickly followed by a number of British sections, primarily as part of the Discovery Expeditions (Deacon 1937). These cruises were very important in forming the early ideas for the patterns of the large-scale ocean circulation. The measurements were made using reversing thermometers and Niskin bottles. Salinity measurements were obtained from bottle samples by using chlorinity titration. In total, there were six sections occupied across Drake Passage between 1926-1934, located between the tip of South America and the Western Antarctic Peninsula (see figure 2.3 -SR01 sections).

b.) Post-War Period (1945-1970)

Very little oceanographic research was carried out in this period, and there are only four sections in the data set from this period. The research ships Ob and Eltanin conducted observations around the Southern Ocean in the 1950's and 60's, resulting in few sections in the Drake Passage region that meet the data set criteria.

c.) The ISOS Period (1975-1980)

The International Southern Ocean Study (ISOS) was the first major research program to be carried out in the region, examining the structure and variability of the ACC. There are six sections from this period in the data set and these form the first group of regular hydrographic measurements in the area. They are all concentrated in the SR01 location (see figure 2.3). All measurements were from bottles and so have limited vertical resolution, however the increased horizontal resolution provides a clearer picture of the detailed frontal structure of the ACC.

d.) WOCE and beyond (1990-2005)

The World Ocean Circulation Experiment (WOCE) was an international collaboration to determine the state of the ocean (e.g. Siedler et al. 2001). It set new measurement standards and saw the introduction of high-quality CTD sections. An annual repeat section was introduced along the SR01b line (figure 2.3), that has been continued post-WOCE by the NOCS/BAS since 1993 (there was no occupation in 1995, or 1998) (e.g. Bacon 2002). This line was chosen to match the satellite track of the ERS satellites so that comparisons could be made with satellite altimetry. In total, the data set contains 22 CTD sections. The majority of occupations are along the SR01b line, but two occupations were made along the SR01W line (figure 2.3) following the western limit of the Scotia Sea, and five sections were conducted across the traditional SR01 line.

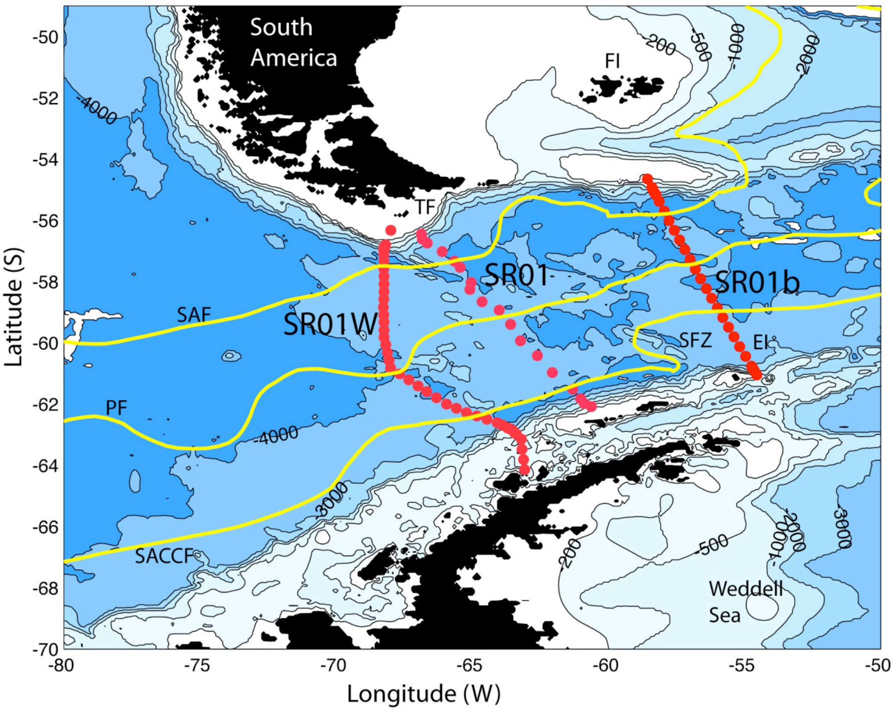

Figure 2.3: Map of the Drake Passage sector of the Southern Ocean. The three main section locations, SR01, SR01b and SR01W are marked by red dots. The mean positions of the three main fronts at Drake Passage (SAF,PF,SACCF) (Orsi et al. 1995) are marked by yellow lines. FI=Falkland Islands, TF= Tierra del Fuego, SFZ=Shackleton Fracture Zone, EI=Elephant Island.

2.2.2 Initial error analysis

The details of this study are outlined in Williams et al. (2006), and the following error analysis used here are based on the work of Saunders (1986), Mantyla (1994) and Gouretski and Jancke (2001). It is useful to treat the errors of each section in the four temporal groups described in section 2.2.1. The main source of error is due to systematic errors in salinity measurements, dominating the effect of errors in temperature measurements for all periods. In the inter-war period, salinity measurements were derived from seawater chloride concentrations and are only accurate to within 0.01psu. Conductivity measurements were introduced in the late 1950's, resulting in measurements accurate to within 0.005psu. Inductive salinometers were introduced in the mid 1970's and have much smaller instrumental errors. A systematic error of 0.003psu was applied to bottle samples after 1970, encompassing the errors identified by Saunders (1986) and Mantlya (1994). Modern offsets from the NOC sections are accurate to within 0.001-0.002 psu (e.g. Bacon 2002) so this value was applied to all modern because the majority of stations from this period are from NOC/BAS cruises.

A major source of bias when comparing historical bottle data to modern CTD data is that features can be missed due to sparse vertical bottle sampling. Additional biases were calculated by sub-sampling a modern NOC section with a vertical spacing comparable to the vertical sampling of the various historical sections. This method involved creating a mean salinity section from the NOC sections (1993-2004) and using this as an approximation to the actual salinity field. This field was sub-sampled with nets that represent each of the bottle spacing regimes (i.e. 1930's, 1950's and 1970's). The vertical position of the net was then varied over a depth range associated with half of the maximum bottle spacing covering the salinity maximum layer up and down the water column (e.g. 125m up and down for a bottle spacing of 250m for the 1970's sections). The difference between these salinity values and the actual salinity maximum value at each station point was averaged to create a mean bias for the bottle measurements due to the bottle samples missing the salinity maximum surface. The method was applied to all of the bottle sections with the individual biases combined to create a set of values representing the three time periods with different vertical bottle spacing. This bias in the salinity measurements was combined with the systematic error and sections standard error estimates to calculate error bars for the analysis described in the following section. In the case of temperature measurements on the salinity maximum surface, the variability across Drake Passage (~0.2 °C) is much greater that the measurement errors or sub-sampling biases, so this is assumed to be the dominant error in the presentation of temperature variability and is used to represent the total temperature error estimates.

2.3 Variability of LCDW

Williams et al.(2006) used the historical data set to examine the variability of LCDW at Drake Passage from 1926-2004. The results of this study will be outlined and expanded upon here, extending the study to other water masses found at Drake Passage.

2.3.1 LCDW: Characteristics of the salinity maximum surface

The salinity signal originating from the NADW is a major feature of the water mass properties of the Southern Ocean. The salinity maximum surface was chosen as a defining property of LCDW in this examination so that a comparison could be made between historical bottle data and modern CTD stations. Issues with the vertical resolution meant that it was not possible to make justifiable comparisons across the data set on density surfaces (or on other parameters) so a sampling bias (outlined in section 2.2.2) was applied instead of relying on interpolated bottle data. The analysis of properties on density surfaces was only applied to the modern sub-set of the data set and is also examined below. The salinity core of the LCDW forms a layer that extends ~700km across the whole of Drake Passage, shoaling from depths of 2500-3000m to the North, up to close to the mixed layer to the South forming a large component of the total water mass of the Southern Ocean (see figure 2.2).

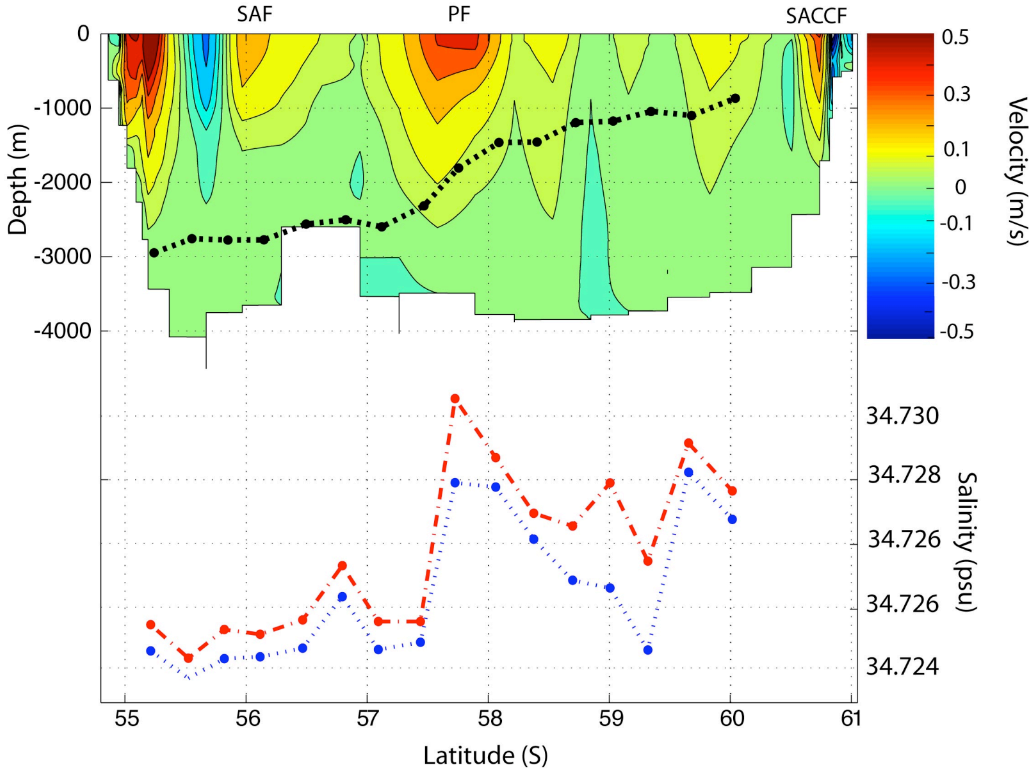

Figure 2.4: Upper Segment: Geostrophic Velocity profile referenced to the deepest common level from the 1996 NOC/BAS section along SR01b. The main frontal positions are marked. The black dots mark the location of the LCDW salinity maximum (see figure 2.2 for the mean salinity structure at Drake Passage). Lower segment: Salinity of LCDW salinity maximum surface (red) and mean salinity on 250m thick layer centred on the salinity maximum surface (blue).

A procedure was determined for selecting stations that included LCDW properties and only these stations were used in compiling the section mean properties. The main criterion was that the maximum salinity was >34.70psu, a limit determined empirically from the θ/S relationship of the whole data set. The LCDW properties of a given station had to be consistent with the adjacent stations and large anomalous values were also discarded. The study was aiming to examine the core properties of the LCDW at Drake Passage, so station properties influenced by eddies and mixing with the fresher continental shelf waters to the North and South were removed from the calculation of the property characteristics.

Examination of the salinity of the LCDW salinity maximum surface within each section showed that there was a meridional salinity gradient within the layer, apparent in two thirds of the sections. The highest salinities were found in the southern half of DP, decreasing northwards, with a typical salinity decrease of 0.005-0.010psu across the whole section. On first inspection, this seems counter-intuitive as the saline signal originates from the northern side of the ACC in the South Atlantic, but the highest salinities at DP are found in the south. This feature is due to the different mixing processes and interactions with other water masses around the Southern Ocean and will be addressed in more detail in the later chapters. There is a large-scale temperature trend of up to 0.4°C across DP with colder waters to the north due to the larger depths of the LCDW. This causes a similar trend in the neutral density of the salinity maximum surface with a decrease of up to 0.04 kg/m^3 from North to South. Figure 2.4 shows a geostrophic velocity section from the NOC/BAS 1996 SR01b transect. The depth and strength of the salinity maximum signal are shown across DP. The figure shows the high salinities observed in the AAZ (and at the PF) and the relatively low values in the SAZ and PFZ. The layer-mean values show that this is a consistent signal in a thick layer of the LCDW and so is representative of the whole water mass and not just a localised part of it, or due to anomalously high in-situ salinity measurements.

2.3.2 LCDW: Temporal variability

The properties on the salinity maximum surface were used to examine temporal variability across the whole of the data-set (1926-2005). The salinity and temperature variability are shown in figure 2.5. The main observation from this figure is that within the limits of experimental errors and higher frequency variability, there core properties of LCDW at DP have remained constant over the period 1926-2005. Focussing on the period 1970-2005, there is no trend in the properties of the LCDW salinity maximum layer greater than the inter-annual variability derived from the annual repeat NOC/BAS sections. Any small observed differences also need to take into account the difference in geographical location of the two sets centred on the SR01W, SR01 and SR01b lines (figure 2.3). The variability in the data did not allow the detection of any significant change in properties between the three locations due to the temporal variations between each transect. After a detailed examination of stations centred on the PF and SAF, there is an approximate difference of -0.002 psu between the sections at SR01 and SR01b. This has not been removed from the time-series in figure 2.5 as it is not statistically significant. The variability of the LCDW salinity maximum around the Southern Ocean along dynamic height contours is examined in Williams et al. (2006) (figure 6 in paper). This analysis shows the gradual salinity and temperature changes on contours associated with the PF and SAF. The spatial variability of the properties of the LCDW is examined in more detail in the discussion of the Inverse Model results in chapter 5.2 where the changes can be examined in terms of a balanced picture of fluxes into and around the Southern Ocean.

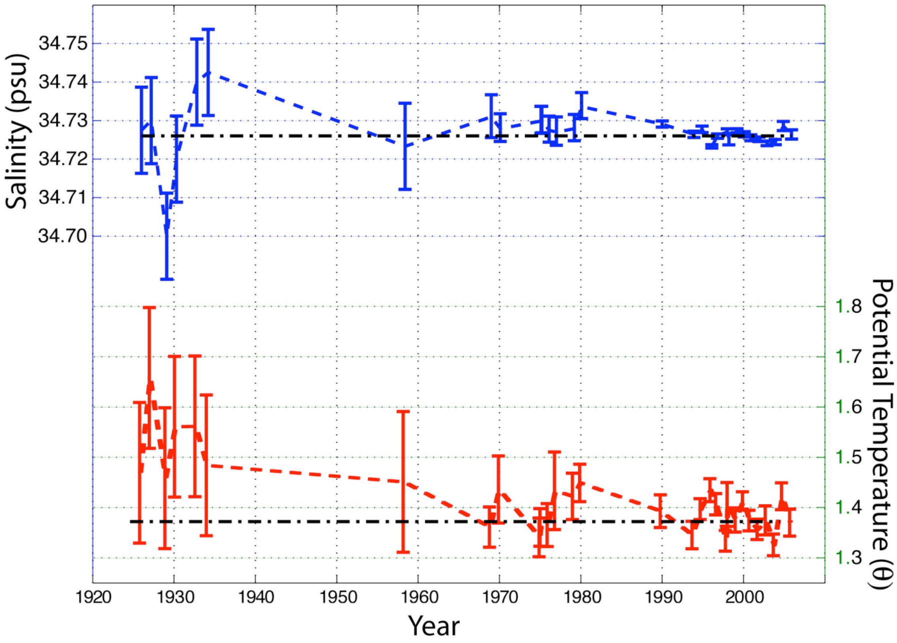

Figure 2.5: Mean salinity (top/blue) and potential temperature (bottom/red) values of the LCDW salinity maximum at Drake Passage vs. time (1926-2005). The black dashed lines represent the mean from 1970-2005. Error bars include a combination of the systematic and standard errors and an additional bias due to bottle sampling where appropriate.

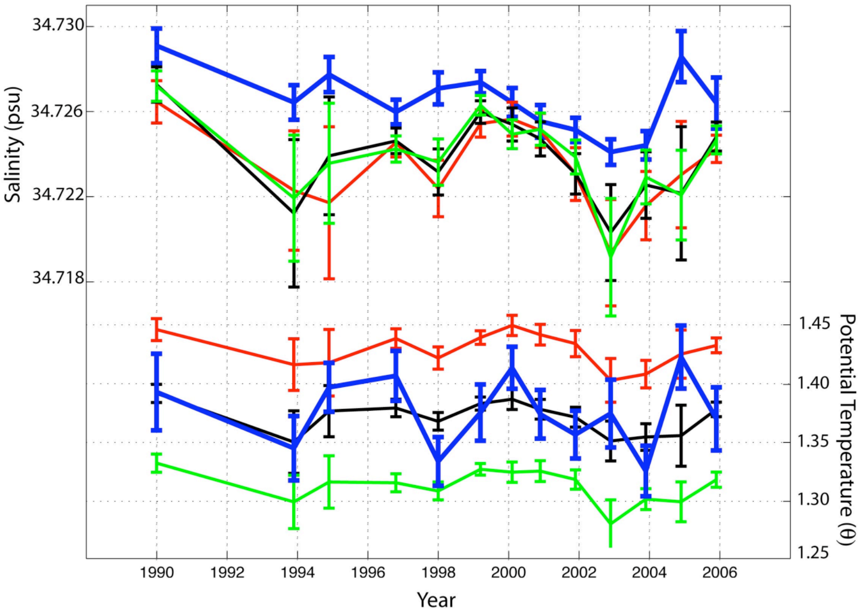

Figure 2.6: Mean Salinity (S)(top) and Potential Temperature (θ)(bottom) from CTD sections (1990-2005)- showing mean S/θ values at the salinity maximum (thick blue lines), and on three iso-neutral surfaces (γ^n=28.07-28.08 kg/m^3 (red), γ^n=28.08-28.09 kg/m^3 (black) and γ^n=28.09-28.10 kg/m^3 (green)). Error bars are ±1 standard error.

A study could not be made on neutral density surfaces for the whole data set due to the poor vertical resolution of bottle measurements. Figure 2.6 shows a comparison of the salinity maximum surface and three neutral density layers cover the density range of the surface. The figure uses CTD data along SR01W and SR01b lines between 1990 and 2005. The property variability is dominated by short-term variability. The mean values are also affected by the mean frontal locations, causing variations of the water volumes in neutral density layers. There is a fairly strong agreement between the trends on density surfaces and on the salinity maximum surface. The temperature values on the salinity maximum surface are similar to those on the γ^n=28.08-28.09 kgm^{-3} layer, and the mean salinities on each density layer are also similar, suggesting that the density changes here are dominated by changes in temperature.

2.4 Variability of the other water masses

2.4.1 Intermediate Waters

Sievers and Nowlin (1984) traced the sub-surface salinity minimum of the AAIW northward from the surface waters of the PFZ, in the stations of the ISOS sections. This method of following the AAIW was adopted for the contemporary sections. The examination of this higher resolution data showed that there were not any consistent patterns in the water mass properties of the salinity minima from stations in the same section. This meant that it was not possible to determine a characteristic density surface or property value that could be objectively used to demonstrate the variability of AAIW at Drake Passage. This is probably due to the localised nature of AAIW formation in the South-East Pacific and the high eddy mixing associated with the PF and SAF at Drake Passage. Figure 2.7 shows the mean transport on density layers from the 11 NOC/BAS sections (1993-2005) and the envelope of variability (one standard deviation). There are two main peaks, associated with the Intermediate waters (between γ^n=27.2-27.6 kg/m^3) and the LCDW (centred around γ^n=28.00 kg/m^3). The greatest variability is associated with the intermediate water peak, which can often be decomposed into two separate peaks for the SAMW and AAIW for individual sections. There are many factors that affect the intermediate water transports, including the frontal locations and the climate conditions in the South-East Pacific that affect the IW formation processes.

Figure 2.8 shows the variability of potential temperature and salinity found in the density layers between γ^n=27.10-27.35 kg/m^3 from an area-averaged mean taken from profiles north of the Polar Front. There is a clear cooling/freshening trend on neutral density surfaces between γ^n=27.10-27.25 kg/m^3 over the time period, corresponding to the top of the SAMW and the bottom of the SASW. This signal is not found in the denser waters associated with the AAIW and the bottom of the SAMW, where there was a large range of inter-annual variability. This trend corresponds to a cooling signal of ~0.3 °C per decade and a freshening of ~0.04 psu per decade over this density range. These changes can be explained by surface warming and increased precipitation in the source regions of this water mass in the Southeast Pacific, similar to the trends found in the AAIW and SAMW in the Indian Ocean by Bindoff and McDougall (2000), the analysis of these trends is outlined in Bindoff and McDougall (1994).

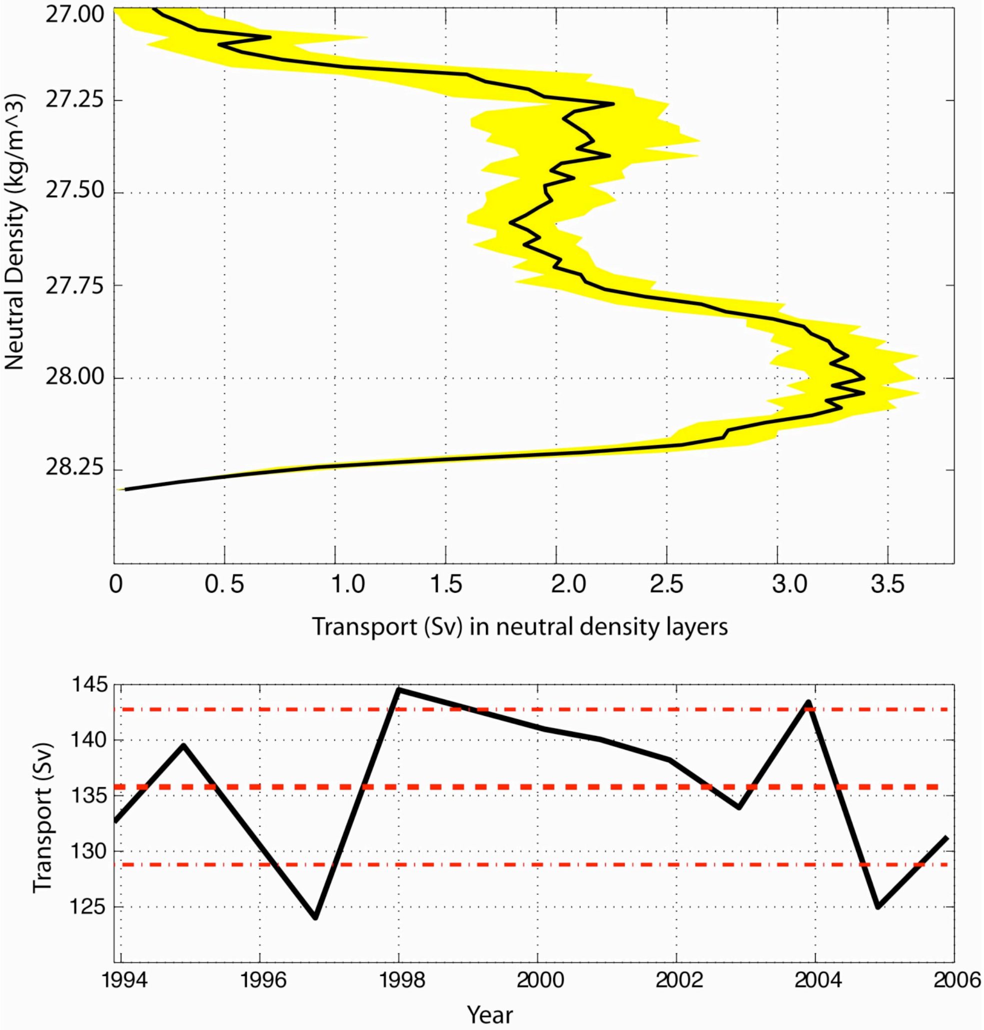

Figure 2.7: Top: Mean baroclinic transport in neutral density layers, with a thickness of 0.02kg/m^3 for the NOC/BAS SR01b sections (1993-2005). The yellow envelope is ±1 standard deviation. Bottom: Baroclinic transports from the NOC/BAS sections (black line), with mean (thick dashed red line), and ±1 standard deviation (dash-dot lines).

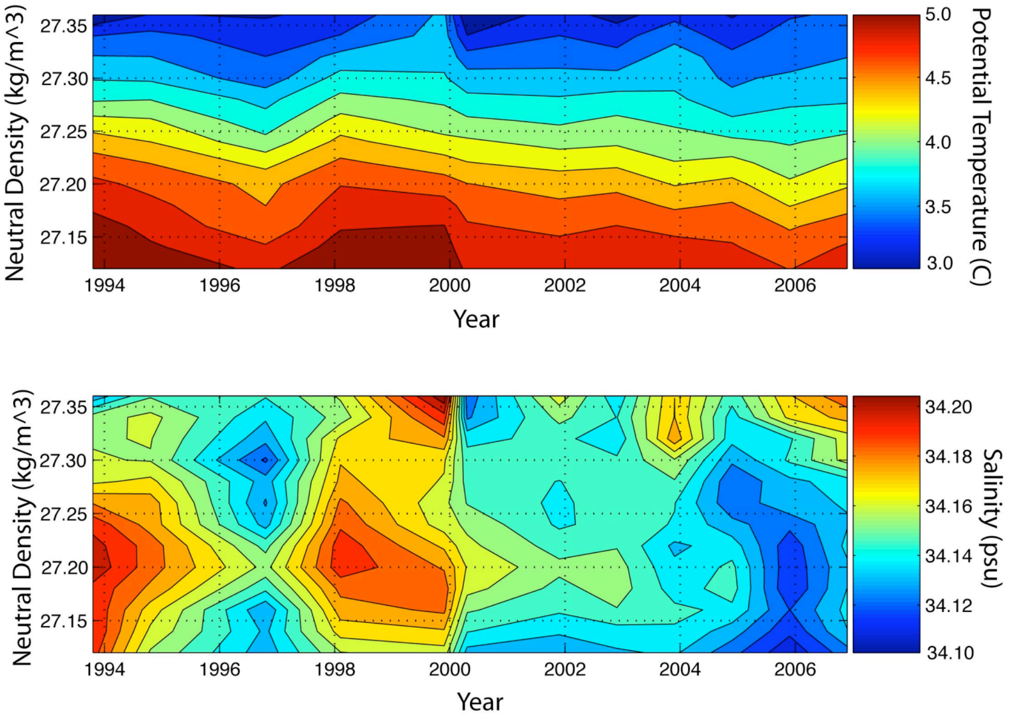

Figure 2.8: Mean properties on neutral density surfaces in the NOC/BAS SR1b sections focussing on the upper intermediate waters/ SAMW (γ^n=27.10-27.35 kgm^{-3}). Top: Potential Temperature (° C) with contour spacing of 0.2 °C. Bottom: Salinity (psu) with contour spacing 0.02 psu.

2.4.2 Weddell Sea Deep Water

Cunningham et al.(2003) provided an analysis of the first six NOC/BAS sections. In this study, they postulated a connection between the amount of Deep/Bottom Water in Drake Passage and the location of the PF. Extending this analysis to the whole data set did not yield any link between the frontal locations and the amount of WSDW (γ^n>28.26 (Naveira Garabato et al. (2002)) found in the sections. No pattern was found in the size or properties of the WSDW found in the data across the timeframe of the data set. The passage of this water mass is not detectable west of the Shackleton Fracture Zone in the sections from the historical data set. The vertical resolution of the bottle stations may also affect the detection of the deeper water properties and any detection of any westward bottom water transport into the Southeast Pacific Basin. Figure 2.9 shows the relationship between the geostrophic transport in the density layers associated with

WSDW and PF location from the NOCS/BAS SR01b sections between 1993 and 2006. There is no long-term trend between the two signals.

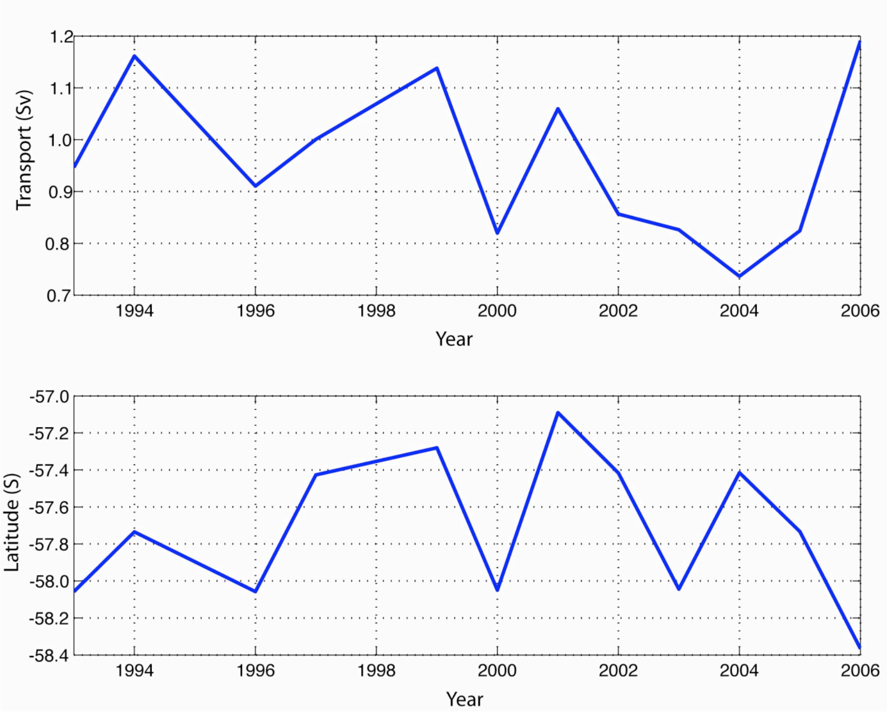

Figure 2.9: Top panel: Geostrophic transport across Drake Passage in the density layers > 28.26 kgm^{-3} associated with WSDW, and (bottom panel): Polar Front location from the NOCS/BAS SR01b hydrographic sections.

2.5 Geostrophic transport variability

The bottom panel of figure 2.7 shows the total geostrophic transport time-series from the NOCS/BAS SR01b data-set between 1993-2005. The mean transport is 136.2±7.2 Sv with a reference level set to the deepest common level (DCL) between station pairs. This value is very similar to the often-quoted value from Cunningham et al.(2003) of 136.7±7.8 Sv that is calculated from the first six sections in the time-series. The transports generally tend to be at the extremes of the transport range found in the data, with years of high or low transport. Figure 2.10 shows a breakdown of this transport on density surfaces. There is a significant amount of variability within the year-to-year transport in density layers. Transport time-series representing the different water masses were compared to regional climate indices (SAM, ENSO) but no significant correlations were found over a wide range of positive and negative time lags. The dominant scales of variability at Drake Passage are much smaller than the annual scale, with measurements on scales of days (Meredith and Hughes, 2005) required to fully capture the barotropic transport variability in this region. The baroclinic transport variability is on longer timescales, in the region of weeks to months. This can be seen from sea-surface height measurements from satellites (e.g. TOPEX-POSEIDON/JASON) following the propagation of baroclinic eddies through Drake Passage, but is still less than the yearly resolution provided by the repeat hydrographic sections,

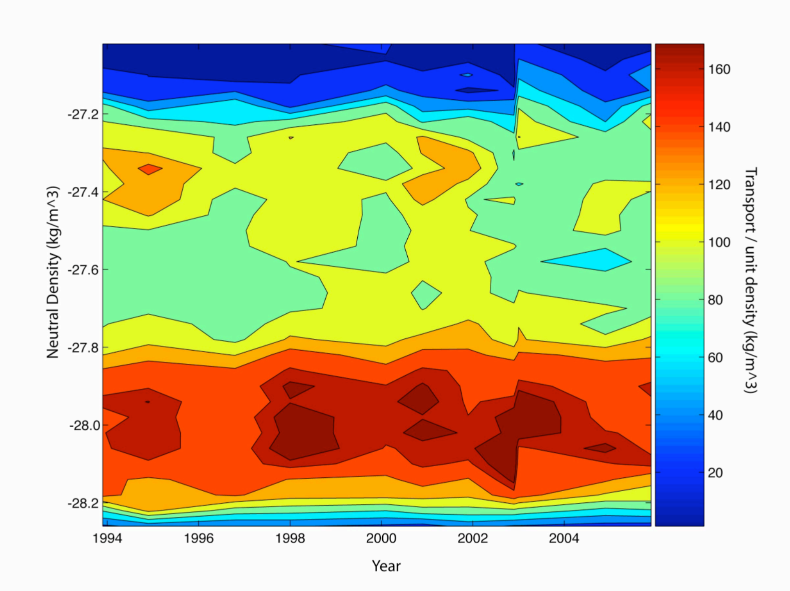

Figure 2.10: A time-series of transport per unit density on neutral density surfaces from the SR01b NOC/BAS repeat hydrographic data-set. The transport is calculated in bins of 0.04 kgm^{-3}.

2.6 Summary

In this chapter, the basic structure and properties of the Southern Ocean at Drake Passage have been outlined. A historical data set was created to examine the property variability of different water masses between 1926-2005. The salinity maximum layer of the LCDW was the only water mass where a consistent variable could be defined throughout the data set. Within the limits of measurement uncertainties and the shorter timescale variability, the properties of the LCDW salinity maximum have remained constant.

Williams et al. (2006) extended this study to the repeat sections at SR03 south of Tasmania (140 E). Even though this data set is more sparsely distributed in time, with a series of sections occupied during WOCE and a Discovery II section from 1932, within errors, the same pattern is found. The shorter timescale and inter-section variability is much larger, with the highest salinities found in the AAZ, south of the PF. The sparseness of the hydrographic data record around the Southern Ocean means that it is not possible to examine the long-term variability apart from in specific locations. WOCE enabled the combination of sections around the Southern Ocean to obtain consistent patterns of the mean flow structure and the ocean fluxes around the ocean basins. Inverse modelling techniques provide the opportunity to construct a consistent mean field and to examine the importance of different physical processes on the mass and heat balance in the Southern Ocean as a whole. The next chapter will outline the details of the Inverse Model used in this study.

Chapter 3: A Southern Ocean Inverse Model

Inverse Modelling has emerged as a powerful technique to combine diverse oceanographic measurements to obtain an internally consistent picture of the mean state of the ocean (e.g. Wunsch 1979, Ganachaud and Wunsch 2001). This chapter will outline the basic theory of inverse modelling, its previous application in the Southern Ocean, and the set-up and design of the Southern Ocean Inverse Model that forms an important part of this study.

3.1 Introduction and basic concepts

3.1.1 The general problem

Inverse techniques are based on finding the values of a set of independent variables (x_i) given the value of a linearly dependent function (y), e.g.

$$a_1x_1 + a_2x_2 + a_3x_3 = y(x_1, x_2, x_3) \tag{3.1}$$

In this context, y usually expresses an observation, and the x_i are some physical variable associated with the observation by some model represented by the a_i. This can be generalised to a set of m equations, with n independent variables, with y becoming a vector of observations or data, of length m.

$$Ex + N = y \tag{3.2}$$

Where E is the model matrix (formed of the coefficients a_{ji} of (3.1), j is the equation number ($j=1,..., m$), and i is the associated variable number ($i=1, ..., n$)), x is a vector (length n). An error vector, N, is added to include the effect of various forms of error and noise. Wunsch (1996) outlines some of the different methods used to solve the equation, depending on the nature of the problem. In oceanographic problems, there are usually more independent variables than equations, so the problem is under-constrained. This means that there are an infinite number of solutions to equation 3.2. In practice, the researcher is actually trying to identify a sub-set of the infinite solution space that best matches the a-priori assumptions and expectations of the problem at hand. The weighting of equations and errors becomes a vital step in the determination of an acceptable solution, and provides the greatest challenge in setting up the initial matrix equation. In general there are two ways of weighting equation 3.2. Row Scaling allows the application of specific weights to individual equations, and is applied by pre-multiplying the equation by $W^{-1/2}$, where W is a square matrix (size *m* x *m*), with elements W_{jj} equalling the square of the weight that is to be applied to the j^{th} equation. *W* is formally defined as the model covariance matrix, containing information on the relative scaling of the equations that form the model matrix.

$$W_{jj}^{-1/2}\sum_i E_{ji}x_i + W_{jj}^{-1/2}N_j = W_{jj}^{-1/2}y_j \tag{3.3}$$

Column weighting applies a weight to the columns of *E,* allowing emphasis to be placed on different independent variables x_i. A square matrix *S* (of size *n*), is applied to equation (3.2). *S* is formally defined as the data covariance matrix, containing information on the scaling of the terms in the model solution.

$$ES^{1/2}S^{-1/2}x + n = y \tag{3.4}$$

resulting in the complete weighted form of equation (3.2)

$$W^{-1/2}ES^{1/2}S^{-1/2}x + W^{-1/2}N = W^{-1/2}y \tag{3.5}$$

This can then be re-scaled to obtain equation 3.2 in a new set of variables *E',x'* ,y'and *n'*. The details of these weighting factors and how they are applied to the solution will be explained in the following sections. The non-diagonal terms of the weighting matrices represent the correlation terms between the variables or equations. In most cases, without specific knowledge of these correlation terms, they are taken to be zero.

3.1.2 The oceanic inverse problem

Inverse Methods are a useful technique to deduce consistent fluxes from hydrographic sections. The data set that resulted from WOCE had unprecedented coverage of the global ocean system and resulted in a global ocean inverse study (Wunsch and Ganachaud 2000 and numerous regional studies (Naveira Garabato et al. 2003, McDonagh and King, 2004) within ocean basins. This study aims to build on this work by adding new data sets, including a southern boundary that is corrected to the output of a regional ocean model and examining different parameterisations of the internal mixing. The primary unknown in all of these studies is the location of the known velocity surface (KVS). The independent variables are barotropic velocity corrections *(b_i)* to geostrophic velocity profiles obtained from the station pairs that constitute the model domain. The model is usually initialised at the 'best guess' state for the individual sections that form the model domain, and the velocity corrections adjust the flow to create a consistent flow pattern that best meets the criteria determined by the researchers a-priori assumptions about the errors and flow structure.

The model equations are generally a set of conservation equations on a series of layers throughout the water column. Inverse methods can be applied to individual sections to determine the effects of various tracers on the transport balance (e.g. McDonagh et al. 2006), up to complicated box configurations spanning the global ocean (e.g. Wunsch and Ganachaud, 2000). In this study, a variety of box configurations are examined spanning the whole of the Southern Ocean. Additional physics can be added by increasing the complexity of the model equations, resulting in more variables to be determined. Mixing across isopycnal surfaces and air-sea interactions provide additional information about the mean state of the ocean and are applied in various forms in this study (the model physics will be explained in section 3.2).

3.2 Model design

3.2.1 The model equation

This inverse study examined a series of boxes around the Southern Ocean on a series of iso-neutral surfaces (Jackett and McDougall 1997). Equation 3.6 outlines the general conservation equation used in this model study.

$$\sum_{j=1}^{s}\Delta x_j\left[\int_{p_m}^{p_{m+1}}\rho C(v_r+b)\left(\frac{\partial p}{\partial z}\right)^{-1}dp+\overline{\rho}^{Ek}\overline{C}^{Ek}\overline{v}^{Ek}h_{Ek}\right]_j-\left[(w^*+k\frac{\partial C}{\partial z})A\overline{\rho C}^A\right]_m+\left[(w^*+k\frac{\partial C}{\partial z})A\overline{\rho C}^A\right]_{m+1}+\ldots\ldots$$
$$\ldots\ldots(F_v+\Delta F_v)+\left[(M_C+\Delta M_C)\right]_m-\left[(M_C+\Delta M_C)\right]_{m+1}+n_{c,m+1}=0 \qquad (3.6)$$

The terms are defined as follows: j is the station pair number, of s station pairs, Δx_j is the distance between the stations. ρ is the density, C is a general tracer (C=1 for mass), v_r is the geostrophic velocity component, b is the barotropic KVS correction, $(\partial p/\partial z)^{-1}$ represents the density layer thickness, ρ^{Ek}, C^{Ek}, v^{Ek}, h_{Ek} represent the mean density, tracer concentration, Ekman velocity and depth of the surface Ekman layer. m refers a density surface within a box of area A, w^* is the dianeutral advective velocity, k is the effective diffusivity coefficient. F and M are dianeutral air-sea induced mass and volume fluxes, and n is the noise term.

The equation contains three main components that will be described individually (sections 3.2.2-3.2.4)

- Barotropic velocity corrections at individual station pairs (*b*)
- Dianeutral advective velocities and diffusivity coefficients (w^*, k)
- Fluxes due to the air-sea interactions (F_v, M_C)

Equation 3.6 can then be re-arranged into the form of equations 3.1/3.2, in terms of known quantities, unknown variables and model parameters, and the noise.

3.2.2 Geostrophic transport corrections

The conservation equation includes the sum of the individual transports on each density layer (*m*) from each station pair ($j=1,...,s$), and the associated Ekman transport. Each Ekman transport is calculated from the annual mean wind-stress field obtained from the NOC Climatology (version 1.1 Josey et al. 1998, Grist and Josey 2003), and advects the mean tracer concentration averaged over a mixed layer of depth 60m for each station pair. The Ekman flux normal to the station pair *(j)* is then calculated. To minimise the number of variables, the Ekman fluxes are kept fixed and do not contain a correction term in the model. The only free variable in this component is the barotropic velocity correction (b_j). The other components are all included in the *y* vector (equation 3.2).

Ganachaud (2003b) examined the effect of different bottom triangle calculations associated with the geostrophic velocity and found quite large variability between the different methods. Various formulations were trialled in this study, but for simplicity, unless otherwise stated, the velocity and tracer concentration at the deepest common level was extrapolated into the bottom triangle, resulting in constant properties within the bottom triangle. This method can cause problems on the continental slopes, or where there are large topographic gradients between station pairs, so each correction was checked to determine whether the extrapolation was creating an unrealistic flux through the bottom triangle.

3.2.3 Dianeutral fluxes

There are various methods for representing the dianeutral fluxes in an inverse model. Some representations were examined by Rintoul and McIntosh (1997) and McIntosh (1991)). In the basic model set-up, the model solves for an advective velocity (w^*) and an effective diffusivity (k) determined by the tracer gradients from the mean field $w^*C + k\,{\partial C}/{\partial z}$, where C denotes a general tracer (for mass, $C=1$). The effective diffusivity takes account of all of the other dianeutral processes not included in the advective term. The WOCE climatology (Gouretski et al. 2004) was used to calculate the mean property gradients and areas of neutral density surfaces in each box. Property means were calculated over a density surface thickness of 0.1kg/m^3 from all of the relevant (area-weighted) climatological profiles. Gradients were calculated for individual profiles and averaged in a similar manner. This method was chosen over the more usual approach to determine gradients from the hydrographic stations (Ganachaud (1999), McDonagh and King (2005)). The reasons for this were the large range of gradients found from different stations within a section, and the uncertainty involved in converting mean section values into box-wide means, especially given the different flow structures associated with zonal and meridional sections in the Southern Ocean .i.e. due to the ACC.

McIntosh and Rintoul (1997) and Sloyan and Rintoul (2001b) examined various formulations of dianeutral fluxes, opting to use property specific advective fluxes only (e.g. $w_C{}^*$). This was because they did not believe that the other processes included in the effective diffusive term were well represented by the Fickian diffusion parameterisation. In this representation, a measure of the effective diffusivity term can be obtained by subtracting the property flux from the basic advective mass term. Two additional dianeutral schemes were included in addition to the standard model set-up. The property specific advective fluxes ($w_C{}^*$), and an adaptation of the standard scheme to include separate property-specific diffusivity terms (k_C). The effect of these different schemes on the model solutions will be discussed in Chapter 6.1.

3.2.4 Air-Sea interactions

Air-sea fluxes play an important role in the mean state of the Southern Ocean. There are large errors associated with climatological and re-analysis estimates of the mean fluxes in the Southern Ocean due to a very sparse record of in-situ observations. In this model, we solve for corrections to the parameters determined from annual mean air-sea fluxes derived from the NOC climatology. Figure 3.1 shows the annual mean fields used in this study, the top panel shows the strong wind stress values associated with the mean zonal winds that drive the ACC eastward. The regional variability in the heat and freshwater surface fluxes is presented in the lower two panels. The parameterisation of air-sea fluxes is adapted from (Naveira Garabato et al. 2003) and is based on the work of Speer and Tziperman (1992).

Air-sea fluxes have two main effects on the surface waters, direct contributions due to net exchanges between the ocean and atmosphere, and indirect contributions e.g. diapycnal air-sea flux induced mass fluxes. The direct contributions are due to exchanges of mass (freshwater/heat flux):

$$M_\rho = \int_T dt \int_A -Q dA \tag{3.7}$$

$$M_\theta = \int_T dt \int_A H dA \tag{3.8}$$

The total exchange is averaged over an annual cycle, taking into account the changing area of an outcropping density surface throughout the year. Q (kg/m^{2}s) is the freshwater flux, and H is the net heat flux (W/m^2).

The air-sea induced diapycnal volume flux is defined as:

$$F_V(\rho) = \int_T dt \int_{\Delta A} dA \left[\frac{1}{\Delta\rho} \left(\frac{-\alpha H}{C_\rho} + \rho\beta Q S \right) \right] \tag{3.9}$$

The integral is taken over an annual cycle, and the area (ΔA) of a thin strip of the surface waters with density $\rho = \rho \pm \Delta\rho$, centred at ρ. Sloyan and Rintoul (2000) and Naveira Garabato et al. (2003) also include a contribution due to the Ekman transport, but this does not induce a change of density at the surface, only moving the surface water properties around. This effect should be taken into account in the climatological monthly-mean surface properties. The effect of Ekman transports only needs to be considered at the box boundaries (see section 3.2.2). The monthly mean surface fields were obtained from the World Ocean Database 2001 (WOA01-Conkwrigh et al. 2001). This is used in place of the WOCE climatology because there is no monthly field in the latter, but the WOCE fields are still preferred for the water-column averages due to the inclusion of all of the WOCE cruises used in this study. The variables are chosen to be deviations (ΔF_v, ΔM_ρ, and ΔM_θ used in the relevant mass and heat conservation equations only) from the climatological mean that is included in the data part (y) of the balance equations.

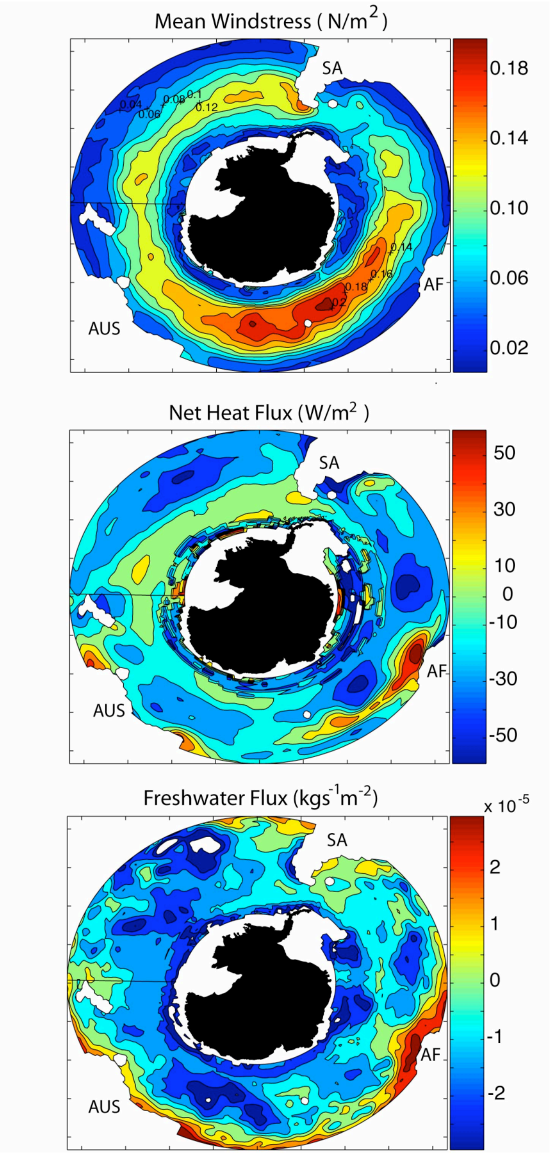

Figure 3.1 Mean fields of Windstress (top), Net Heat flux (middle), and Freshwater flux (bottom) from NOC Climatology (Grist and Josey, 2003). AUS=Australia, AF=Africa, SA=South America. A positive/negative flux is out of/into the ocean.

3.2.5 Solutions: SVD vs. GM

Solutions of the under-constrained inverse problems require some form of closure , typically provided by minimising a suitable metric (e.g. the l_2 norm) of an element of the problem, either of the variable *x*, or of the noise, *N*. There are two main techniques used in the literature to solve oceanographic inverse problems, Singular Value Decomposition (SVD) and Gauss-Markov Estimators (GM). I will briefly outline the two methods here and explain which method was chosen for this study. A more detailed explanation can be found in Wunsch (1996).

3.2.5.1 Singular Value Decomposition

SVD involves the decomposition of the model matrix, *E* into two orthogonal matrices (U,V) and a non-square (as the problem is under-constrained) diagonal matrix, *A*.

$$E = UAV^T \tag{3.10}$$

This operation rotates the solution space from a series of vectors associated with the independent variables, x_i, onto a solution space comprising of orthogonal state vectors, with eigenvalues defined by the diagonal elements of *A*. As *A* is not square (it has dimensions *m*x*n*), some of the eigenvalues are zero or effectively zero. To solve for *x*, equation 3.10 must be truncated so that only the first k (n≥k) eigenvalues are chosen:

$$E = U_k A_k V_k^T$$

If it is assumed that $U_k^T N = 0$, i.e. that the errors are orthogonal to the solution vectors, then an expression for $\tilde{x}$ can be obtained (overbar denotes the solution vector) by substituting equation 3.10 into equation 3.2 and rearranging.

$$\tilde{x} = V_k A_k^{-1} U_k^T y \tag{3.11}$$

and the following expression for the noise

$$\tilde{N} = (I - U_k U_k^T) y \tag{3.12}$$

The resulting values of x and N are dependent on the value of *k* chosen (the solution rank). By reducing k, the dimensionality of the solution is being effectively reduced, confining the smaller eigenvectors *(n>values>k)* to the solution errors.

3.2.5.2 Gauss-Markov Estimators

The Gauss-Markov Theorem is based on the idea that it is possible to explicitly express the relationship between the estimate ($\tilde{x}$) and the observation (*y*) in terms of a matrix *B*:

$$\tilde{x} = By \qquad (3.13)$$

The theory minimises the covariance matrix of $(\tilde{x} - x)$ to find the solution with minimum dispersion between the solution and the true value of *x*,

$$P_{x\tilde{x}} = \left\langle (\tilde{x} - x)(\tilde{x} - x) \right\rangle = \left\langle (By - x)(By - x)^T \right\rangle \qquad (3.14)$$

(In general, the covariance/second-moment matrix of a variable '*a*' is $\mathrm{cov}(a) = R_{aa} =< aa^T >$, and is an important variable in the following analysis)

The Gauss-Markov theorem states that $B = R_{xy}R_{yy}^{-1}$ and therefore $\tilde{x} = R_{xy}R_{yy}^{-1}y$, resulting in the following expressions that can be used to obtain solutions of equation 3.2 given estimates of the error and solution covariance matrices. The full derivation of these equations can be found in Appendix AF, based on the derivations of Wunsch (1996).

$$\tilde{x} = R_{xx}E^T\left(ER_{xx}E^T + R_{nn}\right)^{-1}y \qquad (3.15)$$

$$\tilde{n} = \left\{I - ER_{xx}E^T\left(ER_{xx}E^T + R_{nn}\right)^{-1}\right\}y \qquad (3.16)$$

This solution is identical to a general least-squares solution when the weighting functions (*S, W*) are set to R_{xx}, and R_{nn} respectively. This fact has led to some confusion in the literature (see discussion in Wunsch (1996) p.185), but when using GM estimators, the second moment matrices have to be used as the equation weights.

3.2.5.3 Choice of solution method

Both of these techniques were explored in the model design, but it was decided to use Gauss-Markov estimators for the final model solutions. The main reasons for this were that the solution contains all of the errors in the model. Using SVD, the researcher chooses the solution rank, confining part of the solution to the noise (N). The decision of rank is then determined by some a-priori assumption on the size of the individual errors, choosing the solution with the highest rank that fits within these error estimates. GM estimators provide a straightforward way to examine the a-posteriori errors of the model matrix to be able to derive error estimates for the section transports and the corresponding fluxes. This method transfers the subjective aspect of the error estimation to a more controllable and objective format. The errors in flux transports across each section can be calculated from the a-posteriori error covariance matrix:

$$P_{xx} = R_{xx} - R_{xx}E^T(ER_{xx}E^T + R_{nn})^{-1}ER_{xx} \qquad (3.17)$$

This equation gives an estimate of the errors associated with the estimate of each variable in the solution. In general, the posterior error of the station pair corrections is very similar to the prior estimate (R_{xx}). This shows that the individual corrections are not well defined, but the posterior error matrix contains information about the correlation between station corrections. The error estimate can be found from the following equation:

$$e = \sqrt{a^T P'_{xx} a} \qquad (3.18)$$

where a is a vector of station pair areas for a given section, and P_{xx}' is a subset of the a-posteriori error covariance matrix corresponding to that section. The a-posteriori errors should be within the ranges set by the a-priori errors for a valid solution.

3.3 Model data set

The hydrographic data conducted during WOCE (1990-1997) forms the core of the sections in the model data set. There are a total of 21 hydrographic sections used in a number of configurations to study the flow structure around the Southern Ocean. The details of the hydrographic sections are given in Appendix AB. Figure 3.2 shows the standard model configuration used in this study, with 12 boxes (9 circumpolar and 3 fringing Antarctica). The remaining regions around Antarctica are not used as boxes due to the large uncertainties in the flow patterns and air-sea fluxes in these regions (e.g. Weddell, Ross, Bellingshausen and Amundsen Seas).

The hydrographic sections contain fields of salinity, potential temperature (θ), silicate, phosphate and oxygen. The salinity, θ, and derived neutral density data are from high quality CTD casts and are averaged onto a 2db grid. The other tracer measurements come from bottle data with a limited vertical resolution. The data was interpolated onto a 2db grid to coincide with the CTD data using averaging on neutral density surfaces. A running mean was applied with variable horizontal extent, dependent on the characteristic length scales associated with the stations and the local station spacing. In the case of missing phosphate stations, a mean nitrate:phosphate ratio was determined on neutral density surfaces and then applied to the corresponding nitrate stations to create pseudo-phosphate surfaces. This is similar to the method applied by Ganachaud and Wunsch (2001).

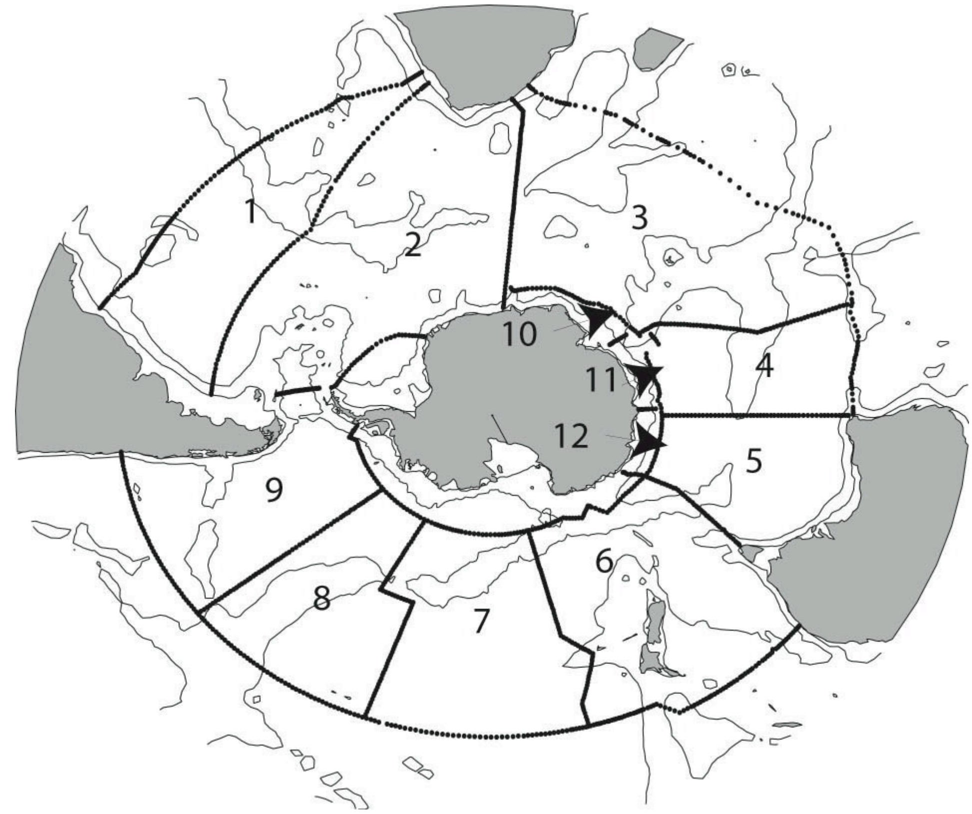

Figure 3.2: The locations of the hydrographic stations forming the boxes of the standard configuration of the Southern Ocean Inverse Model.

3.4 Model errors and weighting

Having outlined the basic methods and data set that make up the Inverse model, this next section will detail the error fields applied to it. The error fields will be discussed in three sections, relating to the error covariance (R_{nn}), the solution covariance (R_{xx}), and the additional model constraints.

3.4.1 The error covariance matrix

From the discussion of weighting matrices in section 3.1.1, it is clear that the error covariance matrix *(R_{nn})* adds a weight to each equation dependent on the assumption of a-priori errors. Garabato et al. (2003) used the baroclinic variability determined from in-situ data to create estimates of the errors on neutral density layers. Ganachaud (1999) used a General Circulation Model to determine the scales of baroclinic variability in his global ocean study. Due to the size of our model domain and the sparse data record in the Southern Ocean, it was not possible to make any data-based conclusions about the variability apart from in select locations from in-situ data (i.e. at Drake Passage and at SR03, south of Tasmania).

An important assumption for this study is that the mean properties of the Southern Ocean are constant within the bounds of short-term variability over the time period of the data (1989-2003). The conclusions regarding the LCDW variability at Drake Passage in chapter 2 support this assumption, at least in terms of the Deep Water variability. The major source of error when trying to conserve the transport and properties of a given layer is due to the assynoptic nature of the sections used in each box (i.e. the length in time is on a much larger scale than the scales of the variability of the baroclinic fields). This can lead to large imbalances in the fluxes, especially in regions where there is a very sparse data record, making it hard to determine what the scales of variability are. For example, at Drake Passage the range of baroclinic transports is > 20 Sv. The mean transport at SR01b (1993-2005) is 136.2Sv, with a standard deviation of 7.2 Sv. This effect could lead to spurious answers, especially when trying to balance the fluxes in a basin-scale box, so model output was used to gain a better understanding of the scales of variability. In general, the variability of the baroclinic field within an individual section is neglected and each section is assumed to be a fair representation of the actual flow field for the whole section at the time of measurement. This assumption may not be as valid for the longer sections, especially in the Pacific Ocean, but it is assumed that this has a much smaller effect than the differences due to sections occupied over timescales of years apart.

The OCCAM 1/4° Eddy permitting Ocean Model (e.g. Lee et al, 2001) was used to examine the variability caused by using non-synoptic hydrographic sections. Representative sections of five day mean properties were collected from a five-year period (1992-1997) from model run 202 to create boxes similar to the Inverse Model configuration. A Monte-Carlo simulation was performed for each box to examine the uncertainty in the flux balances on neutral density surfaces, and in the whole box. The standard deviation of 1000 samples of box boundaries, randomly distributed around the temporal domain of the OCCAM data sub-set was calculated. 1000 samples was chosen after a study over a number of scales found that the results remained stable well within this sample size. Figure 3.3 shows a comparison between the variability of the OCCAM data and the SR01 NOC/BAS sections. The variability is twice as large in the model (even though the standard deviation of the mean flow is lower at 5.1 Sv). There is also a difference in the location of the peak in variability associated with the Intermediate Waters. This is probably due to how well the model represents the formation and structure of these water masses. The model does not seem to reproduce the twin peaks associated with the SAMW and AAIW shown in the real data. The variability in the deep water is very high in the model and is most likely due to the neutral density interpolation of the model output and the resolution of the deeper layers. This effect is assumed to be spurious so the variability of the bottom water is set equal to the CDW in all of the errors used in this study. This also supports the a-priori assumption that the greatest variability will be found in the upper layers, allowing larger errors in the conservation equations relative to the deep waters.

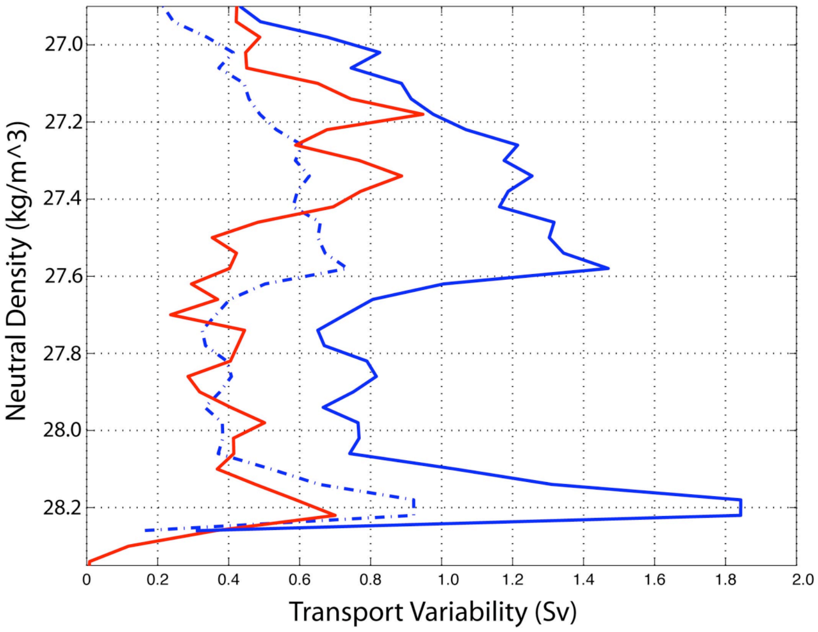

Figure 3.3: Transport variability on neutral density surfaces across SR1 from a.) SR01b sections (1993-2005) (red), b.) OCCAM 1/4° Model run 202, 1992-1997, five-day means (blue-thick), c.) same as b,), but divided by 2 for comparison with a.) (blue-dashed).

The posteriori error covariance can be calculated from the Gauss-Markov estimators, starting from the definition of $P_{nn} = \langle (n - \overline{n})(n - \overline{n}) \rangle$, and substituting in equations 3.15-3.17, leading to the following expression:

$$P_{nn} = ER_{xx}E^T - ER_{xx}E^T(ER_{xx}E^T + R_{nn})^{-1}ER_{xx}E^T = EP_{xx}E^T \qquad (3.19)$$

This provides an estimate of how well the errors are being resolved and how well the model is working. The errors associated with the other tracers apart from mass are applied following the method of Ganachaud (1999), where the standard deviation of the property variability in a given layer is multiplied by the mass transport variability obtained from the model. An additional factor of two is added to account for additional unresolved baroclinic variability effects.

The determination of errors on density layers or on groups of density layers is not so straightforward because there is not an unknown variable in the model equations that directly relates to these parameters, and therefore there is no error estimate either. In this study, I have decided to use a value based on the correlation of uncertainties in the layer fluxes, obtained from the a-posteriori error matrix, P_{nn}. Using a form similar to that of equation 3.18,

$$e_n{}^2 = \sqrt{n_p^T P_{nn}{}' n_p} \tag{3.19}$$

where n_p is a sub-set of the lead diagonal of the a-posteriori error matrix representing the errors of mass balance on the density layers in question. This enables an error term to be determined for groupings of density layers, providing an estimate that takes account of the correlations between the error values. In the data analysis, the calculation of the overturning streamfunction, by integrating transports from the sea floor up through density layers will be required. In this case, the error estimates are calculated in a similar manner, integrated from the surface, with the correlations recalculated at each stage of the summation with the inclusion of each new density layer. This approach relies on the assumption that the errors in the mass balance within a given box layer are similar to the errors associated with the fluxes across a face of the box. In the analysis that follows, the overturning calculations will be made over major boundaries of the box set-up so it is fair to assume that the errors will be dominated by the fluxes across these sections.

3.4.2 The solution covariance matrix

The solution a-priori covariance matrix (R_{xx}) contains information about the expected scale of variables in the solution x. There are three classes of variable in the basic solution and I will explain the errors assigned to each class in turn. R_{xx} is usually chosen to only have non-zero values on the lead diagonal of the matrix. This simplifying assumption implies no correlations between the station pairs.

a.) Barotropic Velocity Corrections (b_i)

A commonly used starting point for setting the a-priori correction velocity variability is taken to be 1cm^2/s^2 (e.g. Ganachaud, 1999, McDonald, 1995, Hogg and Thurnheer 2005). The scale of variability in the ocean interior is of the same order as the velocity correction (~1cm/s). Closer to the basin boundaries and in shallower waters, larger values should be expected requiring a localised adjustment of the elements of R_{xx}. The specific adjustments applied will be explained when the model results are analysed by region (Chapter 4.1-4.3).

The GM method results in values on the lead diagonal of the a-posteriori solution covariance matrix (P_{xx}) that are very similar to that of R_{xx}. This feature was observed by Ganachaud et al (2000) in their GM inversions, leading to poor resolution of the individual velocity corrections. Methods to reduce the individual diagonal elements of P_{xx} were examined by applying correlation terms between stations from the same hydrographic section. This was applied using a combination of Gaussian functions, proportional to the mean barotropic Rossby radii of the two station pairs in question.

Figure 3.4 shows the results from two correlation functions applied to an Indian Ocean Sector inverse model (similar to combining boxes 3 and 4 from figure 3.2). The top panel shows the correction velocities from a full solution along I05 (see appendix AB for hydrographic section definitions). As the correlation is increased (blue-green lines), the individual character of the corrections is lost, resulting in a smoothed solution. This results in values of P_{xx} that are greatly reduced. Even though the individual station pair uncertainties are reduced (from 0.010 m/s to a mean of 0.006 m/s), when the section mean error is calculated using the correlation terms of P_{xx} (equation 3.18), then there is very little effect on the total section-wide error. It actually causes a slight increase from 2.73Sv (no correlations/black line), 3.07Sv (minor correlations/blue line), to 3.21 Sv (large correlations/green line). Due to this effect, no additional correlation terms were included in the study to account for the proximity of station pairs in any given section.

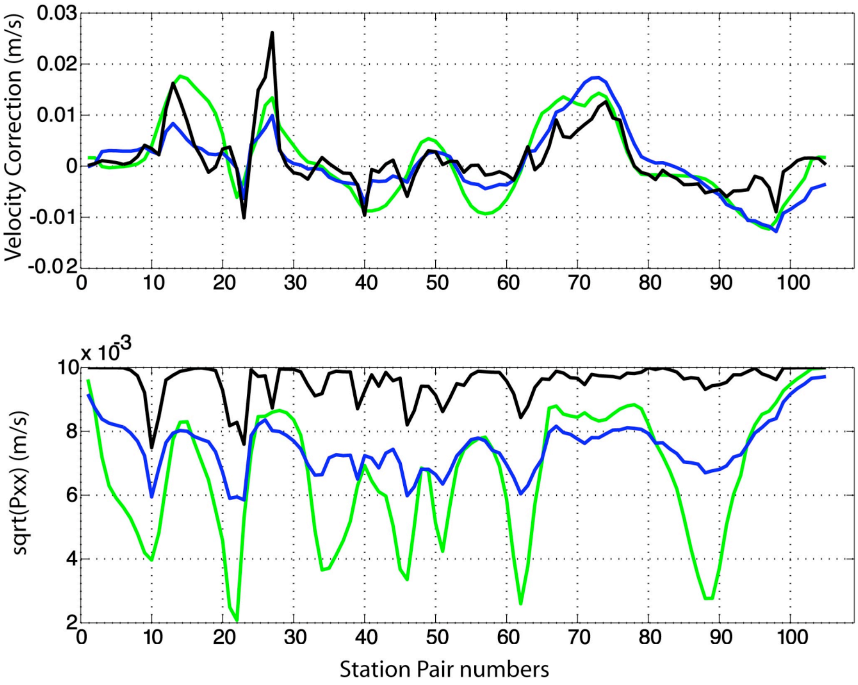

Figure 3.4: An Example of correction velocities (top) and posteriori errors (bottom) along I05 (see Appendix AB) from an Indian Ocean Sector Box model, comparing different correlation schemes in the a-priori error covariance matrix: no station correlation (black), small cross-correlation (blue), large cross-correlation (green).

b.) Dianeutral fluxes (w^* and k)

The values of the dianeutral fluxes are an important component of the Inverse Model solutions. The errors have to be set so that the model will allow significant transports across the density layers, but must also be in balance with the errors of the other variables so that the model is not biased towards these fluxes. Ganachaud (1999) chose values of $w^* = 1\times10^{-5}$ m/s and $k^* = 1\times10^{-3}$ m^2/s for his weights on the dianeutral fluxes. The model results would not be expected to reach these values as in a basin-wide box model, this would equate to very large dianeutral transports. These values were chosen so that the model would find suitable values without being artificially constrained by the imposed error covariances. In this study, a range of values were tested and the effect on the model solutions examined. It was found that slightly lower values provided more realistic solutions. This was shown by examining the posterior error matrix to determine to what extent the model was using the dianeutral fluxes to balance the overall fluxes within the model layers. Initial values of $w^* = 1\times10^{-6}$ m/s and $k^* = 1\times10^{-4}$ m^2/s were chosen as they resulted in values in the deeper layers that were significantly larger than the posterior errors, All of the dianeutral fluxes were initialised at zero in the model, so no a-priori dianeutral flow structure was imposed on the model.

c.) Air-Sea flux variables

The inclusion of air-sea fluxes introduces the largest uncertainties into the model due to the large uncertainties associated with the climatologies, increasing as you move further south in the Southern Ocean toward Antarctica. The model is initialised with parameters derived from the NOC climatology, solving for corrections to the three variables the constitute the physical representation of the air-sea fluxes chosen in this model. Each error is derived as a function of the magnitude of the incident flux and the area it is acting upon. In general, the uncertainty of the dianeutral air-sea induced volume flux (ΔF_ρ) is $O(O(1\times10^9)$ kgms^{-1}, $O(1\times10^{13})$ W for the air-sea induced heat flux (ΔF_θ), and $O(1\times10^6)$kgms^{-1} for the air-sea mass flux (ΔF_ρ). The heat flux error for the boxes is an order of magnitude greater. These errors are then checked before initialisation of the model to ensure that there is no bias to poorly defined variables. Lumpkin and Speer (2007) conducted a detailed study into the different fields obtained from the most commonly used reanalysis products and climatologies (ECMWF. NCEP, and the NOC climatology). They found significant differences between the different products, mainly due to the uncertainties caused by a very sparse data record. Their model results produced an UCDW export across 30 S that varied from 15 Sv to 20 Sv, depending on the climatology used. In this model, the NOC climatology is used, but any model results are effected by the large uncertainty in the air-sea forcing fields.

3.4.3 A Best-Guess Known Velocity Surface

The GM method provides corrections to the properties of the constituent hydrographic sections in the model. The model should be initialised with the velocity profiles adjusted to satisfy any assumptions of the regional flow structures. Numerous data analysis and regional inverse studies have been conducted in the Southern Ocean, so there is a wealth of literature to support adjustments to the flow fields to obtain the 'best-guess' initial model state. Constraints are also added to the model in the form of additional equations, allowing ranges to be set for the values of specific property transports. These adjustments are essential in obtaining the most justifiable solution possible, given the available data. The solution of the inverse problem is purely a mathematical one, finding a suitable region from the infinite solution space that results from the under-constrained problem. The validity of any result is highly dependent on the physics included in the conservation equation, and the constraints and variability scales applied to the solution. The details of the constraints applied to the individual sections are given in Appendix AD.

The standard model set-up includes a series of sections around the coastal waters of Antarctica. Using the in-situ data presents a number of problems that had to be addressed. Studies have found that in the coastal regions between the Weddell and Ross Seas, there are large barotropic currents, resulting in large transports that are not included in a standard geostrophic analysis (Bindoff et al. 2000, Heywood et al.1996). The next section will describe in detail, how a high-resolution, regional model was used to modify the initial velocity fields from the coastal sections.

3.5 BRIOS: An Antarctic Regional Model

3.5.1 Model details

The inner boundary of hydrographic stations was included in the model to better represent the southern part of the Southern Ocean overturning circulation. There is a large uncertainty in the barotropic currents close to the continent, including the western coastal boundary current between 30 W and 160 E (e.g. Bindoff et al. 2000). The BRIOS regional climate system model, developed by the AWI, Bremerhaven (e.g. Timmermann et al. 2001) was used to examine the mean flow field in the coastal region and to construct a consistent barotropic velocity field to apply to all of the coastal hydrographic sections.

The model system contains three main components: a dynamic-thermodynamic sea ice model; a primitive equation, hydrostatic, ocean model with terrain following vertical co-ordinates; and a representation of shelf ice as a flux of heat and freshwater at the ice-shelf base. This model has a mean production rate of ~10 Sv of bottom water denser than σ_2=37.16 kgm^{-3}, and a total production rate of ~21Sv for the whole region of water denser than σ_2=37.15 kgm^{-3} (Hellmer and Beckmann 2001) in basic agreement with tracer-based predictions of Orsi et al (1999). There is a double gyre structure associated with the Weddell Gyre, with magnitudes of 30±10 Sv in the Weddell Sea and 60±10 Sv near the Greenwich meridian (e.g. Beckmann and Timmermann 2001), in agreement with the observations of Fahrbach et al.(1994) and Schroder and Fahrbach (1999) respectively. The model also represents the other gyre circulations with transports of 31 Sv and 23 Sv associated with the Kerguelen circulation and Ross gyre. Figure 3.5 shows meridionally integrated zonal south-north transports and zonally integrated meridional transports on latitude circles from the model mean field. The main circulation features are the ACC to the north of the domain, the Ross and Weddell gyres and the circulation around the Kerguelen Plateau.

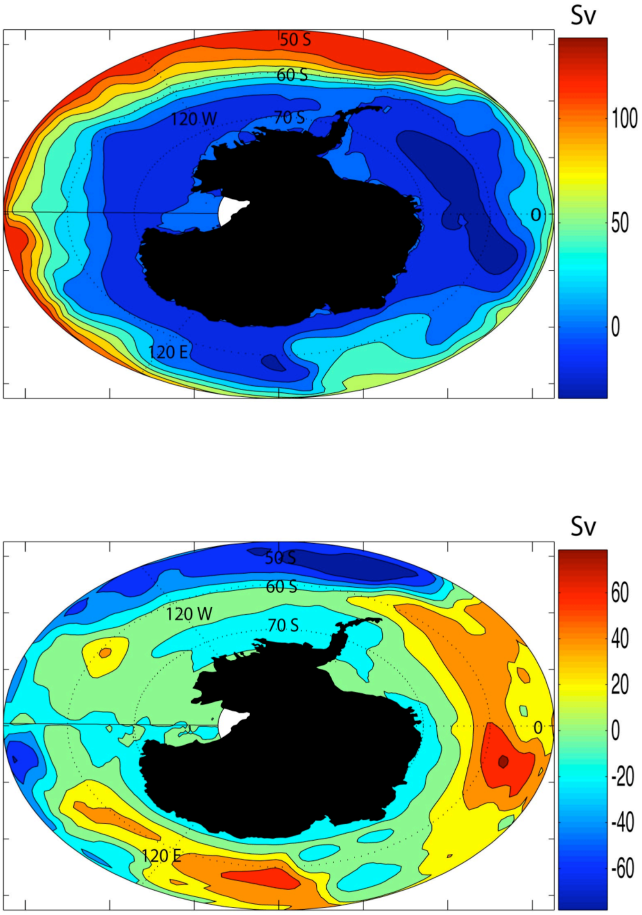

Figure 3.5: Top: Cumulative zonal transport (moving northwards) taken from the BRIOS mean fields. Bottom: Cumulative meridional transport on latitude circles, starting from zero at 180 °E.

3.5.2 Obtaining a velocity reference field

Mean fields of velocities, temperature and salinity were obtained for the period 1990-2000. These fields were used as the basis of a consistent flow field to apply to the hydrographic data in the inverse solutions. The main area of concern was the coastal region between 0 and 160 E, where there is a westward coastal current that is poorly sampled by observations. This was especially important in the region of the Kerguelen Plateau, where three sections meet, and large circulations have been found, both in model output and in-situ data. Figure 3.6 shows mean vertically integrated transport vectors from the BRIOS model annual mean field. There is an apparent large northward transport on the western side of the Kerguelen Plateau, and recirculation flowing back into the westward coastal current. The model has transports with a large barotropic component. The hydrographic sections were adapted to include a barotropic correction that resulted in transports that were similar in magnitude to the BRIOS transports. Unfortunately, we have no information about the variability in the model transports so the a priori transport uncertainties are left relatively high. The fluxes between boxes 3,4,5,10,11 and 12 (see figure 3.2) are constrained in the model using additional constraint equations so that the final solution in this region resembles the BRIOS mean field.

Solutions were also obtained with no Southern boundary. This had little effect on the flow structure of the northern limits of the model domain, but then removed any information about bottom water fluxes into the Southern Ocean from the south. None of the bottom water that enters the Southern Ocean is exported to the north without significant modification due to mixing into ACCbw. The inclusion of a southern boundary ensures that bottom water production around Antarctica is included in the model as a northward flux across the zonal, continental sections.

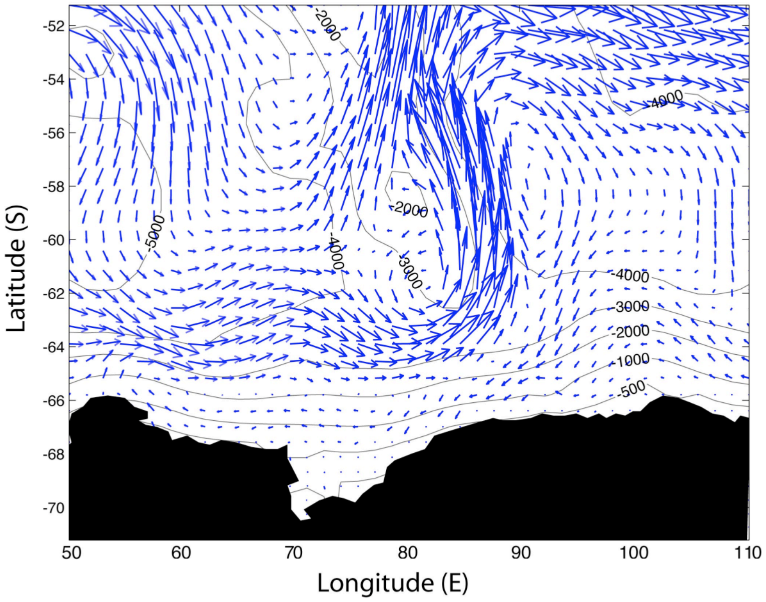

Figure 3.6: Vertically integrated transport vectors from the BRIOS mean field focusing on the flow field in the region of Prydz Bay and the Kerguelen Plateau.

3.6 Effective Diffusivity Estimates

In the standard model set-up, the effective diffusivities are solved as corrections to an initial state of $k=0$, for all layers. Following the work of Mauritzen et al (2002) and Naveira Garabato et al (2004), it is possible to create estimates of turbulent mixing from strain variance measurements derived from CTD measurements. Kunze et al (2006) and Sloyan (2005) have expanded upon on these studies by examining the large-scale variability of the turbulent mixing and the effective choice of parameters to use in the estimates in the global ocean/Southern Oceans respectively (see Appendix AA for a brief summary of the theory of strain-based turbulent diffusivity estimates).

A data-set of over 4000 hydrographic stations was examined to determine box-scale estimates of the turbulent diffusivity. Recent studies, e.g. Naveira Garabato et al (2004), have shown that mixing is greatly increased in Southern Ocean regions of rough topography. This localised mixing effect and the distribution of regions of rough topography in the Southern Ocean lead to a non-gaussian distribution of diffusivities obtained from stations in sub-sets of the Southern Ocean, representing the boxes of the Inverse Model. Figure 3.7.a shows an example of the distribution of diffusivity coefficients obtained for a particular box on a neutral density surface. The distribution is skewed by high values caused by the intense mixing over rough topography. To determine a statistic that could be used to calculate a representative value for this coefficient, the data-set was transformed to obtain an approximately gaussian distribution. This was obtained by examining the natural logarithm of the diffusivity, and calculating the mean of this distribution to create a representative value for each box. An example of the transformed distribution is shown in figure 3.7.b. The transformed distribution is approximately symmetric around the mean, and this pattern is consistent throughout the data set. The mean values for each model box are shown in figure 3.8, along with the standard mean calculations. There is a large difference between the two values of by a factor of 2-5, however the modified mean is preferred in this study due to the nature of the distribution of values.

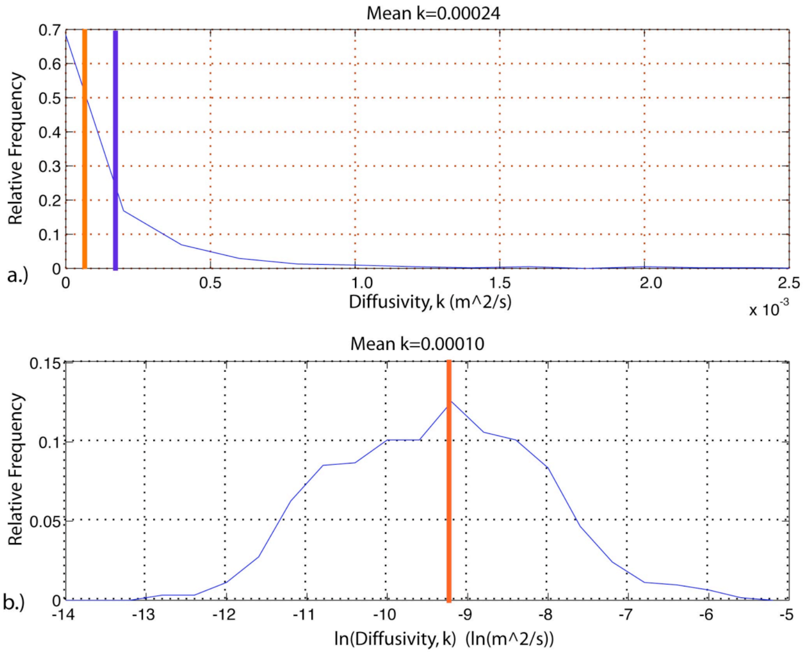

Figure 3.7. a.) The distribution function of turbulent eddy diffusivities (k) calculated from stations located in the Indian Ocean box 3 (see figure 3.2) from the WOCE data-set. The thick blue line shows the location of the mean value of k (0.0024 m^{2}s^{-1}). The thick red line shows the location of the statistic obtained from the mean of log(k). b.) Probability distribution function of log(k), showing a Gaussian-like structure (Red line: mean log(k)=-9.21, equivalent to k=0.00010 m^{2}s^{-1}).

The uncertainty in the parameters used in the method results in an order of magnitude estimate only, but provides useful information on the relative values of the mixing coefficients. This information is not included in the standard model, but will be discussed in Chapter 6, where the model runs with different mixing schemes are discussed, and provides a useful estimate for a comparison and validation of the standard model results. Care needs to be taken in this comparison due to the different definitions of the diffusivity parameter. The eddy diffusivity term represents all diabatic/isoneutral mixing so is not directly comparable to the effective diffusivity term, which only contains additional tracer dependent diffusion terms separate to the advective transports. In this case, a comparison with the total fluxes across dianeutral surfaces is more appropriate.

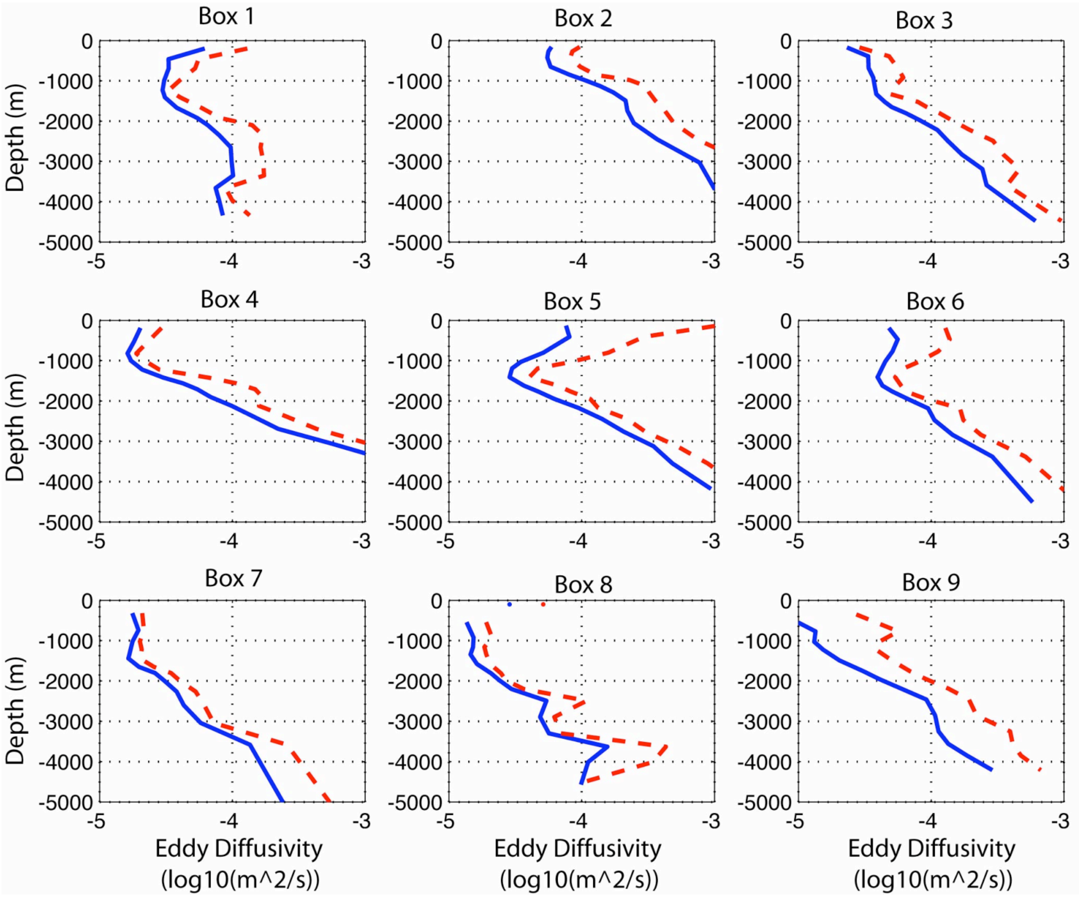

Figure 3.8: Turbulent eddy diffusivity coefficients (m^2s^{-1}) calculated from stations within each model box. The blue line represents the modified mean values on neutral density surfaces, the dashed red line represents the standard mean that is biased by large values.

3.7 Summary

This chapter has outlined the basic techniques involved in inverse modelling applied to oceanography and in this model. The details of the model used in this study have been presented, describing the a-priori assumptions of errors and the scales of variability in the model domain. The next chapter will outline the results of the basic model, analysing the full-depth fluxes throughout the Southern Ocean and the details of the additional physical parameters included in the model to represent dianeutral fluxes and the air-sea interaction.

Chapter 4: The standard model solution

The standard model set-up includes twelve boxes spanning the whole of the Southern Ocean with dianeutral fluxes represented by advective and diffusive components and air-sea interaction induced fluxes (see figure 3.2). In the following discussion of the model solutions, the model domain has been divided up into three sectors (figure 4.1), representing the major regions of the Southern Ocean. The detailed flow structures in each sector (Atlantic, Indian and Pacific) are described in sections 4.1, 4.2 and 4.3 respectively. Section 4.4 describes the dianeutral fluxes, air-sea fluxes and the distribution and scale of errors within the solution. This solution consisted of 729 equations, with 2580 unknowns (velocity corrections, dianeutral velocities and diffusivities and air-sea flux corrections).

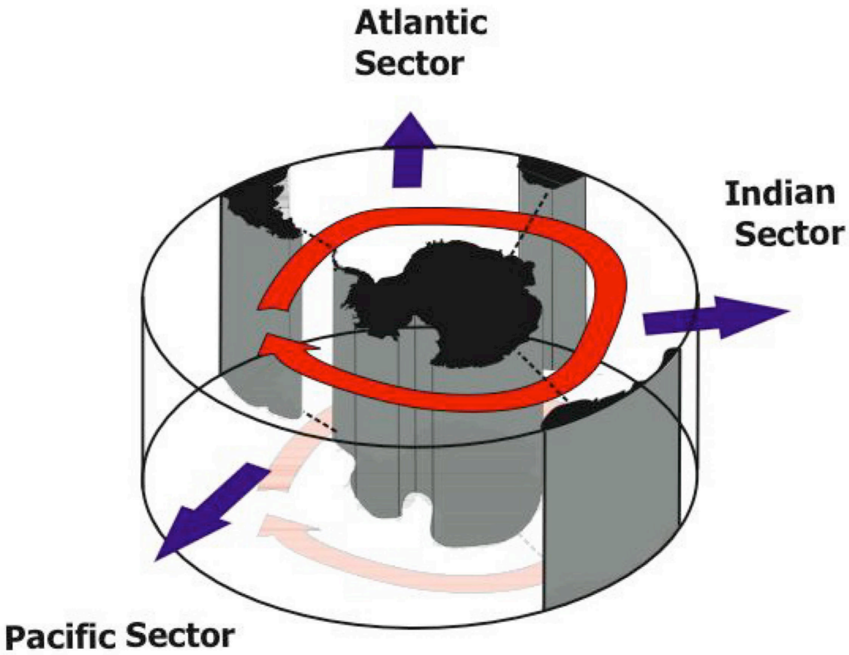

Figure 4.1: Schematic diagram of the Southern Ocean Inverse model showing the division of the model domain into three sectors (Atlantic, Indian and Pacific Oceans). The red arrow represents the ACC, which forms the dominant flow structure in the Southern Ocean. The purple arrows do not represent water mass fluxes.

4.1 The Atlantic Ocean Sector

The Atlantic sector is an important region in the global overturning circulation. The NADW enters from the South Atlantic, mixing with and hence forming a major component of the LCDW. AAIW and AABW/ACCbw are exported northward above and below this water mass. Figure 4.2 depicts the main topographic features of the Atlantic sector. A schematic of the flow structures observed in the standard solution is shown in figure 4.3. The main flow features within this sector are: the ACC circulation moving through Drake Passage, which flows northward, east of the Falkland Islands and then continuing its eastward passage south of Africa; The sub-tropical gyre consisting of a strong southward western boundary current at 30° S, compensated by a northward flow in upper layers in the rest of the Brazil, Angola and Cape Basins; The Agulhas Retroflection passes westward around Africa, with a return flow to the south, and the Benguela current continuing into the South Atlantic, transporting sub-tropical water from the Indian Ocean.

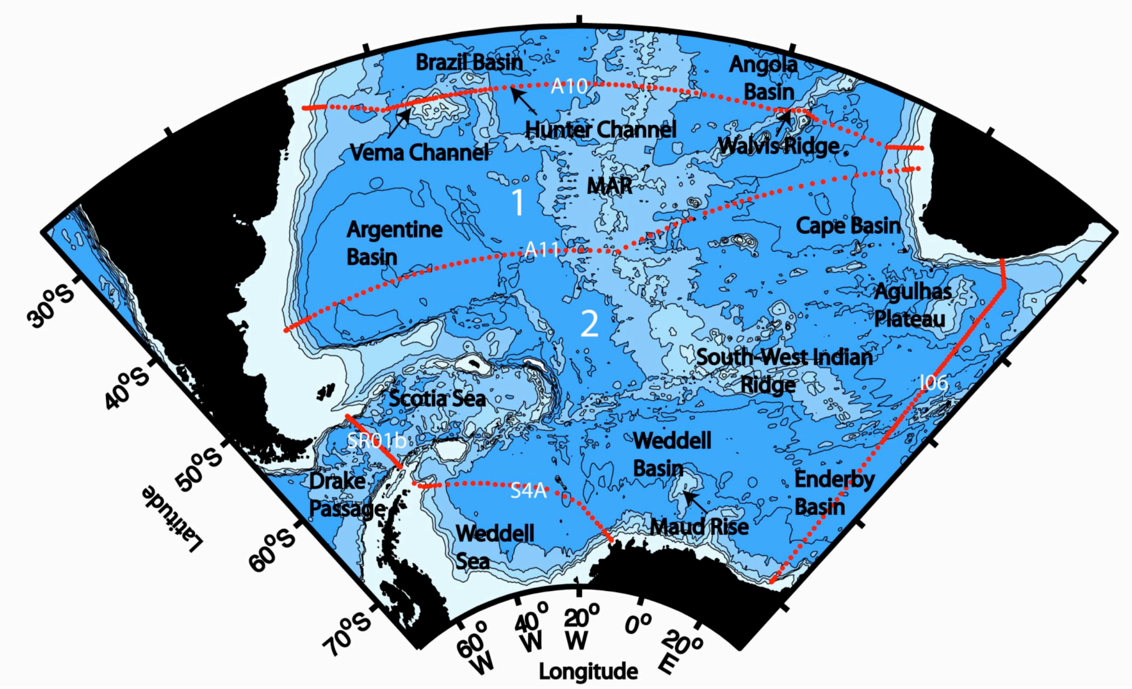

Figure 4.2: A topographic map of the Atlantic Sector of the Southern Ocean detailing the important features. MAR=Mid-Atlantic Ridge. Red lines show locations of hydrographic sections forming the boundaries of boxes 1 and 2.

There are large uncertainties in the surface heat fluxes in the Southern Ocean, which leads to large uncertainties in the balance between surface fluxes and layer heat transports. McDonagh and King (2005) outline some of the main property fluxes across sections A10 and A11 found in a selection of inverse studies. Their presentation is updated in table 4.1, and the solution from this inverse study is included. All of the studies have a near-zero meridional mass flux, but there are large differences between the heat and salt transports found in each solution. The northward heat flux from this study is smaller (but in the same direction) as other studies. There is a tendency for higher heat transports in the global or large-scale inverse studies, with the heat transports from this study in agreement (within errors) with the regional or localised studies. McDonagh and King (2005) suggests that the larger heat fluxes across A11 in the solutions of Ganachaud (1999) and Saunders and King (1996) are due to a larger anti-cyclonic component in the Cape Basin. This is reduced in their solution due to an increased departure from the initial velocity field in the velocity corrections caused by the additional constraints applied to their model. The application of an explicit salt flux constraint, as applied by Holfort and Siedler (2001), was examined but it was found to have no significant effect on the solution so was not included in the study.

Wjiffels et al. (1992) examined the global freshwater transport, using the Bering Strait as an integration point for their calculations. Numerous studies have examined the transports across the Bering Strait (Aagaard et al. 1985, Roach et al. 1995, Woodgate and Aagaard 2005), with estimates of 0.8 Sv entering the Arctic Ocean from the Pacific Ocean. This results in salt and freshwater fluxes of 26.7 Gs^{-1} and 0.7794 kgm^{-3} entering the Arctic Ocean. There are various estimates of the net evaporative loss of fresh water in the Atlantic Ocean between Bering Strait and 40 °S from 1.0 to -0.1 Sv (Wjiffels (2001)), resulting in differing estimates of the freshwater (and corresponding mass flux) across the A10 and A11 sections. In the model, the transport across sections A10 and A11 are constrained to -0.8±0.5 Sv. This value was chosen after examining the magnitude and variability of the meridional transport in the ¼° OCCAM model run 202 between 1992-1997 (-1.1+0.5 Sv) and taking into account the variability in the fresh water fluxes across the section from various studies (e.g. Saunders and King (1994), Holfort and Siedler (2001)). Although no constraints were put on the salt transport, the results are broadly in line with a salt flux consistent with the input through the Bering

Strait of approximately 26.7 Ggs^{-1} calculated form the mean transport and salinity found by Woodgate and Aagaard (2005).

	A10			A11		
Source	**Mass (Sv)**	**Heat (PW)**	**Salt (Ggs^{-1} or Sv psu)**	**Mass (Sv)**	**Heat (PW)**	**Salt (Ggs^{-1} or Sv psu)**
Saunders and King (1995)	-	-	-	0	0.53 ± 0.1	0.8±5.0
Ganachaud (1999)	1±3	0.35±0.15	-	0	0.66 ± 0.12	-
Ganachaud and Wunsch (2003)	0	-	-9±4	-	-	-
Holfort and Siedler (2001)	-0.53 ±0.03	0.29±0.05	-26.75 ± 0.77	-0.56 ± 0.03	0.37 ± 0.02	-26.37 ± 0.73
McDonagh and King	0	0.22±0.08	-9.7 ± 2.9	0	0.43 ± 0.08	-2.9 ± 2.9
Lumpkin and Speer (2006)	-0.2 ± 1.4	0.60 ± 0.08	-3±53	-	-	-
S1 Solution	-0.58 ±0.48	0.14 ± 0.06	-29.2 ± 17.2	-0.70 ± 0.48	0.31 ± 0.04	-13.8 ± 17.1

Table 4.1: Meridional property transports from Inverse studies across WOCE lines A10 and A11, adapted from McDonagh and King (2005). A northward net flux is positive.

A number of constraints are put on the flow features across the A10 and A11 sections. The constraints and the resulting model solutions are shown in Table 4.2 and are based on the flow constraints used by McDonagh and King (2005). The main departure from the constraints is the reduction in the Brazil Current, to -11.4±1.6 Sv, with a constraint of -25±10 Sv. The reduction in the northward heat transport in the Brazil Basin is the main source of the reduction in the heat transport across the section compared to other studies. In the model, the initial velocity field is not adjusted to match the constraints on the Brazil (A10) and Falkland (A11) currents as in McDonagh and King (2005). This was because an artificial adjustment of the flow field before the inversion reduced the effect of the additional constraints on these current systems. Any adjustment to the barotropic velocity corrections (b_i) changes the fluxes in this region, creating an unfavourable increase in the solution variance due to the adjustment of the solution away from the constraints. To remove this effect, the initial velocity field was not adjusted, and the barotropic a-priori velocity errors were increased from the standard 0.01 m^2s^{-2} to allow larger corrections in the model solution. This is a commonly used method in setting the a-priori barotropic errors in the region of strong currents (e.g. Ganachaud, 1999).

Feature/water mass	**Constraint ($1x10^9$ kgm^{-3})**	**Solution ($1x10^9$ kgm^{-3})**
A10: Brazil Current	-25±10	-11.4±1.6
A10: Brazil Current recirculation	7.5±5	6.4±3.9
A10: Vema Channel AABW	2±1	2.9±0.7
A10: Brazil Basin AABW	3±1	2.3±0.9
A10: Cape Basin AABW	0±0.5	0.43±0.48
A11: Falklands Current	45±10	37.0±4.2
A11: Eastern boundary current	-5±2	0.2±0.8
A11: AABW (western section)	6±1	5.6±0.8
A11: AABW (eastern section)	0±0.5	-0.36±0.46

Table 4.2: Details of additional constraints applied to the model in the Atlantic sector, and the model solution. The errors stated are from the residual noise terms from each conservation equation related to the individual constraints. Specific details of constraint boundaries are given in Appendix AD.

The Weddell Sea data was adjusted before the inversion so that the barotropic velocity structure was similar to the mooring data record of Fahrbach et al (1994). The resulting poleward heat flux was 0.031±0.005 PW, this is in agreement with the flux of 0.0251±0.005 PW found in the study. The model also has a poleward salt flux of 9.2±17.3 Ggs^{-1}, which although not negligible, has a very large error range that covers the much smaller and physically justified 0.1±0.2Ggs^{-1} found in the mooring study. This small flux is not significantly different from zero and is due to the balance between the salt gain from ice formation and the freshwater input from melting ice shelves and precipitation.

The model adjusts the ACC transports through Drake Passage and south of Africa (30°S) resulting in a total transport of ~ 140 Sv. The hydrographic section, I06, used in this study initially has a very large geostrophic transport of 172 Sv, which is reduced before initialisation of the model by applying a westward barotropic correction in the southern part of the section related to the Weddell Gyre circulation (Park et al 2001), reducing the transport across the section in the model prior to solution adjustments to 147Sv.

Figures 4.12 and 4.13 show the dianeutral fluxes found in the standard model solution for boxes 1 and 2 respectively. The advective velocities in both boxes are significant on most levels, with values greater than the a-posteriori errors. The velocities are all less than the a-priori range of $\pm 1 \times 10^{-6}$ ms^{-1}. In box 1, the largest dianeutral transports are away from the NADW, centred around $\gamma^n = 28.00$ kgm^{-3}, as this relatively warm and saline water mass enters the South Atlantic in the Brazil Basin, mixing with the intermediate waters above it and the colder Antarctic waters below. In box 2, the largest pattern is in the intermediate waters, with large upward transport of mass in the region between $\gamma^n = 27.2\text{-}27.7$ kgm^{-3}. This corresponds to the modification of inflows of intermediate and mode waters through Drake Passage and from the eastern sector of the Indian Ocean.

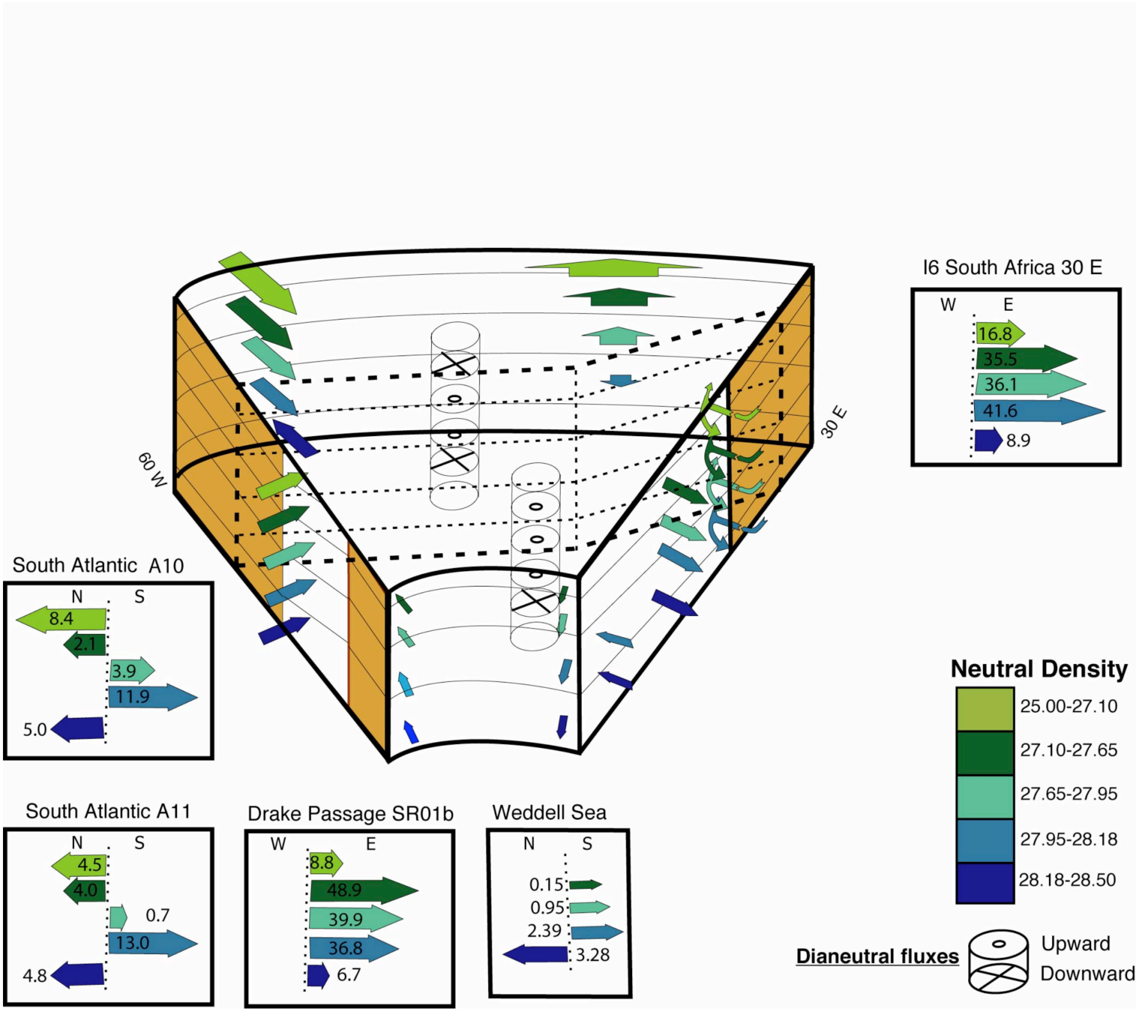

Figure 4.3: Schematic representation of the standard Inverse model for the Atlantic sector of the Southern Ocean. The Box is divided into five core neutral density layers: Surface waters (γ^n=25.00-27.10 kgm^{-3}); Intermediate/Mode waters (γ^n=27.10-27.65 kgm^{-3}); Upper Circumpolar Water (γ^n=27.65-27.95 kgm^{-3}); Lower Circumpolar Water (γ^n=27.95-28.18 kgm^{-3}); and Antarctic Deep/Bottom Water and ACCbw (γ^n=28.18-28.50 kgm^{-3}). The directions of advective dianeutral fluxes are depicted by the cylinders, with flow into or out of each respective layer. Fluxes are shown in Sv (1x10^6 m^{3}s^{-1}).

4.2 The Indian Ocean Sector

Figure 4.4 shows the topography within boxes 3,4, and 5 of the standard model, which form the Indian sector of the model. A schematic representation of the large-scale flow field is presented in figure 4.5, showing the southward flow of the Agulhas Current forming a western boundary current in the Indian Ocean, compensated for by the sub-tropical gyre circulation in the eastern part of the ocean. There is a large circulation on the southern side of the sector due to the imposed gyre flow structure around the Kerguelen Plateau. Box 3 contains the Crozet and Kerguelen Plateaus and the South-East Indian Ridge, which are major topographic features that influence the path of the ACC. The South-east Indian Ridge forms a meridional boundary in boxes 4 and 5, separating the Australia-Antarctic basin to the south and the South Australia basin in the northern region of the boxes.

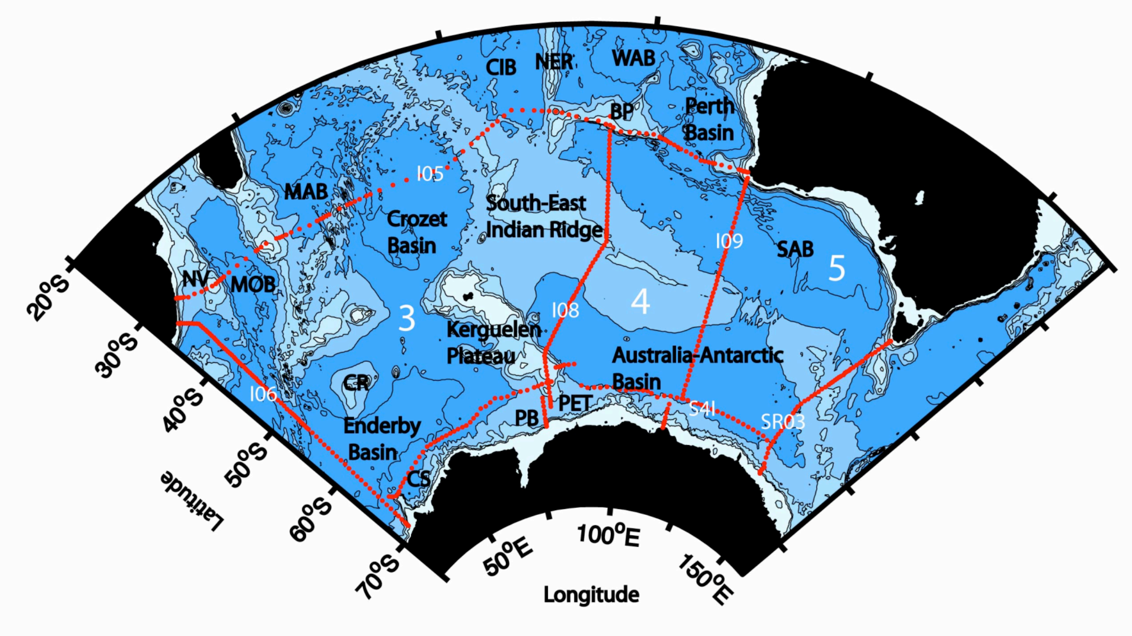

Figure 4.4: A topographic map of the Indian Ocean sector of the Southern Ocean. Hydrographic stations are shown by red dots. NV= Natal valley; MOB=Mozambique Basin; MAB= Madagascar Basin; CIB= Central Indian Basin; NER= Ninety-East Ridge; WAB= West Australian Basin; BP= Broken Plateau; SAB= South Australian Basin; PET= Princess Elizabeth Trough; PB= Prydz Bay; CS= Cosmonaut Sea.

In this study, the OCCAM ¼° model was used to examine the magnitude of the transport at 30°S across the Indian and Pacific Oceans, and hence the magnitude of the ITF between the oceans. Assuming in the mean field, that the total mass flux across this line of latitude is zero, and that the southward flux from the Atlantic is small (O(1)Sv), then the southward flux from the Indian Ocean should approximately balance the northward flux into the Pacific Ocean. In the sample from the OCCAM model, the mean northward Pacific transport of 14.2±4.8 Sv was balanced by a southward transport of 12±5.0 Sv. This is in agreement with the 15±5 Sv ITF transport estimate found by Ganachaud and Wunsch (2003). This transport was also constrained by using the observed mean transport of the Agulhas current at the west of the section of 69.7±4.3 Sv, measured from a mooring array (Bryden et al. 2005c). The total transport in the standard model was 7.2±2.7 Sv, at the lower end of the transport constraint.

The unique component in this study was the sub-division of the Indian Ocean sector into two boxes. The fluxes through the northern face in each box have high error values (6.8 Sv/6.6 Sv for box 3/4), but are highly correlated, resulting in a total a-posteriori error of 2.7 Sv, partly due to the additional constraint on the total transport through both boxes. The southward heat transport of 0.98±0.09 PW is within the range of other studies that vary between 0.87 PW (Sloyan and Rintoul, 2000), and 1.55 PW (Lumpkin and Speer, 2007). This transport is also consistent within the error bounds in a range of model configurations examined in this study, including regional one and two box Indian Ocean models.

One of the main issues surrounding the Indian Ocean is the uncertainty in the magnitude of the meridional overturning circulation across 30°S. In the first analysis of the I05 data, Warren and Toole (1993) found an overturning of 27±10 Sv, while further studies have found values ranging from 23±3 Sv (Sloyan and Rintoul, 2001a) down to 9.2±2.7 Sv (Lumpkin and Speer, 2007). The reduction in the overturning estimates is largely due to the inclusion of silicate constraints because earlier studies resulted in an unphysical source of silicate in the Indian Ocean. Model studies generally have much weaker overturning circulations, which are attributed to the excessively weak vertical mixing prescribed in Ocean General Circulation Models (OCGM) (e.g. Palmer et al. 2007). One exception to this is the study by Marotzke and Ferron (2003) that used a 4-D assimilation model to combine hydrographic WOCE data with an OCGM and obtained an overturning of 17±2 Sv. They also examined the effect of varying the strength of the Indonesian Throughflow (ITF) in the model and found a change of only ±2 Sv when the ITF was changed from 0 to 30 Sv. Observational studies show instantaneous values for the ITF between 20 Sv westward to 1 Sv eastward (Sprintall et al. 2002). Table 4.3 shows a comparison of fluxes and overturning estimates from a range of studies in the Indian Ocean, including the fluxes from the standard model solution.

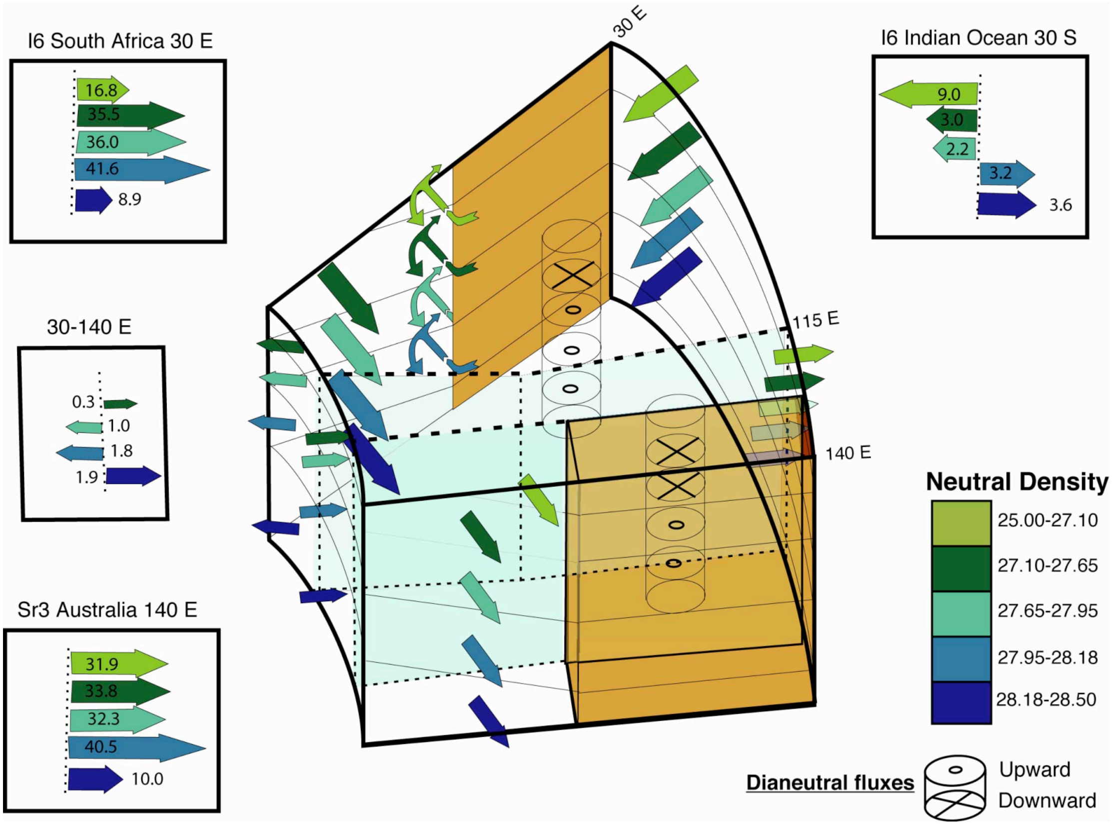

Figure 4.5: Schematic representation of the standard Inverse model for the Indian sector of the Southern Ocean. The Box is divided into five core neutral density layers: Surface waters (γ^n=25.00-27.10 kgm^{-3}); Intermediate/Mode waters (γ^n=27.10-27.65 kgm^{-3}); Upper Circumpolar Water (γ^n=27.65-27.95 kgm^{-3}); Lower Circumpolar Water (γ^n=27.95-28.18 kgm^{-3}); and Antarctic Deep/Bottom Water and ACCbw (γ^n=28.18-28.50 kgm^{-3}). The direction of advective dianeutral fluxes are depicted by the cylinders, with flow into or out of each respective layer. Fluxes are shown in Sv (1x10^6 m^{3}s^{-1}).

Bryden and Beal (2001) examined how the observations of the Agulhas Undercurrent (Beal and Bryden (1997)) effects the fluxes across the I05 section by reducing the total Agulhas current transport. The undercurrent structure was not explicitly applied to the initial velocity field in the model, but the direct observations of the Agulhas transport from a series of moorings of -69.7±4.3 Sv (Bryden, et al 2005c) were applied as additional constraint, reducing the initial estimates of southward Agulhas transports (Toole and Warren (1993)) in the region of 85 Sv. The solution produces a net southward transport of -72.9±2.7 Sv, comprising of 78.7±3.8 Sv moving southward, and 5.8±1.9 Sv moving northward in the denser layers. This is in good agreement with direct estimates of the Agulhas Undercurrent transport of 6.0 Sv (Beal and Bryden (1997)).

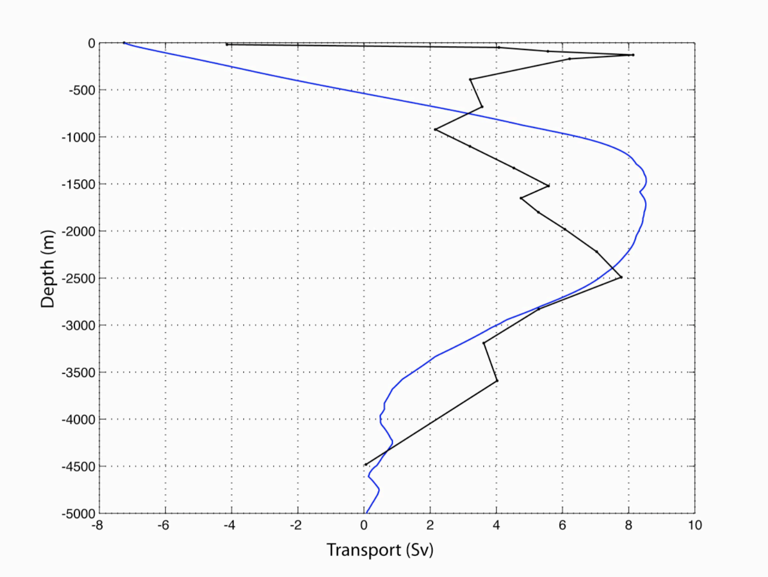

Figure 4.6: Meridional Overturning Circulation (Cumulative transport from sea floor) in depth and neutral density co-ordinates. Black line: overturning streamfunction calculated on density surfaces, blue line: overturning streamfunction calculated on depth surfaces.

Figure 4.6 shows the overturning circulation in the box in neutral density and depth co-ordinates. When integrated over neutral density layers, the model has two overturning cells, the main lower cell of 7.9 Sv, centred at γ^n=28.10-28.14 kgm^{-3}/2500m, and an upper cell in the surface/intermediate waters of 8.0 Sv centred at γ^n=26.70 kgm^{-3}/300m. If the integration is made on depth layers, there is only a lower cell that is centred much higher in the water at γ^n=27.90-27.94 kgm^{-3}/1500m with a northward deep water transport of 8.5 Sv. Schott et al. (2002) describe a shallow overturning cell in the Indian Ocean due to coastal upwelling in the northern hemisphere of subducted sub-tropical waters in the southern hemisphere, completed by a southward Ekman return flow at the surface. They estimate a cross equatorial cell of 6 Sv, which includes a contribution from the ITF in the thermocline waters. This is in broad agreement with the northward transport of ~6 Sv in the upper overturning cell shown in figure 4.6 (black line) averaged on density surfaces. The total deep overturning in the model is also in agreement with the study by Srinivasan et al. (2000) who found an overturning of 8.2±1.5 Sv using a radiocarbon and carbonate chemistry data set.

Source	**Mass ($1x10^9$ kg/s)**	**Heat (PW)**	**Salt (Svpsu or Gg/s)**	**Silicate**	**Deep MOC (Sv)**
Toole and Warren (1993)	-8.07	-1.789	-295.7	-1532	27
Robins and Toole (1997)	-9.88	-	-	-21	12±3
Sloyan and Rintoul (2000)	10.3±2.3	-0.87±0.06	370	-425±316	23±3
McDonagh et al. (2006)	-	-	-	-	10
Lumpkin and Speer (2007)	-13.7±2.6	-1.55±0.12	-498±95	-	9.2±2.7
Talley (2002)	-10.17	-1.12	-	-	13.8
Ganachaud et al (2000)	-16±5	-1.5±0.2	-	-	11±4
Standard Solution	-7.9	-0.99	-240	-274	7.9

Table 4.3: A table of flux estimates from a range of studies in the Indian Ocean. A positive flux is northward.

The inclusion of section I08 dividing up the Indian Ocean sector adds additional constraints to the flow structure observed in boxes 3 and 4 in the model. The barotropic corrections reduce the zonal eastward flow from 175 Sv to 125 Sv to compensate for the large northward transport along the eastern side of the Kerguelen Plateau imposed at the southern boundary of the box. The solution adds a westward barotropic correction of 0.04-0.08 ms^{-1} in the Australia-Antarctic basin, reducing the eastward transport of the ACC into this basin. The flow in the northern half of the box is relatively unchanged. Solutions where boxes 3 and 4 were combined into a single box with the I08 boundary removed were explored. The main features where: a reduction in the balance between the imposed circulation on the southern boundary centred across the Kerguelen Plateau, with a larger southward transport within the Weddell Gyre; an increase in the southward transport across the 30° S boundary to 12 Sv. The magnitude and structure of the overturning were unchanged, with the increased transport occurring primarily in the surface waters.

The transport through box 5, south of Australia balanced the transport of the ACC through the box with a small net 2 Sv flow of bottom water compensated by a 1 Sv overturning in the less dense water on the southern boundary. These transports are much smaller than the ADCP-derived transports observed by Bindoff et al. (1999), but the data was adjusted before initialisation to resemble the mean fluxes in the BRIOS model. There are also large uncertainties associated with ADCP measurements, especially on the continental shelf where tidal effects are more prevalent. The resultant net westward transport through boxes 11 and 12 along the coast was reduced from 11 Sv in the initial field to 4 Sv, caused by a reduction in the westward barotropic current close to the coast (discussed in more detail in chapter 5.3 in relation to AABW).

4.3 The Pacific Ocean Sector

The Pacific sector of the model is divided up into 4 boxes. Figure 4.7 shows the major topographic features in the South Pacific Ocean. The Ross, Amundsen and Bellingshausen seas are not included as boxes because of the large uncertainties in the air-sea fluxes in this area, and the lack of hydrographic data within the seas themselves. The effect of these water masses is imposed by the transports through the southern boundaries of the Pacific boxes 6-9. This is applied in the form of mass transport constraints obtained from the mean transport structure in the BRIOS model. The flow pattern from the regional inverse study of Gille (1999) is used to apply constraints to the zonal transports through boxes 8 and 9.

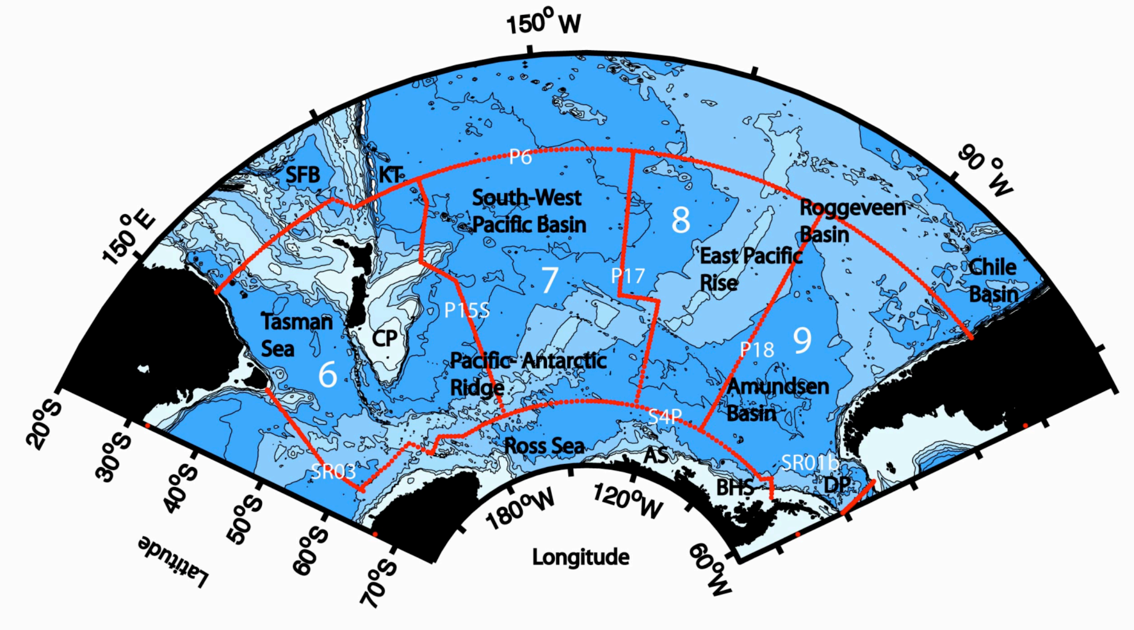

Figure 4.7: A topographic map of the Pacific Ocean sector of the Southern Ocean. Hydrographic stations are shown by red dots. SFB= South Fiji Basin; KT= Kermadec Trench; CP= Campbell Plateau; AS= Amundsen Sea; BHS= Bellingshausen Sea; DP= Drake Passage.

Figure 4.8 is a schematic picture of the flow structure found in the standard solution on five core density layers. The main flow features are the East Australia Current (EAC) flowing southward into the Tasman Sea, and the clockwise gyre circulation in the South-West Pacific Basin. The layer transports at SR03 and SR01 show the different distribution of water masses within the ACC at either side of the Pacific Sector. There is a large reduction in the transport in the top layer at Drake Passage, which is compensated for by an increase in the transport in the Intermediate/Mode water layer and the northward transport of water into the South Pacific.

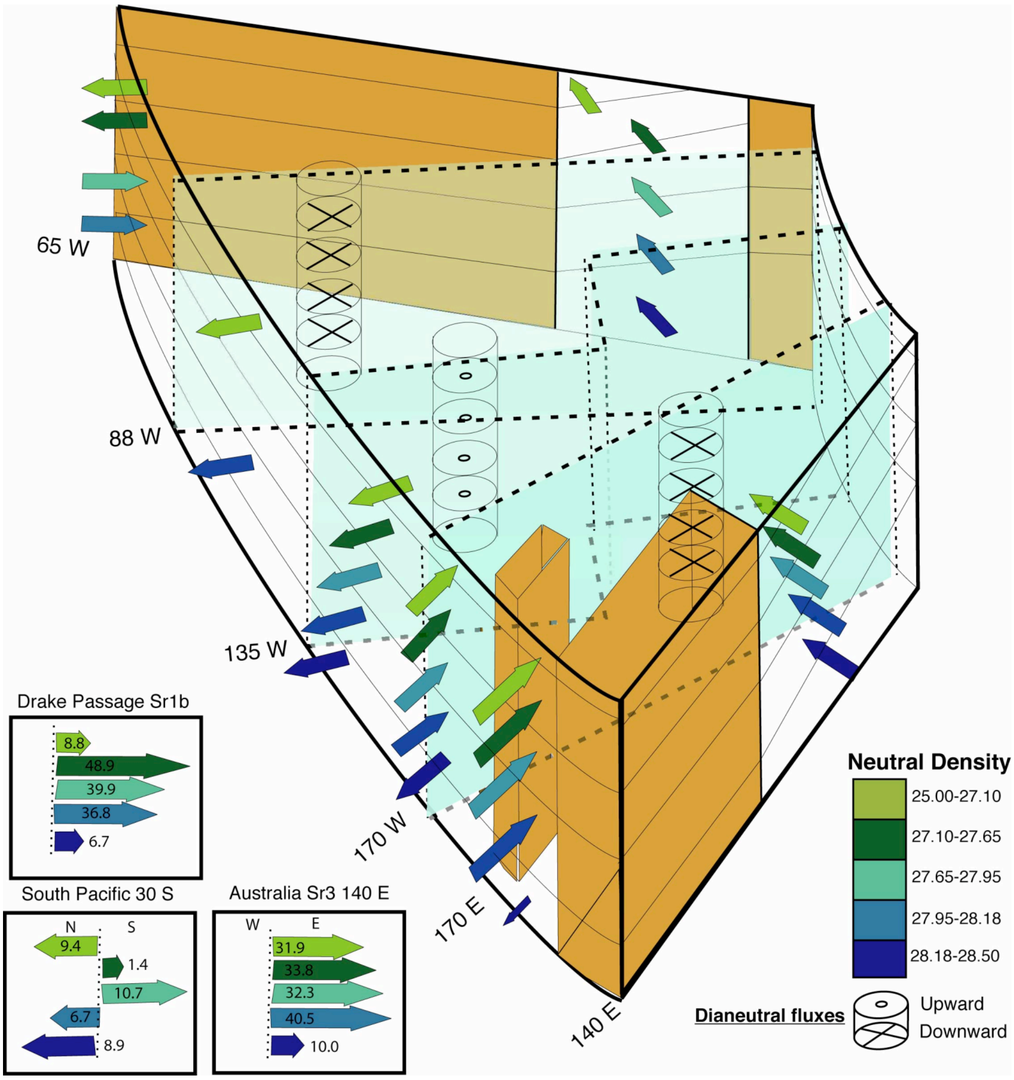

Figure 4.8: Schematic representation of the standard Inverse model for the Pacific sector of the Southern Ocean. The Box is divided into five core neutral density layers: Surface waters (γ^n=25.00-27.10 kgm^{-3}); Intermediate/Mode waters (γ^n=27.10-27.65 kgm^{-3}); Upper Circumpolar Water (γ^n=27.65-27.95 kgm^{-3}); Lower Circumpolar Water (γ^n=27.95-28.18 kgm^{-3}); and Antarctic Deep/Bottom Water and ACCbw (γ^n=28.18-28.50 kgm^{-3}). The direction of advective dianeutral fluxes are depicted by the cylinders, with flow into or out of each respective layer. Fluxes are shown in Sv (1x10^6 m^{3}s^{-1}).

The flow structure across the northern edge of box 6 is further complicated by the complex topography in this region. The section crosses the northern edge of the Tasman Sea, and the southern side of the South Fiji Basin, and a series of ridges in-between. The eastern part of the section contains the western edge of the South-West Pacific Basin and the steep topography of the Kermadec and Louisville ridges. The eastern boundary of the box is in the South-West Pacific Basin at 170° W. The Box completely contains New Zealand, but the boundary contains a small incursion along the 3000m contour at Chatham Rise, to the East of New Zealand. The complex topography and resulting complex flow structure means that some caution should be taken when using inverse methods with non-synoptic sections to interpret the mean circulation in this region. The main features are the large southward transport in the surface waters in the SAC into the Tasman Sea with a maximum transport of 34 Sv. There is a southward surface and intermediate water transport along the western side of the South-West Pacific Basin, with a northern flow along the slope in the deeper waters, concentrated in the deepest layer (γ^n=27.18-28.50 kgm^{-3}) with a magnitude of 6.0 Sv.

Box 7 spans the central and eastern parts of the South-West Pacific Basin. The main circulation feature is the northward transport on all levels balancing the southward flux along the western side of the basin. All of the transport of the deepest layer occurs in this region, with a total northward flux of 8.9 Sv, including AACbw and AABW. This is in strong agreement with Ganachaud and Wunsch (2003) where they found a transport of 8±2 Sv using the same layer boundaries. The northern face of Box 8 covers the East Pacific Rise and has a weak flow structure. There is no transport in the deepest layer, and the mean pattern is northward transport in the region west of the ridge, with a gradual southward flow to the east.

Box 9 contains the Roggeveen Basin and the Chile Basin and there are differences found in the flow structures found in these two regions. The transport is relatively weak across the Roggeveen Basin, with the majority of the transport occurring as a northward flux in the surface layers. In the Chile Basin, there is a northward transport in the intermediate and surface waters with a southward flux in the deeper layers. There is a total flux of 5.1 Sv southward from the Chile Basin in the CDW layer γ^n=27.95-28.18 kgm^{-3}. This is dominated by the lighter water in this layer as the Chile Basin blocks of water denser than γ^n=28.13 kgm^{-3} (Tsuchiya and Talley ,1998). The flow structure is broadly in line with that of Shaffer et al. (2004), which combined hydrographic stations with long-term mooring data to determine the mean state of the Chile Basin. They found a northward flux of 7 Sv of AAIW/SAMW, which is slightly higher than the 4.3 Sv found in this study.

Source	**Mass (1x10^{9}kg/s)**	**Heat (PW)**	**Salt (Ggs^{-1} or Svpsu)**	**Silicate (kmols^{-1})**
Sloyan and Rintoul (2000)	7.4±1.8	0.13±0.04	261.1±43.7	821±283
Tsimplis et al. (1998) -0 Sv/10 Sv	0/10	-0.04±0.25 / 0.44±025	-3.7±5 / -	-
MacDonald (1998)	9.5±6.8	-0.04±0.3	-	-
Lumpkin and Speer (2007)	14.3±3.4	0.52±0.14	507±124	-
Standard Solution	13.0±4.1	0.21±0.01	465±146	744±425

Table 4.4: A table showing a compilation of fluxes from selected studies across P6/32 S in the Pacific Ocean.

The total transport across this section was found to be 12.9±4.1 Sv, and in a similar result was found to that of the sub-division of the Indian Ocean, where the errors of the constituent sections was much larger (see figure 4.10). The equator-ward heat transport was 0.21±0.09 PW. This is within the large range of transports determined from other inverse studies (e.g. 0.13±0.04 PW (Sloyan and Rintoul, 2001a), 0.52±0.14 PW (Lumpkin and Speer, 2007), and 0.44±0.25 PW (Tsimplis et al. 1998)). The heat transport is also dependent on the magnitude and direction of the ITF, as found by Tsimplis et al (1998), where the northward heat flux was reversed from 0.44±0.25 PW to -0.04±0.25 PW when the mass transport was constrained to zero. Table 4.4 summarises other estimates of the main Pacific fluxes from data based studies, in comparison to the standard solution.

4.4 Details of the Model Solution

4.4.1 Southern Ocean fluxes

Figure 4.9 shows the mass and heat fluxes through the model boxes, showing the large-scale patterns of mass and heat transport. The dominant feature is the eastward transport associated with the ACC, however there are large heat transports into the Southern Ocean through the Indian Ocean, that are partially compensated for by northward heat fluxes into the Pacific and Atlantic oceans. There is a net southward ocean heat/potential temperature transport of 0.64±0.15 PW across 30 °S from the standard model solution. The error is only from the model a-posteriori matrix, and does not capture the large variability within the ocean heat transport through the Atlantic, Indian and Pacific Ocean basins, that is highlighted by the large ranges of estimates of ocean heat transport in the literature.

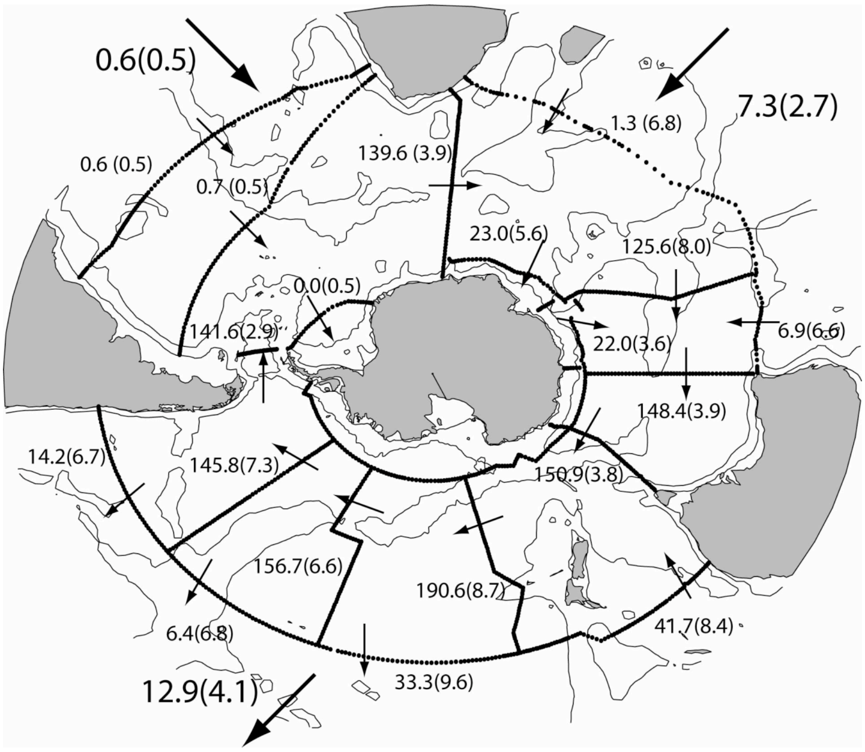

a.)

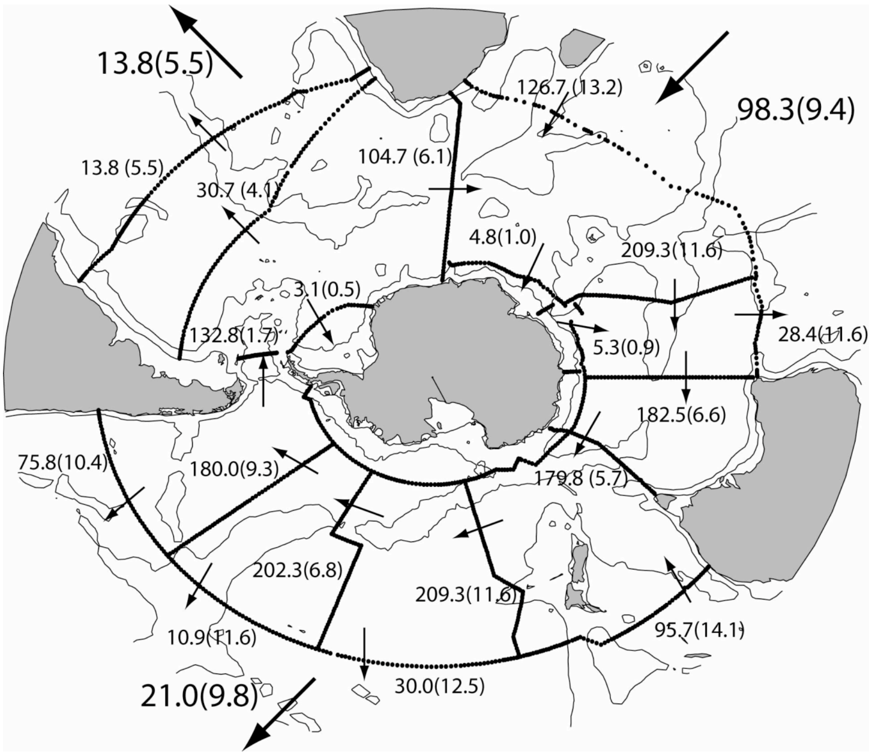

b.)

Figure 4.9: a.) Total Mass fluxes (and errors) from the Standard Inverse Model (Sv). b.) Total heat/Potential Temperature fluxes across the box boundaries from the Standard Inverse Model ($1x10^{13}$W).

4.4.2 Model Errors and Box residuals

The inverse model adjusts the fluxes through the density layers within each box so that mass and other tracer properties are conserved. The OCCAM model was used to determine error bounds for each layer of each box. Figure 4.10 shows the residual flux imbalances for the boxes 1-9 from the standard solution. Boxes 10-12 are not shown as these boxes only contained a sub-set of the neutral density layers found in the other boxes. The red and yellow regions show the a-priori and posteriori errors respectively. In a high proportion of the layers, the posteriori error is significantly lower than the a-priori error, showing the model is working on all of the layers to reduce layer residuals. This is particularly true in the deeper layers. There are only a few layers where the solution results in a flux imbalance greater than the a-priori error estimate. These small discrepancies have been deemed acceptable as they are rare occurrences and they do not depart significantly from the one standard deviation estimate of the layer transport variability centred on the mean flux from the OCCAM study.

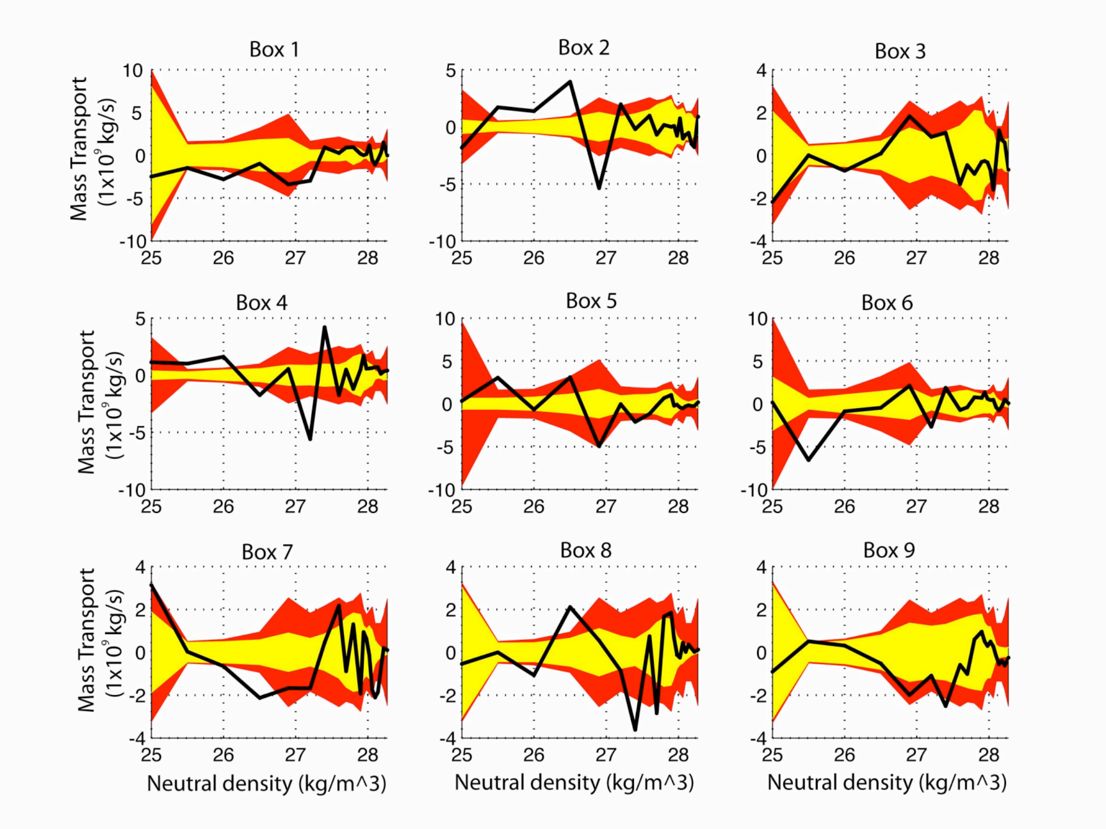

Figure 4.10: Mass Imbalance component of solution error from the mass conservation layer equations for each box 1-9 (black line). The a-priori error determined from the OCCAM model is shown by the red region. The yellow region shows the posteriori model error for each box. Each box contains 20 layers, but for clarity, the errors are plotted vs. neutral density rather than layer number. The figures for boxes 9-11 are not shown because they only contained the denser water masses (and have fewer associated equations in the model) but are consistent with the variability found in the other boxes on these density surfaces.

4.4.3 Dianeutral velocities, effective diffusivities and transports

The global inverse study of Ganachaud (2003) found an area-averaged mean global average dianeutral velocity of $w^*=0.13\pm0.03 \times 10^{-6}$ ms^{-1} and a diffusivity of $k=3.7\pm0.7 \times 10^{-4}$ m^{2}s^{-1} in the deep range between ~2000-3000 dbars. The Southern Ocean Inverse Model of Sloyan and Rintoul (2000) determined dianeutral velocities of a similar magnitude, with higher velocities in the deeper layers, of the order of 1×10^{-6} ms^{-1}. The upper limit of the dianeutral velocity error in the standard model was set to 1×10^{-6} ms^{-1}.

This allows velocities within the ranges of Ganachaud (2003), but is a smaller limit than that chosen in that study (~1×10^{-5} ms^{-1}) because it was found to have a negligible effect on the resulting dianeutral velocities in the solution. The ratios of the a-priori error, a-posteriori error and the solution dianeutral velocities were examined in one-box models representing the nine main boxes in the inverse model. The a-priori errors were changed over orders of magnitude from 5×10^{-7} - 5×10^{-5} ms^{-1}. The optimum setting of the a-priori error range was determined from the values where the ratios of solution velocity : a-posteriori error is a maximum and the ratio of a-posteriori error : a-priori error is at a minimum. As would be expected, there was some variability between the boxes, but the choice of 1×10^{-6} ms^{-1} was shown to be a suitable error range given the balance between the values determined from other studies and the region where the model was producing significant dianeutral velocities greater than the a-posteriori errors.

The dianeutral fluxes for boxes 1-9 are shown in figures 4.11-4.13. They are presented in depth co-ordinates representing the mean neutral density layer depths for the Southern Ocean. The conversion between neutral density and depth is given in figure 4.14. The actual solutions are shown in black, with the range of a-priori errors in blue, and the posteriori errors represented by the yellow region. In each box, the velocities and diffusivities are initially set to zero so the model is solving for the total dianeutral component. Model runs were studied where non-zero effective diffusivities derived from the eddy diffusivity data-set where used to set the initial values of the diffusivity coefficient. This was not found to have a significant effect on the magnitude or distribution of the diffusivity coefficients derived from the model. Figure 4.11 shows the advective velocities from each box. In most boxes, there are features that are significantly larger than the model error. Boxes 1 and 2 generally show water moving away from the NADW/LCDW salinity maximum density layers up into the AAIW/UCDW and down into the LCDW/ACCbw. Box 3 also shows this pattern, but there is also an upward velocity from the deepest layers (>28.18 kgm^{-3}) which is consistent with an upward mixing of AABW in the Indian Ocean sector. Box 4 has a relatively small area and is heavily constrained on the northern and southern boundaries. It is also difficult to define any trends greater than the noise in box 5 where the main constraints are balancing the ACC transports between 115° and 140° E that are dominated by the variability in this region. There is not a clear velocity signal over the model noise in this box.

In the western half of the Pacific sector there is a convergence into the UCDW from above and below, and the large-scale trend of upward transports in the AABW/lower ACCbw and downward transports from the upper layers of the LCDW. The solution for box 8 is dominated by a large upward transport from the UCDW into the intermediate waters. Box 9 shows a reversal of the trend surrounding the LCDW salinity maximum, with transports upward from the deeper waters and downward from the UCDW. This is consistent with the freshening signal of the LCDW salinity maximum in the Scotia Sea/ Drake Passage region described in Williams et al. (2006). Figure 4.12 shows the layer transports associated with the velocity solutions, where the dianeutral advective transports range from ±15 Sv.

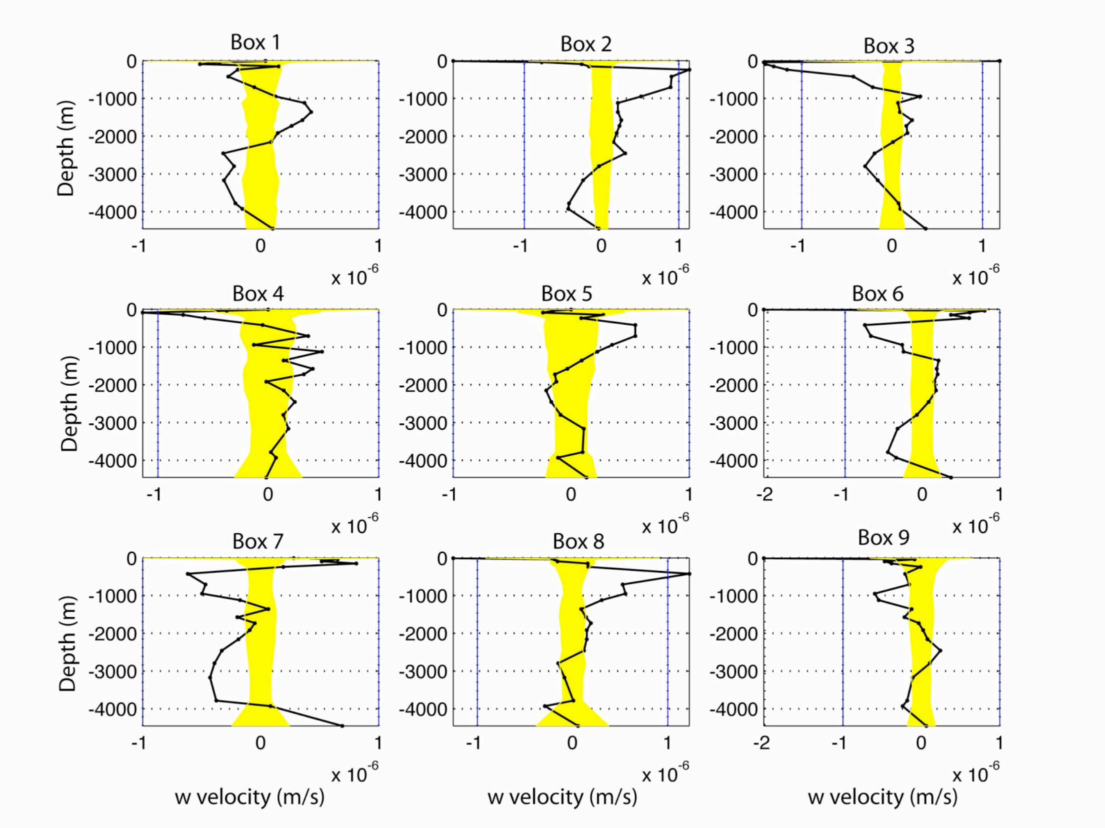

Figure 4.11: Dianeutral velocities (w*, ms^{-1}) for boxes 1-9 from the standard solution (black lines). The a-priori error boundaries are in blue, and the a-posteriori error bounds are shown by the yellow region.

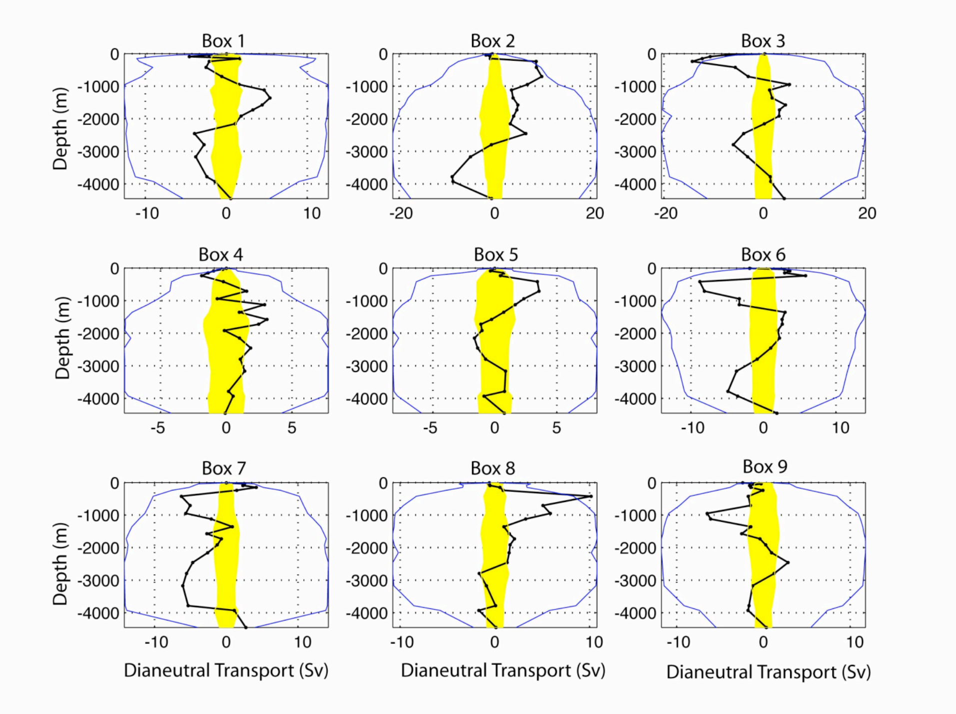

Figure 4.12: Dianeutral advective transports (in Sv) for boxes 1-9 from the standard solution (black lines). The a-priori error boundaries are in blue, and the a-posteriori error bounds are shown by the yellow region.

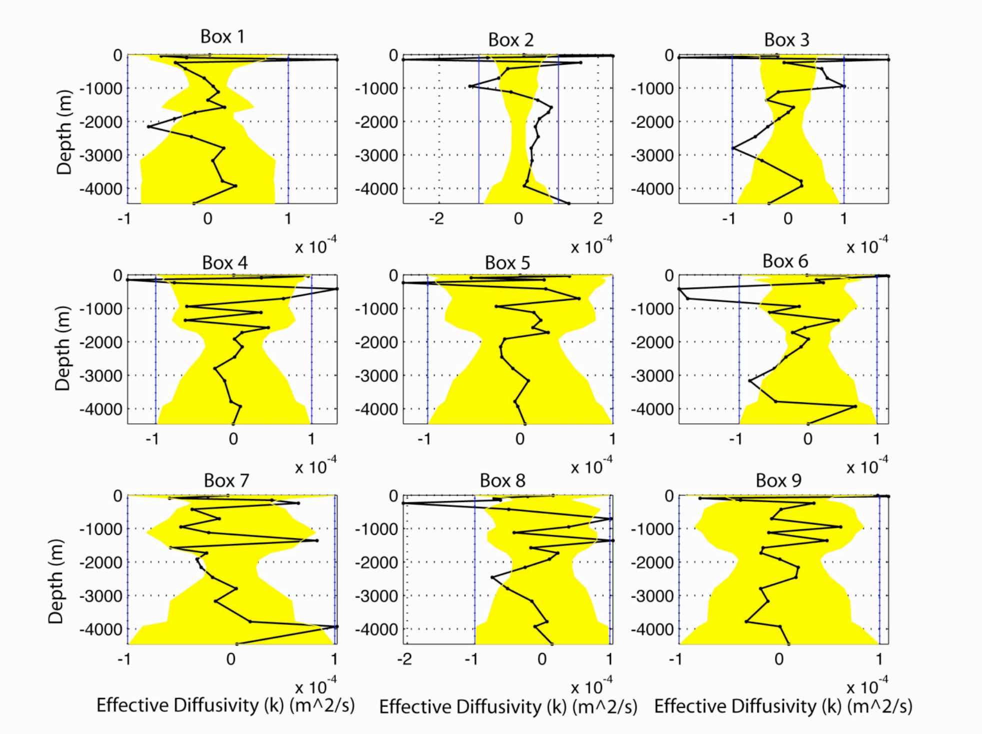

Figure 4.13: Dianeutral effective diffusivities (k*, m^2s^{-1}) for boxes 1-9 from the standard solution (black lines). The a-priori error boundaries are in blue, and the a-posteriori error bounds are shown by the yellow region.

Figure 4.13 shows the values of the effective diffusivity coefficients from each box. This representation allows for the undesirable feature of negative coefficients. These can be justified because the effective diffusivity represents all of the components and processes not included in the advective flux, not just the Fickian diffusion. In all of the boxes, the solutions are of the same order as the a-posteriori errors, so it is not possible to make any significant conclusions about the detailed structure of the diffusion. The a-posteriori errors have a trend with respect to depth, with high values in the surface waters, decreasing to intermediate depths and then increasing towards the sea floor in the deeper waters. This may be explained by the respective property gradients, with smaller k values associated with larger property gradients i.e. surrounding the LCDW salinity maximum layer, which corresponds to the smallest uncertainties in the diffusivity errors.

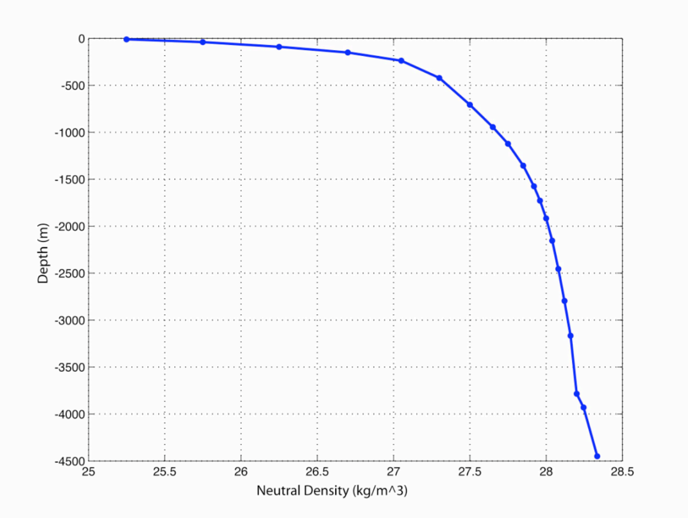

Figure 4.14: Conversion chart between neutral density surfaces and mean depths obtained from the WOCE Climatology of the Southern Ocean (Gouretski and Koltermann, 2004).

4.4.4 Fluxes due to the air-sea interaction

In the standard model, corrections are sought for to mass and heat fluxes due to the interaction at the ocean surface with the atmosphere. Figures 4.15-17 show the initial imposed fluxes, and the model corrections for the freshwater and heat fluxes into box layers at the surface, and the air-sea flux induced dianeutral mass flux. In all cases, the model solution is dominated by adjusting other parameters in the model, resulting in an air-sea flux balance that is within errors, identical to the imposed fields. This is not due to the size of the a-priori errors, and all flux corrections are much smaller than the pre-determined range of model errors. The a-priori error scales were varied over orders of magnitude in the testing phase of the model, but in all cases with realistic error boundaries, there were no significant flux adjustments. The model solution does not reflect the large uncertainty in the climatological fluxes used in this model, and any large-scale observations about the size and direction of mass and heat fluxes should be taken with caution, as the real errors are greater than those defined within the constructs of the model solution. The heat fluxes are the dominant term in the dianeutral surface fluxes throughout the model. The NOC climatology does not cover the coastal region, so the areas where the freshwater fluxes are expected to be dominant in the transformation of water masses are not included in the fluxes used in the initial state of the model.

This feature of the model solution is due to the relative scaling of the correction terms to the fluxes used in the initial state of the model. The dominant terms are the barotropic velocity corrections, which enable the largest degree of freedom to adjust the fluxes within each box and layer with the smallest effect on the total variance of the solution. This is due to the large number of unknowns associated with the station pair corrections compared to the unknowns associated with the dianeutral fluxes and air-sea interaction terms. The error associated with a station pair is of the order of 1 Sv, which when combined across the longer sections leads to errors of the order of 100 Sv. An error of $1\text{x}10^{-6}$ ms^{-1} in the dianeutral velocities equates to an error of between 10-100 Sv in the dianeutral surface flux, depending on the size of the box. The magnitude of the air-sea interaction induced dianeutral fluxes are of the order of 10 Sv, with the uncertainty in these transports being equal to or greater than the fluxes obtained from the initial climatologies.

The general pattern of the dianeutral fluxes throughout the Southern Ocean is a positive flux (from lighter to denser waters) in the lighter water (to the north) and a negative flux towards the lighter waters in the denser surface layers (in the south). The dianeutral air-sea flux induced transports are dominated by the heat component, with only a minor contribution due to the freshwater fluxes throughout the model domain. This is partly due to the resolution of the NOC climatology that has poor coverage in the coastal areas around Antarctica and does not include the effects of the annual sea-ice cycle. The freshwater flux due to sea-ice and from ice-melt from Antarctica is thought to play a major part in the buoyancy balance of the lower cell of the Southern Ocean overturning (e.g. Bryden and Cunningham, 2003), but this effect is largely excluded from the model, apart from the changes in the surface density distribution throughout the year used in the air-sea flux calculations. The effect of the Antarctic freshwater flux will be explored in more detail in chapter 7, where it will be linked to the observed overturning transports found in the model solution.

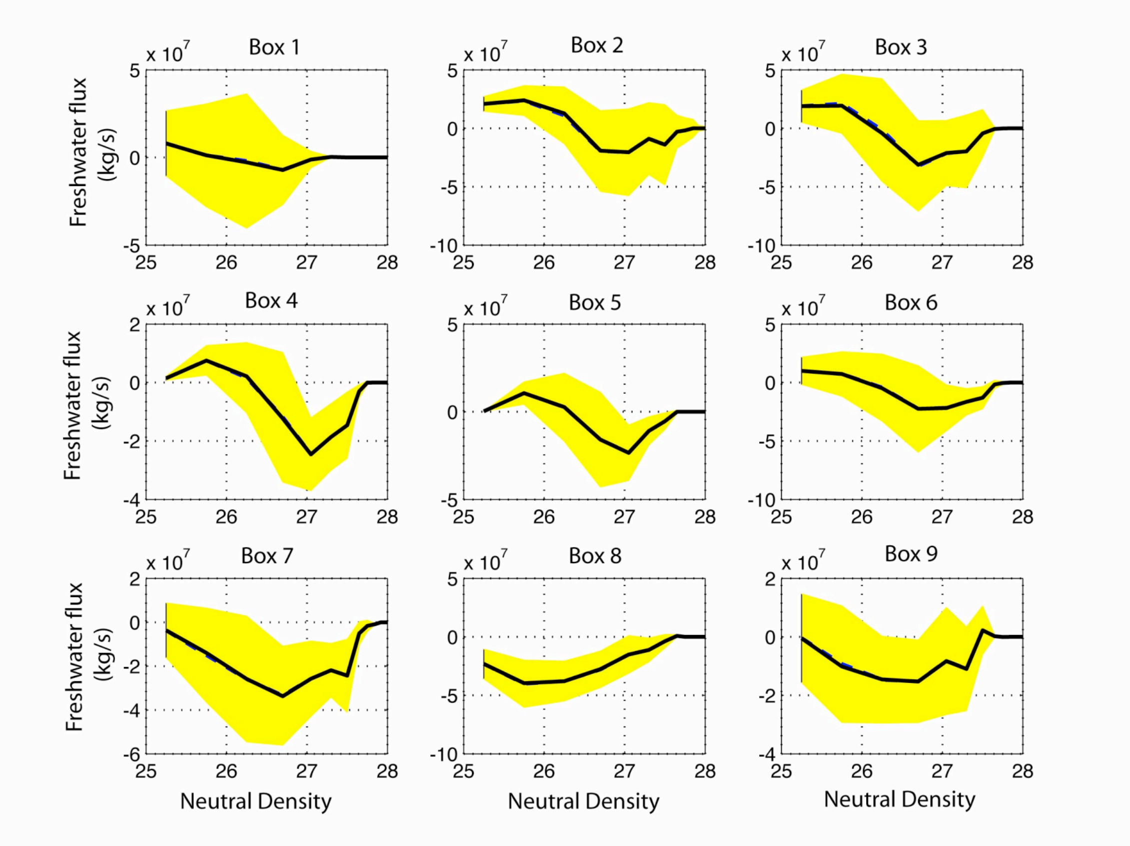

Figure 4.15: Air-Sea freshwater fluxes from the model solution. Black line=flux from NOC climatology. Dashed blue line = corrections to flux from model solution (indistinguishable from initial flux). Yellow region = A-posteriori error boundaries.

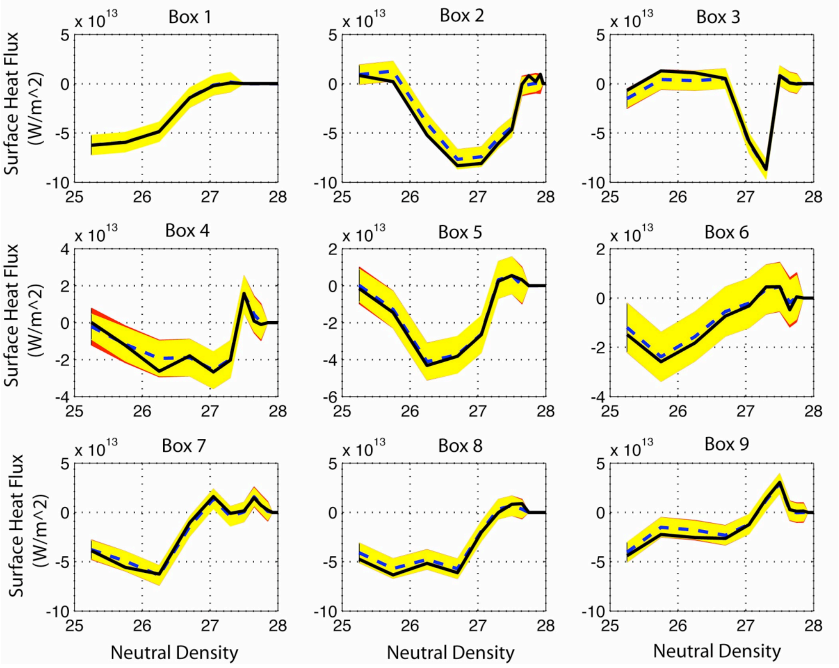

Figure 4.16: Air-sea heat fluxes due to exchanges with the atmosphere (positive flux=out of the ocean). Black line=flux from NOC climatology. Dashed blue line=corrected flux, Yellow region=a-priori error boundary. Red regions=a-priori error boundaries (in most cases indistinguishable from the a-posteriori errors).

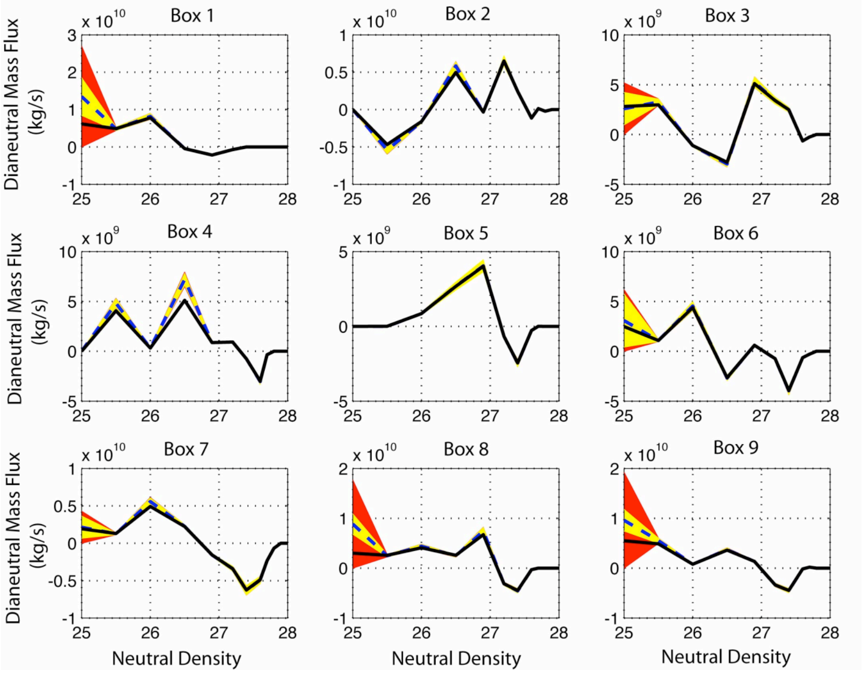

Figure 4.17: Dianeutral air-sea flux induced mass flux (kg/s). Black line= Initial fluxes derived from NOC Climatology. Dashed blue line= correction to flux from model solution, red region= a-priori error boundary, yellow region= a-posteriori error boundary. A positive flux is into a denser layer.

4.5 Summary

The standard model solution produces realistic fluxes throughout the main sections of the model. The ACC transport varies between 140-150 Sv, growing with the mass flux imported from the Indian Ocean, compensated for by the northward flux into the Pacific Ocean and the return circulation via the Indonesian Throughflow. The major western boundary currents in the Atlantic, and Indian Oceans are constrained to be consistent with observations producing circulations that are broadly in agreement with other inverse studies.

The model produces dianeutral velocities that are significant over the a-posteriori errors on a good proportion of the model levels, resulting in dianeutral transports between density surfaces, particularly in the deeper layers. The effective diffusivity coefficients are not well resolved and this will be explored in reference to other model set-ups in chapter 6. The dianeutral transports due to air-sea fluxes are not well represented in the model solution and are not significantly different to the initial fluxes applied in the model.

The next chapter will examine the transport and circulation of the major water masses of the Southern Ocean throughout the model, and outline the overturning in the Southern Ocean determined across the southern and northern boundaries of the model.

Chapter 5: Water masses and the overturning circulation

In this chapter, the structure, properties and circulation of the main Southern Ocean water masses will be detailed, with reference to previous inverse and regional studies. This analysis starts with the intermediate waters, moving down through the water column to the AABW. The vertical structure of the circulation is presented in an examination of the overturning circulations in each basin and around the latitude circle boundaries of the model as a whole.

5.1 Intermediate and Mode Waters

In the model, three layers cover the Intermediate waters, γ^n=26.90-27.20 kgm^{-3} (SAMW), γ^n=27.20-27.40 kgm^{-3} (SAMW/AAIW), and γ^n=27.40-27.60 kgm^{-3} (AAIW). Sloyan and Rintoul (2000a,b) define γ^n=27.40 kgm^{-3} as the bottom of their IW layer, but You (1999) define γ^n=27.45 kgm^{-3} as representing the salinity minimum core of the AAIW in the South Atlantic. The inclusion of denser waters is also consistent with the SR01b repeat sections that has two peaks in transport in density surfaces (see figure 3.8) centred on the top two density layers in the model. SAMW is formed around the ACC in the SAZ (Hanawa and Talley (2001)), with the Southeast Indian Ocean forming a dominant source region due to the deep winter mixed layers in this area (Sallee et al, 2006). The additional contribution of air-sea exchange induced dianeutral mass fluxes will also be included in the following analysis, but due to the poor resolution of flux corrections in the model solution, this discussion will be based on the initial field obtained from the NOC Climatology. There are considerable errors associated with these fluxes, so the mass balances on density layers due to air-sea interactions are stated without error bars, only providing a qualitative description.

AAIW plays an important role in the upper cell of the global overturning circulation, providing a return route for NADW entering the Southern Ocean. You (1999) investigated the circulation of AAIW in the South Atlantic, and how the cold (AAIW originating from Drake Passage) and warm (AAIW entering the South Atlantic from the Indian Ocean) water routes contributed to the northward flux of AAIW from the South Atlantic. This results in a complicated picture of AAIW circulation and modification within the South Atlantic, dominated by the circulations of the tropical and sub-tropical gyres, and the ACC. The model boundary at 30 °S passes through the sub-tropical gyre, containing a complex flow pattern for AAIW, with southward transport in to the west of the section in the Brazil current that is partially compensated for by the recirculation in the Brazil Basin. To the east of the section, the AAIW transport is predominantly northward in the gyre circulation and as part of the Benguela current, moving water northward across the South Atlantic. Across section A11, the transport is northward at the western and eastern sides of the section, with a southward/eastward flux in the central section due to the sub-tropical gyre, passing through the transect.

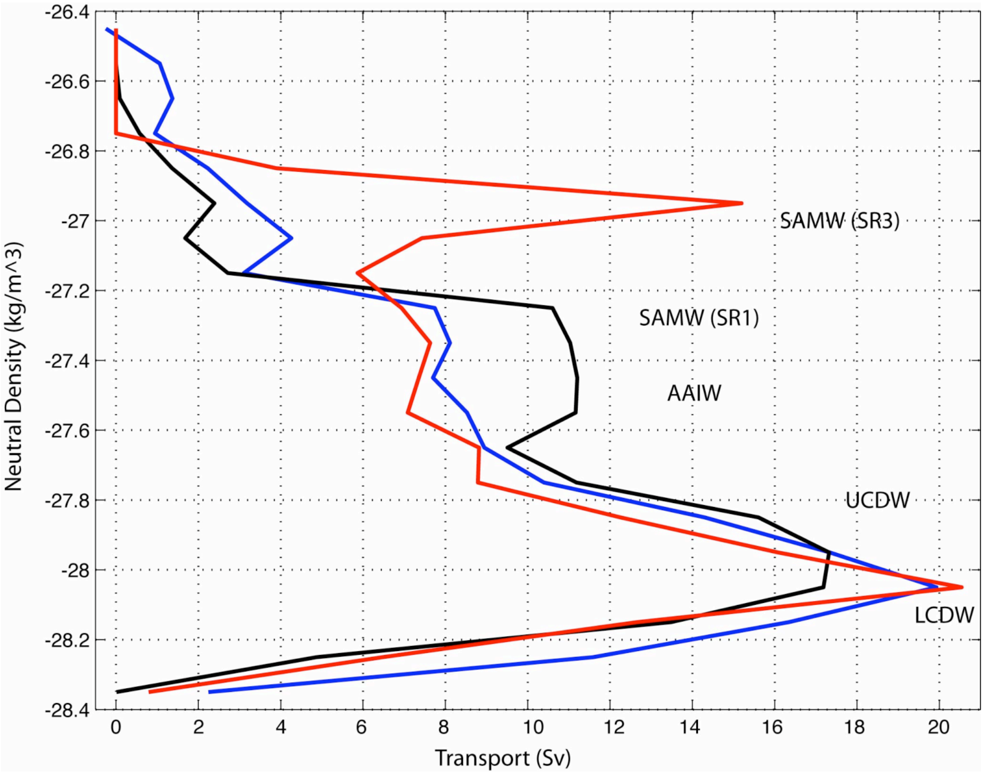

Figure 5.1: Transport on 0.01 kgm^{-3} neutral density surfaces from the model solution at the three major ACC choke points, SR01-Drake Passage (black), I06-Africa (blue) and SR03-Australia (red).

In the South Atlantic, 50.8±0.6 Sv enters through Drake Passage in the IW layers. This is balanced by 42.6+2.2 Sv leaving past Africa, and 5.4±4.2 Sv passing into the South Atlantic. At A11, the northward and southward fluxes are almost balanced, with the mass balance across A10 being completed by dianeutral fluxes into these layers from above and below. In box 2, the model produces large dianeutral fluxes, moving upward across all layers. 13.6±1.2 Sv is transported across the γ^n=26.90 kgm^{-3} surface, with fluxes of 8.2±2.0, 4.2±3.5 and 5.7±3.4 Sv across the other lower surfaces of the IW. At Drake Passage, the IW transport is predominantly eastward, but at I06, south of Africa, there is a considerable westward flux, masked by the net eastward flux of the ACC. The Agulhas current and retroflection transport Indian Ocean IW (~30 Sv) into the South Atlantic, with a significant eastward transport further to the south, north of the SAF and PF. The air-sea interaction induces a net flux out of the top layer into the lower two layers, resulting in a net convergent flux of 7.7 Sv into the bottom two layers and a divergent flux of 6.2 Sv out of the top layer. These fluxes are in the opposite direction to the internal dianeutral transports, acting to reduce the mass imbalance.

In box 3, there is a significant downward transport of 10.9±1.4 Sv into the top IW layer from the warmer, surface waters above. This results in an increase in the flux through the ACC from 10.6±1.2 Sv to 22.0±0.6 Sv between I06 (30 E) and I09 (115 E). There is also a smaller upward flux (4.1±2.1 Sv) from the denser IW layers into the γ^n=26.90-27.20 kgm^{-3} layer contributed to the net gain in mass. The air-sea fluxes produce a convergent flux of 3.1 Sv into the bottom IW layer, with a large flux coming from the lighter waters passing into the three IW layers. This is in agreement with the theory of a northward Ekman flux of denser waters, cooling and freshening the warmer SASW, and creating a dianeutral flux into denser layers (e.g. Sallee et al. 2006).

In box 5, there is a large increase in the transport in the top IW layer. This is shown by the large peak in transport associated with SAMW (centred at γ^n=26.9 kgm^{-3}). This peak is not present at I09, so is indicative of a large increase in the mass of this water mass south of Australia in the South-Australia basin. Rintoul and Sokolov (2001) examine the transport variability on density surfaces in the six SR03 WOCE sections. There are large differences between the mass flux on this density surface (>50 %), which is further complicated due to the different periods of the year that the sections were occupied. Speer et al. (2000) examined the mean potential vorticity (PV) structure across the SR03 line, and there is a significant PV minimum in this layer, associated with the well-mixed nature of SAMW. In terms of SAMW formation, which is due to winter deep mixing, the SAMW transport south of Tasmania will vary throughout the year. There is an increase of 6.5±2.1 Sv in the eastward transport through the top IW layer between I09 and SR03 leading into the Pacific sector, primarily due to an upward flux of 4.6±2.1 Sv from the IW layers below. There is a flux convergence of 6.5 Sv in the top two IW layers in box 5, with fluxes from the lighter waters to the north and from the denser waters to the south.

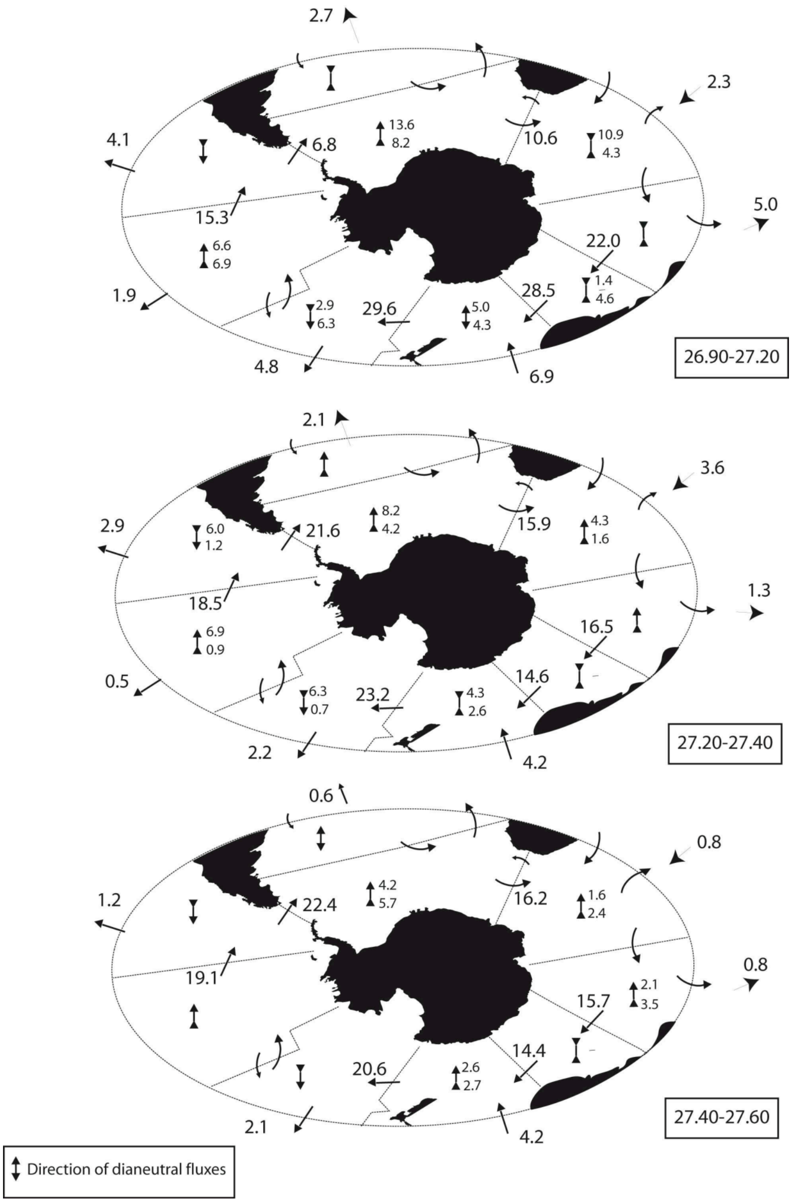

Figure 5.2: Fluxes and circulation on the three model layers representing the Intermediate waters: γ^n=26.90-27.20 kgm^{-3} (Top of the SAMW); γ^n=27.20-27.40 kgm^{-3} (SAMW/AAIW); and γ^n=27.40-27.60 kgm^{-3} (AAIW). The direction of diapycnal fluxes is show for each box, with the magnitude of significant fluxes shown (small lettering). The fluxes are in Sv and represent the total flux across the section, with significant re-circulations shown by the curved arrows.

There is a mean cooling and freshening in this density layer between the two sections, with a freshening signal that increases, moving southward, from ~34.60 psu at the northern extreme of both sections, with a difference of ~0.1 psu at the SAF. This could be due to the SAMW from the Indian Ocean re-circulating within the South Australia Basin (Rintoul and Bullister, 1999), and the export of Intermediate waters into the Pacific sector being dominated by the IW carried by the ACC. Rintoul and England (2002) found differences in SAMW properties were correlated with the northward Ekman transport of cold, fresh water. This variability in mode water properties could also explain some of the mode water property differences between the I09 and SR03 sections due to assynopticity and the effect of variations in wind-stress.

In the Pacific sector, the main features of the circulation are the SAMW entering the region from the west, and the formation of AAIW in the South-east Pacific Basin that is exported through Drake Passage and northward out of the Chile Basin. In box 6, containing the Campbell Plateau, and the southern part of the Tasman Sea, the zonal flux through the top layer is relatively unchanged, but the model struggles to balance the total fluxes in the layer. There are diapycnal fluxes of 5.0±2.2 Sv and 4.3±2.1 Sv into the upper and lower layers that are not completely compensated for by the southward flux from the EAC. In the lower two layers, there is a large increase in the zonal volume transport (8.6±1.1/6.1±1.1 Sv respectively) due to a convergent diapycnal flux into the middle IW layer, and an upward flux from the layers below. In box 8, the sense of the dianeutral fluxes is reversed, with downward velocities throughout the IW layers. This results in a net reduction in the zonal transport through the top layer, due to a flux of 6.9±1.4 Sv into the layer below, and a northward transport into the South-west Pacific basin as part of the gyre circulation within the basin. The eastern boundary of box 6 crosses the Pacific-Antarctic ridge, and contains a recirculation of IW, with a dominant eastward flux with the ACC over the topography, and a westerly transport in the northern part of the section that is in the easterly extreme of the South-west Pacific basin.

Box 9 contains the main AAIW formation region. Drake Passage acts to block the flow of the lightest waters in this box, reducing the zonal transport in the top IW layer from 15.3±1.8 to 6.8±0.1 Sv. This change is compensated for by a 4 Sv northward transport out into the Chile Basin, and a 6.0 Sv dianeutral flux into the layer below. The zonal transport in the bottom two IW layers increases by 6.4 Sv to 46.8±3.3 Sv, with 4.0±1.4 Sv being exported northward into the South-east Pacific. The total northward flux through the Chile Basin of 8.1±1.8 Sv is in rough agreement with Shaffer et al. (2004) that found a total northward flux of 7 Sv from a combination of moorings and hydrographic data (slightly different but comparable layer definitions on potential density surfaces). The general pattern across the Pacific Sector is the reduction in the volume of the top IW layer, from west to east, and the increase in the transport in the bottom two IW layers.

Figure 5.2 shows the main flow features and significant dianeutral transports in these three layers. The regions with the largest transformations are in the South Atlantic, South-west Indian Ocean, and the western and eastern extremes of the Pacific sector. The properties of the IW in the Atlantic Sector are transformed due to a combination of dianeutral and isoneutral mixing in all three layers. It is not possible to break down the individual contributions to this change, due to the complicated interactions and flow pathways of the AAIW within the South Atlantic that have been discussed above. There is a large convergence in the fluxes in the top IW layer associated with SAMW in the Indian Ocean sector. The SAMW export south of Australia is further increased due to mixing with the denser IW layers. The model produces realistic fluxes of IW around the Southern Ocean that will be important in the analysis of the upper component of the meridional overturning circulation that will be discussed in section 5.4. Due to the differences between our definition of the IW layers and that of Sloyan and Rintoul (2001), it is not possible to make direct comparisons of layer fluxes. They found a conversion of 8, 18 and 8 Sv from the UCDW into AAIW/SAMW across the boundary of γ^n=27.40 kgm^{-3} in the Atlantic, Indian and Pacific sectors respectively. If this surface is chosen in this study, the transports are 8.3, 5.7 and 1.7 Sv respectively into the IW layers from the UCDW. There is good agreement in the Atlantic sector, but the fluxes in this study are considerably smaller in the other sectors. Changing the density of the IW/UCDW boundary to γ^n=27.60 kgm^{-3} results in fluxes of 8.9, 5.9 and 4.6 Sv in the Atlantic, Indian and Pacific sectors, which is still much smaller than in the Sloyan and Rintoul (2000a) solutions.

5.2 Circumpolar Deep Water

5.2.1 Upper Circumpolar Deep Water

UCDW forms an important component of the upper cell of the meridional overturning circulation. Defining UCDW as the model layers between γ^n=27.70-27.94 kgm^{-3}, in this section, the basic features of the UCDW circulation and its interaction with the surrounding water masses will be discussed. Figure 5.1 shows the transport on density layers at the main choke points of the Southern Ocean. In all three locations, the transport increases with density through the UCDW layer, and there is little variability in the magnitude of gradient of transport change with increasing density around Antarctica. Starting in the South Atlantic, 33.7±0.4 Sv enters this layer from Drake Passage, with a further 3.5±2.2 Sv across 30 °S, primarily in the Brazil Current into the Argentine Basin. Across the A11 section, the net flux is 0.2 ±4.0 Sv, as there is a divergence in the dianeutral fluxes, mixing the UCDW with the AAIW above and the NADW entering the South Atlantic below. In box 2, there dianeutral fluxes are balanced and positive, with 4.8±3.5/5.0±2.7 Sv passing upward through the bottom/top surfaces of the layer.

In the Indian Ocean sector, 30.5±1.3 Sv enters south of Africa, but this has fallen to 21.9±1.2 Sv at the interface between boxes 3 and 4. This is mainly due to divergent dianeutral fluxes in box 3 of 3.1±2.4/-4.1±1.8 Sv across the top/bottom surfaces of the UCDW layer. There is a small net flux of 1.5±2.4 Sv out of the box into the Indian Ocean, which is due to 4 Sv moving southward in the Agulhas current, a return flow on the eastern flank of the Natal Valley, and a more gradual circulation as part of the sub-tropical gyre. In this box, the mixing with the LCDW below plays an important role in the changing properties between the two zonal sections, I06 and I08. Figure 5.3 shows the differences (I06-I08) between the mean properties on density surfaces. The largest changes are associated with the LCDW and with the NADW salinity maximum layer. These differences reduce upward throughout the UCDW, until ~27.65 kgm^{-3}, which is the approximate interface between the AAIW and UCDW. The smallest dianeutral transports occur in the centre of the UCDW layer (~27.85 kgm^{-3}), with increased mixing at the top and bottom of the layer. There is a similar pattern in mean oxygen concentrations, except in the IW region (γ^n=27.20-27.60 kgm^{-3}), where the gradient is reversed, due to higher oxygen concentrations on the eastern boundary of the box, implying more recently renewed IW across this side of the box. A net southward flux of 3.7±1.2 Sv enters box 4 from the Perth Basin, and the dianeutral fluxes bring up 1.9±1.1 Sv from the LCDW, resulting in 26.6±1.6 Sv that remains steady south of Australia in to the Pacific sector.

A net flux of 13.3±2.0 Sv leaves the Tasman Sea into box 6, creating a zonal transport of 38.1±1.9 Sv into box 7. The dianeutral fluxes are upward throughout the UCDW in this box. This implies mixing with the LCDW below, which is consistent with increased mixing in this box due to interactions with the complex topography of the Campbell Plateau that steers the ACC south of New Zealand into the South-west Pacific Basin. This is also an area of high eddy activity within the Southern Ocean in model and satellite data (e.g. Hughes and Ash, 2001). This is also a region where large turbulent eddy diffusivities are found in strain-based calculations (see chapter 3.4). The mixing rates increase with depth, but are still significant at depths associated with the UCDW, especially on the northern flank of the SAF that is forced southward due to the Campbell Plateau. The transport of UCDW in the central region of the sector is again dominated by the gyre circulation in the South-west Pacific Basin, but the net transports across the northern faces of boxes 8 and 9 in the eastern side of the sector are all small. This can be partly explained by the fluxes in the Chile Basin, where the UCDW-like waters are between the Northward flowing AAIW and the southward flowing Pacific DW.

Figure 5.3 shows the main isoneutral and significant dianeutral fluxes from the model solution in the circumpolar boxes, dividing the UCDW into three layers, highlighting the interactions with the IW above, and the LCDW below. There is a net southward flux of all of the layers associated with the UCDW into the Southern Ocean across the 30° S boundary. The dianeutral fluxes transport water down into the LCDW in the central Pacific, with upward fluxes in the Indian sector and the Southeast Pacific Basin. The UCDW layers interact with the atmosphere, resulting in dianeutral fluxes due to surface interactions. In all of the circumpolar boxes (2-9), the dianeutral fluxes associated with the UCDW are into lighter layers, resulting in a convergence of air-sea induced dianeutral fluxes in the IW layers. These fluxes are all small compared with the fluxes on lighter layers, primarily due to the smaller surface area of these layers that interact with the surface of each box.

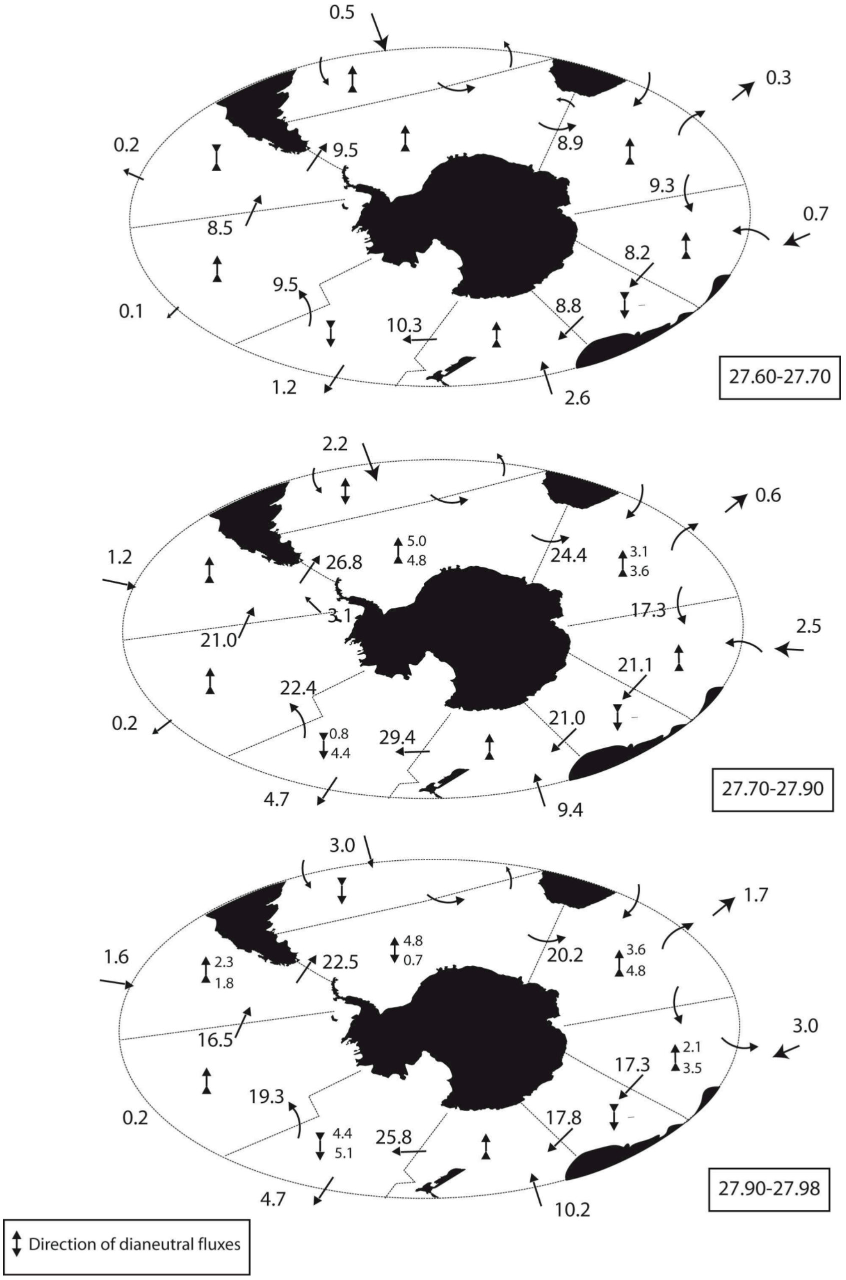

Figure 5.3: Fluxes and circulation on the three model layers representing the Upper Circumpolar Deep Water (UCDW): γ^n=27.60-27.70 kgm^{-3} (Top of the UCDW); γ^n=27.70-27.90 kgm^{-3} (core of UCDW); and γ^n=27.90-27.98 kgm^{-3} (bottom of UCDW/top of LCDW). The direction of diapycnal fluxes are show for each box, with the magnitude of significant fluxes greater than errors shown (small lettering). The fluxes are in Sv and represent the total flux across the section, with significant re-circulations shown by the curved arrows.

5.2.2 Lower Circumpolar Deep Water

The Circumpolar Deep Water is the largest and oldest water mass in the Southern Ocean. Figure 5.5 shows the mean salinity and potential temperature profiles on neutral density surfaces associated with LCDW from meridional sections around the ACC. The main feature is the salinity maximum that occurs between 28.00-28.10 kgm^{-3} that is a signal from the relatively warm and saline NADW entering the Southern Ocean in the South Atlantic. In the Indian Ocean sector, there is a large cooling and freshening trend, which continues into the Pacific Ocean and through Drake Passage, before the LCDW mixes with the NADW in the South Atlantic once again. Due to the range of processes and water masses that interact with the LCDW, in is not possible to determine the balance of mixing that occurs by just examining property data on individual sections. Mixing triangle methods are not very useful due to the difficulties in defining representative property values for the interacting water masses, which obscure any useful information that might be obtained. Figure 5.5 is a mean across density layers, so does not show the added complication of property differences either side of the ACC. There is a significant meridional structure within the LCDW (see chapter 2), with the ACC separating the polar and sub-tropical waters.

The solutions of the inverse model provide a consistent set of fluxes that can be used to examine how the LCDW properties change around the ACC due to interactions with neighbouring water masses, to the north and above and below. Figure 5.6 shows a schematic representation of the LCDW fluxes on three density layers associated with the LCDW. These layers were chosen to examine the core salinity maximum layer and its interaction with the lighter and denser waters that make up LCDW. The top layer (γ^n=27.94-28.02 kgm^{-3}) contains the boundary between the Upper and Lower CDW, and is generally characterised by lower salinities, warmer temperatures and a lower oxygen concentration. The middle layer (γ^n=28.02-28.10 kgm^{-3}) is centred at the core of the LCDW salinity maximum. This is located at the top of the layer in the South-East Atlantic and gradually deepens to the bottom of the layer at Drake Passage due to interactions with other water masses around the Southern Ocean. The bottom layer contains older, fresher and colder UCDW and deep waters from the Pacific and Indian Oceans. Some of the water has made numerous laps of the Southern Ocean (Orsi et al. 1999). The ACCbw is not included in this analysis and is described along with the

AABW as water in this density range is exported northward across the northern boundary.

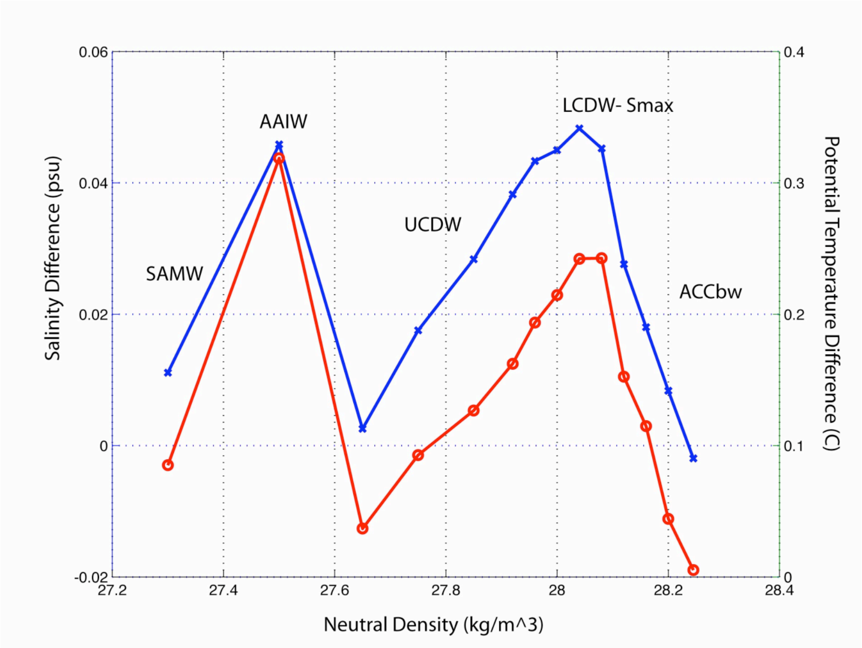

Figure 5.4: Salinity (blue) and Potential Temperature (red) difference between the mean property values on the zonal faces of box 3 (I06 value minus I08 value).

The largest changes in LCDW properties around the Southern Ocean occur in box 3 in the western part of the Indian Ocean sector. The Agulhas current transports lighter waters southward along the coast, but there is a net northward transport of NADW/LCDW into the Mozambique and Madagascar basins, especially in the salinity maximum layer (~9.2 Sv). The export of mass is compensated for by a convergence of dianeutral fluxes from the adjacent layers (~6.4 Sv), with 4.9 Sv moving downward, and 1.5 Sv moving up into the middle layer. The model solution shows that the large property changes are due to a combination of northward mass transport (and therefore of salt and heat) into the Indian Ocean and mixing with the adjacent surfaces, dominated by fluxes with the lighter waters. This is consistent with the change in the density of the salinity maximum surface, due to more intense mixing with fresher waters in the upper part of this layer. The northward flow into the Indian Ocean is partially compensated for by a net southward flux through the Perth Basin in all three layers. In box 5, South of Australia, the circulation is dominated by the ACC, with a small southward flux in these layers into box 12 along the Adelie Coast. The dianeutral fluxes are small and the corrections to the KVS dominate the model solution, acting to adjust the ACC transport so that it is similar throughout the Australia-Antarctic and South Australia basins.

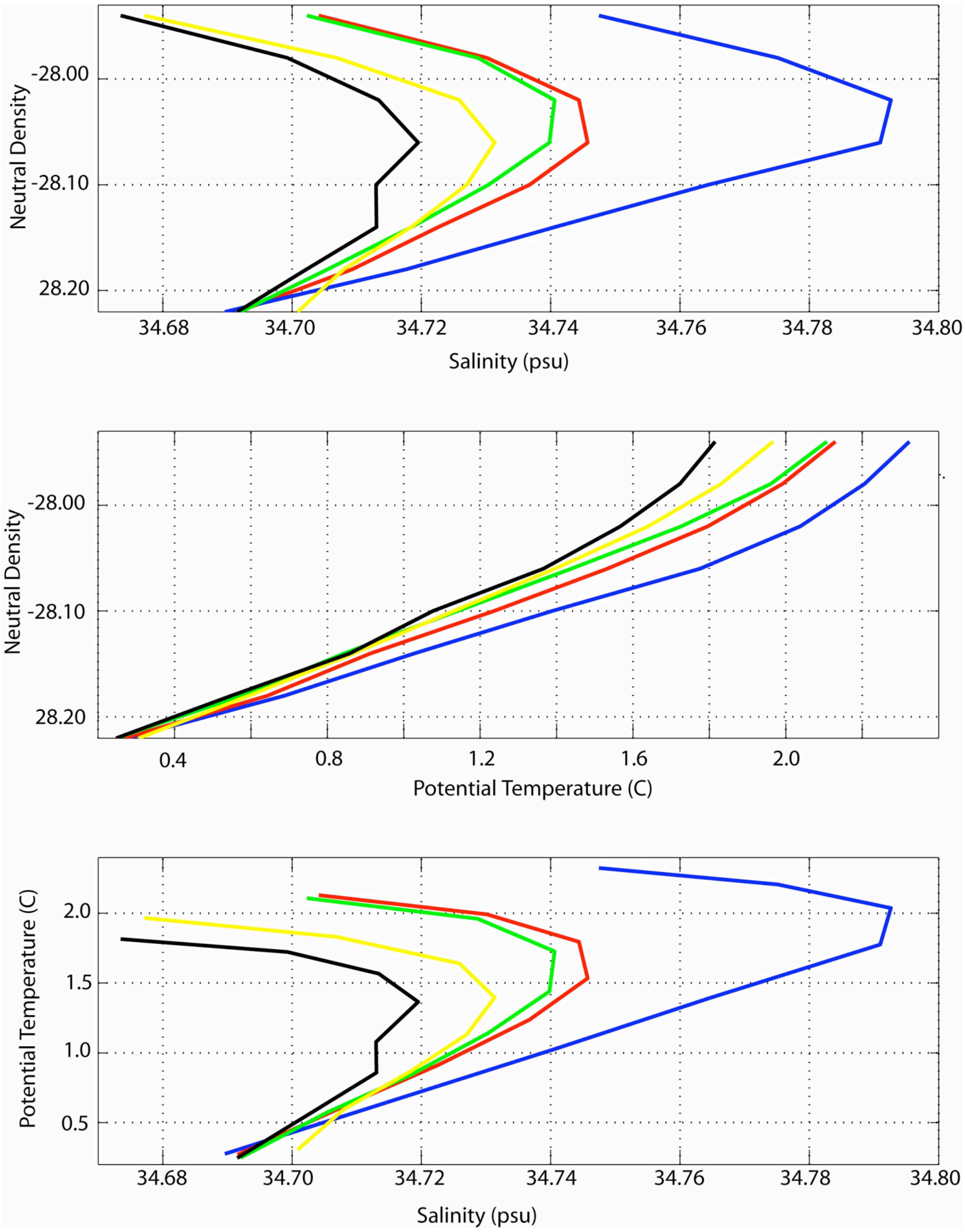

Figure 5.5: Mean Salinity/Potential temperature relationships on model density layers around the Southern Ocean, centred on the LCDW, from selected sections, I06/30 E (blue), I08/85 E (red), SR03/140 E (green), 170 W/P15 (yellow), and SR01b (black). Top: Salinity (psu) vs. neutral density (kgm^{-3}); Middle: Potential temperature (°C) vs. neutral density (kgm^{-3}); Bottom: Salinity vs. Potential Temperature plot.

In the Pacific sector, the ACC moves across the Southeast Indian ridge and the Pacific-Antarctic ridge, transporting water from the Southwest to the South-east Pacific basins. This sector is divided into four boxes, with two boxes within each basin. The western-most box (box 6) contains a number of topographic features and flow features. The ACC enters south of Tasmania and is joined by the southward flux of the East Australia Current out of the Tasman Sea. The path continues around the Campbell Plateau south of New Zealand, where the northward flank of the Ross Gyre and the boundary currents along the western edge of the South-west Pacific basin enter the box. The water mass changes in this box are a complex combination of advective and dianeutral mixing that has a large spatial variability that is masked by the mean fields used in the inverse model. The model solution has a southward flux into all three LCDW layers, which is largest in the top layer, increasing the eastward transport in this layer from 14.3 Sv to 20.0 Sv. The dianeutral fluxes advect mass downward through the layers, and grow in magnitude with 1-3 Sv moving down through the layers associated with LCDW.

Box 7 contains the eastern part of the South-west Pacific Basin, and there is a large northward recirculation in the LCDW layers compensating for the southward transport entering box 6 through the Tasman Sea and the western boundary current in the basin. The model produces a large circulation within this basin, which is in broad agreement with other estimates of the large-scale structure e.g. (Reid, 1986, Tsimplis et al, 1998). In the East Pacific Basin, the topography restricts the density of the water on the northern boundary of box 9 in the Chile Basin. There is a total southward transport of 5.6 Sv which is in strong agreement with the study by Shaffer et al (2004), that found ~5 Sv of Deep Water transport across this section. On the southern boundary of the Pacific sector, the LCDW transports are dominated by the gyre circulations associated with the basins of the Bellingshausen, Amundsen and Ross Seas. Most of this transport is in the densest layer of this analysis, with a circulation of 2 Sv associated with the Amundsen Sea, and a 6 Sv in the Ross Gyre. The majority of the southward export of deep waters is in the density class associated with the ACCbw (γ^n=28.18-28.27 kgm^{-3}), which is explained in more detail in section 5.3 in reference to the transport and production of AABW.

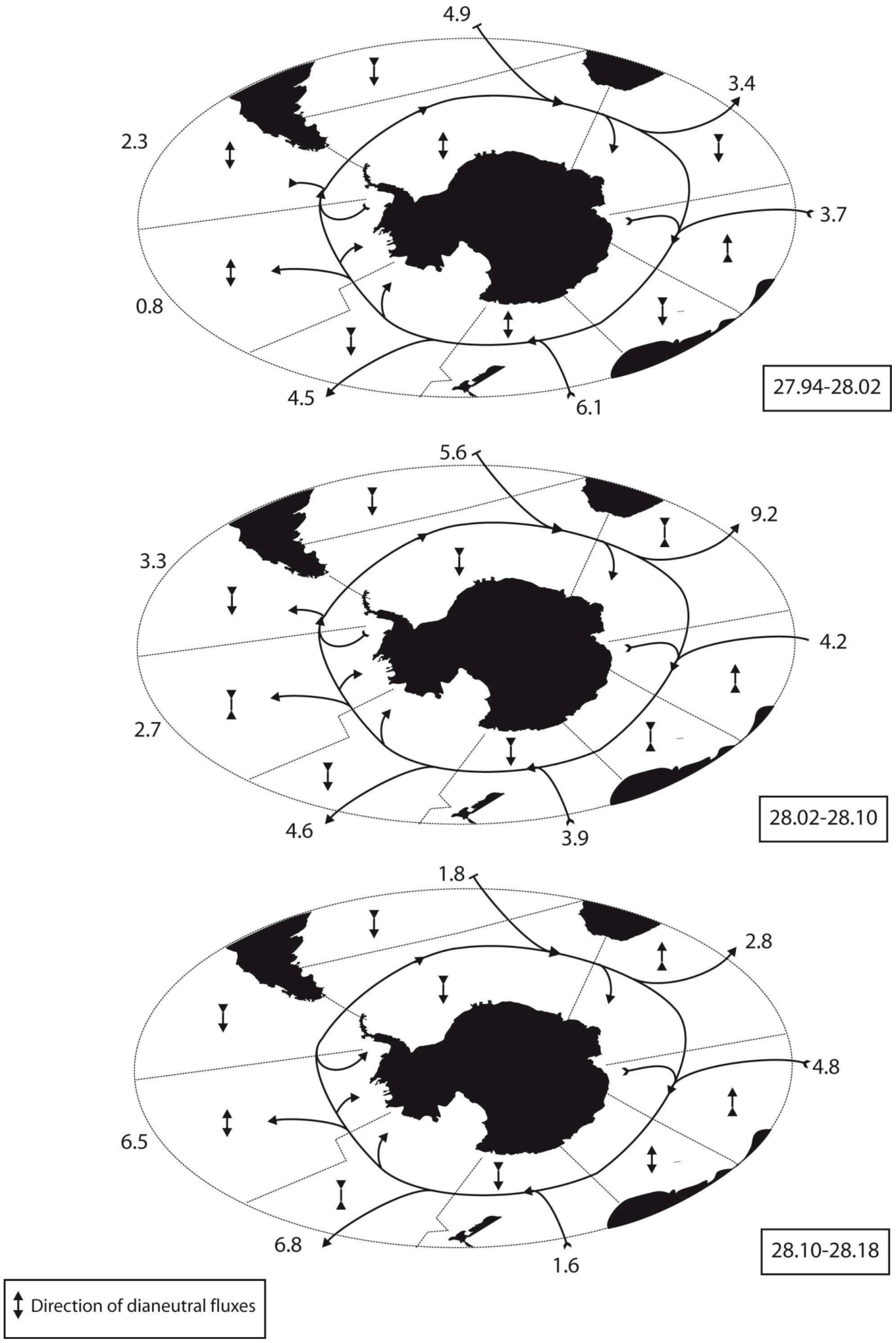

Figure 5.6: A schematic representation of the model solution on three neutral density layers associated with the LCDW (γ^n=27.94-28.02 kgm^{-3} (top), γ^n=28.02-28.10 kgm^{-3} (middle), γ^n=28.10-28.18 kgm^{-3} (bottom)). The direction of dianeutral fluxes at the upper and lower interfaces of each layer for each box are shown by the vertical arrows. Significant meridional transports are shown (Sv).

5.3 Antarctic Bottom Water

Determining the location and magnitude of bottom water formation is an important component in the understanding of the global circulation. The southern boundary of the Inverse model contains hydrographic stations all around the Antarctic coast or across the continental seas, except between 0° and 30° E, where the Antarctic coastline forms the boundary. The solution provides a view of the flux balance around this boundary and an estimate of the sources and magnitudes of AABW production. Figure 5.6 shows the cumulative transport, integrated eastward around the continent, starting at the Weddell Sea. It outlines the clockwise gyre circulation in the Weddell Sea, the gradual southward transport to the west of the Kerguelen Plateau, and the northward current along the eastern side of the Plateau. There is a net southward transport along the Adelie coast, which is compensated for by the Antarctic Slope front, transporting the excess water westward. In the Pacific sector, the Ross Gyre is apparent, along with smaller re-circulations associated with the Amundsen and Bellingshausen seas to the west.

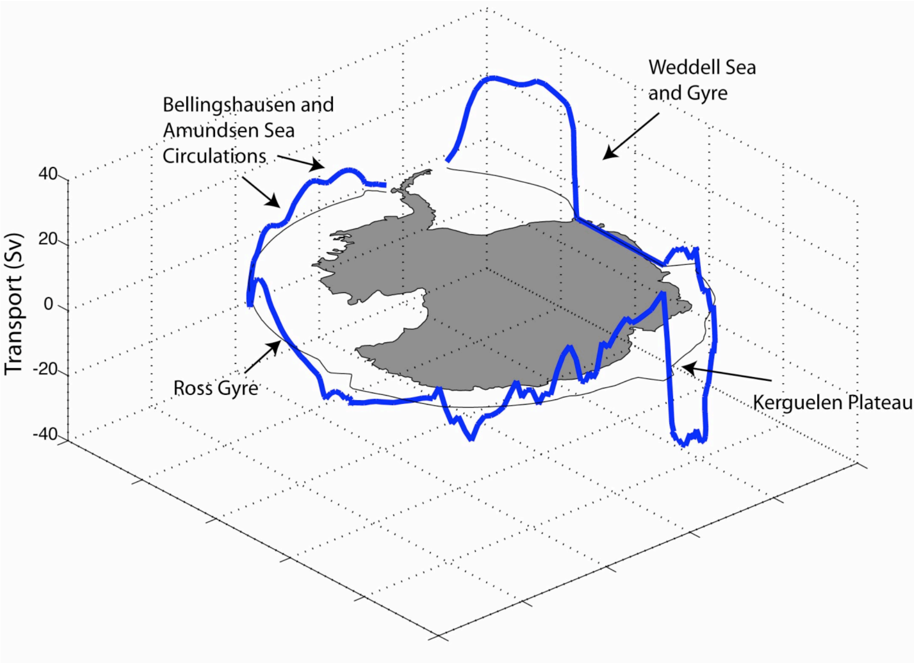

Figure 5.7: Cumulative total transport around the southern boundary of the box (Sv), integrated eastward from the Weddell Sea (50° W). Positive/upward transports are

northward. There is a net imbalance of 0.5 Sv across the southern boundary.

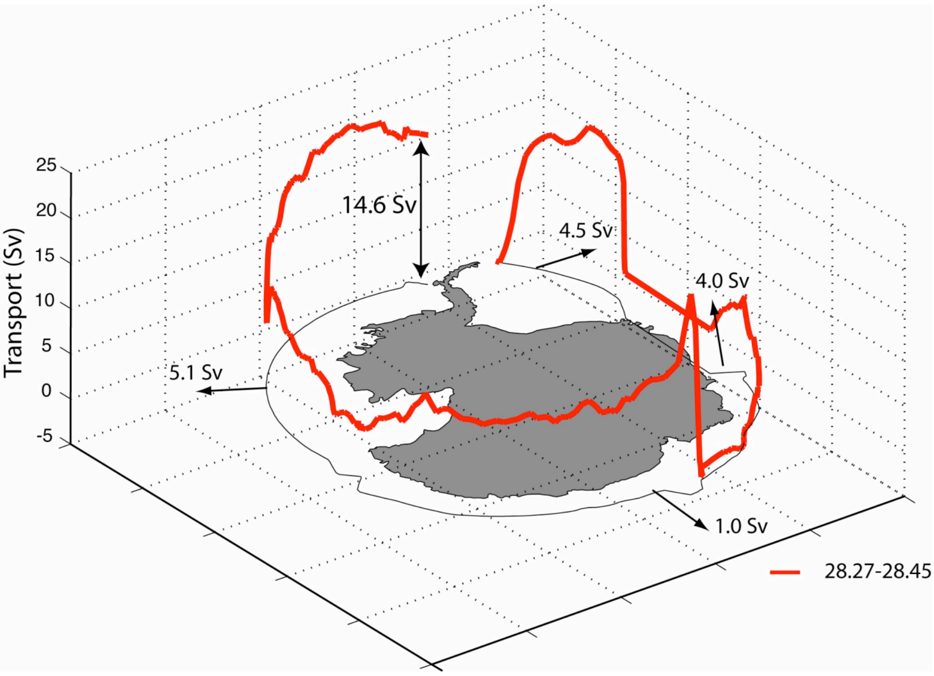

Figure 5.8: Cumulative transport on the deepest model layer (γ^n=28.27-28.45 kgm^{-3}), associated with AABW. The main regions of net northward transport and AABW export are located on the figure. The total northward transport is 14.6 Sv.

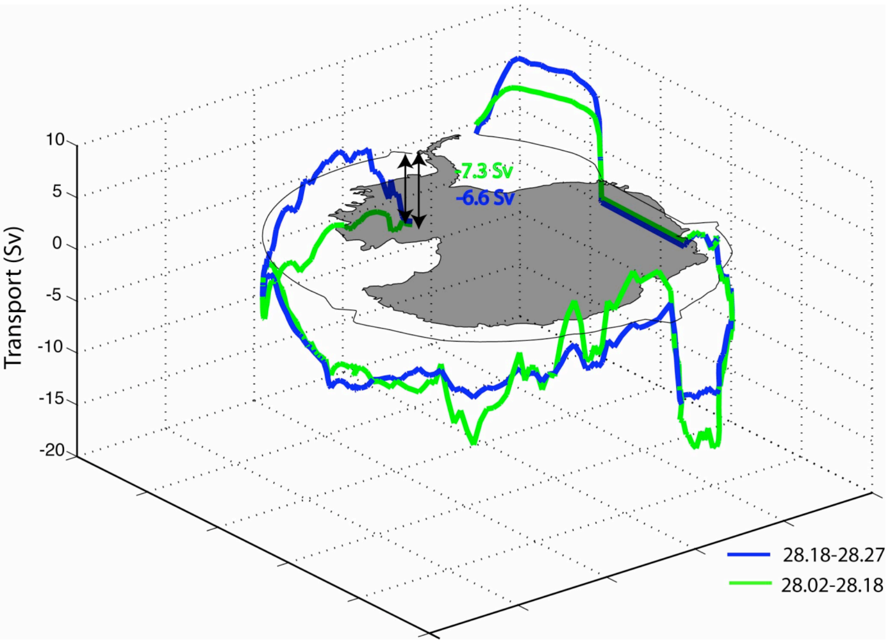

Figure 5.9: Cumulative transport on two density layers integrated eastward around the southern boundary of the box model from the Weddell Sea (50 °W). The blue line represents the density layer γ^n=28.18-28.27 kgm^{-3}, associated with ACCbw. the green line (γ^n=28.02-28.18 kgm^{-3}) covers the LCDW.

The strength of the Weddell Gyre is 32.3 Sv, resulting in a slight correction to the initial gyre strength measured from the adjusted data set of 31.8 Sv. The solution reduces the poleward heat transport from 0.035 PW to 0.025±0.005 PW, in agreement with the heat flux obtained from the mooring time-series of Fahrbach et al. (1994). Figure 5.9 shows the horizontal and vertical structure of the density layers between γ^n=28.18-28.45 kgm^{-3} that accounts for a large proportion of the water masses across this section. The circulation is concentrated in the southward/northward coastal currents at the eastern/westerns sides of the basin respectively that are balanced so that, within errors, there is no net transport across the section. The left-hand panel of figure 5.9 shows that there is a finer-scale structure in the balance of fluxes within the AABW layer (γ^n>28.27 kgm^{-3}). There is an equator-ward flow of the densest water (γ^n>28.40 kgm^{-3}) along the western continental boundary, containing Weddell Sea Bottom Water (WSBW), formed on the continental shelf. There is a layered structure to the transport in the rest of the AABW density layer, where the direction of the transport within the interior reverses. Between γ^n=28.35-28.40 kgm^{-3} the flow is southward, which reverses to a northward flux between γ^n=28.27-28.35 kgm^{-3}. Above this surface, the flow is predominantly southward, associated with the southward transport of LCDW/ACCbw and Weddell Deep Water (WDW) that it is LCDW modified within the Weddell Gyre.

Moving eastward around the Southern Ocean passed the Greenwich meridian (0° E), The main feature is a gradual southward flux of AABW associated with the Weddell Gyre. There is an outflow of 4.0 Sv that is an artefact of the model boundaries, as the box boundary switches from following the coastline, to a hydrographic station boundary east of 30 °E. The imposed initial field from the BRIOS Model influences the region centred on the Kerguelen Plateau. The model solution has three boxes along the Antarctic coastline from 30 °E to 150 °E. The 4.0 Sv AABW flux is through the western face of box 10 (see figure 3.6). The eastern face of this box is located across the Princess Elizabeth Trough (PET), and the solution has a 25 Sv eastward flux through the PET, and a westward current along the continental slope of 3.5 Sv. This additional eastward transport through boxes 10 and 11 compensate for the small circumpolar transport between boxes 3 and 4 because the SACCF/SB ACC transports are not captured within the main boxes. This also makes up a major component of the high transports through the northern faces of boxes 10 and 11 due to the presence of these fronts crossing the model boundaries and do not represent large-scale transports into the main circumpolar boxes. This is shown in figures 5.7-5.8 where there are large northward and southward transports in all layers in the region of the Kerguelen Plateau, but there is only a small net northward flux of bottom waters ~1.0 Sv. This also results in a small poleward heat transport in this section but it is not significant above the model errors.

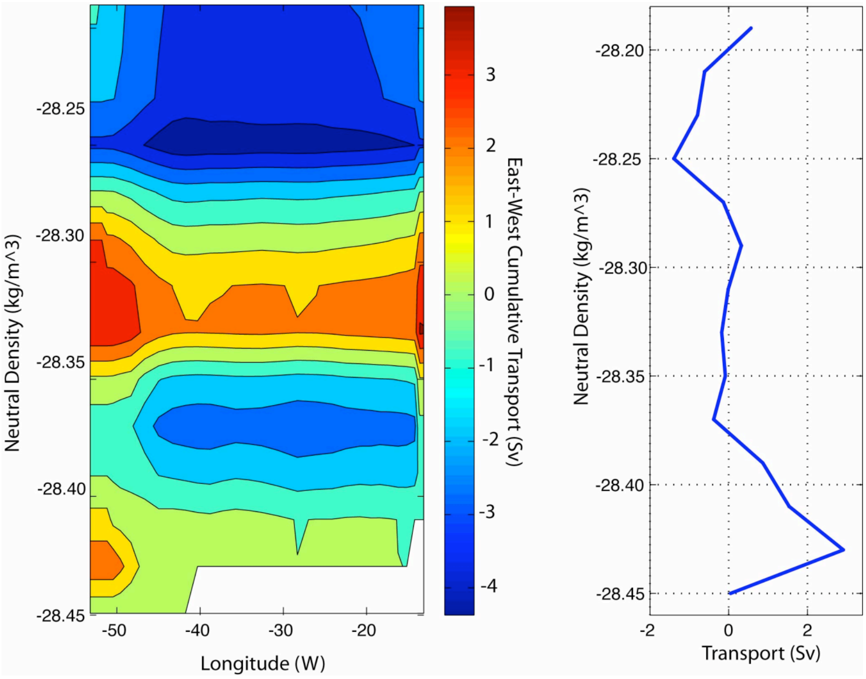

Figure 5.10: Left: Cumulative East-to-West (right-to-left) transport on neutral density surfaces across the Weddell Sea. Right: Total transport on neutral density surfaces in the ACCbw (γ^n=28.18-28.27 kgm^{-3}) and AABW (γ^n=28.27-28.45 kgm^{-3}) in layers of thickness 0.02 kgm^{-3}. In both figures, a positive transport is northward.

Box 12 contains a signature of a westward transport along the continental slope, and an eastward transport further north, due to the southern limits of the ACC being found within the box. A 7.6 Sv current enters the eastern face of box 12, which reduces to 6.3 Sv on the western face leading to the PET (box 11). There is an eastward flux of 3.2-3.3 Sv through the box, representing the SACCF/SB transports. These model transports are similar in magnitude to the balance of fluxes obtained from the BRIOS model. They are considerably smaller than the fluxes calculated from in-situ estimates combining hydrographic stations and LADCP measurements. This can be partly explained by the southerly location of the northern boundary of these boxes, which reduces the eastward component of the flow due to the ACC within these models. It was decided to use the BRIOS model output as a base field for the flow structure because it was a mean picture of this flow pattern as opposed to a data-based snapshot of a highly variable region. The northern face of box 12 has a small net flux (-1.2±2.2 Sv) that masks a large circulation through the section of up to 10 Sv. There is a poleward heat transport across this section of 0.013±0.006 PW, which is significant above the errors of the posterior model solution). This is mainly due to a northward export of bottom water in the lowest layer of 0.75 Sv compensated by a southward flux of lighter waters.

The S4P section across the Bellingshausen, Amundsen and Ross Seas forms the southern boundary of boxes 6-9 within the Pacific sector of the model. The BRIOS mean field was used to adjust the data so that the model was initialised with barotropic gyre circulations within each basin. Figure 5.10a shows the west-east cumulative transport on 0.02 kgm^{-3} density surfaces within the bottom two density layers (γ^n=28.18-28.45 kgm^{-3}). The model solution has large re-circulations within the Bellingshausen and Amundsen Basins that contribute to the total northward export of AABW from the Pacific sector. Figure 5.10a shows that this flux is mainly at the very top of this density layer and is not associated with the production of AABW, but due to the modification of LCDW/ACCbw within the South-east Pacific basin. There is a Ross Gyre circulation of 20.8 Sv that is in strong agreement with the circulation obtained by Assmann and Timmermann (2005) of ~20 Sv, even though the initial field has a circulation of 30 Sv, so this is due to the model and not just a feature of the imposed field. Data-based observations come from meridional sections that can miss the centre of the gyre, so are all lower than the model circulations. Gouretski (1999) estimated a flux of 8.5 Sv, while Locarnini (1994) found a circulation of 5-9 Sv. In both of these cases, the level of no motion was taken to be at the deepest common level.

The densest waters are found in the Ross Gyre, and contain Ross Sea Bottom Water (RSBW) formed on the continental shelf of the Ross Sea. Figure 5.10b shows the oxygen concentrations on the density layers associated with the AABW and ACCbw. The highest oxygen levels are found along the Adelie coast, and there are local maxima associated with the northward circulation of the Ross gyre exporting RSBW into the

South-west Pacific Basin. The western boundary of box 12 also contains a considerable westward transport of RSBW that is not included in the net northward bottom water export budget. This forms an important part of the renewed bottom water with high oxygen concentrations found on the southern boundary of the boxes south of Australia. The model does not have the resolution to make any statements above the error boundaries about the localised sources of AABW along this coast, or the magnitude of the Antarctic Slope current along the continental shelf. The study by Bindoff et al. (2000) examines hydrographic data and ACDP measurements along this section, finding very large eastward and westward fluxes.

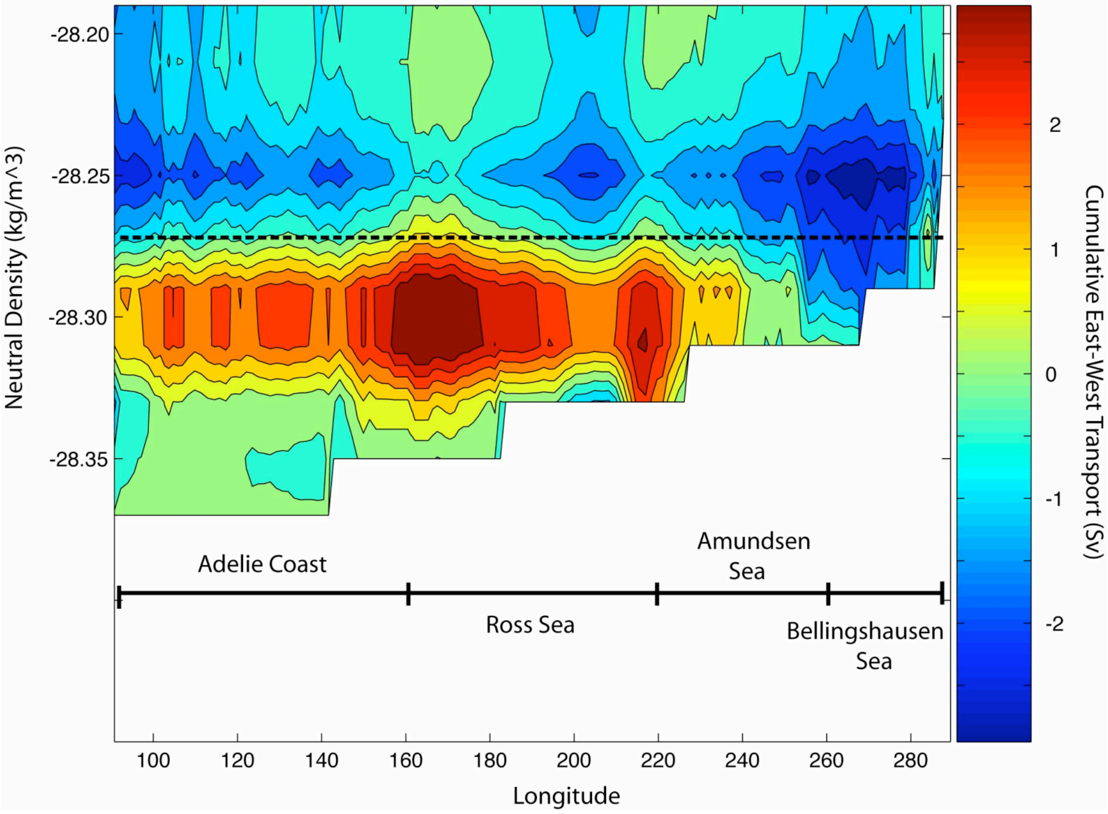

Figure 5.11.a: Cumulative West-East (right to left) transport on density layers of thickness 0.02kgm^{-3}. The dashed line shows the boundary between the AACbw and AABW.

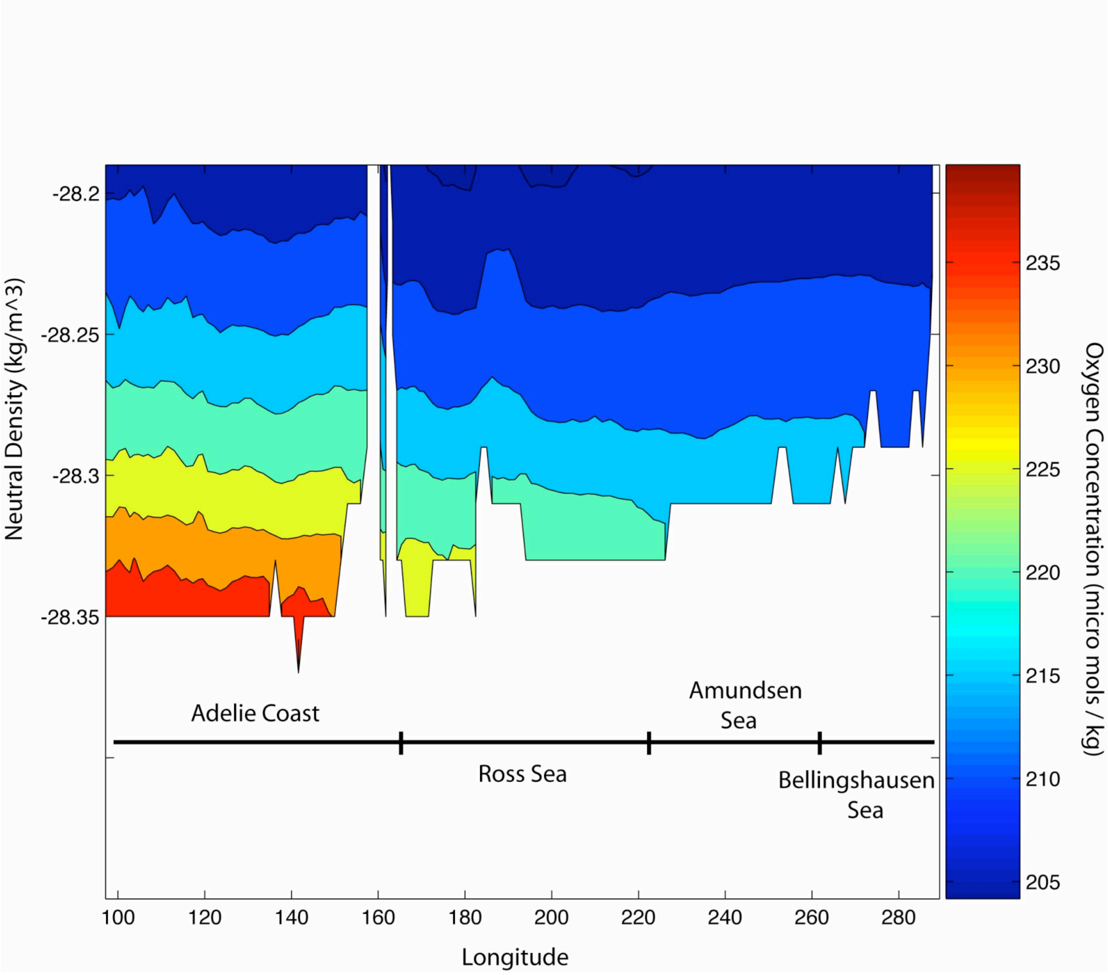

Figure 5.11.b: Oxygen concentrations (μmols/kg) averaged on density surfaces (of thickness 0.02 kgm^{-3}) in the bottom two density layers in the box model around the Southern boundary between 100°E and 80 °W.

5.4 The 3D circulation of the Southern Ocean

5.4.1 Overturning at 30 °S

The total flux across the northern boundary of the model is 3.2±4.9 Sv so within the range of errors, there is no net flux across this section, as expected. The slight difference from zero is due to the lack of a flux constraint for the whole boundary. Figure 5.12 (left) shows the overturning on density surfaces across the Atlantic, Indian, and Pacific basins, that combine to form the total overturning across the 30 °S latitude circle. The main features of the total overturning are the two overturning cells associated with the southward transport of U/LCDW and the northward export of AAIW and AABW in the layers above and below this. There appears to be a third cell in the surface waters with a northward flux of the denser variety of SASW compensated by a southward transport of lighter SASW. The errors associated with the surface layers are relatively high due to the uncertainties in the mass balance and the imposed surface forcing fields. These factors dominate any feature in these layers as the model has a lot of freedom to adjust these layers to balance the fluxes throughout the water column. The balance of the surface waters is also sensitive to the balance of fluxes between the Pacific and Indian Oceans, which shows the greatest variability between different model configurations. If the overturning is integrated on depth surfaces then this third cell disappears.

5.4.2 The Upper Cell

The Upper cell of the overturning circulation is composed of southward flowing UCDW/NADW compensated by a northward flux of Intermediate and surface waters. The cell is centred at 27.5 kgm^{-3}, on the layer separating the AAIW and UCDW. There is a northward flux of 18.8±5.5 Sv, but it is not possible to sub-divide the relative contribution of the CDW to either cell. There is a net southward transport of 25.5±5.5 Sv between γ^n=27.50-28.08 kgm^{-3} , this is considerably less than the 52 Sv in the Sloyan and Rintoul (2000a) solution between γ^n=27.4-28.0 kgm^{-3}. The northward branch of the cell is not well determined in that study, where the majority of the transport is in the surface waters.

Karsten and Marshall (2002) applied residual mean theory to the overturning of the upper cell(s) in the Southern Ocean. They found an upper cell centred on the AAIW (~27.5 kgm^{-3}) with a magnitude of 16 Sv. In this formulation, there is also a third upper cell consisting of southward moving surface water compensated by a northward transport of SAMW (of ~ 12 Sv). The spatial resolution of the inverse model is not able to determine whether this is the case or not, as these fluxes would all occur well within the model domain, and the surface water transport at the northern boundaries of the model are dominated by the Ekman fluxes and the gyre circulations at 30° S. In the Transformed Eulerian Mean solution, the upper cell is driven by eddies on the northern flank of the ACC, but this inverse study does not have the meridional or spatial resolution to investigate that aspect of the meridional overturning structure, and can only determine the overturning at the northern and southern boundaries that result from the solutions to the conservation equations of the model.

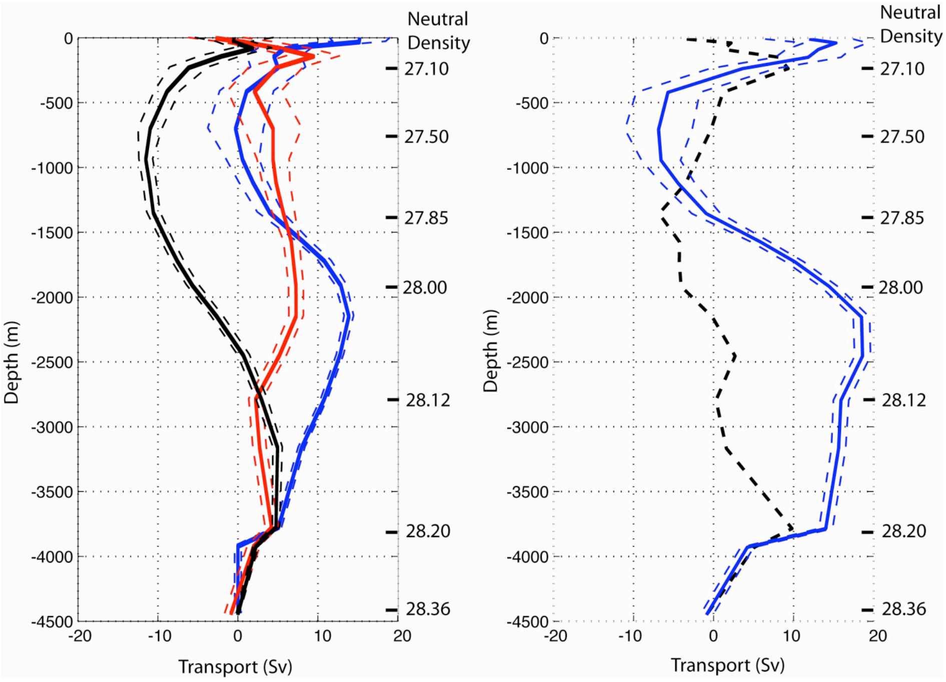

Figure 5.12: a.) Meridional overturning streamfunction at 30° S in Atlantic Ocean (black), Indian Ocean (red) and Pacific Ocean (blue), summed on density layers and integrated from the surface. The dashed lines represent ± correlated layer flux uncertainties from the posterior error matrix. b.) Total Meridional overturning circulation on depth layers (blue), and net meridional transport on neutral density layers (black-dashed) plotted with a representative depth scale.

Expanding the zonal mean picture to focus on the individual ocean basins reveals significant differences in fluxes across the northern boundary of the model between the ocean basins. Figure 5.13 shows the basin-scale components of the total transports on density layers across the 30 °S boundary. SAMW is exported northward in all three oceans, but for layers lighter than this, there is a northward export in the Atlantic and Indian Oceans, and a southward flux in the Pacific Ocean, dominated by the EAC transport into the Tasman Sea. There is a net southward transport of AAIW in the Indian Ocean, in contrast to the northward exports in the other basins. In all three basins, the boundary between northward and southward flow is below the IW layers, at around γ^n=27.60 kgm^{-3}.

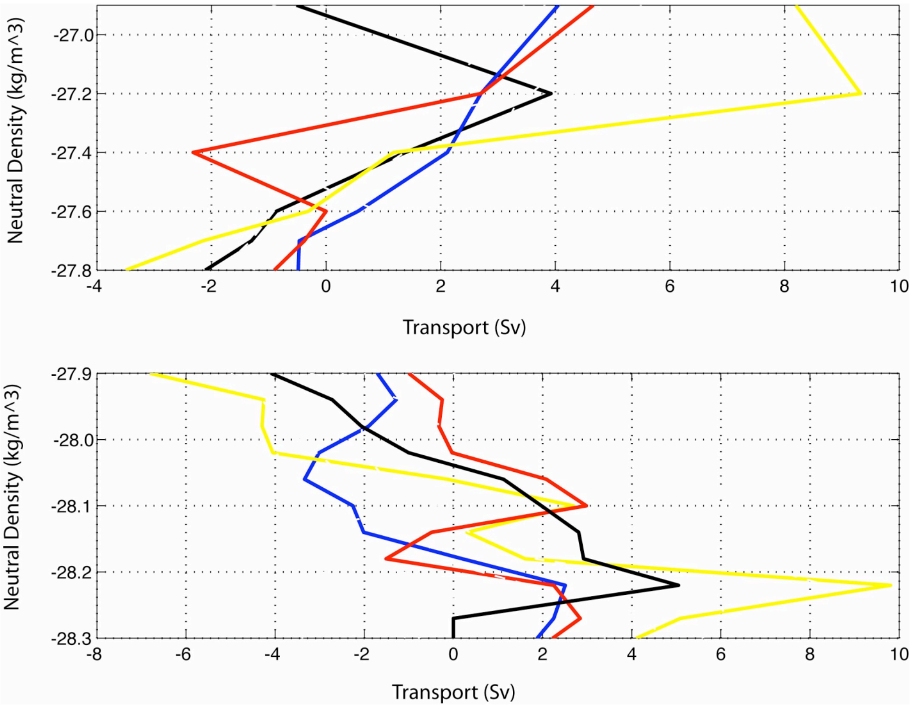

Figure 5.13: Model transports on density layers associated with the upper (top panel) and lower (bottom panel) across the 30 °S boundary. Yellow=total transport, blue= transport across A10 (Atlantic), red=transport across I05 (Indian), and black= transport across P6 (Pacific). Positive transports are northwards.

5.4.3 The Lower Cell

The lower cell involves the southward export of CDW/NADW that is modified within the Southern Ocean returning northward in the form of AABW. The cell is centred at γ^n=28.08 kgm^{-3}, which is just below the salinity maximum surface, with an overturning of 18.6±0.9 Sv. There is a northward export of AABW in all three sectors, with a total transport of 15.6 Sv in the bottom three layers (γ^n>28.18 kgm^{-3}) , dominated by the Pacific Ocean (8.0 Sv). The transport into the South Atlantic is 5.0 Sv, and into the Indian Ocean, the net flux is 2.6 Sv. In this case, the ACCbw is included in the northward flux calculations because the water mass that spreads northward across the boundary is not the same as the AABW found around the continent, but includes components of the densest UCDW and AACbw. This overturning is considerably smaller than the Sloyan and Rintoul (2000a) solution, that has a total transport of 25 Sv (6 Sv in the Atlantic Ocean, 10 Sv from the Indian Ocean and 8 Sv from the Pacific Ocean) below γ^n=28.20 kgm^{-3}. The main difference is the bottom water flux into the Indian Ocean that can be explained by the use of a silicate constraint in this study that significantly modifies the flow circulation and reduces the magnitude of the deep overturning in this basin. Lumpkin and Speer (2007) obtain an overturning across 30 °S of 20.9±6.7, which is, within errors, in good agreement with this solution.

The lower panel of figure 5.13 shows the density layer transport across 30 °S in the deep water layers. The transport structure in the three basins is very different to the mean picture. In the Indian Ocean, there is no large-scale structure to the deep water transport with north and southward fluxes in the AABW and ACCbw. This is due to the complex topography across the I05 section with the ACCbw transport confined to the western basins. In general, the transport in densities greater than γ^n= 28.18 kgm^{-3} is northward, with the 15.6 Sv total transport fairly evenly distributed. In the UCDW, the balance fluxes is very different between the basins. The transport is predominantly northward in the Pacific and Indian Oceans between γ^n= 28.00-28.18 kgm^{-3}, with a compensating southward flux in the Atlantic Ocean. There are two northward peaks in the total flux centred around the density surfaces at γ^n= 28.10 kgm^{-3}, associated with the LCDW salinity maximum layer, and γ^n= 28.24 kgm^{-3} containing modified AABW.

In the UCDW, all of the transport is southward, in keeping with the schematic pictures of the ACC, with a large southward flux of CDW flowing into the two meridional circulation cells. In the standard solution, the largest southward transport is between the γ^n= 27.70-28.08 kgm^{-3}, which is above the LCDW salinity maximum layer. There is only a small net transport in the density layers below the LCDW salinity maximum layer, which contains some of the oldest water in the Southern Ocean (e.g. Orsi et al. 1999). This suggests that a large part of the CDW that enters the Southern Ocean returns in the upper cell, outcropping around the ACC and being modified in the mixed layer. The denser LCDW remains in the Southern Ocean where it is gradually mixes with the fresh AABW entering from the south or shoals in the waters to the south of the ACC. The balance of freshwater fluxes and the buoyancy forcing driving the upper and lower cells will be discussed in detail in chapter 7.

5.5 Summary

This chapter has described the flow structure of the model solution with relation to the major water masses of the Southern Ocean, outlining the transformations and dianeutral transports in these waters. The internal dianeutral transports dominate the dianeutral mixing in the denser waters, and the balance of the air-sea buoyancy forcing and internal mixing will be examined in chapter 7. Although these components play an important role in the changes of water mass properties around the Southern Ocean, the lateral fluxes and isoneutral mixing have the dominant role in causing the observed changes in the properties of the U/LCDW. Large dianeutral fluxes are only found in localised regions (South Atlantic, Southwest Indian and Pacific Oceans), and are in regions where there are large property differences on isoneutral surfaces or large fluxes of sub-tropical deep waters.

The zonal mean picture of the overturning circulation masks the differences between the ocean basins. There is a northward export of Intermediate water in all three oceans, but this occurs on different density layers. IW in the Indian Ocean is on a lighter density layer, so at densities associated with AAIW (γ^n= 27.4-27.6 kgm^{-3}) that is exported into the Atlantic and Pacific Oceans, the flux is actually southward, with a northward flux in the lighter layers. This feature can be lost when the IWs are classed in broad density classes that treat the SAMW and AAIW together. In the LCDW, there is an asymmetry in the meridional fluxes into the ocean basins across 30 °S. The southward flux of NADW in the South Atlantic is balanced by a northward transport is corresponding density layers in the other basins. It is also important to note that within each basin there are large gyre circulations, so although the net transports are relatively small, the fluxes are of a size comparable to the ACC to the south. In the Indian Ocean, the Aguhlas current of 72±2.7 Sv is balanced by the northward sub-tropical gyre circulation across the rest of the basin.

The next chapter will examine the stability of the model by examining the effect of changing the hydrographic section data by utilising the SR01b repeat sections. There are a number of different mixing schemes that are favoured in the literature, so the model solutions are examined with different parameterisations for the internal dianeutral mixing.

Chapter 6: Variations to the Standard Inverse Model

6.1 Mixing Schemes

The standard model incorporates dianeutral fluxes in the form of an advective flux and an effective diffusivity component. There are a number of other mixing schemes that are generally adopted to model these additional fluxes and two of these representations are examined with adapted versions of the standard model.

6.1.1 Tracer-dependent effective diffusivities

In the standard model, it is assumed that the same effective diffusivity coefficient can be used for each of the tracers conserved on layers within the box model. A series of model experiments were conducted where this assumption is removed, and additional unknowns are added representing property-specific effective diffusivity coefficients. In the case of the standard model, this equates to separate coefficients for the heat and salt conservation equations (k_H, k_S). Within the LCDW, the salinity signal of the NADW causes an inversion in the salinity gradient, so it is interesting to examine the effect of this on the resulting diffusivities, and any differences between coefficients for salt and heat. Figure 6.1 shows the separate solutions for the salt and heat equations, compared with the diffusivity from the standard model. The magnitude of diffusivities is similar in each case with localised differences between the solutions. In all cases, the a-posteriori error is similar in scale to the model solutions. The structure from the strain based eddy diffusivities derived from the WOCE data set, described in chapter 3, is not found in any of the model solutions where diffusivity is explicitly defined in the model. To determine whether this was due to the use of a constant error constraint on all layers, the effects of the imposition of a structured error field derived from the strain eddy diffusivities was studied. In this case, the model solutions did not differ from the standard model above the errors. In all of these model runs, the a -posteriori errors are the same as, or greater than the solutions. The large error bounds relative to the solutions mean that is not possible to make any definite statements on the detailed structure of the diffusivities. In general, the diffusivities appear to decrease with depth/density, with the lowest values found in the deepest layers.

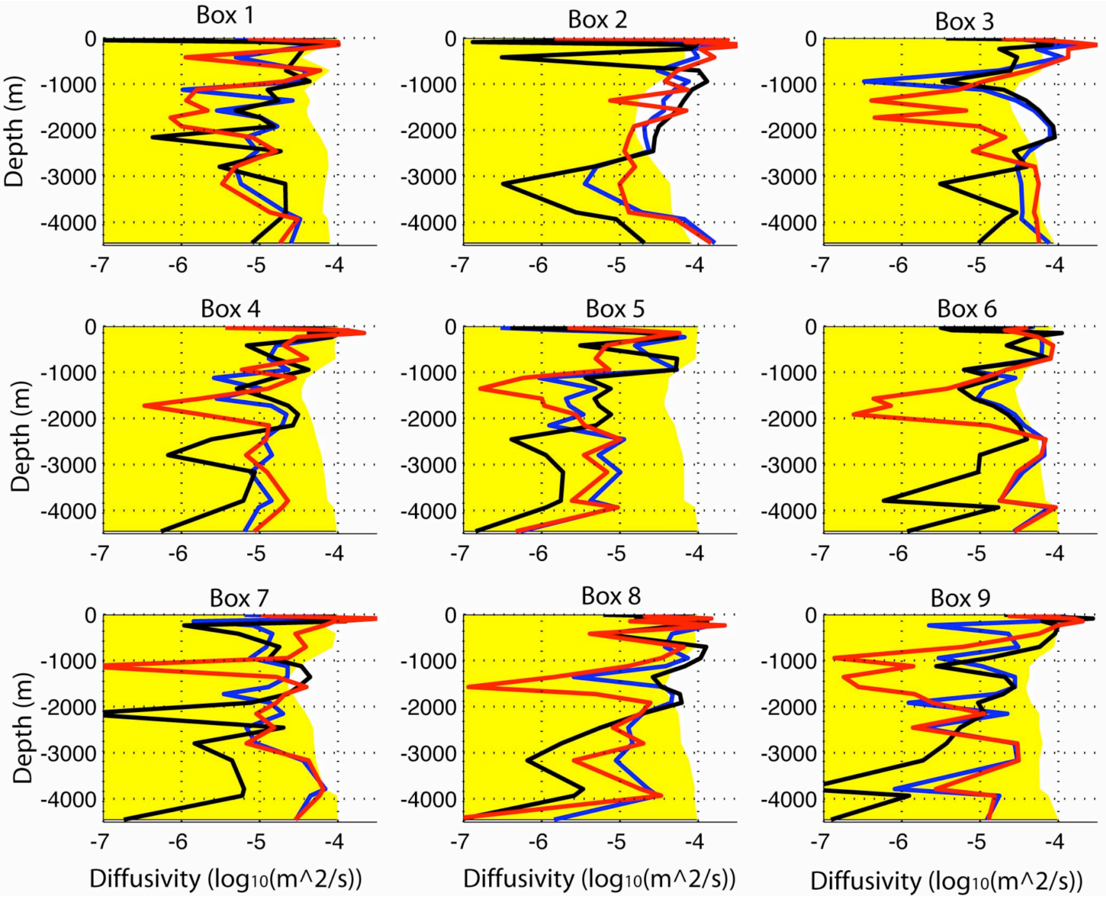

Figure 6.1: Effective diffusivities from the standard model run (blue), and from the model run with property-specific diffusivity coefficients, salt (black) and heat (red). It is plotted on a representative depth co-ordinate, but the flux is across constant neutral density surfaces. The yellow region shows the a-posteriori errors from the standard model solution.

Table 6.1 shows a comparison of the fluxes across major sections in the Southern Ocean in the three model configurations. The additional freedom in the solution afforded by the property-specific diffusivities acts to improve the flux balance from that of the standard solution. The mass transport across the Indian Ocean section at I05 is increased to -9.5 Sv, resulting in a better flux balance into the Southern Ocean. The southward temperature transport is also increased to -1.075 PW, due to the increase in surface/intermediate water transport in the Agulhas current region. The balance of AAIW/SAMW and UCDW is adjusted, with a smaller net northward flow between γ^n=26.8-27.5 kgm^{-3}. The deep overturning in the Indian Ocean increases to 9.4 Sv with a small increase in the northward transport of the ACCbw. The additional solution flexibility due to the uncoupling of the salt and heat diffusion across neutral density surfaces has the greatest effect in boxes 3 and 4, where the balance of the intermediate/surface water circulation is modified, resulting in a more balanced solution, but the additional unknowns do not add any additional insight into the structure of the diffusivity in these layers due to the model noise and errors. In the other sections the changes are much smaller, with a slight decrease (~1.5 Sv) in the NADW entering the Southern Ocean and a negligible change in the overturning in the Pacific Ocean, which are identical within the bounds of model errors.

In the standard model solution, dianeutral fluxes of silicate were not solved for as they did not appear to significantly change the model solution whilst increasing the number of unknowns (and the uncertainty of the solution). Silicate was still included as a constraint mass constraint across the whole water column where it played an importnat part in setting the overall circulation, especially in the Indian Ocean.

Model / Section	**Standard Model**		**Tracer Diffusivities**		**Advective velocities**	
	Mass (1×10^9kgs^{-1})	**Heat (PW)**	**Mass (1×10^9kgs^{-1})**	**Heat (PW)**	**Mass (1×10^9kgs^{-1})**	**Heat (PW)**
A10	-0.6	0.138	-0.6	0.134	-0.4	0.116
I05	-7.3	-0.983	-9.5	-1.075	-11.9	-1.269
P6	12.9	0.197	9.4	0.218	10.7	0.141
A11	-0.7	0.307	-0.8	0.293	-0.8	0.339
SR1b	141.6	1.328	143.9	1.340	140.4	1.327
I06	139.6	1.047	140.3	0.986	136.4	0.873
SR3	150.9	1.798	149.5	1.808	152.0	1.813

Table 6.1. A summary of the fluxes across major sections around the Southern Ocean from the main model runs. The errors are not shown, but due to the method of error

definition, the a-posteriori error ranges are all similar to the errors from the standard solution.

6.1.2 Property-specific advective fluxes

A commonly adopted methodology (e.g. Sloyan and Rintoul (2001b), Lumpkin and Speer (2007)) is to solve for a single independent dianeutral velocity component for each tracer in the model at each surface interface (w_ρ*, w_S* and w_H*). This can then be used to calculate a measure of the effective diffusion by removing the purely advective component obtained from the solution for the dianeutral mass velocities (w_ρ*). The results can then be used to derive a representative effective diffusivity by assuming that the difference between the mass velocity and the tracer velocity is due to the non-advective processes contained in the effective diffusivity approximation. This results in an equation for k:

$$k_S = \frac{(w_s - w_\rho)\rho S}{\partial(\rho S)/\partial z} \tag{6.1}$$

S is either heat or salt anomaly values and the gradients are derived from the WOCE climatology sub-set for the model domain averaged over boxes.

The heat and mass fluxes across the major sections in the model are given in table 6.1. The major change is the adjustment to the flow pattern in the Indian Ocean, where the transport is increased to -11.9 Sv. This adjustment improves the flux balance across the northern boundary of the model, with similar corrections to the previous model set-up described in chapter 6.1.1. It appears that the de-coupling of the heat and salt dianeutral transports allows the model to obtain a solution in the Indian Ocean that is more consistent with the constraints placed on it.

Figure 6.2 shows the three velocity components from this model run. In general, the velocity structures are similar, within the error bounds of the model. In boxes 2 and 3, there are large-scale features in the salinity transport centred on the UCDW. There is a large convergence in the advective salt flux into this layer in the Atlantic box 2. This pattern is reversed in the Indian Ocean box 3, where there is a divergence in the salt flux in this layer into the lighter and denser layers. This feature is not detected in the mass or heat advective fluxes. This implies that in box 2 there is a deficit in salt content on this layer that the model is compensating for by increasing the dianeutral flux of salt into that layer. In box 3, the situation is reversed, with a surplus amount of salt that must be compensated by a net flux of salt out of the layer. This could imply that the model solution is moving too much salt across section I06 between the two boxes within this layer, forcing the observed structure in the dianeutral salt flux. Figure 6.3 shows the mean velocities for the whole of the model domain. Apart from the feature in the salt flux in the UCDW, the mean mass and salt velocities are similar throughout the water column. The heat velocities have a different structure, with larger positive fluxes in the AAIW/UCDW, and lower/negative fluxes in the AACbw/AABW. In this water mass, this is compatible with the downward diffusion of heat, from the warmer, lighter waters, and the overall upward mixing of the AABW into the ACCbw and the bottom of the LCDW that is represented by the upward fluxes from the mass and salt equations.

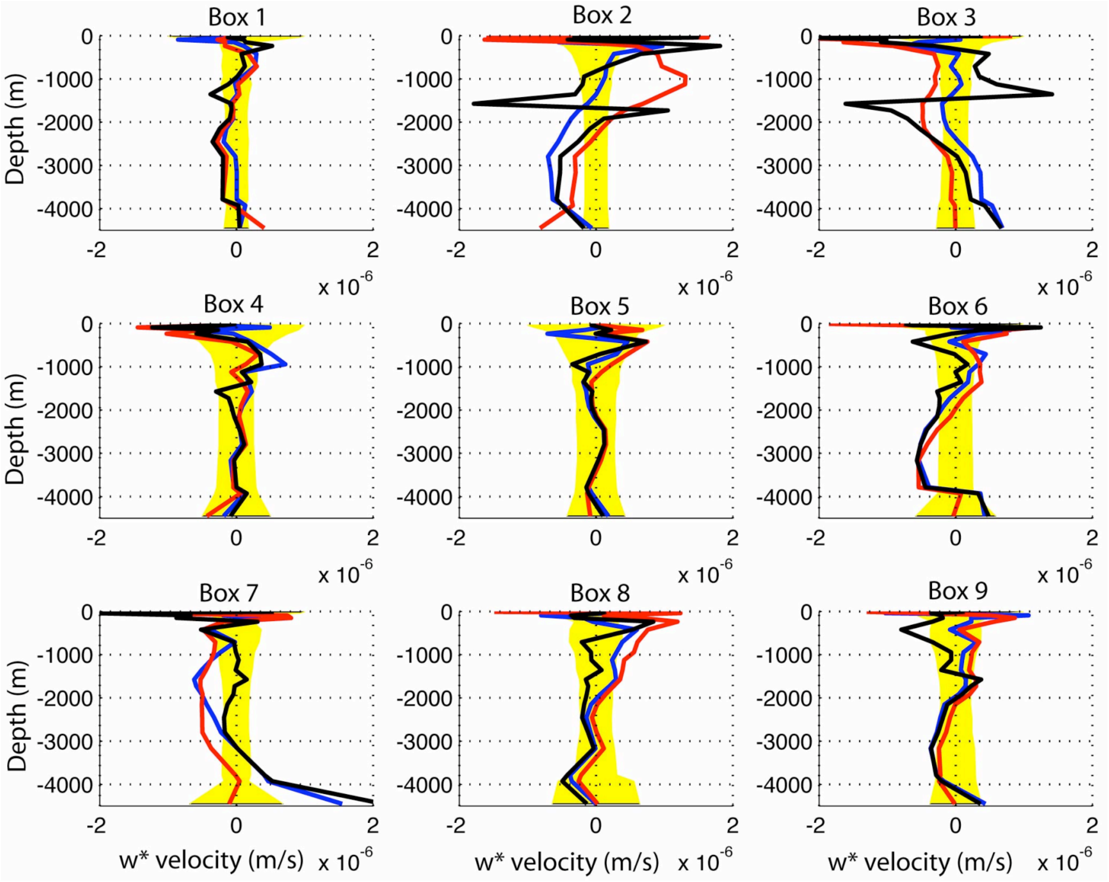

Figure 6.2: Dianeutral velocities from model run with property-specific advective velocities. Mass (blue), salt (black), and heat (red). The a-posteriori errors are shown by the yellow region.

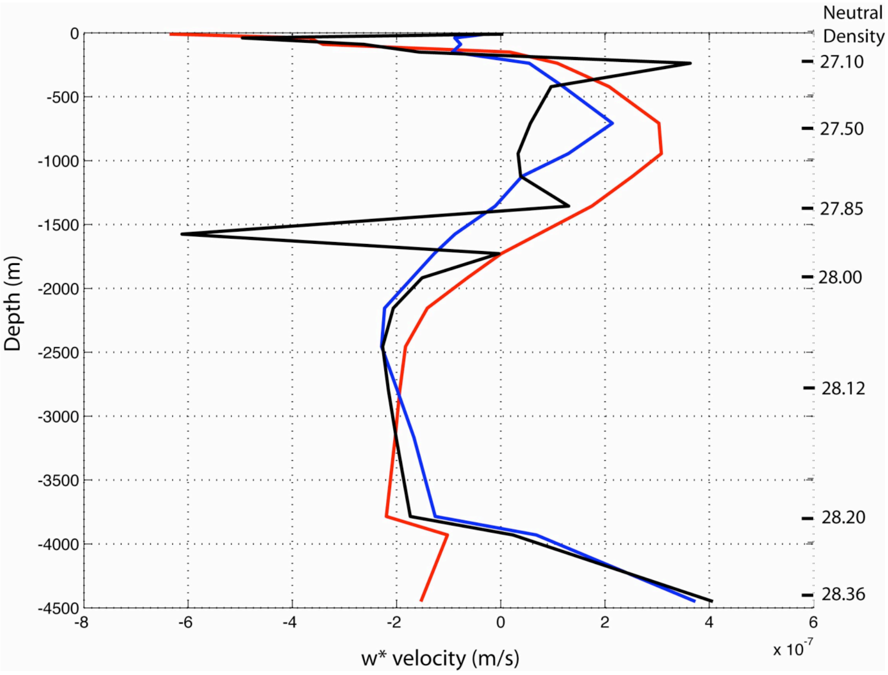

Figure 6.3: Dianeutral tracer-specific velocities, mass (blue), salt anomaly (black) and heat (red) (all ms^{-1}). Velocities are plotted on a representative depth scale, and are velocities on neutral density surfaces.

Representative effective diffusivity coefficients were calculated for each box using equation 6.1. The diffusivities are shown in figure 6.4 and the mean eddy diffusivities from the strain-based calculations are also shown. The magnitudes of the diffusivities in the standard model are all orders of magnitude less than the strain-based diffusivities. Figure 6.4 shows that the representative diffusivities from this model set-up have similar magnitudes and structures to that of the strain-based measurements. Importantly, they also show the same increase in magnitude with depth that is a major feature of the strain-based estimates. This feature is partially caused by the inclusion of a background gradient field that already as this structure, with smaller gradients in the deeper waters, leading to higher diffusivities if the differences between w_S and w_ρ are similar throughout the water column. This does not account for the higher values near the surface that are in rough agreement with the strain-based estimates. This is a very interesting result, given the use of two very different methods in determining a diffusivity coefficient, based on different physical processes. Caution must be taken in making any direct comparisons because the eddy diffusivity calculations contain all diabatic processes, which includes the advective dianeutral fluxes and effective diffusive fluxes used in the standard model. The representative diffusive fluxes were also calculated using a modified equation to 6.1, where the advective mass flux was not subtracted. This new estimate includes all dianeutral terms, which is strictly a more accurate variable to use to make comparisons with the eddy diffusive terms. The adjusted representative fluxes are similar in magnitude to the salt and heat fluxes plotted in figure 6.4, but are not shown for reasons of clarity only.

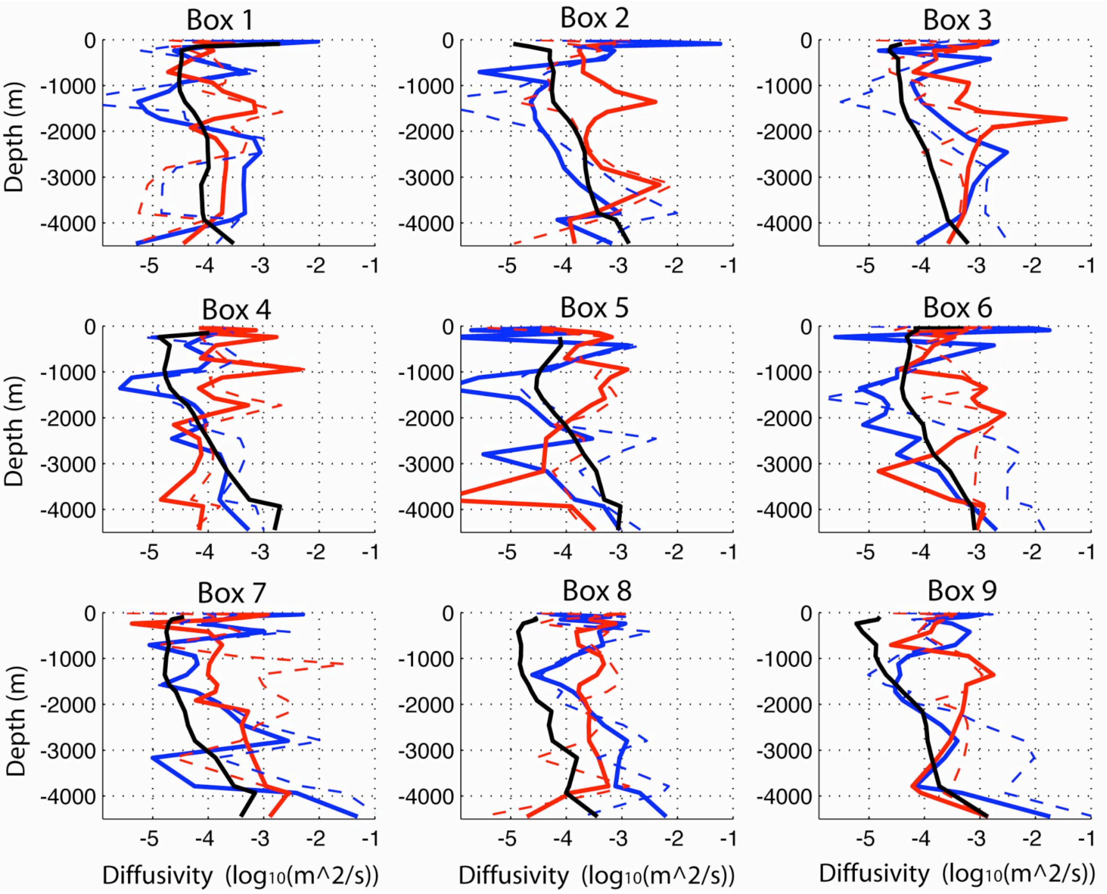

Figure 6.4: Representative Effective diffusivity coefficients calculated from the model run with property-specific dianeutral velocities from the salt velocity (blue), the heat velocity (red). The mean strain-derived eddy diffusivities from the WOCE data set (see chapter 3.5.1) are shown (black line).

6.1.3 Evaluation of the three mixing schemes

The three model set-ups result in similar fluxes across the major sections within the model. The uncoupling of the heat and salt dianeutral terms results in a larger southward mass and heat transport in the Indian Ocean that is more consistent with the flow out of the Southern Ocean through the Pacific Ocean. The diffusivities from the standard model and tracer-specific diffusivity model are not well resolved over the model error. Despite a relatively large a-priori error for the diffusivity components, the model solutions are all smaller than $1\text{x}10^{-4}$ m^2s^{-1} and they generally have no large-scale vertical structure, or decrease with depth. When diffusivities are calculated from the tracer-specific velocity model, they exhibit a structure that is broadly similar to the strain-based eddy diffusivity estimates. This poses an interesting question on the most suitable representation of dianeutral processes in inverse models of the Southern Ocean. The effective diffusive term includes all of the non-advective components of the dianeutral flux, so the Fickian representation of this transport is neglecting all of the other processes involved in transporting tracer properties across isoneutral surfaces. In all of the model runs using an effective diffusive term, the total dianeutral fluxes were dominated by the advective terms, with only a small contribution due to the diffusive terms. This was not due to the initial a-priori error fields, as this feature was found over a range of model runs covering a wide range of error boundaries.

Figure 6.5 shows the mean advective velocity from each model set-up. The models with explicit diffusion terms have very similar velocity structures. Starting from the sea floor, there is a positive flux from the AABW into the ACCbw and deep LCDW. Further up in the water column, there is a mass divergence away from the LCDW, centred on densities associated with the NADW salinity maximum signal. The dianeutral fluxes transport mass into the layers above and below this layer. The upward flux continues through the UCDW, with a maxima in-between the UCDW and AAIW, which then declines as the surface is approached. Close to the surface, there are high downward velocities, but caution should be taken in inferring too much from this observation due to the uncertainties associated with the surface waters and the imposed balance with the atmospheric fluxes. In all model runs there is a similar transport of bottom water in the densest layers, and throughout the LCDW, the transport is downward. The dianeutral flow reverses direction in the centre of the UCDW (γ^n~27.9 kgm^{-3}), with a mass divergence in this water mass into the AAIW above and the LCDW below. There are only marginal differences between the three mixing schemes, which are not significant over the a-posteriori errors. For this reason, the standard model set-up was chosen are a fair representation of the Inverse model and was used to describe the more detailed flow structures and fluxes throughout the model domain.

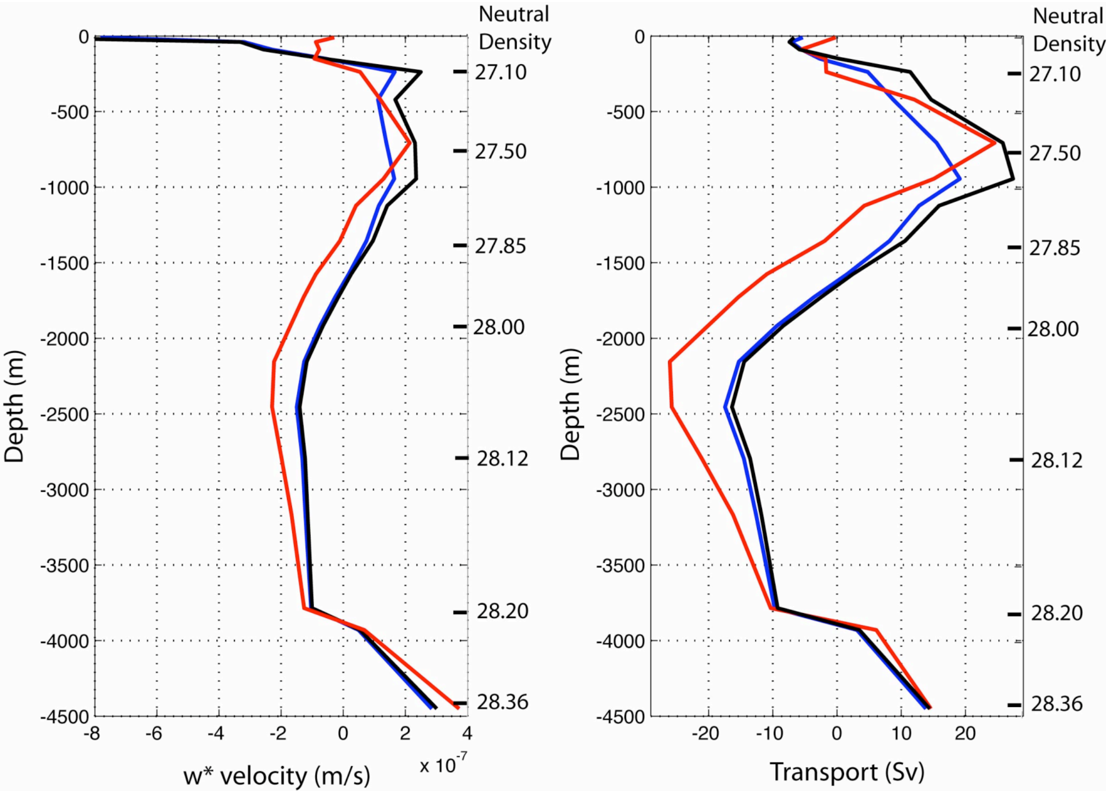

Figure 6.5: (Left) Dianeutral velocities from the standard model (blue), tracer-specific diffusivity coefficients (black) and tracer-specific advective velocities (red). (Right) total volume transports from the same model runs.

6.1.4 Intense Deep Interior Mixing

The study of the mean strain-based eddy diffusivity estimates throughout the model domain suggests that there is a vertical structure to the diffusivity that should be accounted for in the model design. The standard model uses a depth independent weighting for the dianeutral velocities and diffusivity coefficients, in a similar way to other inverse studies (e.g. MK2005, Sloyan and Rintoul 2000a). Model runs were examined with a depth-dependent a-priori vertical velocity error structure, based on the mean eddy diffusivity estimates. These estimates can only be applied in the a-priori errors because the eddy diffusivity estimates only provide an estimate of the mixing strength and not on the direction of the flow. Starting the model with vertical velocities different from zero, reflecting the expected magnitudes of the solution velocities may create unrealistic solutions because there is no information about the direction of the assumed flux.

A number of model runs were conducted with density dependent a-priori vertical velocity uncertainties, designed to model the variability in the eddy diffusivities. In all cases the model solutions were not sensitive to these changes, resulting in dianeutral fluxes that were not significantly different from the standard model solution. Applying error bars ranging from $5x10^{-7}$-$2.5x10^{-6}$ ms^{-1} did not change the structure of the solution, or of the a-posteriori errors, that decreased with density, as with the standard model. Reducing the constraints only resulted in unacceptable transports across the northern boundary of the model so were disregarded.

6.2 The 2002/3 30°S Northern Boundary

A recent re-occupation of the 30° S sections across the Atlantic, Pacific and Indian Oceans (Fukasawa and Watanabe (2003), Yoshikawa (2003), Bryden (2002)) provides an opportunity to examine the effect of a new northern boundary to the model. It is assumed that sections from 2002/3 are still representative of the mean state of the Southern Ocean during the WOCE period (1990-1996) and can be consistently combined with the WOCE sections, and that any trends over this period are within the scales of variability over the WOCE period. This can be partially confirmed by an examination of the SR01b repeat data-set that spans this whole period and there have been no significant property or transport trends detected at Drake Passage.

The sections across the Atlantic and Pacific Oceans follow similar paths to the original sections used in this study. The Indian Ocean section takes a different path towards the east of the section, moving southward into the South Australian Basin and avoiding the Broken Plateau. The examination of the OCCAM model provided some insight into the variability in the transports between these ocean basins. The flux through the Atlantic Ocean into the Southern Ocean is fairly well constrained, but uncertainty and variability of the ITF result in a high uncertainty in the flux balance between the Indian and Pacific Oceans. In this study, the constraints for all of the sectors will remain the same, with only minor adjustments to reflect the differences between the WOCE and 2002/3 sections.

In the Atlantic, the A10 repeat section is broadly similar in structure to the WOCE section. There is a large eddy feature in the region of the Cape and Angola basins (see chapter 4). This eddy is kept in the model run, as its removal did not significantly alter the mass and heat fluxes across this section within the bounds of the solution error. The structure of the transport is adjusted, with an increase of 3 Sv in the NADW entering the Southern Ocean. This additional transport is not found in the A11 section to the south where the solutions for both models have similar transports on density surfaces. The additional inflow is dispersed in the model errors and in the form of increased dianeutral fluxes.

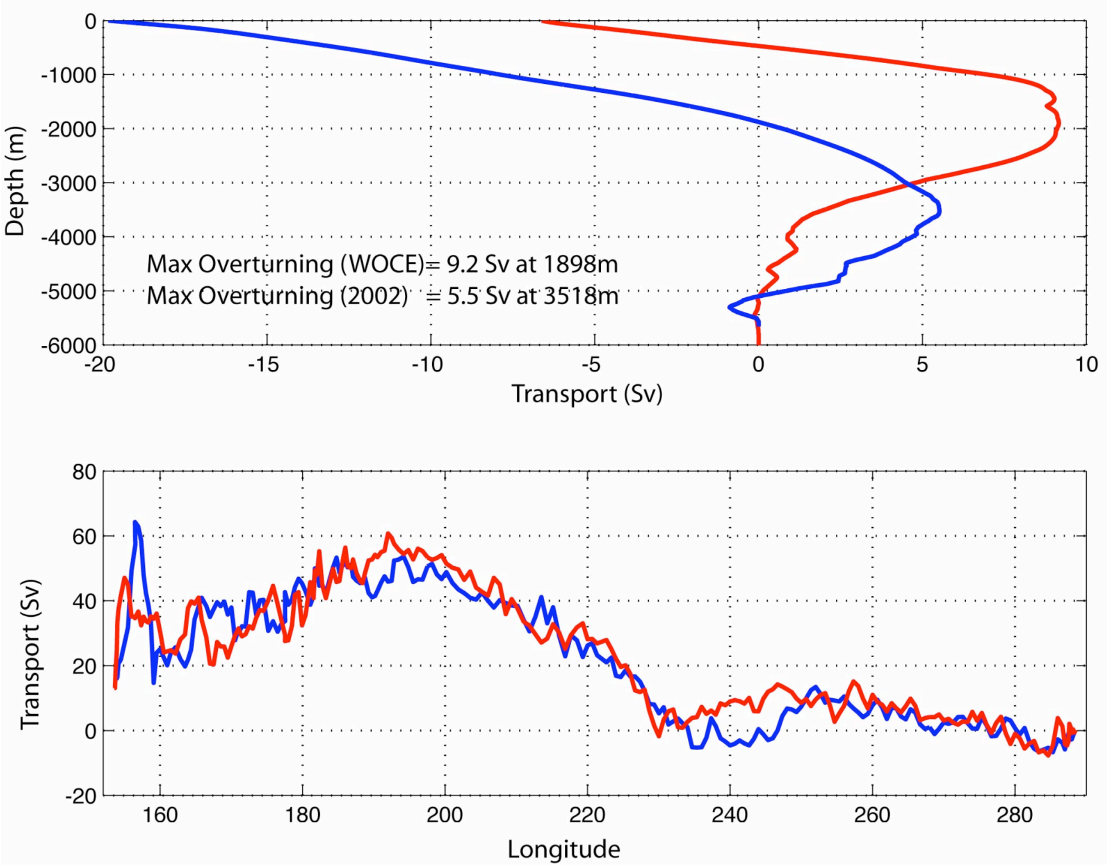

Figure 6.6: Top: Meridional overturning integrated from depth across the I05 Indian Ocean section (WOCE (red), 2002 (blue)). The magnitude and location of the deep overturning maximum is noted. Bottom: Cumulative transport along the P6 Pacific section (WOCE (red), 2003 (blue)), from west to east.

The top segment of figure 6.6 shows the depth integrated meridional overturning from the WOCE and 2002 sections. The two sections have significantly different fluxes in the gyre recirculation to the west of the Agulhas current. There is a large difference in the structure and magnitude of the fluxes on density surfaces between the two sections. McDonagh et al. (2006) used inverse methods to combine LADCP velocities with the data to obtain a picture of the transport from the 2002 section. They found a deep overturning of 10.0 Sv at 3310m (ADCP referenced solution), which is larger than our estimate, but at a similar depth. The overturning from the WOCE section is of a similar magnitude but is located much higher in the water column and therefore is centred on a different density layer. The overturning of 5.5 Sv obtained in our solution is lower than other estimates and could be a feature of incompatible hydrographic sections, especially at the northern interface of model boxes 3 and 4. The total Indian Ocean sector transport of -19.8 Sv is at the top end of the error limits and does not balance with the transport 0f 13.5 Sv northward into the Pacific Ocean.

The bottom panel of figure 6.6 shows the cumulative transport across the Pacific P6 section from the WOCE and 2003 transects. The large-scale features of the mean circulation appear to be consistent between the two sections. The heat transports of 0.197±0.098 PW and 0.174±0.098 PW from the WOCE and 2003 sections respectively are in strong agreement. The results from the Pacific sector could be similar due to the dominance of the meridional sections on the solution. With four boxes in this sector, any changes in the initial state of the northern boundary may be compensated for by very small changes in the adjoining sections, without altering the large-scale features of the solution.

The 2002/3 solution was in broad agreement with the standard model, except for the modified Indian Ocean transport. The large differences between the two transects highlights the difficulties in obtaining estimates of overturning circulations from single hydrographic sections. Figure 6.7 shows the overturning transports at 30°S in the Atlantic and Pacific Oceans in the WOCE and 2002/2003 sections. They are both similar in structure, with the largest difference occurring in the Pacific Ocean, where the overturning strength of the lower cell is reduced, from 15 Sv to 10 Sv between the two sections. The cell centred on the intermediate water is also reduced by up to 50%, but this result is less significant due to larger uncertainty in the lighter waters. A greater number of repeat observations are useful in improving estimates of the stability of the mean circulation patterns obtained in an inverse solution. The next section examines the effect of a larger data set of co-located repeat transects.

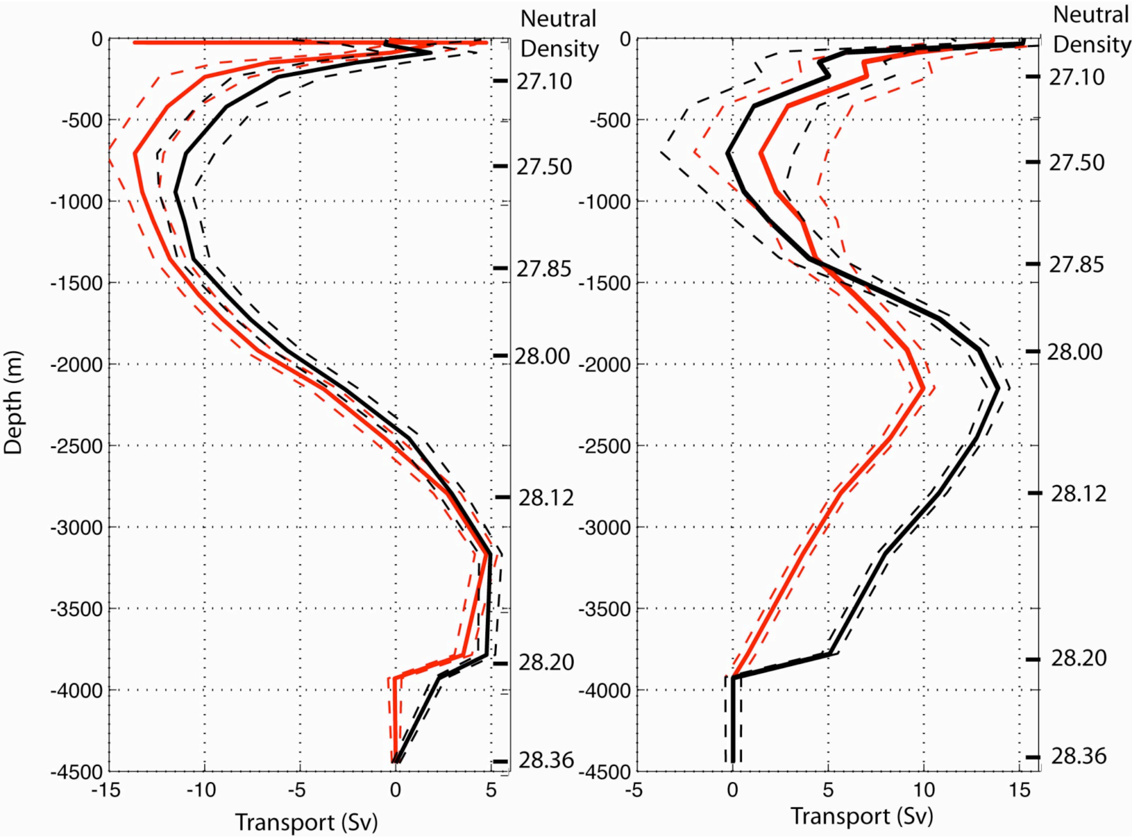

Figure 6.7: A comparison of the overturning streamfunctions across the Atlantic (left) and Pacific Oceans (right panel) at 30 °S using the WOCE data (black line) and the 2002/2003 sections (red line). The dashed lines represent error limits calculated from the a-posteriori error matrix.

6.3 Solution Stability at Drake Passage

A key test on the stability of the inverse model is to examine the variability of the solutions when the hydrographic sections are changed. This kind of study is only possible at SR01b and SR03 where there is a sub-set of repeat measurements. Sloyan and Rintoul (2000) used the six WOCE SR03 sections to test the variability of their model solutions and found that it had little effect on the large-scale solution. Unfortunately, only the 1997 SR01b section contains silicate measurements so in this study, the inverse model was adapted to conserve mass, salt and heat fluxes only.

In a modified model configuration, boxes 1-2, 3-4, and 5-6-7-8 from the standard set-up (figure 3.3) were combined to create sector-scale boxes. The mass, heat and salt fields from the 11 SR1b repeat sections between 1993-2006 were substituted into the model to obtain 11 model runs. All of the model constraints were kept constant, with the same flux constraint on the Drake Passage transport. The mean transport at Drake Passage from the 11 model runs was 135.0±3.3 Sv, compared to the mean from the data set (1993-2006) of 135.6±6.7 Sv. The mean heat and salt transports was 1.230±0.098 PW and 480.0±11.5 Ggs^{-1}. The standard model solution is within the errors of the Drake Passage model mean, and the transport variability is significantly reduced. Figure 6.8 shows the variability of the volume and heat transports in density surfaces compared with the observed variability from the data set. The variability in the volume transport in the model is similar to that obtained from the data. The one region with any discrepancy is in the Intermediate water region. This is partly due to the resolution of the model layers in the intermediate waters. At Drake Passage, the structure of the variability in this density band is not resolved properly by the Inverse model. Unfortunately, this is unavoidable, without biasing this density layer throughout the rest of the model domain. The variability in the heat transport in density layers is reduced in the model simulation, but a peak in the heat transport located at the top of the SAMW (γ^n~27.2 kgm^{-3}) is not replicated in the model transports or variability.

Changing the Drake Passage transport had only a small effect on the fluxes at major sections in the model. The volume/heat flux variability at P6 in the Pacific sector was 0.9 Sv/0.046 PW. At A10, it was 0.04 Sv/0.032 PW, and at I05 in the Indian Ocean it was 0.4 Sv/0.093 PW. These values are all much smaller than the model error bounds obtained from the standard model solution (see figure 4.9 a/b). This study shows that the model solution at Drake Passage is very stable, and that the choice of section has little effect on the fluxes obtained at other locations around the model domain.

In all of the other large-scale inverse studies, Drake Passage was represented by the SR01 section (Roether, 1993) from the WOCE period. This section has a westerly location, compared to SR01b, along the western edge of the Scotia Sea (see chapter 2 for details). The transect has a geostrophic velocity of 126 Sv, which is at the low end of the range from the historical record. This is in contrast to the 1997 SR1b section used in the standard model, with a geostrophic transport of 145 Sv, which is at the top end of the measured range of transports from observations. A consequence of this is that if the model is constrained to achieve a Drake Passage within the estimates of the mean flow

(135.6±6.7Sv calculated from the SR1b repeat sections), then the barotropic corrections are either increasing or reducing the total flow for each model respectively.

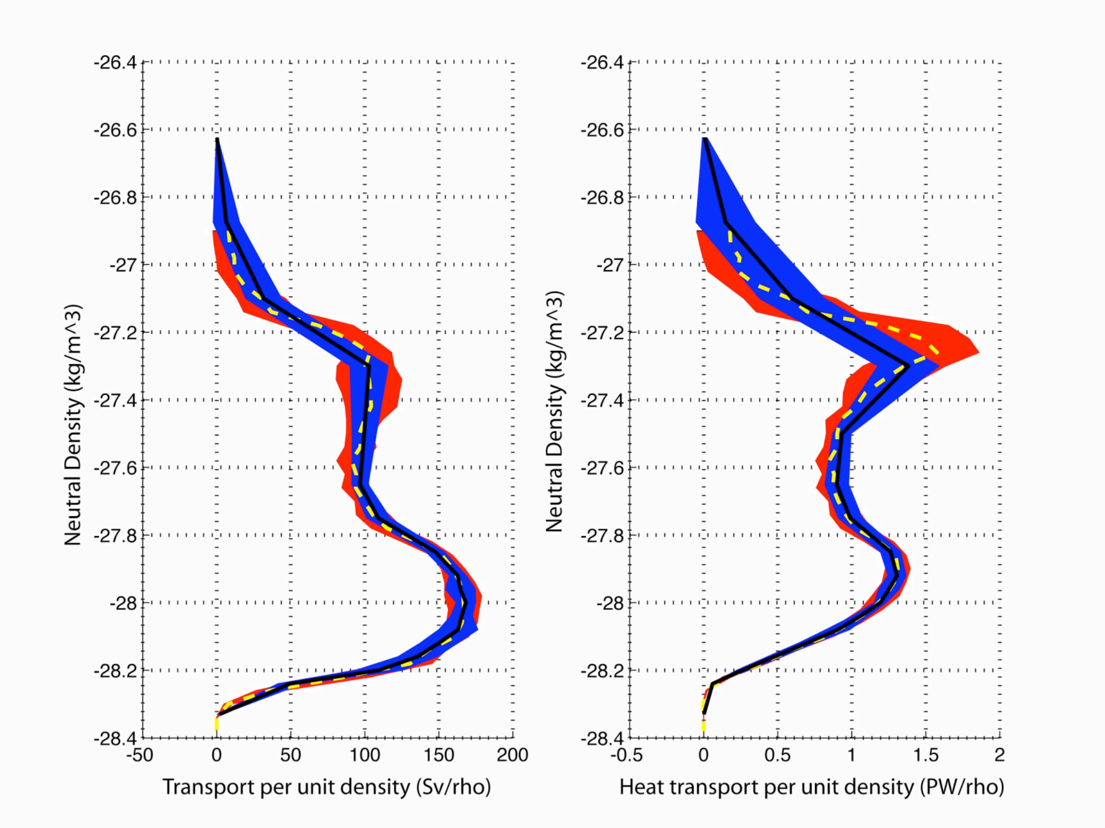

Figure 6.8: Mean volume/heat transport across Drake Passage: Mean ± 1 standard deviation from SR1b hydrographic data (red region); Model solutions using SR1b data (1993-2006) (blue region). The model mean transport is shown by the black line and the mean of the data is shown by the dashed yellow line.

The size of the variability at Drake Passage does not make it possible to make any statements about the bottom flow structure, because any apparent corrections are dominated by the model constraints adjusting the flow towards the mean/constrained total transport. The standard model solution adjusts the SR01 section, resulting in a transport of 139.3 Sv, and a temperature transport of 1.49 PW. The largest difference between the two solutions is the implied temperature transport between the two sections. The inclusion of this section has a negligible effect on the other fluxes around the model, with surrounding fluxes remaining constant well within the model error boundaries.

6.4 Summary

This chapter has demonstrated the stability of the standard model solution under a number of different conditions. This suggests that the model results are fairly robust under a range of conditions. The analysis of the different mixing schemes showed that they produced similar dianeutral vertical velocities, which dominated the effective diffusive terms. The inclusion of tracer-specific velocities created larger departures from the advective vertical mass velocity than in the case with effective diffusivities. The relative strengths and weaknesses of the different mixing schemes requires further investigation within the model over a range of a-priori error scales to determine which method produces the most realistic and balanced results.

The growing evidence suggesting the importance of intense deep turbulent mixing near steep topography requires further investigation within the model to see if it is possible to obtain a solution that exhibits a strong mixing signal in the deeper layers. The next chapter will focus on the three dimensional circulation around the Southern Ocean and examine the relative effects of buoyancy forcing and dianeutral mixing on the overturning circulation and water mass modification within the model.

Chapter 7. Water mass transformation and modification

The solutions to the inverse model provide a tool to examine the detailed circulation patterns and water mass transformation that occur in the Southern Ocean. In this chapter, the buoyancy forcing and the effect of internal dianeutral mixing on the overturning circulation will be discussed. Finally, the three-dimensional circulation of the Southern Ocean will be explored, focussing on the modification of the LCDW salinity maximum surface from its origins in the NADW to the salinity structure observed at Drake Passage.

7.1 Water mass transformation around the ACC

7.1.1 Freshwater fluxes in the Antarctic Zone

The buoyancy fluxes used in the standard model set-up were described in section 4.4. The heat flux dominated the freshwater flux throughout the model domain, but the climatological fluxes have large error bars in the Southern Ocean that increase towards Antarctica. In the overturning picture of the Southern Ocean, the westward wind-stress that drives the ACC creates a northward Ekman flux. If the assumption is made that the Intermediate water has its origin in the AASW that is subducted north of the Polar front, then it is possible to obtain a qualitative picture of the buoyancy forcing on the surface layer before it is subducted into the ocean interior. Using the monthly mean fields from the World Ocean Atlas 2001 Climatology (Conkwrigh et al. 2001), and the mean frontal locations of the PF and SB from Orsi et al. (1995) it was possible to estimate the mean property changes between the SB and the PF in the surface layer. Mean salinity and temperature fields for the top 75 m were obtained from the climatology, and monthly mean salinities and temperatures along the paths of the mean PF and SB positions were calculated.

The monthly and annual mean properties are shown in figure 7.1. Throughout the year, there is very little difference between the mean temperatures at both fronts. The mean difference is 3.23 °C and is in good agreement with the mean difference of 3.20 °C (PF-SB) from a similar calculation made using the annual mean fields from the WOCE Climatology (Gouretski and Koltermann, 2004). There is a clear signal due to the sea-ice cycle in the monthly mean salinities at the southern boundary. From March (the beginning of the Antarctic Winter), the surface salinities begin to increase, and this trend continues until July where the salinity levels off at ~34.03-34.05 psu until October, where the salinity falls back to its lower levels. The salinification during the winter months is due to sea-ice formation that increases the salinity of the surface waters due to brine rejection. As the winter ends and the sea-ice begins to recede, the surface layer is then freshened due to the increased freshwater input from sea-ice melt (e.g. Bamber and Payne, 2004). In figure 7.1, this process is not symmetric throughout the year, with a long freezing period, and a quick freshening period due to the sea-ice melt. The salinity at the PF has a much smaller variability, with gradual increase in salinity from March until November, and then a steeper freshening gradient throughout the Antarctic summer. The mean salinity difference is 0.042 psu (SB-PF) and is larger than the equivalent value obtained from the annual mean fields from the WOCE climatology of 0.008 psu (SB-PF). The mean salinities at both fronts are very similar in the summer months (December-March), but change by up to 0.08 psu at the end of the winter in October when the sea ice begins to retreat.

Mean values of the thermal expansion coefficient, $\alpha=6.3\text{x}10^{-5}$, and haline contraction coefficient, $\beta=7.82\text{x}10^{-4}$, were calculated as an average between the values for the two fronts. Assuming a linear density relationship, $\Delta\rho = \rho_0(\beta\Delta S - \alpha\Delta T)$, (e.g. Houghton, 1990) it is possible to estimate the relative contribution to the buoyancy forcing that has modified the surface waters as they move north in the Ekman layer, before they are subducted at the PF. In this case, the ratio of haline (freshwater) and heat components in the overall buoyancy budget is $(\alpha\Delta T : \beta\Delta S)$ ~ 6.3:1. Approximately 85% of the buoyancy forcing is due to thermal forcing, with 15% due to freshwater fluxes in the region between the southern boundary. This is an interesting observation because it shows that although the thermal component is dominant north of the ACC, the haline component of the is not negligible in the southern part of the ACC. The residual mean studies of Karsten and Marshall (2002) assume that the buoyancy forcing that drives the upper meridional cell in the thermocline can be modelled by only including the thermal component. Bryden and Cunningham (2002) constructed a model of the stratification of the ACC in terms of the air-sea heat exchange and the eastward wind-stress, but restrict their model to the base of the Ekman layer due to uncertainties in the total buoyancy fluxes that they state are actually dominated by the freshwater fluxes in a way that is not fully understood. The simple schematic model outlined above only covers the Antarctic zone, and the freshwater forcing further south would be expected to be much larger due to the increased effect of the seasonal sea-ice cover. Estimates of the ice mass balance of Antarctica and the freshwater flux due to continental run-off are very uncertain and are dominated by error bars (e.g. Bamber and Payne, 2004), but they may play an important part of the freshwater component of the buoyancy forcing and the overturning circulation and water mass transformation in the Southern Ocean.

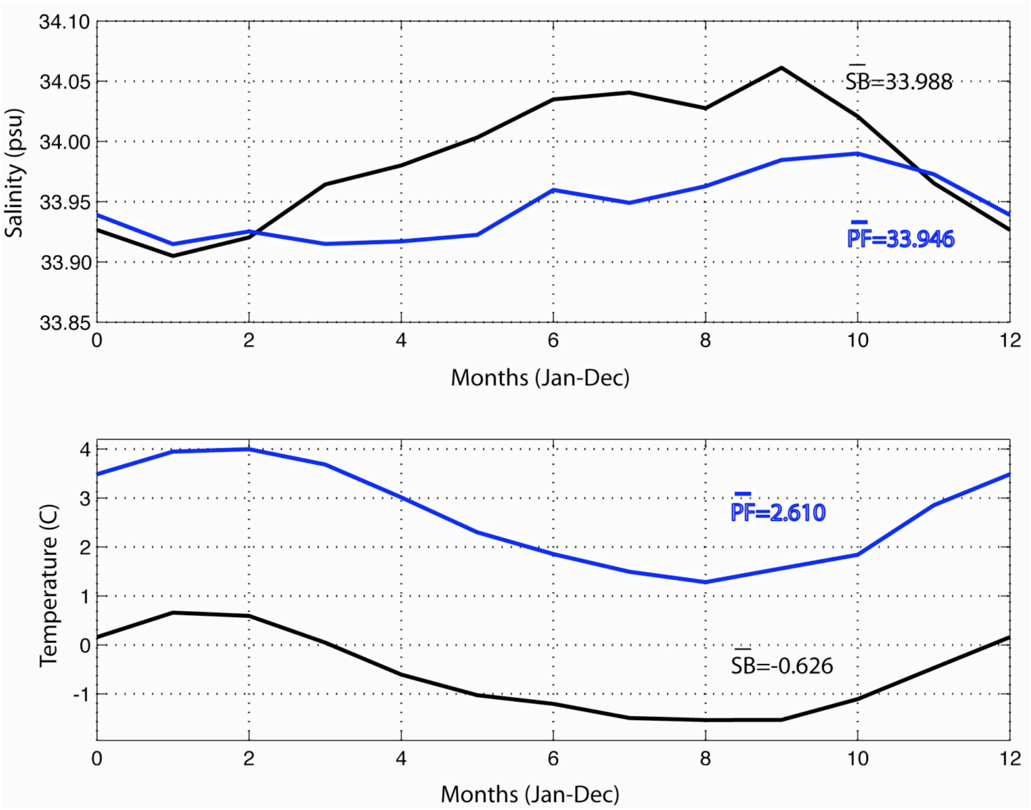

Figure 7.1: Mean salinity (top) and temperature (bottom) of the surface layer (top 75m) in the locations of the Polar Front (blue) and Southern boundary (black) from monthly fields from the WOA2005 Climatology (Locarnini et al. 2005). The annual mean values are shown for each front.

The inverse study has an export of ~15 Sv in the intermediate water layers, so if this value is taken as representative of the total northward flux between the SB and PF, it is possible to estimate the total freshwater flux that enters the ocean in the Antarctic zone. Karsten and Marshall (2002), find 13.2 Sv flowing equatorward on the poleward flank of the ACC in their residual mean study. A freshening of 0.04 psu between the SB and PF implies a freshwater input of 0.02 Sv around the ACC.

Using the same definitions of the frontal locations, the NOC Climatology was used to calculate the total freshwater flux due to Precipitation-Evaporation for the same region in between the SB and PF. These results should be taken with caution due to the large uncertainties surrounding the climatology in the Southern Ocean, but it provides a starting point for a comparative analysis. The total freshwater flux into the ocean in the AAZ from the climatology is 0.12 Sv. This is larger than the freshwater flux estimated from the salinity difference in the mixed layer but within errors is not significantly different from 0. Figure 7.2 shows a simplified model of the freshwater forcing on the overturning circulation. In the upper cell, the freshwater flux exported in the AAIW can be expressed as :

$$F_{AAIW} = F_{UCDW} + (P - E) - F_{surface} \tag{7.1}$$

where F is the freshwater fluxes for respective water masses and a surface flux north of the PF is also included. In the lower cell, Ablation from Antarctica is taken into account:

$$F_{AABW} = F_{LCDW} + (P - E) + A \tag{7.2}$$

There are large uncertainties associated with most of these terms which will be examined below. A term due to sea-ice is initially omitted due to the zero net flux of seasonal sea-ice. This is because the sea-ice term leads to a large spatial flux of freshwater, but in density space, the net flux into density layers is much smaller due to the seasonal spatial variability of the surface density layer caused by the sea-ice cycle.

The ablation rate from Antarctica is linked to the Antarctic mass balance. Due to the complexity of calculating the mass balance of the whole continent, there is a large uncertainty in the net balance, with estimates ranging from a 60±76 Gt yr^{-1} source of ocean mass (Wingham et al. 1998), to a 45±7 Gt yr^{-1} sink (Davis et al. 2005). Jacobs et al.(1992) quote the Antarctic ice mass balance as -469 Gt yr^{-1}, taking into account ice sheet accumulation, run-off, iceberg calving and ice shelf melting. Despite this uncertainty, which has major implications for total sea-level rise or fall (Wingham et al. 2006), ablation only provides a small contribution to the net freshwater flux balance. A freshwater flux of 0.01 Sv is roughly equivalent to 300 Gt yr^{-1}, so the contribution due to Antarctic ablation is an order of magnitude less than the net Precipitation-Evaporation (P-E) and much smaller than the uncertainty in the P-E values.

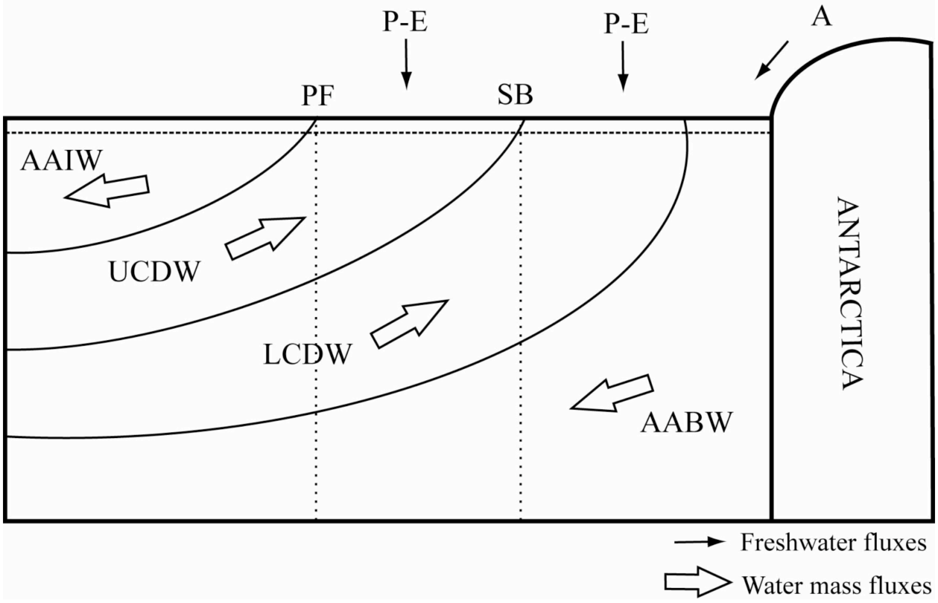

Figure 7.2: Schematic diagram of the freshwater forcing on the upper and lower overturning cells of the Southern Ocean. P-E= Precipitation - Evaporation, A= Ablation, PF= Polar Front, SB= Southern Boundary.

In the inverse model, the freshwater flux through the southern boundary is approximately 0.001-0.003 Sv, depending on the value of the mean salinity chosen. This is because of the small salinity difference between the southward-flowing CDW and the newly formed AABW. Using the NOC climatology, the net P-E south of the SB is 0.12 Sv, which is larger than all of the expected terms. Using an approximate formula for the freshwater flux:

$$F = \frac{\Delta S}{\overline{S}} T \tag{7.3}$$

where T is the volume transport, $\overline{S}$ is a reference/mean velocity and ΔS is the salinity difference between the two water masses being compared. Using the AABW production rate of 14.6 Sv found in the inverse model, this would imply a salinity change of ~0.3 psu due to a freshwater flux of 0.12 Sv. This value is much higher than the salinity difference between LCDW and AABW. Across the southern boundary of the model, the salinity difference between the LCDW and AABW is ~0.01 psu. Using equation 7.3, this results in a predicted freshwater flux of 0.0042 Sv, which is in good agreement with the more robust calculations from the inverse model. This also suggests that the Antarctic ablation term may also in fact form a leading order contribution to the freshwater flux balance in the lower cell.

In the case of the upper cell, if the value of 15 Sv of AAIW production used above is applied, the P-E flux between the PF and SB of 0.25 Sv would result in a salinity difference of 0.6 psu. This indicates that a freshwater flux of this magnitude is required to drive the upper cell of the overturning circulation, as the salinity range of UCDW is 34.65-34.70 psu, and the range of AAIW salinities is ~34.1-34.2 psu. This does not imply that this is only due to the P-E flux, as the sub-surface winter water layer due to sea-ice melt is related to the low salinity of the AAIW. There should be no net gain in fresh water due to the seasonal sea-ice, but the spatial and temporal variability of sea ice formation and melting may result in a net freshwater gain on some density surfaces and a net salinification in denser layers.

The zonal mean picture is useful in understanding the main mechanisms driving the overturning circulation, but the actual circulation is further complicated by spatial in-homogeneity and the three dimensional structure of the Southern Ocean. Figure 7.3 shows the variability in the salinity and temperature from a mean over the top 200m using the WOCE climatology (Gouretski and Koltermann, 2004) in the location of the PF and SB. The temperature difference is roughly constant around the Southern Ocean, but there are large differences between the salinity values. Regional differences in the frontal separations and the surface properties mean that the water mass transformation rates of upwelling CDW vary around the ACC.

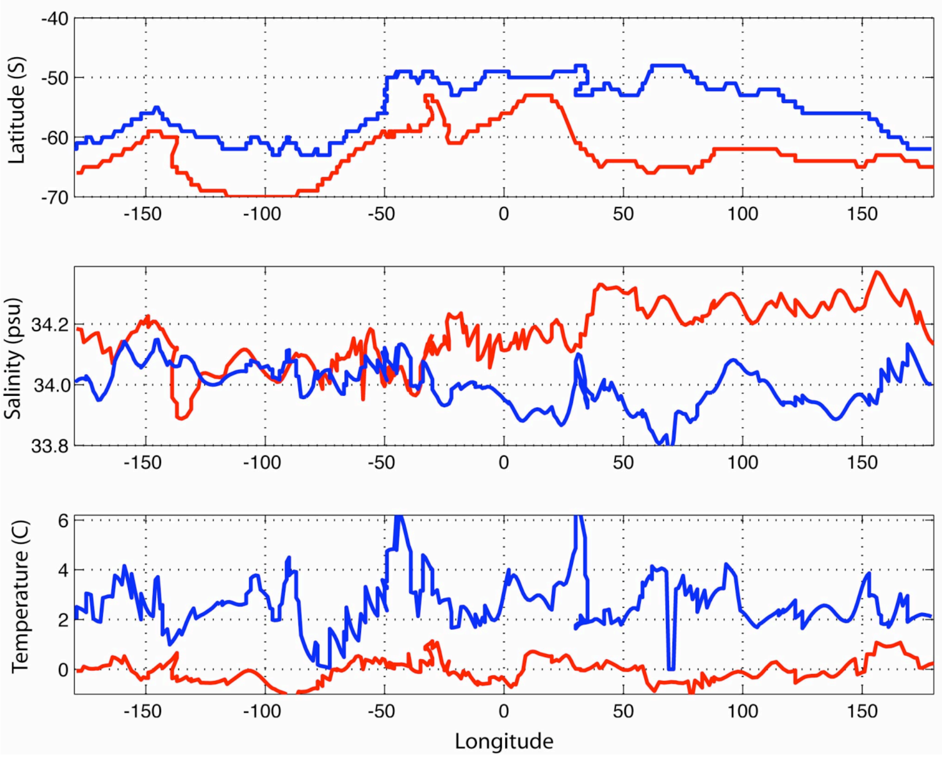

Figure 7.3: Mean tracer properties averaged over the top 200m from the WOCE Climatology (Gouretski and Koltermann, 2004). Top: Mean PF(blue) and SB(red) locations. Middle: Mean salinity (psu) of the top 200m around Antarctica in the PF(blue) and SB (red) latitude locations. Bottom: Mean temperature of the top 200m around Antarctica.

7.1.2 The balance of buoyancy forcing and dianeutral mixing

The inclusion of dianeutral mixing and air-sea forcing terms in the inverse model provides an estimate of the balance between the relative magnitudes of the fluxes across neutral surfaces driven by the surface buoyancy forcing and the internal mixing in the interior. The strain-based eddy diffusivity estimates from hydrographic data used in the model suggest that deep mixing in the region of steep topography could play an important role in the overturning circulation, at least in localised regions, for example at Drake Passage (Naveira Garabato et al. 2007). Due to the error ranges of the interior dianeutral fluxes and the insignificant adjustment from the initial air-sea flux field used in the model, it is only possible to make qualitative statements about the balance of these dianeutral flux processes.

In the South Atlantic, the model has large internal dianeutral fluxes in the intermediate waters to balance the mass fluxes through boxes 1 and 2. In both cases, there is a flux into lighter waters in the layers between γ^n=26.90-27.40 kgm^{-3}, of between 5-15 Sv, and within errors, the contributions from internal fluxes and buoyancy fluxes are of a similar magnitude. The air-sea fluxes only act on the upper layers (see figure 4.18), with insignificant fluxes in layers associated with the UCDW and the denser waters. The dianeutral fluxes on these layers are only due to interior dianeutral fluxes. In the other boxes, the magnitudes of air-sea induced buoyancy fluxes are of a similar magnitude to the interior fluxes, but there are not the large fluxes (O(10 Sv)) that are found in the interior transports in the intermediate water layers in the South Atlantic and Southwest Indian Ocean. High internal dianeutral mixing values may also be due to turbulent mixing in the mixed layer. This leads to the possibility that the model uses the dianeutral fluxes in the layers that outcrop at the surface to balance the mass fluxes between asynoptic sections.

Figure 7.4 shows the total dianeutral transports from the model solution broken down into the two components: interior fluxes; and air-sea induced fluxes. The air-sea induced buoyancy fluxes are consistent with ocean heat loss in the southern regions of the model (e.g. south of the PF) and ocean heat gain in the northern regions (e.g. in the sub-tropical regions). The interior fluxes show a large flux from the AABW of ~15 Sv from the densest layers into the ACCbw and the densest LCDW. All of the AABW that enters through the southern boundary is mixed up into the ACCbw layers above. This observation highlights the importance of deep mixing in closing off the lower cell of the overturning circulation. Throughout the LCDW, there is a downward flux into denser water, with a maximum centred around γ^n=28.08 kgm^{-3} of ~17 Sv down into the denser layers.

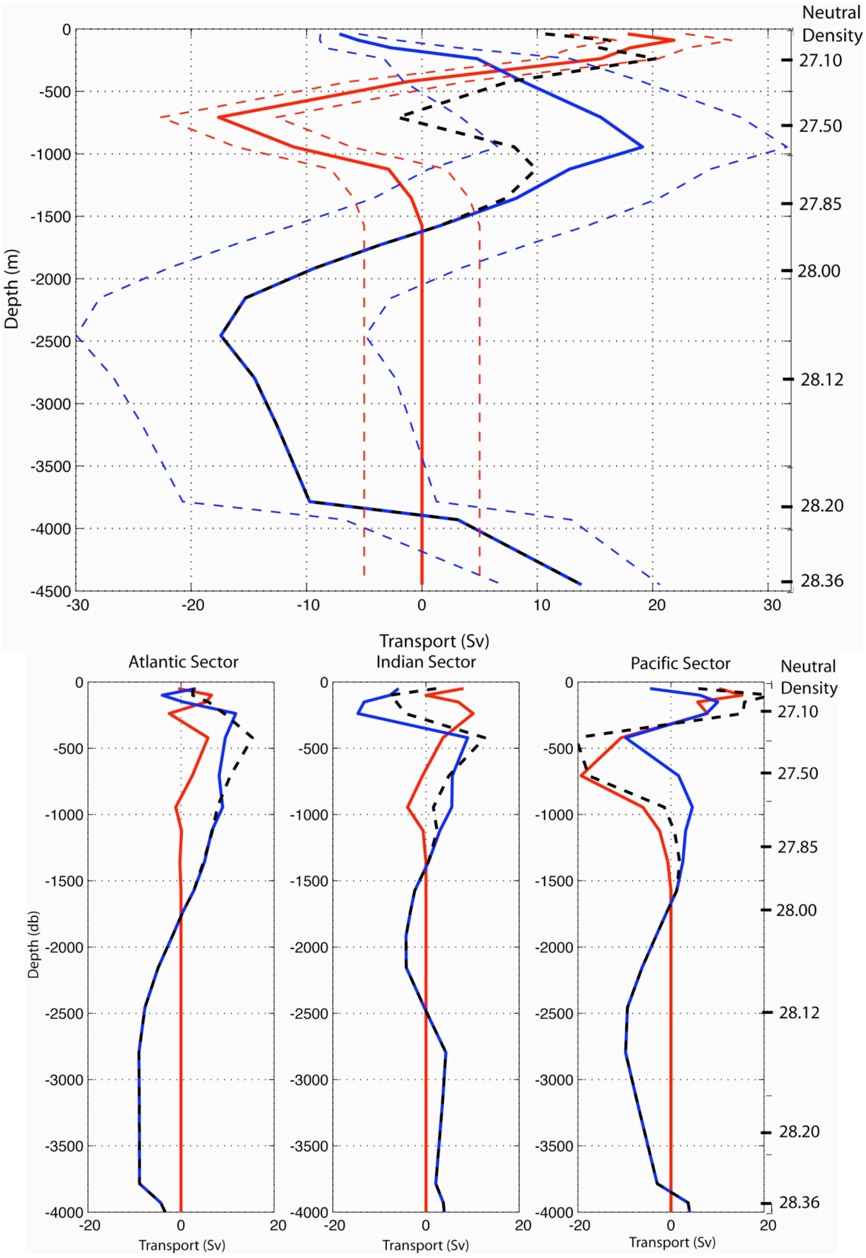

Figure 7.4: (top) Total dianeutral fluxes from the model solution, interior dianeutral transports (blue), air-sea buoyancy flux induced transports (red), and total dianeutral transports (dashed black line). A positive transport is into a lighter density layer/buoyancy loss from the ocean. **(bottom)** The fluxes broken down into the 3 main sectors of the Southern Ocean.

7.2 The salinity variability of the LCDW layer

The study of the properties of the LCDW salinity maximum layer at Drake Passage in chapter 2 posed questions relating to how the amount of salt in the LCDW layer changes, and what can this tell us about the three-dimensional circulation in the Southern Ocean. The solutions of the inverse model provide a consistent flux field that can be used to examine the transport of salt around the model domain, and determine the flux balances that cause the observed salinity profiles in the region. A salt anomaly was used in all of the Inverse model conservation equations to improve the conditioning of the salt conservation equations (e.g. Wunsch, 1996). An analysis of the salinity anomaly transport also reduces the effect of the eastward mass transport of the ACC, which tends to dominate any signals in the total salt transport throughout the model.

Figures 7.5a/b are adapted from the WOCE Southern Ocean Atlas, showing the salinity distribution on the γ^n=28.05 kgm^{-3} neutral density surface. As described in section 2, this is a fairly good approximation to the LCDW salinity maximum surface, which starts off at γ^n~28.00 kgm^{-3} in the South Atlantic, and deepens to γ^n~28.10 kgm^{-3} at Drake Passage. The main feature is the high salinity tongue that enters the Southern Ocean in the Southeast Atlantic and gradually freshens around the ACC's eastward path. The freshening is increased due to mixing to the north and south of the ACC, resulting in a high salinity core centred on the PF and SAF within the ACC. At Drake Passage, the salinity maximum is found south of the PF, in the AAZ. The figure also shows the relatively high salinities to the north of the region in the Atlantic and Indian basins, and fresher waters in the Pacific Ocean.

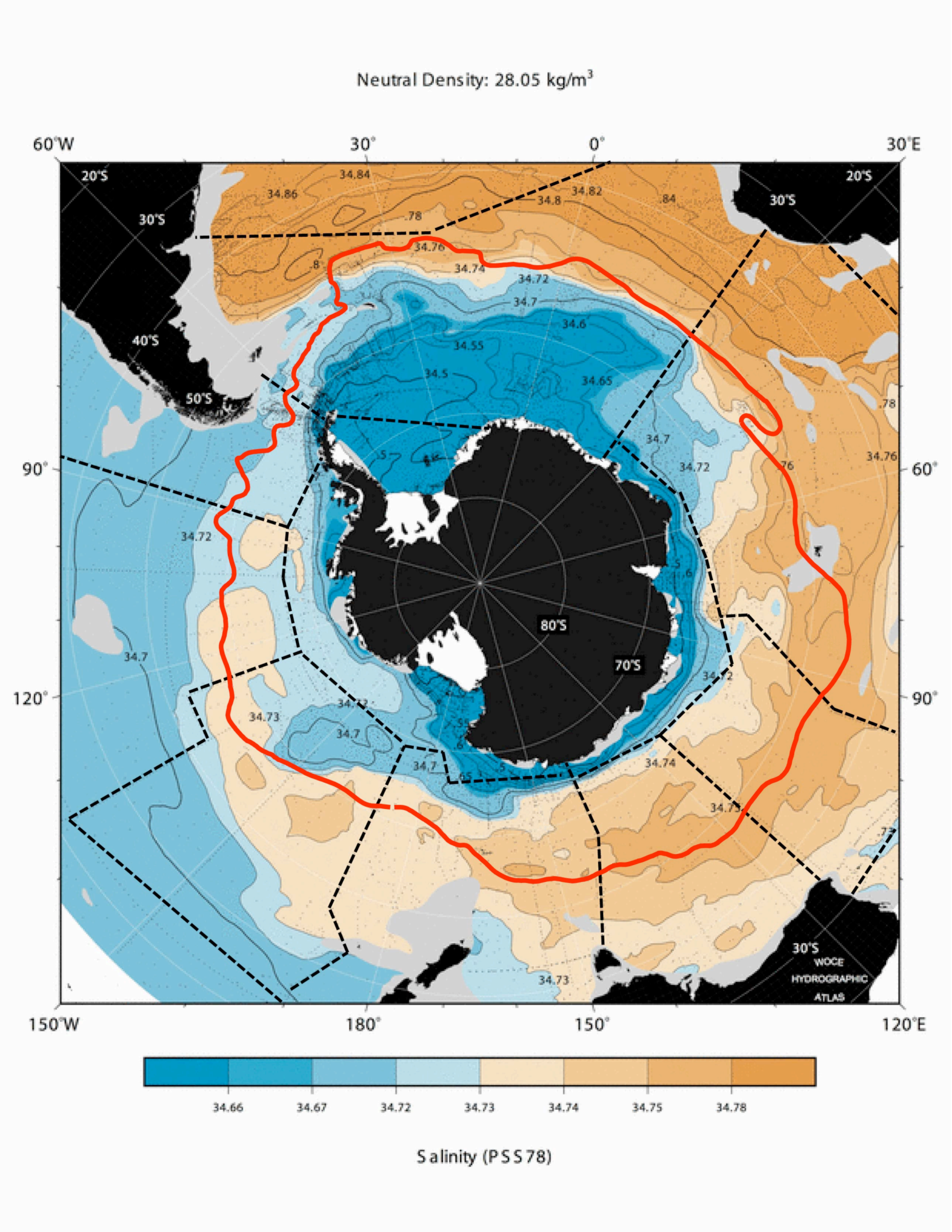

Figure 7.5a : A slide adapted from the WOCE Southern Ocean Atlas (Orsi and Whitworth, 2005), showing the salinity on the γ^n=28.05 kgm^{-3} neutral density surface, associated with the LCDW salinity maximum layer. The box boundaries are shown by dashed black lines. An approximate Polar Frontal position is shown (red line) from Orsi et al. 1995.

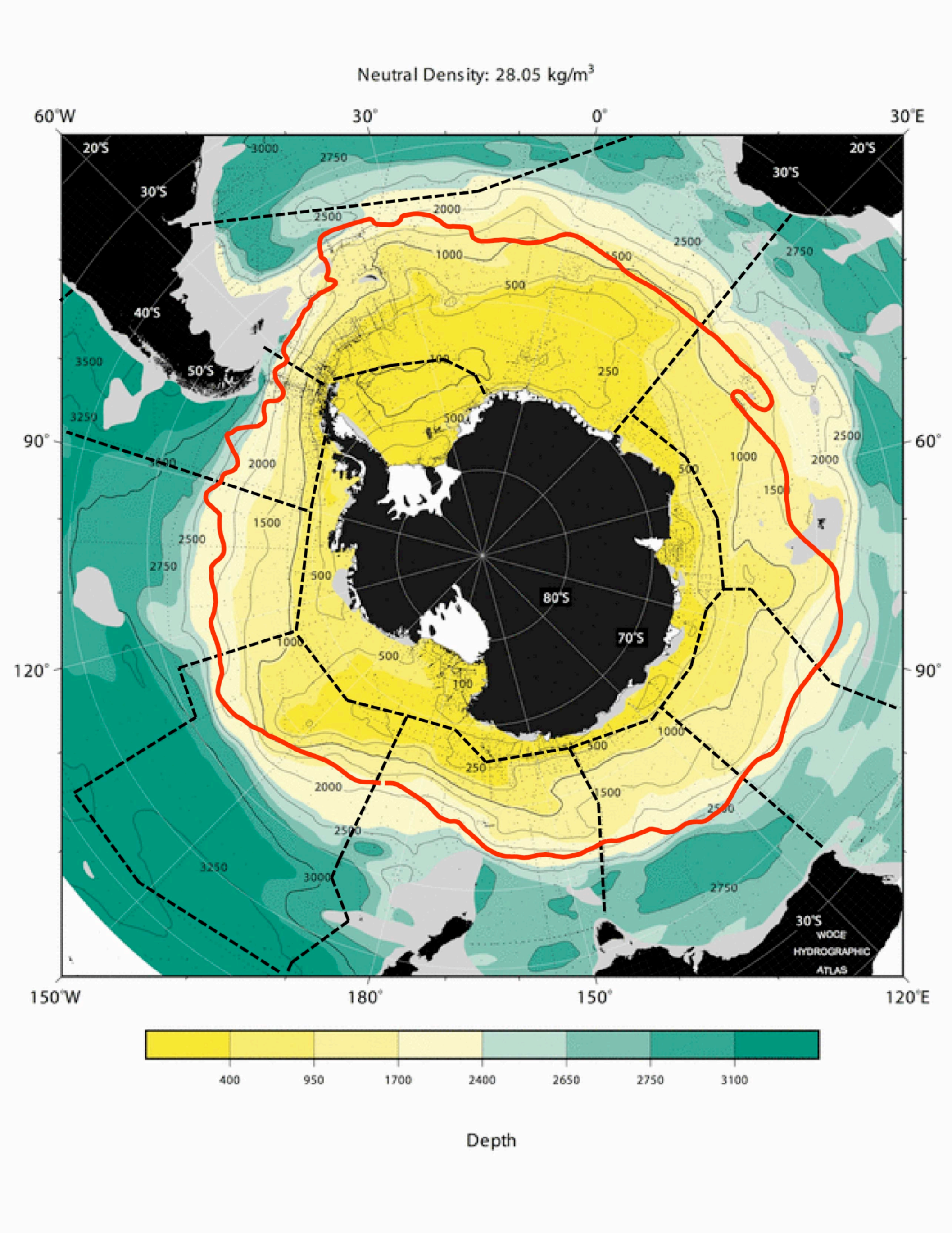

Figure 7.5b : A slide adapted from the WOCE Southern Ocean Atlas (Orsi and Whitworth, 2005), showing the depth of the γ^n=28.05 kgm^{-3} neutral density surface, associated with the LCDW salinity maximum layer. The box boundaries are shown by dashed black lines. An approximate Polar Frontal position is shown (red line) from Orsi et al. 1995.

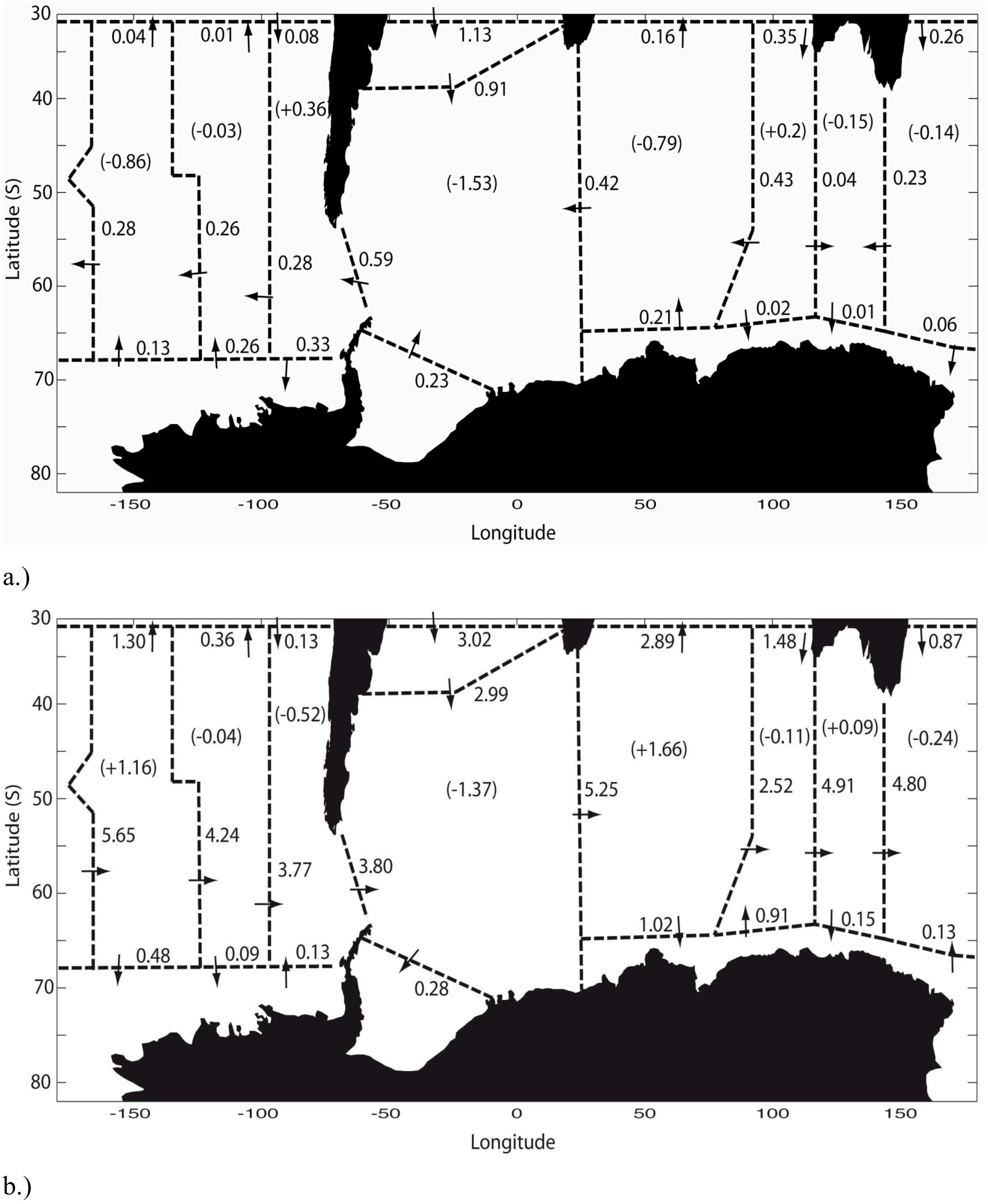

Figure 7.6: Salt anomaly transports (Ggs^{-1}) on a.) UCDW density layers (γ^n=27.70-27.98 kgm^{-3}) and b.) LCDW density layers (γ^n=27.98-28.18 kgm^{-3}). The values in brackets are the net salt anomaly flux into the layer (i.e. positive value = flux into the layer).

Figure 7.6 shows the salt anomaly transport throughout the model domain on two core density layers associated with the UCDW (γ^n=27.70-27.98 kgm^{-3}) and LCDW (γ^n=27.98-28.18 kgm^{-3}). The general pattern in the LCDW layer is a gradual decrease in the salt flux around the Southern Ocean from Africa, flowing eastward to South America and Drake Passage. The northern extent of the model domains means that the model includes the ACC and the sub-tropical gyres in the Atlantic, Indian and Pacific basins. These gyre circulations and their resultant salt transport are therefore superimposed on the salt anomaly signal due to the ACC.

The largest dianeutral salt tranpsorts occur in boxes 2 and 3, in the South Atlantic and Southwest Indian Ocean. The largest zonal salinity gradients on the LCDW salinity maximum layer are found in this region, and the model shows that dianeutral fluxes play an important role in the observed changes in the salinity distribution. In figure 7.5b, the topography associated with the southwest Indian ridge and the Kerguelen Plateau (see also figure 4.5) forms an obstruction to the 28.05 kgm^{-3} density surface. This supports the direct observations of increased mixing in the ocean interior associated with topographic features (e.g. Sloyan 2005, Mauritzen et al. 2002), and the mass balance found in the standard model solution in box 3. The Southwest Indian ridge acts to obstruct the eastward flow of the most saline water in the LCDW layer that has entered the Southern Ocean as NADW. This results in a large salt anomaly transport into the Indian Ocean that is partially balanced by a southward flux to the eastern side of the ocean. The net zonal salt anomaly transport across the Indian Ocean sector is fairly constant, with a small reduction of 0.34 Ggs^{-1} between the I06 and I09 sections.

In the Pacific sector, the salinity distribution on the LCDW layer changes due to the interaction with the relatively fresh deep water of the Pacific Ocean. In box 6, directly east of Australia, there is an input of 0.87 Ggs^{-1} along the western side of the Southwest Pacific Basin. The northward return flow in this basin transports 1.66 Ggs^{-1} , resulting in a net salt anomaly flux into the Pacific Ocean. The reduction in the salt anomaly transport from the standard model in the LCDW layer is in agreement with the salinity structure of figure 6.1. There is a large freshening in the Southeast Pacific basin, and a reduction in the salt anomaly transport, from 4.24 Ggs^{-1} across the Pacific-Antarctic Ridge and the Southeast Pacific Rise, to 3.80 Ggs^{-1} at Drake Passage. This is in agreement with the salinity structure of the LCDW layer shown in figure 5.4, where the high salinity signal and large salinity gradient found at I06 (30 E, blue line), changes gradually around the Southern Ocean to the fresher, more homogenous salinity structure observed at Drake Passage (black line). There is an additional salt flux into the Southeast Pacific basin due to the southward transport on density layers associated with the Deep Water lighter than γ^n=28.13 kgm^{-3} through the Chile Basin.

The southern boundary of the model enables a view of the salt fluxes associated with the southern region of the ACC and the interactions with the continental waters. Starting at the Weddell Sea, in the LCDW, there is a net salt anomaly flux into the Weddell Sea. The total net flux should be approximately zero, with the northward flux coming in the lighter surface waters, and the WSDW/BW flowing out into the Weddell Basin. The gyre circulations associated with the Weddell Sea, Kerguelen Plateau, and Ross Sea have large mass transports, resulting in relatively significant salt anomaly fluxes across the southern boundary. The saline tongue feature of the high salinity signal of the salinity maximum layer of figure 7.5a shows that there is also a considerable amount of isoneutral mixing around the ACC as well as the main isoneutral advective components. The saltier waters are freshened to the north and south of the ACC by mixing with the fresher waters on similar density layers. There are southward salt anomaly fluxes of 1.02 and 0.48 Ggs^{-1} associated with the Kerguelen circulation and the Ross gyre, resulting in a net southward flux of 0.11 and 0.35 Ggs^{-1} in the LCDW layer in these regions.

The origins of the salinity gradient of the LCDW salinity maximum layer described in section 2, are primarily in the Southeast Pacific Ocean, where the fresher deep water to the north of the SAF passes from the Pacific Ocean through Drake Passage, and the more saline LCDW in the Antarctic and Continental zones re-circulate in the Amundsen and Bellingshausen basins and within the South-East Pacific. The changes in the neutral density of the salinity maximum layer are due a combination of isoneutral and dianeutral mixing. The salt anomaly fluxes show that the dianeutral fluxes play an important role in the salt transport around the Southern Ocean, and the deepening of the salinity maximum layer can be explained by the effect of dianeutral mixing with the lighter and denser waters, reducing the salinity of the LCDW. The largest changes in this density horizon are co-incident with the regions of significant dianeutral fluxes found in the model (South Atlantic, Southwest Indian Ocean, and Southwest Pacific

Ocean). It is difficult to separate out the relative contributions of the mixing into the lighter and denser waters. A dianeutral flux into the LCDW layer of fresher water acts to reduce the mean salinity of the layer, and under mass balance reduces the total salt transport as well. The top panel of figure 7.6 shows the salt anomaly flux in the UCDW layer. In this figure, a westward flux is equivalent to a negative eastward salinity anomaly flux, so the salt content in this layer increases around the Southern Ocean moving with the ACC from I06 (30 E) to the Southeast Pacific Basin. There is an imbalance in the salt anomaly flux in box 9, resulting in a fresher UCDW salt anomaly into the South Atlantic through Drake Passage.

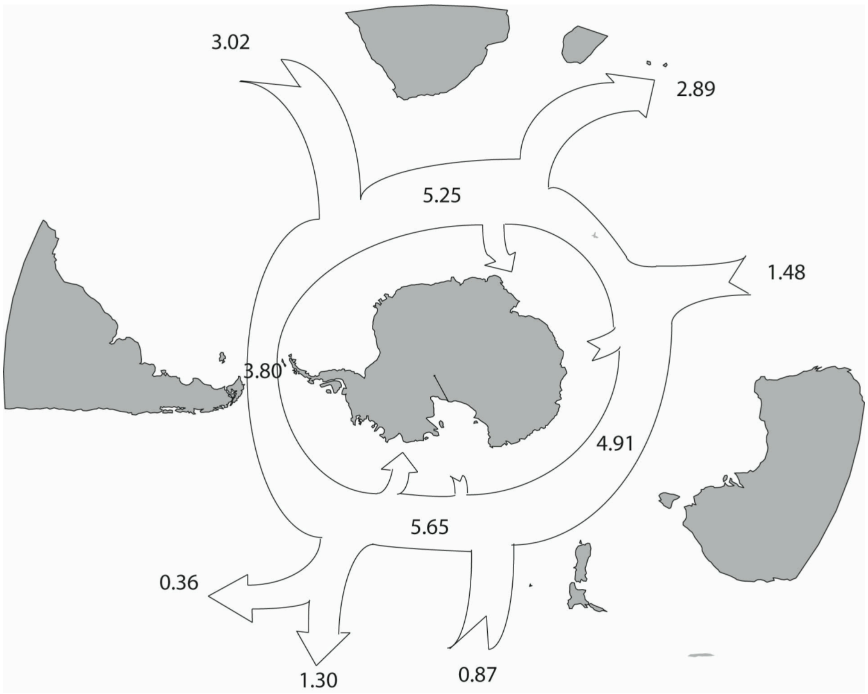

Figure 7.7: A schematic representation of the major salt anomaly fluxes around the ACC in the LCDW layer (γ^n=27.98-28.18 kgm^{-3}).

One of the main features of the LCDW is the sub-surface salinity maximum that originates from the NADW entering the Southern Ocean through the South Atlantic. Figure 7.7 is a schematic representation of the changing salt anomaly flux around the ACC in the LCDW. The main features are that there are large meridional salt anomaly fluxes in each basin that play an important role in the modification of the water mass properties and the salinity distribution of the salinity maximum layer shown in figure 7.5a. Vertical mixing within the LCDW acts to reduce the salinity gradient throughout the LCDW resulting in a more homogenous salinity distribution, and smaller salinity gradient throughout the layer (see figure 5.5). The PF location shown in figure 7.5a shows how the PF separates the fresher, cooler continental waters from the warmer CDW. The centred of the salinity maximum tongue spreading across the Indian Ocean and Southwest Pacific is centred around the PF, as it acts to transport the more saline LCDW eastward around the ACC.

Chapter 8: Summary and Conclusions

8.1 The Southern Ocean at Drake Passage

An historical data-set of hydrographic data across Drake Passage between 1926 and 2005 was compiled to examine the variability in the water mass properties in this important region of the Southern Ocean. A method was defined to trace the salinity maximum of the LCDW in each of the hydrographic sections in the data-set to examine the variability throughout the last century. The use of complete sections rather than individual stations or station pairs provided a consistent snap-shot of the properties across Drake Passage at the time of the data collection. In previous studies e.g. Gille 2002, sets of station pairs were examined that were located in the same regions, but with large temporal separation (the data were grouped in decadal boxes). This may be applicable to other regions of the Southern Ocean where the latitudinal spread of the ACC is greater, but in the region of the Drake Passage, with the steep latitudinal property gradients and the high eddy activity, then it is not so suitable to make the same comparisons. This study chose some core properties representative of the main water masses to examine any observed variability over time. It was found that within the errors, the salinity and temperature of this layer has not changed over the data-set period (1926-2005). Figure 2.5 is repeated below depicting this feature.

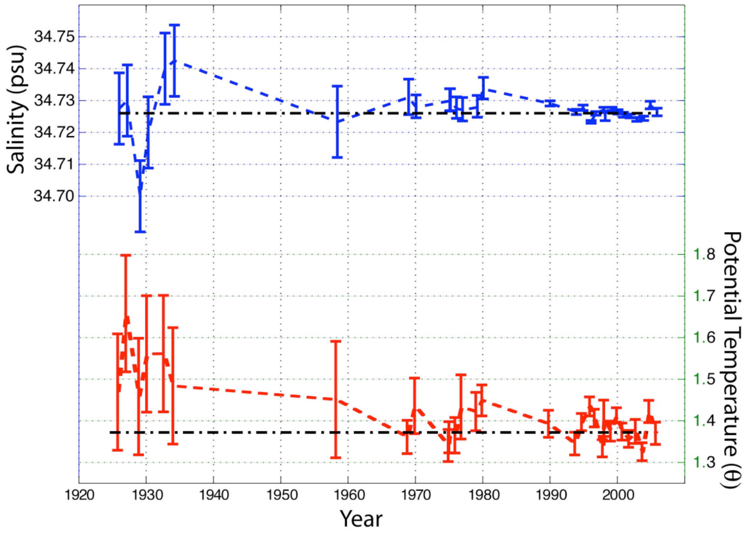

Figure 2.5: Mean salinity (top/blue) and potential temperature (bottom/red) values of the LCDW salinity maximum at Drake Passage vs. time (1926-2005). The black dashed lines represent the mean from 1970-2005. Error bars include a combination of the

systematic and standard errors and an additional bias due to bottle sampling where appropriate.

The main conclusion from this analysis is that there are no long-term trends or variability in the key water properties greater than the shorter-term annual/inter-annual variability. The constant properties are in contrast to the large property changes that occur on this density surface around the Southern Ocean. Williams et al. 2006 examined this variability in detail, using WOCE sections around the Southern Ocean to follow the changing properties of the LCDW salinity maximum layer around the eastward path of the ACC. This study could only go so far without taking into account the fluxes through the sections and the effects of the interactions with the Indian, Pacific and Atlantic Oceans to the north. An Inverse model of the Southern Ocean was designed to examine the overturning circulation and the large-scale exchanges between the basins. Section 7.2 examined this feature in the model demonstrating that there are large lateral salt anomaly fluxes across the 30 S boundary of the model that play an important part in the mixing of the saline NADW signal with the fresher CDW of the Southern Ocean. The observed changes are also due to the interior mixing along the path of the ACC, depicted by the saline tongue of the salinity maximum layer around Antarctica in figure 7.5a. The model solutions showed that this mixing requires both dianeutral and lateral isoneutral components to explain the property changes around the ACC, especially in the regions of high property gradients found in the South Atlantic and South-west Indian Ocean.

The higher quality of the WOCE/post-WOCE sections also enabled a more detailed examination of water properties from annual sections between 1993 and 2005. This modern study enabled an examination of the annual variability in the Drake Passage region over a longer time period than has been possible in previous studies and included sections that are not currently included in the commonly used data sets (i.e. Southern Ocean Database, Orsi and Whitworth 2005, or the WOCE dataset, Gouretski and Koltermann 2004). It was not possible to define a consistent variable to compare the less dense surface layers due to the large variability in the relative water properties and the variability in the location of the structural features that are commonly used to define the SAMW and AAIW. The one pattern that was observed was a cooling and freshening on density layers above the SAMW since 1998, which is consistent with freshening and warming at the surface in the SAMW formation regions in the South-east Pacific. This pattern will need continued monitoring in the data from the SR01 NOCS/BAS repeat surveys to detect whether the trend continues or is due to a longer time-scale oscillations as found in the Indian Ocean (Bryden et al. 2003).

8.2 An Inverse Study of the Southern Ocean

A number of Inverse studies have been conducted around the Southern Ocean, focussing on small regions (e.g. McDonagh and King, 2005, Robbins and Toole, 1998), or as part of global inverse models (Ganachaud and Wunsch 2000, Lumpkin and Speer, 2007). This study differs from the existing studies in a number of ways: it uses a number of new hydrographic sections moving on from the initial WOCE sections; An examination of the three-dimensional nature of the Southern Ocean is made by having box configurations on the sub-basin scale; using a regional ocean model that includes sea-ice to constrain the Antarctic southern boundaries of the model and to have a realistic continental AABW flux imposed on the model; and a range of parameterisations of the large-scale internal mixing and diffusion driven by data-based turbulent mixing estimates.

A number of new sections, including the NOCS/BAS SR01 sections, were used which have not been used in the basin-wide inverse studies (these sections were used in the inverse study of Garabato et al. 2003 focussing on the Drake Passage and Scotia Sea region). These sections were used to examine the sensitivity of the model to the mass and property transport through Drake Passage. The inclusion of model-driven constraints that take into account the effects of sea-ice and the coastal environment provide a different picture of the Southern Ocean than to one relying purely on fields derived from climatologies based on very limited observations in the Southern Ocean. The large barotropic velocities that have been detected in hydrographic sections around the coastal regions (e.g Heywood et al. 1999) present an additional difficulty when using inverse methods when trying to determine an initial best-guess reference level of no motion. The use of the BRIOS model in this study, which includes AABW formation, is an important feature to the model design as it allows the examination of how the model adapts to this AABW input from the continental waters. This also led to a larger flux of AABW into the ACC region, than used in other studies (e.g. Lumpkin and Speer, 2006) which are based on flux estimates derived from CFC constraints (Orsi et al. 1999). This feature leads to a stronger lower cell of the overturning circulation which is driven by this increased rate of AABW production.

A range of box configurations were explored, starting with a simple 3 box model (one box for the Atlantic, Indian and Pacific sectors) with additional data sections added to create sub-basin boxes and the standard model solution presented in Chapter 4.
The key features from the standard solution were:

- A Drake Passage ACC transport of 141.6 ± 2.9 Sv, within the range from observations of 136±7 Sv. The SR03 ACC transport south of Tasmania was 150.9 ± 3.8 Sv.

- Across the 30 °S boundary, there is a southward flow of 0.6±0.5 Sv from the South Atlantic, a 7.3±2.7 Sv southward flux from the Indian Ocean and a 12.9±4.1 Sv northward export into the Pacific Ocean. This is consistent with an ITF of ~7 to 12 Sv, which is within estimates from other studies.

- An Agulhas Current of -72.9±2.7 Sv was obtained given a constraint of -69.7±4.3 Sv from mooring data (Bryden et al. 2005). There was also an Agulhas undercurrent of 5.8±1.9 Sv moving northward along the continental slope.

- Dianeutral fluxes consisting of a dianeutral advective flux and an effective diffusive component were obtained from the model solution. The regions of the largest dianeutral fluxes were in the South Atlantic, Southwest Indian Ocean and the Southwest Pacific Ocean.

- Advective vertical velocities ranged from $1x10^{-7}$ ms^{-1} up to $1x10^{-6}$ ms^{-1}. The application of an a-priori error estimate of $1x10^{-6}$ ms^{-1} which allowed the model solution to adjust with large dianeutral fluxes did not result in large solutions for the dianeutral vertical velocities. The a-posteriori error estimates were of a similar magnitude to the solutions, which were a factor of 2-10 times smaller than the a-priori error range.

- The solution across the southern boundary of the model produced an estimate of the AABW production and the balance of LCDW/AABW fluxes around the continent. In the model, there was a northward AABW export of 14.6 Sv ($\gamma^n >$ 28.27 kgm^{-3}) across the southern boundary compensated for by a southward flow of CDW. The main components of this flow were 4.5 Sv from the Weddell Sea and 5.1 Sv from the Ross Sea. There was a net transport of 1 Sv along the Adelie Coast between 30 °E and 150 °E. The AABW flux is then mixed up into the lighter LCDW/ACCbw above around the model domain.

- At the 30 S boundary, there are two overturning cells, with a net northward flow of intermediate and ACCbw (18.8±5.5 Sv and 18.6±0.9 Sv respectively) , and a southward transport of CDW (in both the UCDW and LCDW layers) of 25.5±5.5 Sv that is then converted in the Southern Ocean in either the upper or lower overturning cell.

8.4 Discussion

In chapter 1, two predominant views relating to the dynamic balance of the Southern Ocean, between the wind driven and the buoyancy driven regimes were presented. This inverse study can be used to examine to what extent this balance is due to these two components and how suitable this simplified view of the Southern Ocean is. The model contains parameterisation of the wind-driven Ekman transports across the box boundaries, the air-sea fluxes into the surface layers, and the dianeutral fluxes between the neutral density layers.

Applying a zonal mean view to the overturning circulation in the Southern Ocean does not take into account the large differences between the properties in the three oceans that interact in this region. The air-sea fluxes along the ACC are not uniform in each sector of the Southern Ocean, as the ACC moves further south towards Antarctica as it travels east past Africa into the Pacific Ocean, before it moves northward again on the eastern side of Drake Passage and into the Scotia Sea. These differences in surface buoyancy forcing along the path of the ACC make it difficult to apply a zonal mean view of the Southern Ocean. This is also not consistent with large differences in the fluxes across the 30 S boundary found in the model solution.

The following sub-sections will describe how the model solutions describe the three-dimensional nature of the circulation of the Southern Ocean, in terms of the mass fluxes, the balance of air-sea forcing and interior mixing, and the spatial variability of deep turbulent mixing.

8.4.1 The Overturning Circulation

The circulation across the Southern boundary of the model is similar to the imposed flow field from the BRIOS model, with a northward flux of 14.6 Sv. This northward flux is localised to the formation regions in the Weddell and Ross Seas and along the Adelie Coast. There is no water denser than $\gamma^n = 28.26$ kgm^{-3} flowing across the model's northern boundary at 30° S, so the model has to export all of the AABW flux into the relatively less dense CDW layers above it. The model mixes the resulting water mass due to this flux into the less-dense layers above in the boxes with significant northward injections of AABW. The overturning across the 30 S boundary is in broad agreement with other studies, with the main features being the gyre circulations found within each major basin. The picture described by the net mass flux across this boundary is different to the individual basin-wide balances. The zonal net flux picture (black dotted line in the right-hand panel of figure 5.2 below) shows the standard overturning view with a southward flux in the U/LCDW layers, and a compensating northward flux in the Intermediate and Deep/Bottom waters forming the return paths of the overturning circulations.

In the Atlantic sector, NADW enters the Southern Ocean roughly balanced by a net northward transport of AAIW and AABW/ACCbw. In the Indian Ocean, the gyre circulation plays an important role in the flux balance across the 30 S boundary. Saline NADW is exported northward in the South-west Indian Ocean, where it mixes with the fresher surrounding waters, so that the southward flux due to the gyre in these density layers is fresher. The full circulation patterns observed in the Inverse Model show a Southern Ocean where the lateral exchanges with the surrounding oceans also play an important role in modifying the major water masses around the Southern Ocean.

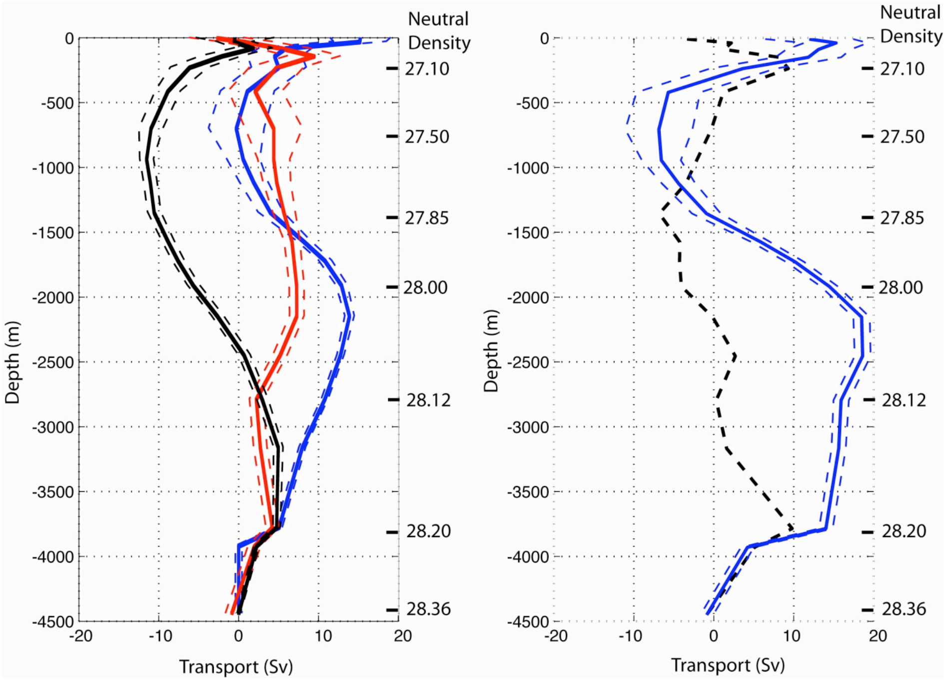

Figure 5.12: a.) Meridional overturning streamfunction at 30° S in Atlantic Ocean (black), Indian Ocean (red) and Pacific Ocean (blue), summed on density layers and integrated from the surface. The dashed lines represent ± correlated layer flux uncertainties from the posterior error matrix. b.) Total Meridional overturning circulation on depth layers (blue), and net meridional transport on neutral density layers (black-dashed) plotted with a representative depth scale.

8.4.2 Buoyancy forcing vs. Interior Mixing

Figure 7.4, reproduced below shows the balance between the fluxes induced by buoyancy forcing and interior mixing in the inverse model. The total zonal view shows the expected picture from the overturning circulation, with a convergence centred on the cores of the upper and lower cells around γ^n ~27.6 kgm^{-3} (associated with the top of the UCDW) and γ^n ~ 28.1 kgm^{-3} (associated with CDW/ACCbw). These are in agreement with the picture of the overturning circulation detailed above. The basin-scale resolution of the inverse model allows this view to be broken down into the major sectors (shown in the lower panel of figure 7.4). This shows that there is a large amount of spatial variability and that some of the main features are actually due to fluxes in individual basins. The negative flux due to the buoyancy forcing in the overall picture is mainly due to forcing within the Pacific sector, with a flux into the layers associated with AAIW. This is also in line with the different properties of Indian and Pacific mode waters, where AAIW/SAMW originating in the Southeast Pacific is found in a denser isoneutral layer ($\gamma^n \sim 27.4$-27.6 kgm^{-3}) than in the Indian Ocean ($\gamma^n \sim 26.9$-27.1 kgm^{-3}). The less dense layers are also not well resolved in the model due to their relative thickness and the larger associated uncertainties with the mass transports in these upper layers. The result of this was that the model could not resolve the structure of fluxes into or out of the water masses associated with the less dense mode waters found in the Indian Ocean.

In the surface waters, in the model it is not possible to separate the effect of turbulent mixing below the mixed layer and eddy-driven mixing within the layer itself. Due to the parameterisation of both mixing and buoyancy fluxes, the null hypothesis of the effects of either forcing mechanism. The model resolved the corrections to the mixing parameters above the error estimates but this should not be taken to suggest that the interior mixing is more significant than the air-sea forcing in the model solutions. The model was more sensitive to changes in the mixing coefficients than the air-sea flux parameterisation. Solutions of the model were sought that were corrections to a best-guess of the actual field, but this can not address the issues with the imposed parameters. An examination of the set of model runs suggests that both forcing mechanisms play an important part in dynamical balance of the Southern Ocean and the resultant overturning circulation.

Unfortunately, the model was not very sensitive to the imposed buoyancy forcing field, with none of the corrections being significant above the model errors. This coupled with the large uncertainties in the initial climatological fields means that any conclusions about the relative effects of the buoyancy forcing and interior mixing must be taken with some caution and quantitative estimates are only indicative of the general patterns (as shown by the uncertainties associated with the flux contributions in figure 7.4). The differences between the surface salinity and temperature properties between the Southern Boundary and the Polar Front in the annual cycle presented in figure 7.1 show the importance of the sea-ice freshwater flux in the continental waters and that the haline component of the buoyancy forcing is also important in the dynamical balance of the Southern Ocean, at least to the south of the ACC, and must be included with the thermal component which dominates further north.

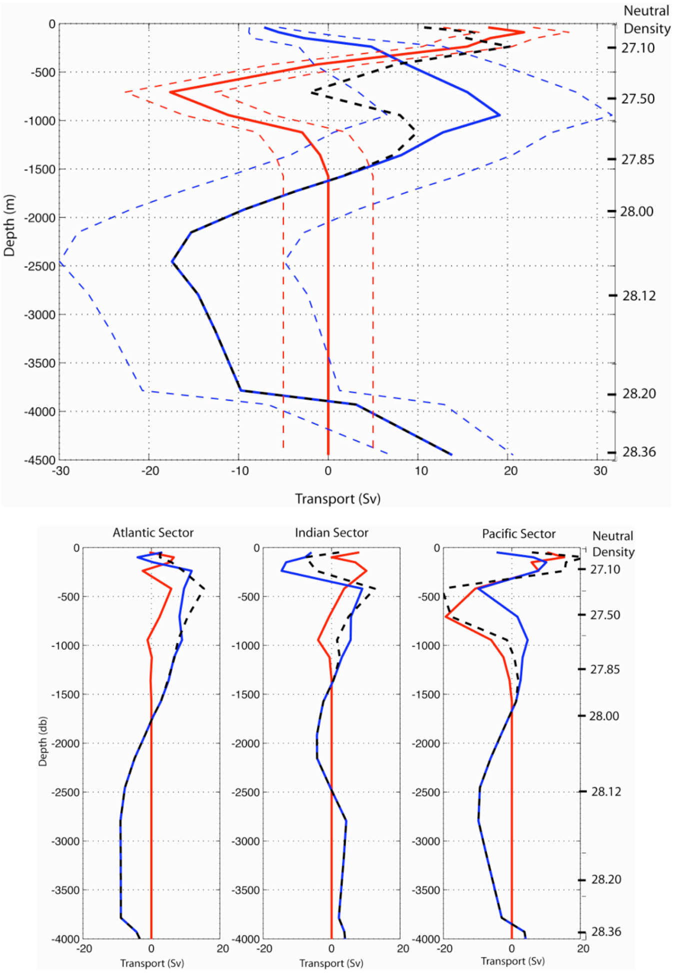

Figure 7.4: (top) Total dianeutral fluxes from the model solution, interior dianeutral transports (blue), air-sea buoyancy flux induced transports (red), and total dianeutral transports (dashed black line). A positive transport is into a lighter density layer/buoyancy loss from the ocean. **(bottom)** The fluxes broken down into the 3 main sectors of the Southern Ocean.

The distribution of the dianeutral fluxes in the ocean interior not uniform across the Southern Ocean. In the Pacific and Atlantic sectors, there is a downward flux into denser layers associated with CDW/ACCbw, whilst in the Indian Ocean, the mass flux is into less dense water masses in the same density layers. The form of the mixing parameterisation did not have a large effect on the circulation patterns of the model solutions, as the model was found to be relatively in-sensitive to changes in the dianeutral components. The data-set of in-situ turbulence measurements was useful to compare the expected structure of deep mixing with that found in the model. Unfortunately, when this structure was imposed on the model in the form of a-priori error estimates, in the solution the resulting structure was not sensitive to changes in the vertical structure of these error estimates. The largest dianeutral transports were found in the South Atlantic and South-west Pacific, in regions with rough topography and high values for the turbulent mixing coefficient, but it is also worth noting that in the model, this also coincides with boxes that had large net fluxes of AABW which the model had to mix into the less dense layers to balance the layer fluxes, so this may also have contributed to the large isoneutral fluxes found in the deeper layers in these regions.

To obtain a full picture of the overturning and pathways, the fluxes across the box boundaries and the internal layer transports need to be examined together to determine the movement of water masses and properties around the model domain. The model solution has highlighted the importance of examining the three-dimensional nature of the Southern Ocean which is required to fully understand the observed fluxes and property changes found in observations made around the Southern Ocean. The range of model solutions explored have shown that air-sea fluxes and internal mixing both play an important role in the dynamical balance of the Southern Ocean, resulting in a view that is between the two extremes of a wind-driven (with no water mass transformation) and buoyancy-driven regimes.

8.5 Future Work

This Southern Ocean Inverse Study has helped to examine some of the important questions about the Southern Ocean and its role in the global overturning circulation. The consistent flux field around the Southern Ocean has allowed an examination of the fluxes and processes that cause the property variations found in the individual sections around the Antarctic. The Drake Passage SR01b repeat hydrography provides a unique insight into the variability and water mass properties in the waters of the Southern Ocean. The length of the record is beginning to allow examination of variability on multi-year timescales, and the ability to determine long-term trends in the highly variable (both spatially and temporally) intermediate waters. Further monitoring of the surface warming signal will allow us to determine whether it is a trend or an oscillation, as in the Indian Ocean (Bryden et al. 2003).

Further examination within the model of the effect of imposing an initial field based on the eddy diffusivity estimates will provide more insight into the balance of processes that determine the observed overturning circulation within the Southern Ocean. With an ever-increasing data-set of Southern Ocean hydrographic sections, it will soon be possible to use a completely closed southern boundary for the model, which will improve the estimates of bottom water fluxes across the Southern boundary. The weak adjustment to the air-sea buoyancy forcing requires further investigation with the inclusion of different forcing climatologies (e.g. NCEP/NCAR reanalysis, ECMWF) to be able to determine about the errors associated with the balance of surface buoyancy forcing and internal diabatic mixing processes. The adaptability of the model design means that it can also be used to conduct focussed regional analyses to examine the differences between solutions that are affected by the whole model domain, and ones that are only influenced by individual boxes.

Appendix AA

Strain-based Turbulent Diffusivity Estimates

The following description is based on the method outlined by Kunze et al. (2006), and is similar to the studies of Mauritzen et al (2002), and Sloyan (2006).
The turbulent eddy diffusivity, K, is obtained from estimates of the dissipation rate, ε, where $K = \gamma\varepsilon/N$, where γ is a mixing efficiency parameter, and N is the buoyancy frequency (Osborn 1980). The Garrett and Munk Model obtains estimates of the strain variance $\langle \xi_z^2 \rangle$ based on internal wave interaction theory (Munk 1981) and is used as a reference to scale the turbulence derived from the microstructure of a given CTD cast. The diffusivity can be expressed as

$$K = K_0 \frac{\langle \xi_z^2 \rangle^2}{{}_{GM}\langle \xi_z^2 \rangle^2} h_2(R_\omega) j(f/N) \qquad \text{(AA.1)}$$

where K$_0$ is a reference coefficient ($0.05 \times 10^{-4} m^2 s^{-1}$), $\langle \xi_z^2 \rangle$ is the strain variance (GM denotes strain variance obtained from the application of the Garrett and Munk model), h$_2$ is a function of the shear/strain ratio, R$_\omega$,

$$h_2(R_\omega) = \frac{1}{6\sqrt{2}} \frac{R_\omega(R_\omega + 1)}{\sqrt{R_\omega - 1}} \qquad \text{(AA.2)}$$

and j is a function of the coriolis parameter, f, and the buoyancy frequency, N,

$$j(f/N) = \frac{f \operatorname{arccos} h(N/f)}{f_{30} \operatorname{arccos} h(N_o/f_{30})} \qquad \text{(AA.3)}$$

where the subscripts are from a reference state for the Garrett and Munk Model. The strain variance is calculated from the buoyancy frequency, N^2, and a time mean buoyancy frequency, $\overline{N}^2$, obtained by applying the adiabatic levelling method of Bray and Fofonoff (1981).

$$\xi_z = \frac{(N^2 - \overline{N}^2)}{N^2} \qquad \text{(AA.4)}$$

The Garrett and Munk shear/strain ratio, R$_\omega$, is set to 3, but Kunze et al. (2006) used a data-set of CTD and LADCP stations and found a value closer to 7. Naveira Garabato et al. (2006) found values between 9-12 in the region of Drake Passage and the Scotia Sea, so for this study, a value of 10 was chosen to take account of the high mixing estimates obtained from measurements within the Southern Ocean. The diffusivities obtained in the analysis of a data-set of nearly 5000 WOCE CTD stations is similar to that of Sloyan (2006), but in that study, a value of $R_\omega = 3$ was used, resulting in lower estimates. Within the data-set, the top 150m and stations around the coast of Antarctica were removed because the assumptions used in the above derivation are not valid in these regions.

Appendix AB

Inverse Model Sections

Location	Code/Cruise	Date/Year	Reference/PO
Atlantic	A10	1992/3	Mueller
	A10	2003	Yoshikawa
	A11	1992/3	Saunders and King (1995)
Weddell Sea	S4A	1990	E. Fahrbach
Drake Passage	SR01	1990	W. Roether
	SR01b	1993/4/6/7/9, 2000/1/2/3/4/5/6	Cunningham et al. (2003), Bacon (2001/2),
Indian Ocean	I05	1987	Warren and O'Toole (1993)
	I05	2003	Bryden et al (2003)
	I06	1996	Park et al (2003)
	I08	1994/95	M. McCartney, T. Whitworth
	I09	1994/95	M. McCartney, T. Whitworh
Australia	SR03	1996	Rintoul and Sokolov (2000)
Pacific	P6E	1992	H. Bryden
	P6C	1992	M. McCartney
	P6W	1992	J. Toole
	P15	1996	J.Bullister and G. Johnson
	P17	1994	S. Jacobs
	P19	1992/93	J. Swift
	P6E	2003	Fukasawa
	P6W	2003	Watanabe
Antarctica	S4I	1996	T. Whitworth, J. Swift
Adelie Coast	S4Ib	1994	S. Rintoul
Ross Sea	S4P	1992	Koshlyakov, Richman

Appendix AC

Drake Passage Historical Sections

Ship	Month/Year	Project/Cruise/Country	Data Source
Meteor	Jan 1926	GER	NODC
Discovery	Apr 1927	UK	NODC
William Scoresby	Feb 1929	UK	NODC
Discovery II	Apr 1930	UK	NODC
Discovery II	Nov 1932	UK	NODC
Discovery II	Mar 1934	UK	NODC
Ob	Jun 1958	USA	NODC
Eltanin		USSR	NODC
Thomas Washington	Jan 1969	USA	NODC
Hudson	Feb 1970	CAN	NODC
Melville	Mar 1975	ISOS-USA	NODC
Melville	Apr 1975	ISOS-USA	NODC
Thompson	Feb 1976	ISOS-USA	NODC
Melville	Jan 1977	ISOS-USA	NODC
Yelcho	Apr 1979	ISOS-CH	NODC
Atlantis II	Feb 1980	ISOS-CH	NODC
Meteor	Jan 1990	WOCE-GER	NODC
Polarstern	Aug 1992	WOCE-GER	WHPO
JCR	Dec 1993	WOCE-UK	NOCS
JCR	Nov 1994	WOCE-UK	NOCS
Hesperides	Feb 1995	WOCE-SPA	CSIC
JCR	Nov 1996	WOCE-UK	NOCS
JCR	Jan 1998	WOCE-UK	NOCS
Hesperides	Feb 1998	DOVETAIL-SPA	CSIC
Hesperides	Nov 1998	DHARMA-SPA	CSIC
JCR	Mar 1999	ALBATROSS-UK	UEA(ANG)
JCR	Feb 2000	BAS-UK	NOCS
JCR	Nov 2000	NOCS/BAS-UK	NOCS

Ship	Month/Year	Project/Cruise/Country	Data Source
JCR	Dec 2001	NOCS/BAS-UK	NOCS
JCR	Dec 2002	NOCS/BAS-UK	NOCS
JCR	Dec 2003	NOCS/BAS-UK	NOCS
JCR	Dec 2004	NOCS/BAS-UK	NOCS
JCR	Dec 2005	NOCS/BAS-UK	NOCS
JCR	Dec 2006	NOCS/BAS-UK	NOCS

Key

JCR=RRS James Clark Ross

NODC=National Oceanographic Data Centre (USA), *www.nodc.noaa.gov*

WHPO=WOCE Hydrographic Project Office, *whpo.ucsd.edu*

UEA=University of East Anglia

BAS=British Antarctic Survey

NOCS=National Oceanography Centre, Southampton

ISOS=International Southern Ocean Study

CSIC= Consejo Superior de Investigaciones Cientificas (Spain)

Appendix AD

Inverse Model Additional Constraints

Section	Description	Constraint	Reference
Atlantic			
A10	Total Flux	-1.1 ± 0.5 Sv	OCCAM Study
A10	Brazil Current	-25 ± 10 Sv	McDonagh and King (2003)
	Brazil Current Recirculation	7.5 ± 5 Sv	As above
	Vema Channel AABW	2 ± 1 Sv	As above
	Brazil Basin AABW	3 ± 1 Sv	As above
	Cape Basin AABW	0 ± 0.5 Sv	As above
A11	Total Flux	-1.1 ± 0.5 Sv	OCCAM Study
	Falklands Current	45 ± 10 Sv	McDonagh and King (2003)
	Falklands Recirculation	-5 ±2 Sv	As above
	AABW (West)	6 ± 1 Sv	As above
	AABW (East)	0 ± 0.5 Sv	As above
Weddell	Total Flux	0 ± 0.5 Sv	Fahrbach et al. (1996)
SR01b	Total Flux	136 ± 7 Sv	SR01b sections
Indian			
I05	Total Flux	-12 ± 5 Sv	OCCAM Study
	Total Silicate	340±100 kmols^{-1}	McDonagh et al (2006)
	Aghulas Current	-69.7 ±4.3 Sv	Bryden et al (2003)
	Natal Valley (28.11<γ<28.23)	0.25 ± 0.25 Sv	Robbins and Toole (1997)
	Mozambique Basin (28.11<γ<28.23)	0.75 ± 0.75 Sv	As above
	Mozambique Basin (γ>28.23)	0.5 ± 0.5 Sv	As above
	Madagascar Basin	2.5 ± 2 Sv	As above

Section	Description	Constraint	Reference
	(28.11<γ<28.23)		
	Crozet Basin (28.11<γ<28.23)	1.5 ± 1 Sv	As above
	Crozet Basin (γ>28.23)	1.5 ± 1 Sv	As above
	Central Indian Basin (28.11<γ<28.23)	0 ± 0.5 Sv	As above
	Perth Basin (28.11<γ<28.23)	6 ± 3 Sv	As above
I09	Total flux	150 ± 7.5 Sv	OCCAM Study
SR03	Total flux	150 ± 7.5 Sv	Rintoul and Sokolov (2000)/Data Analysis
S4A	Total flux (Cosmonaut Sea)	-20 ± 10 Sv	BRIOS Analysis
	Total flux (Prdz Bay)	20 ±10 Sv	BRIOS Analysis
	Total flux (Adelie Land)	-6 ± 5 Sv	BRIOS Analysis
Pacific			
P6	Total flux	-14.2 ± 4.8 Sv	OCCAM Study
	Deep Water	0.75 ± 0.75 Sv	Wjiffels et al. (1999)
	Deep Water	0 ± 0.5 Sv	As above
	Deep Water	0 ± 0.5 Sv	As above
	Deep Water	-0.5 ± 0.5 Sv	As above
S4P	Total flux	0 ± 0.5 Sv	BRIOS Analysis
	Flux (80-103W)	-11± 5 Sv	As above
	Flux (103W-160E)	0 ± 2 Sv	As above
	Flux (160W-140E)	4 ± 5 Sv	As above

Appendix AE

Southern Ocean Inverse Model

Matlab Script	**Description**
Soim_1.m	This routine requires soim.mat (the entire hydrographic data set), an array containing the sections to be used in the model, an array describing the layout of the model, and an array defining the neutral density levels of the model. The routine calculates velocity and property fields, and applies corrections to the initial levels of no motion.
Get_area.m	This routine calculates the areas of each model box by defining a 1x1 degree grid covering each box.
Soim_surfaces_z.m	Uses WOCE Climatology to create mean property fields and property gradients for each box.
Soim_wind.m	Calculates Ekman fluxes across each section from the mean windstress fields in the NOC Climatology
Soim_2.m	Creates general model equations (E,y) containing mass, salt, heat and silicate equations.
Soim_means.m	Calculates property means for each section from the hydrographic data.
Surface Fluxes:	
Soim_wind_NOC.m	Extracts box-wide surface fluxes from NOC climatoogy
Soim_heat_2.m	Calculates mean heat fluxes over annual cycle.
Soim_airsea.m	Calculates annual mean surface fluxes for each box.
Soim_gm.m	Creates data and model covariance matrices, including error estimates from OCCAM analysis.
Soim_3.m	Adds surface flux constraints.
Soim_sort_basic_4.m	Resorts model equations in terms of properties enabling selection of tracer conservation to include in the model.
Soim_constraint_1.m	Adds additional model contraints obtained from observations and models.
Soim_gm2.m	Combines model data, performs inversion and calculates fluxes

Matlab Script	Description
	across each section. Outputs a structure array containing all of the model data (Results.mat).
Errors_1.m	Calculates flux errors across each section

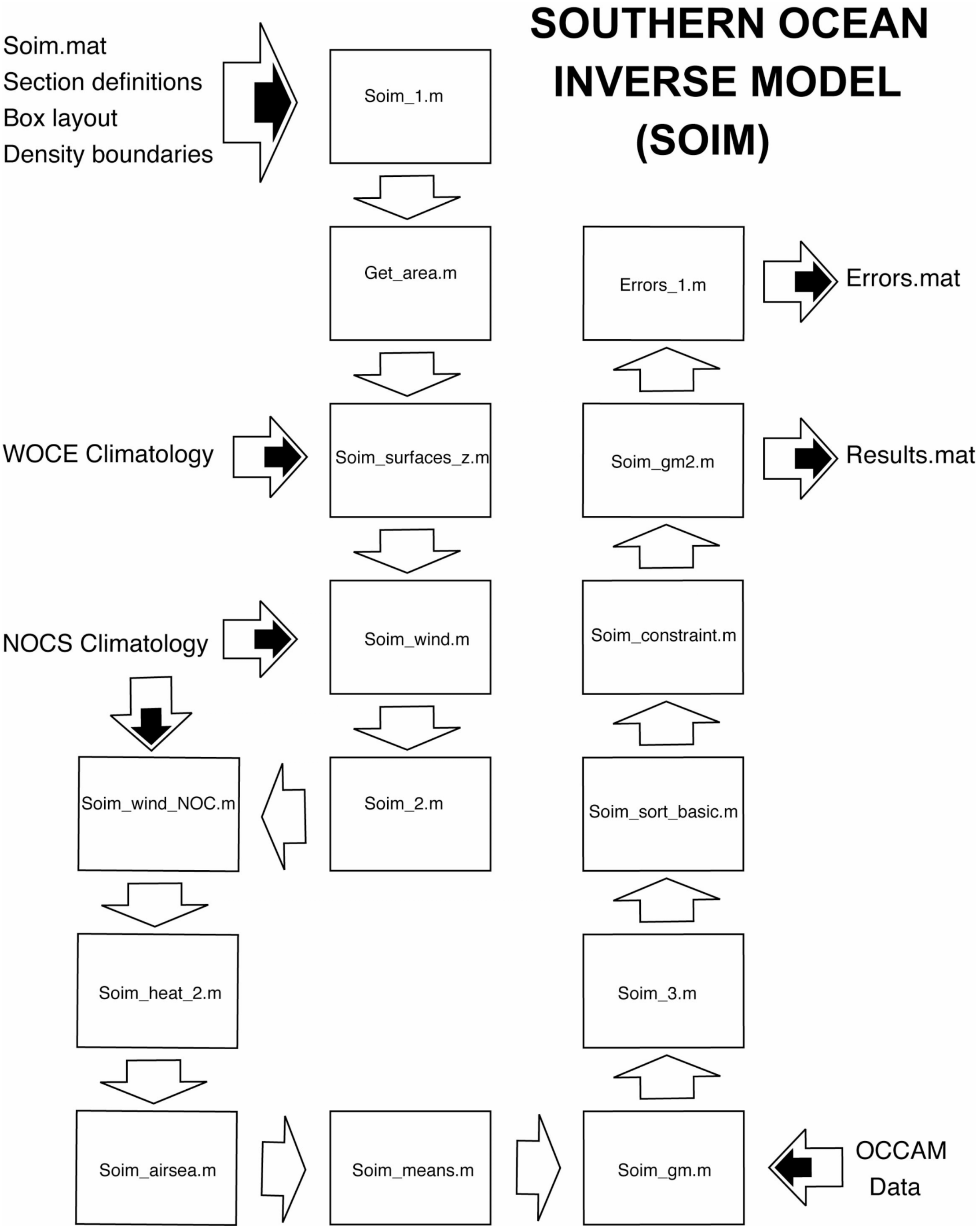

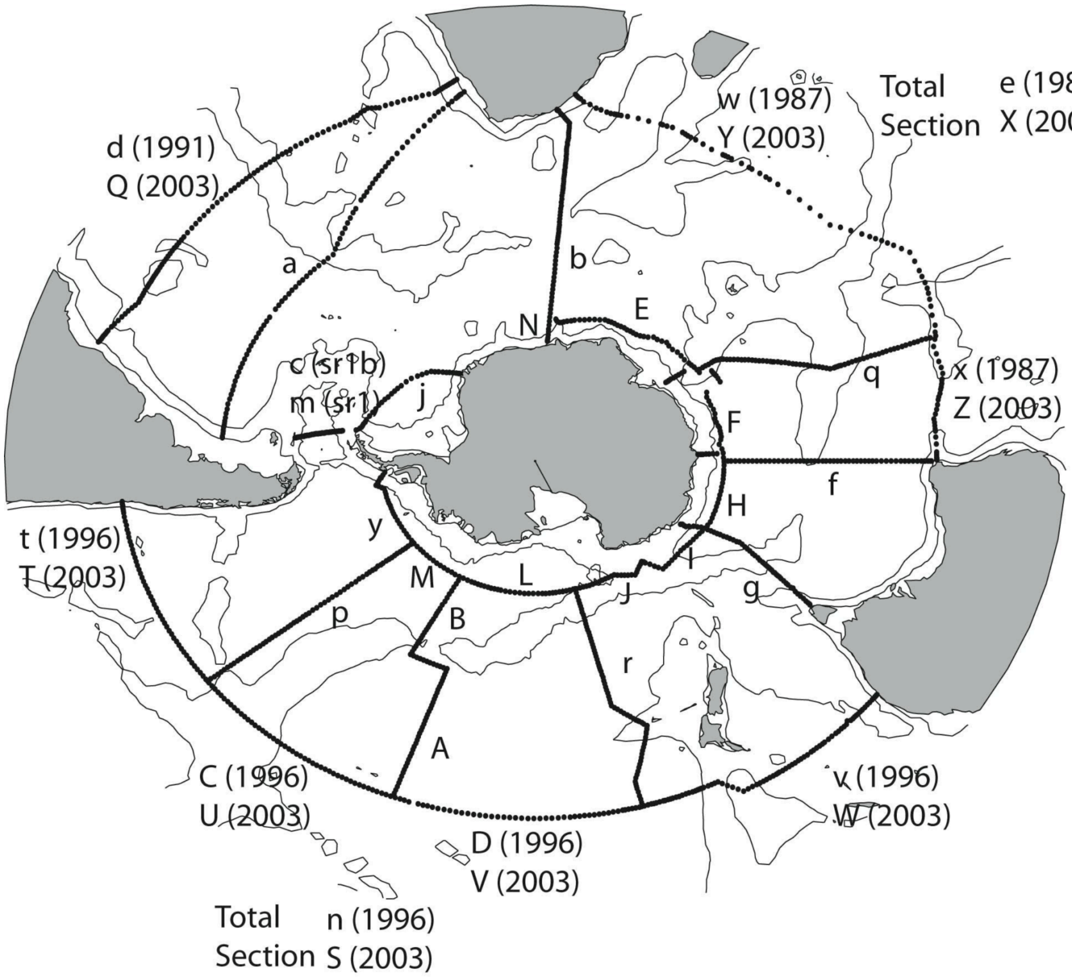

Figure AE2: Map of Southern Ocean showing locations of hydrographic sections in the data set soim.mat. The letters correspond to the symbols given to each section and are used by the model routines to perform the inverse analysis.

Appendix AF

Derivation of Gauss-Markov Estimators

The following is based on the derivations of Wunsch (1996) which examines the Oceanographic Inverse problem in great detail. The Gauss-Markov Theorem is based on the idea that it is possible to explicitly express the relationship between the estimate ($\tilde{x}$) and the observation (y) in terms of a matrix B:

$$\tilde{x} = By \tag{3.13}$$

The theory minimises the covariance matrix of $(\tilde{x} - x)$ to find the solution with minimum dispersion between the solution and the true value of x,

$$P_{x\tilde{x}} = \left\langle (\tilde{x} - x)(\tilde{x} - x) \right\rangle = \left\langle (By - x)(By - x)^T \right\rangle \tag{3.14}$$

(In general, the covariance/second-moment matrix of a variable 'a' is $\mathrm{cov}(a) = R_{aa} =< aa^T >$, and is an important variable in the following analysis).

Substituting in equation 3.13 into 3.14,

$$P_{x\tilde{x}} = \left\langle (By - x)(By - x) \right\rangle \tag{AF1}$$

Expanding AF1, and using the fact that $(AB)^T = B^T A^T$ leads to:

$$P = B\left\langle yy^T \right\rangle B^T - \left\langle xy^T \right\rangle B^T - B\left\langle yx^T \right\rangle + \left\langle xx^T \right\rangle \tag{AF2}$$

Using the notation for the second-monent matrices (cov(a)) leads to:

$$P = BR_{yy}B^T - R_{xy}B^T - BR_{xy}^T + R_{xx} \tag{AF3}$$

The next step uses a large matrix identity (equation 3.1.26 in Wunsch 1996):

$$ACA^T - BA^T - AB^T = (A - BC^{-1})C(A - BC^{-1}) - BC^{-1}B^T \tag{AF4}$$

Leading to the modified equation for P_{xx}:

$$P = (B - R_{xy}R_{yy}^{-1})R_{yy}(B - R_{xy}R_{yy}^{-1}) - R_{xy}R_{yy}^{-1}R_{xy}^T + R_{xx} \tag{AF5}$$

It can be shown that P is at a minimum when the first term on the right hand side of AF5 is zero, resulting in the expression for B:

$$B = R_{xy}R_{yy}^{-1} \tag{AF6}$$

and therefore the minimum variance estimate of x is:

$$\tilde{x} = R_{xy}R_{yy}^{-1}y \tag{AF7}$$

Substituting (AF6) into the original definition for B results in the following expression (after cancelling out equal terms):

$$P_{x\tilde{x}} = R_{xx} - R_{xy}(R_{xy}R_{yy}^{-1})^T \qquad \text{(AF8)}$$

Expressions for R_{yy} and R_{xy} can be derived from the original equation relating x to y, y=Ex+n. Therefore, $R_{yy} = \left\langle yy^T \right\rangle = E\left\langle xx^T \right\rangle + \left\langle nn^T \right\rangle = ER_{xx}E^T + R_{nn}$, where cross terms of x and n are assumed to be zero.. In the same fashion,

$$R_{xy} = \left\langle xy^T \right\rangle = \left\langle x(Ex+n)^T \right\rangle = R_{xx}E^T$$

Substituting these values back into the expression for P (AF8), leads to an expression for P in terms of the covariance matrices that we can determine from observations.

$$P_{x\tilde{x}} = R_{xx} - R_{xx}E^T(ER_{xx}E^T + R_{nn})^{-1}ER_{xx} \qquad \text{(AF9)}$$

This leads to expressions for the noise and solution vectors

$$\tilde{x} = R_{xx}E^T\left(ER_{xx}E^T + R_{nn}\right)^{-1}y \qquad \text{(3.15)/(AF10)}$$

$$\tilde{n} = \left\{I - ER_{xx}E^T\left(ER_{xx}E^T + R_{nn}\right)^{-1}\right\}y \qquad \text{(3.16)/(AF11).}$$

These solutions can then be used to calculate the relevant unknowns from the inverse model and form the basis of the inverse model used in this study.

References

Aagaard, K., A.T. Roach, and J.D. Schumacher, 1985: On the wind-driven variability of the flow through Bering Strait, *J. Geophys. Res*., **90**, 7213-7221.

Aoki, S., N.L. Bindoff, and J.A. Church, 2005: Interdecadal water mass changes in the Southern Ocean between 30°E and 160°E. *Geophys. Res. Lett*. **32** (7) 7607-7611.

Andrews, D.G., and M.E. McIntyre, 1978: Generalised Eliassen-Palm and Charney-Drazin theorems for waves on axisymmetric mean flows in compressible atmospheres. *J. Atmos. Sci*. **35**. 175-185.

Andrews, D.G., C.B. Leovy, and J.R.Holton, 1987: Middle Atmosphere Dynamics (book), pub: Elsevier, 489 pp.

Assmann, K.M., and R. Timmermann, 2005: variability of dense water formation in the Ross Sea. *Ocean Dynamics*, **55**, 68-87.

Bacon, S., 2002: RRS James Clark Ross cruise 67: 19 Nov-17 Dec 2001: Drake Passage repeat hydrography WOCE Southern repeat section 1b. Southampton Oceanography Centre.

Baker, D.J.Jr, 1982: A note on Sverdrup balance in the Southern Ocean, *J. Mar. Res*., **40** (suppl), 21-26.

Bamber, J.L., and A.J. Payne, 2004: Mass Balance of the Cryosphere- Observations and Modelling of contemporary and future changes. (eds) CUP, Cambridge.

Banks, H.T., R.A. Woods, J.M. Gregory, T.C. Johns and G.S. Jones, 2000: Are observed decadal changes in intermediate water masses a signature of anthropogenic climate change? *Geophys. Res. Lett*. **27** (18) 2961-2964.

Banks, H.T., and N.L. Bindoff, 2003: Comparison of observed temperature and salinity changes in the Indo-Pacific with results from a coupled climate model HadCM3: Processes and mechanisms. *J. Climate*. **16**, 156-166.

Beal, L.M., and H.L. Bryden, 1997: Observation of an Agulhas undercurrent, *Deep-Sea Res., Part I.*, **44**, 1715-1724.

Beckmann, A., and R. Timmermann, 2001: Circumpolar influences on the Weddell Sea: indication of an Antarctic circumpolar coastal wave. *J. Climate*, **14**, 3785-3792.

Belkin, I.M., and A.L. Gordon, 1996: Southern Ocean fronts from the Greenwich meridian to Tasmania. *J. Geophys. Res.*, **101**, 3675-3696.

Bindoff. N.L. and T.J. McDougall, 1994: Diagnosing climate change and ocean ventilation using hydrographic data. *J. Phys. Oceanogr*. **24** 1137-1152.

Bindoff, N.L., M.A. Rosenberg, and M.J. Warner, 2000: On the circulation and water masses over the Antarctic continental slope and rise between 80 and 150 E., *Deep-Sea Res. Part II.*, **47**, 2299-2326.

Bindoff, N.L. and T.J. McDougall, 2000: Decadal changes along an Indian Ocean section at 32° S and their interpretation. *J. Phys. Oceanogr*. **30**, 1207-1222.

Botnikov, V.N., 1963: Geographical postition of the Antarctic Convergence zone in the Southern Ocean. *Sov. Antarct. Exped. Inf. Bull.*, Engl transl.

Bray, N.A., and N.P. Fofonoff, 1981: Available potential energy for MODE eddies, *J. Phys. Oceanogr.*, **11**, 30-46.

Bryden, H.L., and S.A. Cunningham, 2003: How wind forcing and air-sea heat exchange determine the meridional temperature gradient and stratification for the Antarctic Circumpolar Current. *J. Geophys. Res*., **108**., Bryden, H.L., and L.M. Beal, 2001: Role of the Agulhas current in Indian Ocean circulation and associated heat and freshwater fluxes. *Deep-Sea Res. Part I.,* **44**, 1715-1724.

Bryden, H.L. et al. 2003: RRS Charles Darwin Cruise 139, 01 Mar-15 Apr 2002, Trans-Indian Hydrographic section across 32 S, *Southampton Oceanography Centre report*, No. **45**, 122pp.

Bryden, H.L., E.L. McDonagh, and B.A. King, 2003: Changes in Ocean Water Mass properties: Oscillations or trends? *Science*, **300**, 2086-2088.

Bryden, H.L., L.M. Beal, and L.M. Duncan, 2005: Structure and transport of the Agulhas current and Its temporal variability*, Journal of Oceanography*, **61**, 479-492.

Bryden, H.L., H.R. Longworth, and S.A. Cunnungham, 2005: Slowing of the Atlantic meridional overturning circulation at 25 N, *Nature***, 438(1)**, doi:10.1038/nature04385.

Callahan, J.E., 1972: The structure and circulation of Deep water in the Antarctic. *Deep-Sea Res*., **19**, 563-575.

Conkwright, M.E., R.A. Lorcarnini, H.E. Garcia, T.D. O'Brien, T.P. Boyer, C. Stephens, J.I. Antonov, 2002: World Ocean Atlas 2001: Objective analyes, Data Statistics and Figures, CD-ROM documentation. NODC, Silver Spring, MD. 17pp.

Cunningham, S.A., S.G. Alderson, B.A. King and M.A. Brandon, 2003: Transport and variability of the Antarctic Circumpolar Current in Drake Passage. *J. Geophys. Res-Oceans*, **108(C5)**, 8084.

Davis, C. H., Li, Y., McConnell, J. R., Frey, M. M. & Hanna, E. 2005: Snowfall-driven growth in East Antarctic ice sheet mitigates recent sea-level rise. *Science*, **308**, 1898–1901.

Deacon, G., 1937: The Hydrology of the Southern Ocean. The Discovery Reports. XV, 1-124.1937.

Dickson B., I. Yashayaev, J. Meincke, B. Turrell, S. Dye, J. Holfort, 2002: Rapid freshening of the deep North Atlantic Ocean over the past four decades. *Nature* **416** 832-836.

Döös, K. and D.J. Webb, 1994: The Deacon Cell and the other meridional cells of the Southern Ocean*. J. Phys. Oceanogr*. **24**, 429-442.

Fahrbach, E., G. Rohardt, M. Schroder, and V. Strass, 1994: Transport and Structure of the Weddell Sea., *Ann. Geophys*., **12**, 840-855.

Ferron, B., and J. Marotzke, 2003: Impact of 4D-variational assimilation of WOCE hydrography on the meridional circulation of the Indian Ocean. *Deep-Sea Res. Part II.*, **50**, 2005-2021.

Ganachaud, A., Large scale oceanic circulation and fluxes of freshwater, heat, nutrients and oxygen, Ph.D. Thesis, 267, pp,. Mass. Inst. of Technol./Woods Hole Oceanogr. Inst. Joint Program, Cambridge.

Ganachaud, A. and C. Wunsch, 2000: Improved estimates of global ocean circulation, heat transport and mixing from hydrographic data. *Nature* **408**, 453-457.

Ganachaud, A., 2003a: Large-scale mass transports, water mass formation and diffusivities estimated from thr World Ocean Circulation Experiment (WOCE) hydrographic data. *J. Geophys. Res.*, **108(C7)**, 3213.

Ganachaud, A., 2003b: Error budget of inverse box models: The North Atlantic. *J. Atmos. Oceanic Technol,,* **20**, 1641-1655.

Ganachaud,. A., C. Wunsch, J. Marotzke, and J. Toole, 2000: The meridional overturning and large-scale circulation of the Indian Ocean. *J. Geophys. Res.,* **105**, 26117-26134.

Gille, S.T., 1999: Mass, Heat, and salt transport in the southeastern Pacific: A Circumpolar Current inverse model. *J. Geophys. Res*., **104(C3)**, 5191-5209.

Gille, S., 2002: Warming of the Southern Ocean since the 1950's. *Science* **295** 1275-1277.

Gregg, M.C., 1987: Diapycnal mixing in the thermocline, A review. *J. Geophys. Res*, **92**, 9686-9698.

Gnanadesikan, A. and R.W. Hallberg, 2000: On the relationship of the Circumpolar Current to Southern Hemisphere winds in coarse-resolution ocean models. *J. Phys. Oceanogr.*. **30**, 2013-2034.

Gordon, A.L., 1967: Structure of Antarctic Waters between 20 W and 170 W, *Antarctic Map folio series*, **6**, V. Bushnell, ed. American Geographical Society.

Gouretski, V.V., 1999: The large-scale thermohaline structure of the Ross Gyre. In Spezie G. Manzella GMR (eds) *Oceanography of the Ross Sea*. Springer, pp 77-102.

Gouretski, V.V., and K. Jancke, 2001: Systematic errors as the cause for an apparent deep-water property variability: global analysis of the WOCE and historical hydrographic data. *Progress in Oceanography.* **48**, 337-402.

Gouretski, V. V. and K. P. Koltermann, 2004: Berichte des Bundesamtes für Seeschifffahrt und Hydrographie Nr. 35/2004.

Grist, J. P. and S. A. Josey, 2003: Inverse analysis adjustment of the SOC air-sea flux climatology using ocean heat transport constraints. *J. Climate* **20**, 3274-3295.

Hanawa, K., and L.D. Talley, 2001: Mode Waters, In *Ocean Circulation and Climate*, Siedler et al. (2001), International Geophysics Series. pp 373-386.

Hellmer, H.H., and A. Beckmann, 2001: The Southern Ocean: A Ventilation Contributor with Multiple Sources. *Geophys. Res. Lett.*, **28(15)**, 2927-2930.

Heywood, K.J., M.D. Sparrow, J. Brown, and R.R. Dickson, 1999: Frontal Structure and Antarctic Bottom watr flow through the Princess Elizabeth Trough, Antarctica. *Deep-Sea Res. Part I.*, **46**, 1181-1200.

Holfort, J., and G. Siedler, 2001: The meridional oceanic transports of heat and nutrients in the South Atlantic. *J. Phys. Oceanogr.*, **31**, 5-29.

Houghton, J., 2002: The Physics of Atmospheres. CUP, pp. 336.

Hughes, C. W. 1997: Comments on "on the obscurantist Physics of Form Drag in Theorising about the Circumpolar Current. *J. Phys. Oceanogr.*,**27**: 209-210.

Hughes, C.W., and E.R. Ash, 2001: Eddy forcing of the mean flow in the Southern Ocean, *J. Geophys. Res.-Oceans*. **106(C2)**, 2713-2722.

Hughes, C.W., 2002: Sverdrup-like theories of the Antarctic Circumpolar Current. *J. Mar. Res,.***60**: 1-17.

Jackett, D. R. and T. J. McDougall, 1997: A neutral density variable for the world's oceans. *J. Phys. Oceanogr.* **27**, 237-263.

Jacobs, S. S., H. H. Hellmer, C. S. M. Doake, A. Jenkins and R. M. Frolich, 1992: Melting of Ice Shelves and the Mass Balance of Antarctica. *Journal of Glaciology,* **38**(130): 375-387.

Johnson, G.C., and H.L. Bryden, 1989: On the size of the Antarctic Circumpolar Current. *Deep-Sea Res*. **56**, 329-347.

Johnson, G. C., D. L. Rudnick, and B. A. Taft, 1994: Bottom water variability in the Samoa Passage. *J. Mar. Res.* **52** 177–196.

Johnson G.C. and A.H. Orsi, 1997: Southwest Pacific Ocean Water-Mass Changes between 1968/9 and 1990/91. *J. Climate*. **10** 306-316.

Josey, S. A., E. C. Kent and P. K. Taylor, 1998: The Southampton Oceanography Centre (SOC) Ocean - Atmosphere Heat, Momentum and Freshwater Flux Atlas. Southampton Oceanography Centre Report No. 6, 30 pp. plus figures.

Karsten, R., and J. Marshall, 2002: Constructing the residual circulation of the Antarctic Circumpolar Current from observations. *J. Phys. Oceanogr*. **32**, 3315-3327.

Kunze, E., E. Firing, J. Hummon, T. Chereskin and A. Thurnherr, 2006: Global Abyssal Mixing Inferred from Lowered ADCP Shear and CTD Strain Profiles. *J. Phys. Oceanogr.***36(8)**. 1553-1576.

Lee, M.M., A. Coward, 2003: Eddy mass transport for the Southern Ocean ina na eddy-permitting global ocean model. *Ocean Modelling*, **5(3)**, 249-266.

Ledwell, J.R., A.J. Watson, and C.S. Law, 1998: Mixing of a tracer on the Pycnocline. *J. Geophys. Res. (Oceans).* **103(C10)**, 21,499.

Locarnini, R.A., 1994: water masses and circulation in the Ross Gyre and environs. PhD Thesis, Texas A&M University, 87 pp.

Macdonald, A., 1995: Oceanic fluxes of mass, heat and freshwater: A global estimate and perspective., Ph.D. Thesis, Mass. Inst. of Technol./Woods Hole Oceanogr. Inst. Joint Program, Cambridge.

MacDonald, A., 1998: The global ocean circulation: A hydrographic estimate and regional analysis, *Prog. Oceanogr.*, **41**, 281-382.

Mantyla, A. 1994: The treatment of inconsistencies in Atlantic Deep Water Salinity Data.*Deep Sea Res. Part 1,* **41**, 1387-1405.

Marshall, J., and T. Radko, 2003: Residual Mean solutions for the Antartic Circumpolar Current and its Associated Overturning Circulation. *J. Phys. Oceanogr.* **33(11),** 2341-2354.

Mauritzen, C., K.L. Polzin, M.S. McCartney, R.C. Millard, and D.E. West-Mack, 2000: Evidence in hydrography and density finestructure for enhanced vertical mixing over the Mid-Atlantic Ridge in the western Atlantic. *J. Geophys. Res.*, **107(C10)**, 3147.

McCartney, M.S., 1977: Subantarctic Mode Water., *Deep-Sea Res*., **24**, 103-119.

McCartney, M.S., 1982: The subtropical recirculation of mode waters. *J. Mar. Res*., **40**(suppl), 427-464.

McDonagh, E.L., and B.A. King, 2005: Oceanic fluxes in the South Atlantic, *J. Phys. Oceanogr*., **35**, 109-122.

McDonagh, E.L., H.L. Bryden, B.A. King, and R.J. Saunders, 2006: The circulation of the Indian Ocean at 32 S. *Prog. Oceanogr. submitted*

McDougall, T.J., 1991: Parameterising mixing in Inverse Models, paper presented at Parameterization of small-scale processes, Hawaiian Aha Huliko'a Winter Workshop, Univ. of Hawaii at Manoa, Honolulu.

McIntosh, P.C., and T.J. McDougall, 1996: Isopycnal Averaging and the Residual Mean Circulation. *J. Phys. Oceanogr.* **26**, 1655-1660.

McIntosh, P.C., and S.R. Rintoul, 1997: Do box inverse models work? *J. Phys. Oceanogr*., **27**, 291-308.

Meredith, M.P., and C.W. Hughes, 2005: On the sampling timescale required to reliably monitor interannual variability in the Antarctic circumpolar transport. *Geophys. Res. Lett.*, **32**, L03609.

Molinelli, E.T., 1981: The Antarctic influence on Antarctic Intermediate water. *J. Mar. Res*. **39**, 267-293.

Moore, J.K., M.R. Abbott and J.G. Richmann, 1997: Variability in the location of the Antarctic Polar Front (90-20 W) from satellite sea surface temperature data. *J. Geophys. Res.,* **102**: 27,825-27,833.

Munk, W., 1966: Abyssal Recipes. *Deep-Sea Res*, **13**, 707-730.

Munk, W., and E. Palmen, 1951: Note on dynamics of the Antarctic Circumpolar Current. *Tellus*, **3**, 53-55.

Munk, W., and C. Wunsch, 1998: Abyssal Recipes II: energetics of tidal and wind mixing. *Deep−Sea Res*. **45**, 1976−2000.

Naveira Garabato, A.C., K.J. Heywood, and D.P. Stevens, 2002: Modification and pathways of Southern Ocean Deep Waters in the Scotia Sea. *Deep Sea Res*., **49**, 681-705.

Naveira Garabato, A.C., D.P. Stevens and K.J. Heywood, 2003: Water Mass Conversion, Fluxes, and Mixing in the Scotia Sea Diagnosed by an Inverse Model. *J. Phys. Oceanogr*., **33(12),** 2565-2587.

Naveira Garabato, A.C., K.L. Polzin, B.A. King, K.J. Heywood, and M. Visbeck, 2004: Widespread intense turbulent mixing in the Southern Ocean, *Science,* **303**, 210-213.

Naveira Garabato, A.C., D.P. Stevens, A.J. Watson, and W. Roether, 2007: Short-circuiting of the overturning circulation in the Antarctic Circumpolar Current. *Nature*, **447**(7141), 194-7.

Olbers, D.,1998: Comments on "on the obscurantist Physics of Form Drag in Theorising about the Circumpolar Current*, J. Phys. Oceanogr.,* **28**: 1647-1654.

Olbers, D., D. Borowski, C. Volker and J.O Wolff, 2004: The dynamical balance, transport and circulation of the Antarctic Circumpolar Current. *Ant. Sci*. **16(4),** 439-470.

Olbers, D., and M. Visbeck 2005; A model of the Zonally averaged Stratification and Overturning in the Southern Ocean*. J. Phys. Oceanogr*. **35(7**), 1190-1205.

Orsi, A.H., T. Whitworth III, and W.D. Nowlin Jr., 1995: On the meridional extent and fronts of the Antarctic Circumpolar Current. *Deep-Sea Res I* **42** 641-673.

Orsi, A.H., G.C. Johnson and J.L. Bullister, 1999: Circulation, mixing and production of Antarctic Bottom Water, *Prog. Oceanogr.*, **43**, 55-109.

Orsi, A. H., T. Whitworth III, 2005: Hydrographic Atlas of the World Ocean Circulation Experiment (WOCE). Volume 1: Southern Ocean (eds. M. Sparrow, P. Chapman and J. Gould), International WOCE Project Office, Southampton, U.K., ISBN 0-904175-49-9.

Osborn, T.R., 1980: Estimates of the local rate diffusion from dissipation measurements. *J. Phys. Oceanogr*. **10**, 83-89.

Palmer M. D., A.C. Naveira Garabato, J. Stark, J. Hirschi, J. Marotzke, 2007: The influence of diapycnal mixing on quasi-steady overturning states in the Indian Ocean*. J. Phys. Oceanogr*,, [in press]

Park, Y.H., E. Charriaud, P. Craneguy, and A. Kartavtseff, 2001: Fronts, transports, and the Weddell Gyre at 30E between Africa and Antarctica., *J. Geophys. Res,* **106**, 2857-2879.

Piola, A.R., and A.L. Gordon, 1989: Intermediate water in the southwestern South Atlantic, *Deep-Sea Res.*, **36**, 1-16.

Reid, J.L., 1986: On the total geostrophic circulation of the South Pacific Ocean: Flow patterns, tracers and transports. *Prog. Oceanogr.*, **16**, 1-61.

Radko, T., and J. Marshall, 2006: The Antarctic Circumpolar Current in Three Dimensions. *J. Phys. Oceanogr***. 36(4**), 651-669.

Ribbe, J., and M. Tomczak, 1997: Effect of the Missing Indonesian Throughflow in the Fine Resolution Antarctic Model. *J. Phys. Oceanogr.*,**27(3)**, 445-455.

Rintoul, S.R., and J.L. Bullister, A late winter hydrographic section from Tasmania to Antarctica, *Deep-Sea Res., Part I.*, **46**, 1417-1454.

Rintoul, S. and S. Sokolov, 2001: Baroclinic transport variability of the Antarctic Circumpolar Current south of Australia (WOCE repeat section SR3). *J. Geophys Res.* **106** 2815-2832.

Rintoul, S.R., C.W. Hughes, and D. Olbers 2001: The Antarctic Circumpolar Current System. Chapter 4.6, p 271-302, *Ocean Observing and Climate*. see (Siedler et al. 2001).

Rintoul, S.R., and M.H. England, 2002: Ekman Transport dominates air-sea fluxes in driving variability of Subantarctic Mode Water. *J. Phys. Oceanogr.*, **32**, 1308-1321.

Roach, A.T., K. Aargaard, C.H. Pease, S.A. Salo, T. Weingartner, V. Pavlov, adn M. Kulakov, 1995: Direct measurements of transport and water properties through Bering Strait, *J. Geophys. Res.*, **100**, 18443-18457.

Robbins, P. E. and J. M. Toole, 1997: The dissolved silica budget as a constraint on the meridional overturning circulation in the Indian Ocean. *Deep-Sea Res.* **41**, 143-168.

Roether, W., R. Schlitzer, A. Putzka, P. Beining, K. Bulsiewicz, G. Rohardt, and F. Delahoyde, 1993: A chlorofluoromethane and hydrographic section across Drake Passage: Deep water ventilation and meridional property transport. *J. Geophys. Res.,* **98**(C8), 14423-14436.

Sallee, J.B., N. Wienders, K. Speer, and R. Morrow, 2006: Formation of subantarctic mode water in the southeastern Indian Ocean. *Ocean Dynamics*, **56**, 525-542.

Saunders, P. 1986: The Accuracy of measurements of Salinity, Oxygen and Temperature in the Deep Ocean. *J. Phys. Oceanogr*. 189-195.

Saunders, P., and B.A. King, 1995: Oceanic fluxes on the WOCE A11 section, *J. Phys. Oceanogr.,* **25**, 1942-1958.

Schmitz, W.J. 1996: On the World Ocean Circulation, Vol. II: The Pacific and Indian Oceans/A Global Update. Woods Hole Oceanographic Institution, Technical report, WHOI-96-08, 237 pp.

Schott, F.A., M. Dengler, R. Schoenefeldt, 2002: The shallow overturning circulation of the Indian Ocean. *Prog. Oceanogr*., **53**, 57-103.

Schroder, M., and E. Fahrbach, 1999: On the structure and the transport of the eastern Weddell Gyre. *Deep-Sea Res. Part II*., **46(1),** 501-527.

Shaffer, G., S. Hormazabal, O. Pizarro, M. Ramos, 2004: Circulation and variability in the Chile Basin. *Deep-Sea Res. Part I*, **52**, 1367-1386.

Siedler, G., J. Church, and J. Gould (eds.), 2001: *Ocean Circulation and Climate: Observing and Modelling the Global Ocean*. International Geophysics Series (77) Academic Press, London.

Sievers, M.A., and W.J. Emery, 1978: Variability of the Antarctic polar frontal zone in the Drake Passage- Summer 1976-1977. *J. Geophys. Res*., **83(C6)**, 3010-3022.

Sievers M.A., and W.D. Nowlin Jr. 1984: The stratification and water masses at Drake Passage. *J. Geophys. Res.* **89** 10,489-10,514.

Sloyan, B. M. and S. R. Rintoul, 2001: The Southern Ocean limb of the global deep overturning circulation. *J. Phys. Oceanogr.* **31**, 143-173.

Sloyan., B.M. and S.R. Rintoul, 2000: Estimates of area-averaged diapycnal fluxes from basin-scale budgets, *J. Phys. Oceanogr*, **30**, 2320-2341.

Sloyan, B.M., and S.R. Rintoul, 2001b: Circulation, renewal, and modification of Antarctic Mode and Intermediate Water. *J. Phys. Oceanogr*. **31**, 1005-1030.

Sloyan, B.M., 2005: Spatial variability of mixing in the Southern Ocean. *Geophys. Res. Lett.*, **32**,L18603, doi:10.1029/2005GL023568.

Speer, K. and E. Tziperman, 1990: Convection from a source in an ocean basin. *Deep-Sea Res.*, **37**, 431-446.

Speer, K., and E. Tziperman, 1992: Rates of Water Mass formation in the North Atlantic Ocean. *J. Phys. Oceanogr*., **22(1)**, 93-104.

Speer, K., S. R. Rintoul and B. Sloyan, 2000: The Diabatic Deacon Cell. *J. Phys. Oceanogr*. **30**, 3212-3222.

Sprintall, J., 2003: Seasonal to interannual upper-ocean variability in the Drake Passage. *J. Mar. Res.,***61**: 27-57.

Srinivasan, A., C.G.H. Rooth, Z. Top, and D.B. Olson, 2000: Abyssal upwelling in the Indian Ocean: Radiocarbon diagnostics. *J. Mar. Res*., **58**, 755-778.

Stommel, H., 1957: A survey of ocean current theory. *Deep-Sea Res*. **4**, 149-184.

Talley, L.D., 1996: Antarctic Intermediate Water in the South Atlantic. *The South Atlantic: Present and Past circulation*. G. Wefer, W.H. Berger, G. Siedler, and D.J. Webb, Eds. Springer-Verlag. 219-238.

Talley, L.D., 2003: Shallow, intermediate and deep overturning components of the global heat budget, *J. Phys. Oceanogr.*, **33**, 530-560.

Talley, L. D., J. L. Reid and P. E. Robbins, 2003: Data-based meridional overturning streamfunctions for the global ocean. *J. Climate* **16**, 3213-3226.

Thompson, D.W.J., and S. Solomon, 2002: Interpretation of recent southern hemisphere climate change. *Science*, **296**, 895-899.

Timmermann, R., A. Beckmann, and H.H. Hellmer, 2002: Simulation of ice-ocen dynamics in the Weddell Sea. Part I: model configuration and validation. *J. Geophys. Res.* **107(C3),** doi: 10.1029/2000JC000471.

Toole, J., and B.A. Warren, 1993: A hydrographic section across the sub-tropical south Indian Ocean, *Deep-Sea Res., Part I.*, **40**, 1973-2019.

Townsend, R.D., and D.R. Johnson, 1985: A Diagnostic Study of the Isentropic Zonally averaged Mass Circulation during the first GARP Global Experiment. *J. Atmos. Sci***., 42(15),** 1565-1579.

Tsimplis, M.N., S. Bacon, and H.L. Bryden, 1998: The circulation of the sub-tropical South Pacific derived from hydrographic data, *J. Geophys. Res.*, **103**, 21433-21468.

Tsuchiya, M. and L.D. Talley, 1998. A Pacific hydrographic section at 88oW: water property distribution. *J. Geophys. Res.*, **103**, 12899-12918.

Warren, B.A., J.H. LaCasce, and P.E. Robbins, 1996: On the obscurantist physics of ‘form drag’ in theorizing about the circumpolar current. *J. Phys. Oceanogr.*, **26**, 2297-2301.

Webb, D.J., 1993: A simple model of the effect of the Kerguelen Plateau on the strength of the Antarctic Circumpolar Current. *Geophys. Astrophys. Fluid Dyn*. **70**, 57-84.

Whitworth, T. III., 1980: Zonation and geostrophic flow of the Antarctic Circumpolar Current at Drake Passage. *Deep-Sea Res.,***27**(7): 497-507.

Whitworth III, T, 1983: Monitoring the transport of the Antarctic Circumpolar Current at Drake Passage. *J. Phys. Oceanogr.* **13**, 2045-2057.

Whitworth, T., III, and R.G. Peterson, 1985: Volume Transport of the Antarctic Circumpolar Current from bottom pressure measurements. *J. Phys. Oceanogr.*, **15**: 810-816.

Wijffels, S.E., R.W. Schmidt, H.L. Bryden, and A. Stigebrandt, 1992: Transport of freshwater by the oceans*, J. Phys. Oceanogr.*, **24**, 1666-1679.

Wijffels, S., J. Toole and R. Davis, 2001. Revisiting the South Pacific subtropical circulation: A synthesis of World Ocean Circulation Experiment observations along 32°S. *J. Geophys. Res.* **106**, 19481-19514.

Wijffels, S.E., 2001: Ocean transport of freshwater, *Ocean Circulation and Climate*, Siedler et al. (2001), International Geophysical Series, pp 475-488.

Wijffels, S.E., J. Sprintall, M. Fieux, and N. Bray, 2002: The JADE and WOCE i10/IR6 Throughflow sections in the southeast Indian Ocean, Part 1:water mass distribution and varaibility. *Deep-Sea Res, Part II.*, **49(7)**, 1341-1362.

Williams, A.P., S. Bacon, and S.A. Cunningham, 2006: Variability of the Lower Circumpolar deep water in Drake Passage 1926-2004., *Geophys. Res. Lett.* **33**, L03603.

Wingham, D. J., Ridout, A., Scharroo, R., Arthern, R. & Shum, C. K. 1998: Antarctic elevation change from 1992 to 1996. *Science*, **282**, 456–458.

Wingham, D.J., A. Shepherd, A. Muir, and G.J. Marshall, 2006: Mass balance of the Antarctic Ice Sheet. *Phil. Trans. R. Soc. A*., **364,** 1627-1635.

Wong, A.P.S., N.L. Bindoff, and J.A. Church, 1999: Large-scale freshening of intermediate waters in the Pacific and Indian Oceans, *Nature*, **400**, 440-443.

Woodgate, R.A., and K. Aagaard, 2005: Revising the Bering Strait freshwater flux into the Arctic Ocean. *Geophys. Res. Lett*., **32**, L02602.

Wunsch, C., 1979: The North Atlantic general circulation west of 50W determined by inverse methods., *Rev. Geophys*., **16**, 583-620.

Wunsch, C., 1996: The Ocean Circulation Inverse Problem. Cambridge University Press, 442 pp.

Wunsch, C., and R. Ferrari, 2004: Vertical Mixing, Energy and the general circulation of the oceans. *Ann. Rev. Fluid Mech*, **36**, 281-314.

Wust, G., 1935: Die Stratosphare des Atlantischen Ozeans. Wissenschaftliche Ergebnisse der Deutschen Atlantischen Expedition auf dem Forshungs und Vermessungsschiff, Meteor 1925-1927.

You, Y., 1999: Dianeutral mixing, transformation and transport of Antarctic Intermediate water in the South Atlantic Ocean. *Deep-Sea Res*. **46**, 393-435.